Highly efficient absorption heat pump and refrigeration systems based on ionic liquids
Fundamentals & Applications

Wang, Meng

DOI
10.4233/uuid:0913c6df-9f01-42a5-add2-302ff0f2b156

Publication date
2019

Document Version
Final published version

Citation (APA)
Wang, M. (2019). *Highly efficient absorption heat pump and refrigeration systems based on ionic liquids: Fundamentals & Applications*. [Dissertation (TU Delft), Delft University of Technology]. https://doi.org/10.4233/uuid:0913c6df-9f01-42a5-add2-302ff0f2b156

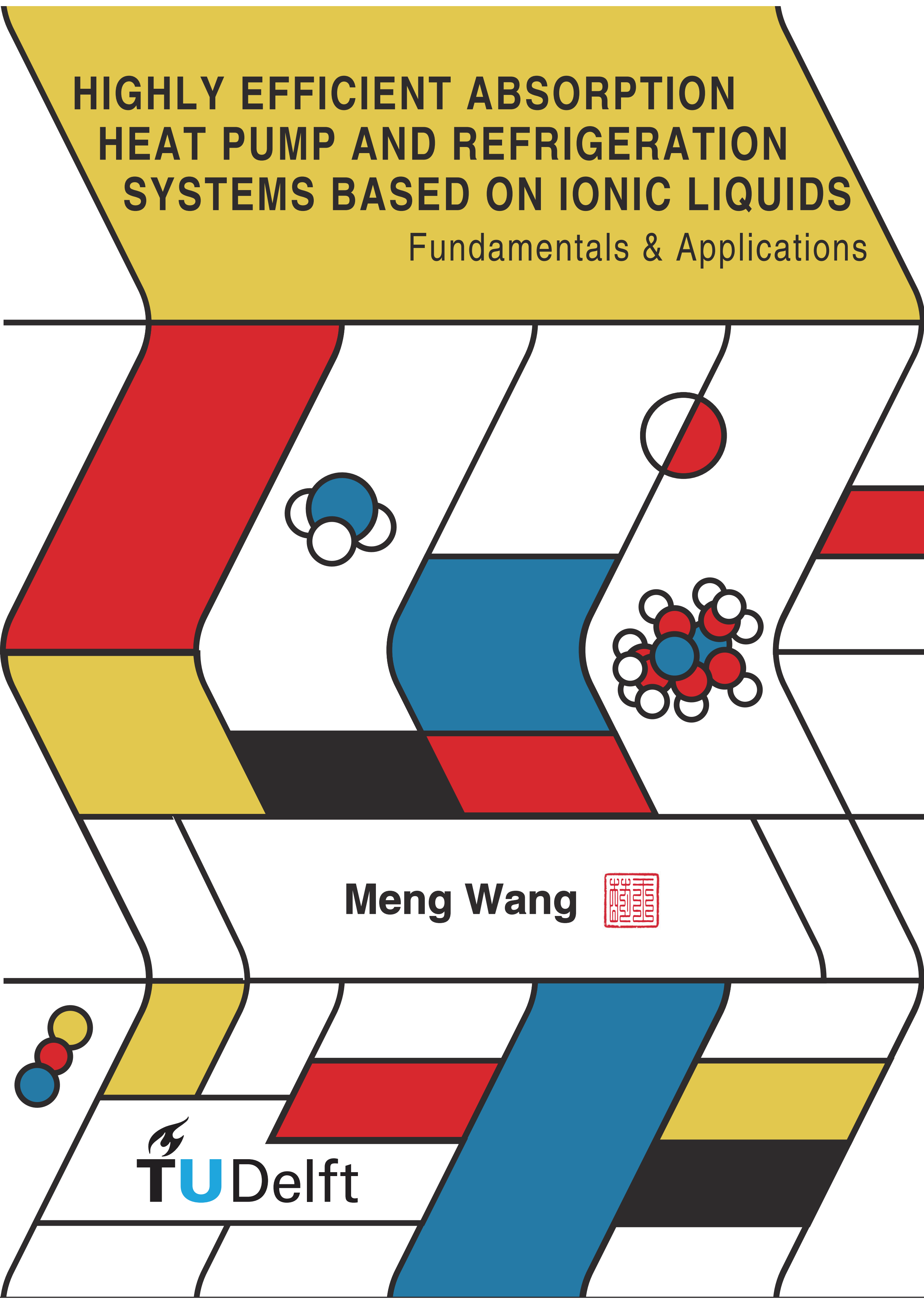

HIGHLY EFFICIENT ABSORPTION HEAT PUMP AND REFRIGERATION SYSTEMS BASED ON IONIC LIQUIDS

Fundamentals & Applications

Meng Wang

TU Delft

HIGHLY EFFICIENT ABSORPTION HEAT PUMP AND REFRIGERATION SYSTEMS BASED ON IONIC LIQUIDS

FUNDAMENTALS & APPLICATIONS

HIGHLY EFFICIENT ABSORPTION HEAT PUMP AND REFRIGERATION SYSTEMS BASED ON IONIC LIQUIDS

FUNDAMENTALS & APPLICATIONS

Proefschrift

ter verkrijging van de graad van doctor
aan de Technische Universiteit Delft,
op gezag van de Rector Magnificus Prof. dr.ir. T.J.H van der Hagen
voorzitter van het College voor Promoties,
in het openbaar te verdedigen op donderdag 28 februari 2019 om 10:00 uur

door

Meng WANG

Master of Science in Power Engineering & Engineering Thermophysics,
Zhejiang University, China
geboren te Shouxian, Anhui Province, China.

Dit proefschrift is goedgekeurd door de

promotor: Dr. ir. C.A. Infante Ferreira
promotor: Prof. dr. ir. T.J.H. Vlugt

Samenstelling promotiecommissie:

Rector Magnificus,	voorzitter
Dr. ir. C.A. Infante Ferreira	Promotor
Prof. dr. ir. T.J.H. Vlugt	Promotor
Onafhankelijke leden:	
Prof. dr. A. Coronas	Universitat Rovira i Virgili
Prof. dr. -Ing. F. Ziegler	Technische Universität Berlin
Dr. ir. M. van der Pal	ECN part of TNO
Prof. dr. L.C.M. Itard	Technische Universiteit Delft
Prof. dr. ir. B.J. Boersma	Technische Universiteit Delft

Koudegroep
Delft-Wageningen

This research was carried out with financial supports from the China Scholarship Council (Scholarship 201406320184), and Koudegroep Delft-Wageningen. This work was sponsored by NWO Exacte Wetenschappen (Physical Sciences) for the use of supercomputer facilities, with financial support from the Nederlandse Organisatie voor Wetenschappelijk Onderzoek (Netherlands Organization for Scientific Research, NWO). TJHV acknowledges NWO-CW for a VICI grant.

Keywords: Absorption cycle, Ionic liquid, Ammonia, Refrigeration, Heat pump, Plate heat exchanger

Printed by: Gildeprint

Cover design by Y. Wu & M. Wang

ISBN 978-94-6366-134-8

An electronic version of this dissertation is available at
`http://repository.tudelft.nl/`.

知行合一

– 王阳明

Minds and Hands

– Yangming Wang

CONTENTS

SUMMARY

Improving efficiencies of thermal energy conversion systems is an important way to slow down global warming and mitigate climate change. Vapor absorption heat pump and refrigeration cycles are highly efficient ways of heating and cooling. These thermally activated systems also provide opportunities for the integration with a wide spectrum of low-grade and renewable heat sources, such as district heating networks, exhaust industrial heat, concentrated solar thermal energy and biomass.

New fluids - ionic liquids - have been introduced into the absorption refrigeration/heat pump field as absorbents to overcome drawbacks of traditional working fluids and to improve the energetic efficiency of systems. Some ionic liquids show high boiling points, superior thermal and chemical stabilities and strong affinities with refrigerants. Ammonia (NH_3) is an environmentally friendly refrigerant with favorable thermodynamic and transport performance. Thus, studies in this thesis placed emphasis on the ammonia/ionic liquids working pairs.

Studies in this thesis focus on exploring applications of ammonia/ionic liquid based vapor absorption refrigeration cycles, from a practical point of view in the refrigeration and heat pump field. By applying multi-scale evaluations covering thermodynamic and heat and mass transport aspects, it is intended to further understand the fundamentals of applying ionic liquids in heating and cooling systems. The highlights include: Assessments of equilibrium models applied for ammonia-ionic liquid working fluids; Prediction of properties of ammonia-ionic liquid fluids using molecular simulation; Collection and modeling of relevant thermophysical properties; Evaluation of the heat and mass transfer performance. Besides, concepts of using ionic liquids as absorbents with ammonia as the refrigerant in various thermodynamic cycles are analyzed and evaluated for applications in the built environment and industry.

Chapter 1 provides an introduction to the topic of this thesis. It presents background information, for instance the large share of thermal energy in the total energy consumption, and attractive options of using VAR technologies for highly efficient heating and cooling. The basic knowledge of vapor absorption refrigeration cycles is briefly introduced as well as the advanced cycle configurations and possible NH_3-based working fluids. The outline of this thesis is provided after pointing out the missing knowledge in the previous studies.

Chapter 2 assesses the performance of various vapor-liquid equilibrium models for the natural refrigerant/ionic liquid working fluids in vapor absorption refrigeration cycles. The evaluated models include equation-of-state based models, activity coefficient based models, and generic Clausius-Clapeyron relations. Studied fluids are the pairs of H_2O/[emim][DMP] and NH_3/[bmim][BF_4]. Performances of the different models in reproducing vapor-liquid equilibrium data and estimating mixing enthalpies are compared. The influence of these models on total enthalpies and thermodynamic performance of absorption refrigeration cycles is studied. The assessment reveals that the studied generic Redlich-Kwong equation of state and the NRTL model perform best in reproducing VLE data. Moreover, the Redlich-Kwong equation of state and the UNIFAC model show the best performance in estimating mixing enthalpies.

In **Chapter 3**, the performance of NH_3 with nine currently commercialized ionic liquids is compared in terms of the application in single-effect absorption heat pump cycles for floor heating in buildings. Four working pairs are identified which show better performance than that of the NH_3/H_2O pair (heating coefficient of performance of 1.61). With an optimization study, it is shown that the optimized mixture can reach a heating coefficient of performance of 1.84. This study helps to conclude that the ideal ionic liquid candidates should show high absorption capabilities, large solubility difference between the inlet and outlet of the generator, low molecular weights, and low heat capacities. Additionally, an economic analysis of an absorption heat pump using NH_3/[emim][SCN] as working pair and plate heat exchangers as components is carried out. The results indicate that NH_3/ionic liquid absorption heat pumps can be economically beneficial, showing 42% energy saving and 29% economic saving in comparison with conventional boilers.

The use of high-temperature waste heat generated by diesel engines for onboard refrigeration of fishing vessels to drive an NH_3-based double-effect vapor absorption refrigeration cycle has been proposed in **Chapter 4**. A multiscale method is applied to study its performance, from a molecular level to a system integration level. Classical force field-based Monte Carlo simulations provide reasonable vapor-liquid equilibrium predictions. After taking into account the performance of the system and the thermal stability of ionic liquids, [bmim][BF4] is found to be the best performing candidate among the investigated commercialized ionic liquids (cooling coefficient of performance is above 1.1). Integrated with the exhaust gas from diesel engines, the cooling capacity of the system, with a cooling medium at 16 °C, is able to reach 3220 kW, recovering 2756 kW waste heat and consuming 191 kW pump work. The annual energy savings can reach 7.6 TJ and the prevented CO_2 emissions are 1634 tons for a single fishing vessel.

Heat and mass transfer studies of the NH_3/ionic liquid absorption are carried out considering corrugated plate heat exchangers as absorbers. The work introduced in **Chapter 5** provides a semi-empirical framework to study the absorption performance of NH_3 into NH_3/non-volatile salts solutions. The framework includes quantifications of the heat and mass transfer processes based on experimental data of absorption of NH_3 into NH_3/$LiNO_3$, and a numerical modeling with frequently applied theories. It has been demonstrated that the heat transfer performance of NH_3/[emim][SCN] working fluids in the absorber is the most promising one with heat transfer coefficients around 1.4 kW/(m^2K).

Finally, **Chapter 6** provides the overall conclusions of the studies reported in this thesis. Recommendations for further research are also provided.

SAMENVATTING

Het verhogen van de efficiëntie van thermische energieconversiesystemen is een belangrijke manier om het broeikaseffect en de klimaatverandering te reduceren. Dampabsorptie-warmtepompen en koelsystemen zijn zeer efficiënt in het verwarmen en koelen. Deze thermische systemen bieden mogelijkheden tot integratie van een breed spectrum van laagwaardige en hernieuwbare warmtebronnen, zoals stadsverwarmingsnetten, restwarmte van de industrie, geconcentreerde thermische zonne-energie en energie uit biomassa.

Een nieuwe klasse van vloeistoffen - ionische vloeistoffen - wordt geïntroduceerd als absorptiemiddel voor absorptiekoelsystemen en -warmtepompen om de efficiëntie van deze systemen te verhogen en de nadelen van traditionele werkmedia te voorkomen. Sommige ionische vloeistoffen hebben een hoog kookpunt, uitstekende thermische en chemische stabiliteit en gunstige affiniteit met traditionele koudemiddelen. Ammoniak (NH_3) is een milieuvriendelijk natuurlijk koudemiddel met gunstige thermodynamische en -transporteigenschappen. In dit proefschrift wordt daarom de nadruk gelegd op combinaties van ammoniak en ionische vloeistoffen.

Dit proefschrift verkent, vanuit een praktisch oogpunt, toepassingen van ammoniak-ionische vloeistoffen in absorptiekoelsystemen en -warmtepompen. Het onderzoek richt zich op het begrijpen en verklaren van de grondbeginselen van het gebruik van ammoniak-ionische vloeistofmengsels in verwarmings- en koelsystemen. Hierbij wordt gebruikt gemaakt van evaluaties op verschillende schaalniveaus, bijvoorbeeld van de thermodynamische eigenschappen en warmte- en stofoverdracht-eigenschappen van de mengsels. Belangrijke punten zijn: de beoordeling van thermodynamische evenwichtsmodellen toegepast op ammoniak-ionische werkvloeistoffen, de voorspelling van eigenschappen van ammoniak-ionische vloeistofmengsels met behulp van moleculaire simulaties, de modellering en verzameling van relevante thermofysische eigenschappen en de evaluatie van warmte- en stofoverdracht. Bovendien wordt de toepasbaarheid van ionische vloeistoffen met ammoniak als koudemiddel onderzocht in verschillende thermodynamische systemen voor toepassingen in de gebouwde omgeving en industrie.

Hoofdstuk 1 geeft een inleiding op het hoofdonderwerp van dit proefschrift. Er wordt achtergrondinformatie gegeven, zoals informatie over het aandeel thermische energie van het totale energiegebruik in Nederland en wat het gebruik van dampabsorptietechnieken voor verwarming en koeling aantrekkelijk maakt. De werkingsprincipes van eenvoudige dampabsorptiekoelsystemen worden uitgelegd, evenals de werking van meer geavanceerde configuraties. Ook wordt een inventarisatie gemaakt van eerdere studies naar mengsels van ammoniak met ionische vloeistoffen. Er wordt gewezen op de ontbrekende kennis in deze studies en op basis hiervan worden de hoofdlijnen van dit proefschrift ingedeeld.

In **Hoofdstuk 2** worden de prestaties van verschillende evenwichtsmodellen van damp en-vloeistof vergeleken voor werkvloeistoffen met een natuurlijk koudemiddel-ionische vloeistof in dampabsorptiesystemen. De onderzochte modellen zijn gebaseerd op toestandsvergelijkingen, op activiteitscoëfficiënten en generieke Clausius-Clapeyron-relaties. De onderzochte mengsels zijn de combinaties (stoffenparen)van water met [emim][DMP] (= 1-ethyl-3-methylimidazolium dimethylfosfaat) en ammoniak met [bmim][BF_4] (= 1-butyl-3-methylimidazolium tetrafluorboraat. De verschillende modellen worden vergelijkt op basis van hoe goed ze in staat zijn om de dampvloeistofevenwichten te reproduceren en om de mengenthalpie te voorspellen. De invloed van deze modellen op de totale enthalpie en de thermodynamische prestaties van dampabsorptiesystemen wordt onderzocht. Het blijkt dat de bestudeerde generieke Redlich-Kwong-toestandsvergelijking en het NRTL-model het beste resultaat opleveren voor het reproduceren van het damp-vloeistofevenwicht. Bovendien presteren de Redlich-Kwong-toestandsvergelijking en het UNIFAC model het beste bij het schatten van de mengenthalpie.

In **Hoofdstuk 3** wordt de prestatie van ammoniakmengsels met negen commercieel beschikbare ionische vloeistoffen vergeleken in termen van toepasbaarheid in absorptiewarmtepompsystemen voor vloerverwarming in gebouwen. Vier combinaties worden geïdentificeerd die betere prestaties vertonen dan die van de ammoniak-watercombinatie (verwarmingscoëfficiënt van 1,61). Met een optimalisatiestudie wordt aangetoond dat het geoptimaliseerde mengsel een verwarmingscoëfficiënt van 1,84 kan bereiken. Uit deze studie valt te concluderen dat de ideale ionische vloeistofkandidaten hoge absorptiecapaciteiten, een groot oplosbaarheidsverschil tussen de instroom en uitstroom van de generator, lage molecuulmassa en lage warmtecapaciteiten moeten bezitten. Bovendien wordt een economische haalbaarheidsstudie uitgevoerd voor een absorptiewarmtepomp met ammoniak en [emim][SCN] (= 1-ethyl-3-methyl-imidazolium-thiocyanaat) als combinatie en platenwarmtewisselaars als componenten. De resultaten laten zien dat ammoniak-ionische vloeistof absorptiewarmtepompen met ammoniak-ionische vloeistof economisch aantrekkelijk zijn. Vergeleken met conventionele ketels leiden ze namelijk tot een energiebesparing van 42% en een economische besparing van 29%.

Het gebruik van hogetemperatuur-restwarmte van dieselmotoren om een dubbeleffect-dampabsorptiesysteem met ammoniak en [bmin][BF_4] aan te drijven, wordt besproken in **Hoofdstuk 4**. Het systeem wordt gebruikt voor het aan boord koelen van de visvangst. Onderzoek wordt verricht op verschillende schaalniveaus, van moleculair niveau tot systeemintegratie. Klassieke Monte Carlo simulaties leveren acceptabele voorspellingen voor damp-vloeistofevenwichten. Rekening houdend met de prestaties van het systeem en de thermische stabiliteit van ionische vloeistoffen, blijkt dat [bmim][BF_4] de best presterende kandidaat is van de onderzochte commercieel beschikbare ionische vloeistoffen (de koelprestatiecoëfficiënt is meer dan 1,1). Geïntegreerd met het uitlaatgas van dieselmotoren kan het systeem bij een mediumtemperatuur van 16 °C een koelvermogen van 3220 kW bereiken en daarbij 2756 kW restwarmte terugwinnen en 191 kW pompvermogen gebruiken. De jaarlijkse energiebesparing, voor één enkel vissersvaartuig, kan 7,6 TJ bedragen en de jaarlijkse uitstoot van CO_2 kan verminderd worden met 1634 ton.

Warmte- en stofoverdracht van ammoniak in ammoniak-ionische vloeistof in de platenwarmtewisselaars van absorptiesystemen worden bestudeerd in **Hoofdstuk 5**. Het onderzoek geïntroduceerd in Hoofdstuk 5 biedt een semi-empirisch model om de absorptieprestaties van ammoniak in mengsels van ammoniak met zouten te bestuderen. Het model omvat kwantificering van de warmte- en stofoverdracht-processen op basis van experimentele resultaten van absorptie van ammoniak in ammoniak-$LiNO_3$ mengsels en een numerieke modellering gebaseerd op veelgebruikte theorieën. Er wordt aangetoond dat de warmteoverdrachtscoëfficiënt van het ammoniak-[emim][SCN] werkvloeistof hoog is met waardes voor de warmteoverdrachtscoëfficiënten rond 1,4 kW/(m^2K).

Hoofdstuk 6 vat de algemene conclusies samen van dit proefschrift. Tot slot worden er aanbevelingen voor verder onderzoek gedaan.

NOMENCLATURE

List of symbols

A	Area	[m^2]
ARD	Average relative deviation	[-]
C	Cost	[k€]
c	Molar concentration	[$\mathrm{kmol/m}^3$]
$\bar{c}$	Coefficient in heat capacity	[-]
COP	Coefficient of performance	[-]
c_p	Specific heat capacity	[$\mathrm{kJ/(kg{\cdot}K)}$]
$\bar{c}_\mathrm{p}$	Specific heat capacity	[$\mathrm{kJ/(kmol{\cdot}K)}$ / $\mathrm{kJ/(mol{\cdot}K)}$]
D	Diffusivity	[m^2/s]
d	Diameter	[m]
DR	Distribution ratio	[-]
F	Objective function	[-]
f	Circulation ratio	[-]
$\hat{f}$	Fugacity	[MPa]
G	Parameters in NRTL model	[-]
g	Gravitational acceleration	[$9.8\ \mathrm{m/s}^2$]
$\dot{G}$	Mass flux	[$\mathrm{kg/(m^2{\cdot}s)}$]
$\bar{g}$	Specific Gibbs energy	[kJ/mol]
$h/\Delta h$	Specific enthalpy (difference)	[kJ/kg]
$\bar{h}/\Delta\bar{h}$	Specific enthalpy (difference)	[kJ/kmol]

$\hat{h}$	Component partial enthalpy	[kJ/kg]
k	Scaling parameter	[-]
L	Length	[m]
$LMTD$	Logarithmic mean temperature difference	[K]
M	A general representation of thermophysical properties	[-]
$\dot{m}$	Mass flow rate	[kg/s]
M_w	Molecular weight	[kg/kmol]
N	Counting number	[-]
P	Pressure	[MPa]
q	Vapor quality	[kg/kg]
$\dot{Q}$	Heat flow	[W]
$\bar{R}$	Radius of the spherical particle	[m]
R	Ideal gas constant	[8.314472 kJ/(kmol·K)]
r	Correlation coefficient	[-]
RD	Relative deviation	[-]
$RMSD$	Root-mean-square deviation	[-]
$T/\Delta T$	Temperature (difference)	[°C or K]
U	Overall heat transfer coefficient	[W/(m^2·K)]
$v/\bar{v}$	Velocity/ average velocity	[m/s]
w	Mass fraction	[kg/kg]
$\dot{W}$	Power	[kW]
x/y	Molar fraction in liquid/vapor	[mol/mol]
Z	Compressibility factor	[-]

Dimensionless Numbers

$\mathrm{Fr} = \frac{v_\mathrm{V}}{\sqrt{g L_\mathrm{ch}(\rho_\mathrm{L}/\rho_\mathrm{V}-1)}}$	Froude number	[-]
$\mathrm{Nu} = \frac{\bar{\alpha} L_\mathrm{ch}}{\lambda}$	Nusselt number	[-]
$\mathrm{Pr} = \frac{c_\mathrm{p}\mu}{\lambda}$	Prandtl number	[-]
$\mathrm{Re} = \frac{\rho v L_\mathrm{ch}}{\mu}$	Reynolds number	[-]
$\mathrm{Sc} = \frac{\mu}{\rho D}$	Schmidt number	[-]
$\mathrm{Sh} = \frac{\bar{\beta} L_\mathrm{ch}}{D}$	Sherwood number	[-]

Greek letters

α	Interaction parameters in NRTL or UNIFAC models	[-]
$\bar{\alpha}$	Heat transfer coefficient	[W/(m^2·K)]
$\bar{\beta}$	Mass transfer coefficient	[m/s]
β	Input parameters in RK-EOS	[-]
δ	Thickness	[m]
ϵ	Void-fraction	[m^3/m^3]
η	Efficiency	[-]
γ	Activity coefficient	[-]
$\hat{\phi}$	Fugacity coefficient	[-]
κ	Boltzmann constant	[1.38064852×10^{-23}J/K]
λ	Thermal conductivity	[W/(m·K)]
μ	Viscosity	[Pa·s]
ω	Acentric factor	[-]
Φ	Poynting correction	[-]
ψ	Lennard-Jones energy parameter	[-]

ρ	Density	[kg/m^3]
σ	Surface tension	[N/m]
Λ	Correction factor of fluid property	[-]
ξ	Friction factor	[-]
τ	Parameter in NRTL model	[-]

Sub- and superscripts

0	Reference state
1	Component of refrigerant
1, 2 ...	State point
A/B	Component A or B
abs	Absorption
ave	Average
c	Critical point
calc	Calculated data
ch	Characteristic (length)
con	Condensation
cw	Cooling water
e	Excess properties
eva	Evaporation
ex	Exhaust gas
exp	Experimental data
f	Film
g	(Plates) gap
gen	Generation
h	Hydraulic (diameter)

H_2O	H_2O component
hc	high pressure condenser
hpg	High pressure generation
i	i-th component or point
ig	Properties in the ideal gas state
IL	Ionic liquid component
in	Inlet
ini	Initial
int	Interface
is	Ideal solution
L	Liquid phase
lc	Low pressure condenser
lg	Low pressure generator
mix	Mixing properties
mt	Mass transfer
NH_3	NH_3 component
onset	Onset
ori	Orifice
out	Outlet
p	Pump
phx	Plate heat exchanger
r	Refrigerant stream
real	Real properties
rec	Rectifier
res	Residual properties

s	Strong (of refrigerant) solution stream
sat	Saturated state properties
sol	Solution
sthx	Shell-and-tube heat exchanger
sub	Properties of a subcooled system
V	Vapor phase
w	Weak (of refrigerant) solution stream / Wall
whr	Recovered waste heat

Abbreviations

ABS	Absorber
AHP	Absorption heat pump
AHT	Absorption heat transformer
ARD	Average relative deviation
C-C	Clausius-Clapeyron equation
CCHP	Combined cold, heat and power
CCP	Combined cold and power
CFC	Chlorofluorocarbon
CON	Condenser
COP	Coefficient of performance
COSMO	Conductor-like screening model
COSMO-RS	Conductor-like screening model for real solvents
CWP	Chilled water plant
DE	Double-effect
EOS	Equation of state
EVA	Evaporator

EXP	Experimental (data)
FIT	Fitting (data)
FP	Freezing plant
G^e	Activity coefficient model
G-H	Gibbs-Helmholtz equations
GA	Genetic algorithm
GAX	Generator/absorber heat exchange
GEN	Generator
GWP	Global Warming Potential
HC	High pressure condenser
HCFC	Hydrochlorofluorocarbon
HE	Half-effect
HFC	Hydrofluorocarbon
HFO	Hydrofluoroolefin
HG	High pressure generator
HP-	High pressure
HT-	High temperature
HX	Heat exchanger
iHX	Intermediate heat exchanger
IL	Ionic liquid
IS	Ideal solution
LG	Low pressure generator
LP-	Low pressure
LT-	Low temperature
MC	Monte Carlo

MP-	Medium pressure
NRTL	Non-random two-liquid model
ODP	Ozone-Depletion Potential
PHX	Plate heat exchanger
PR-EOS	Peng-Robinson EOS
PRVdW-EOS	Peng-Robinson EOS with van der Waals mixing rules
PRWS-EOS	Peng-Robinson EOS with Wong-Sandler mixing rules
RD	Relative deviation
REC	Rectifier
RK-EOS	Redlich-Kwong EOS
RSW	Refrigeration seawater (plant)
SE	Single-effect
SHX	Solution heat exchanger
SIM	Simulated (data)
TCM	Thermodynamically consistent model
UNIFAC	UNIQUAC functional-group activity coefficients model
VAR	Vapor absorption refrigeration
VCR	Vapor compression refrigeration
VLE	Vapor-liquid equlibrium
WHR	Waste heat recovery

1

INTRODUCTION

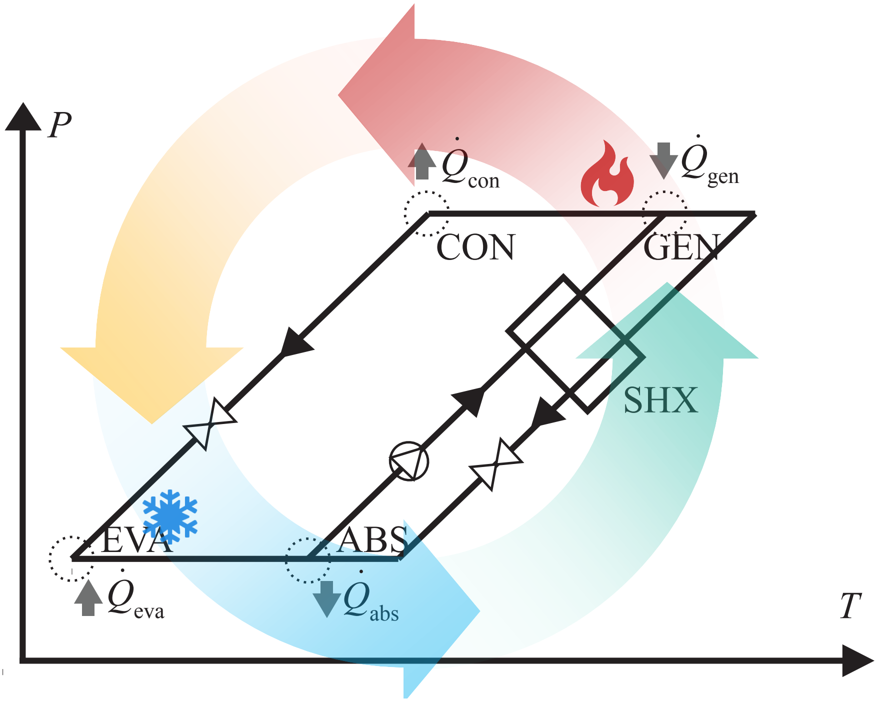

This chapter provides a general introduction to this work. The background information on thermal energy applications and on vapor absorption refrigeration cycles is presented. The basic knowledge of advanced cycle configurations and possible NH_3-based working fluids of vapor absorption refrigeration cycles is briefly introduced. Before outlining the structure of this thesis, missing knowledge in previous studies is also discussed.

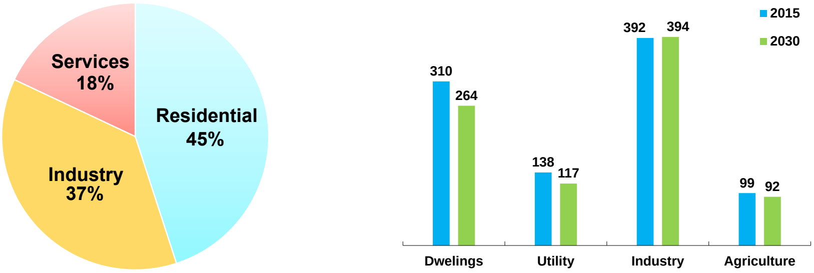

(a) (b)

Figure 1.1: (a) Final energy consumption for heating and cooling per sector in the European Union in 2012 (Data was taken from Ref. [3]). (b) Final thermal energy used in 2015 and expected to be used in 2030 in the Netherlands (Data was taken from Ref. [4]).

1.1. BACKGROUND

Climate change is one of the most significant issues for human beings. The Paris Agreement reached in 2015 during the United Nations Climate Change Conference (COP 21) reset the global climate ambition: limiting the temperature rise from pre-industrial levels “well below 2 K” with efforts to pursue 1.5 K. Efforts responding to climate change are also accelerating the way the energy sector is developing [1]. Increasing energetic efficiencies, for instance in the buildings, industry and transport sectors is one of the main measures, which will lead to a reduction of the greenhouse-gas emissions[2].

Fig.1.1 provides the thermal energy consumption for heating and cooling purposes in Europe and the Netherlands, respectively.

According to the EU Commission [3], heating and cooling were responsible for 50% (22.85 EJ) of the final energy consumption in 2012, of which the energy used for the residential sector took up 45% (Fig. 1.1(a)). Specifically in the Netherlands, the thermal energy used in 2015 was 939 PJ, which corresponds to 46% of the Dutch final energy consumption in 2015. The final thermal energy use in 2030 is expected to reduce to 867 PJ [4]. As shown in Fig. 1.1(b), the predicted reduction will mainly be contributed by the built environment. This confirms the statement of Hieminga [5], that the built environment offers the greatest energy saving potential.

In Europe, the energy consumption for heating and cooling in the industrial sector is basically comparable to that in the residential sector. A more detailed breakdown of the thermal energy used in industry is shown in Fig. 1.2 which

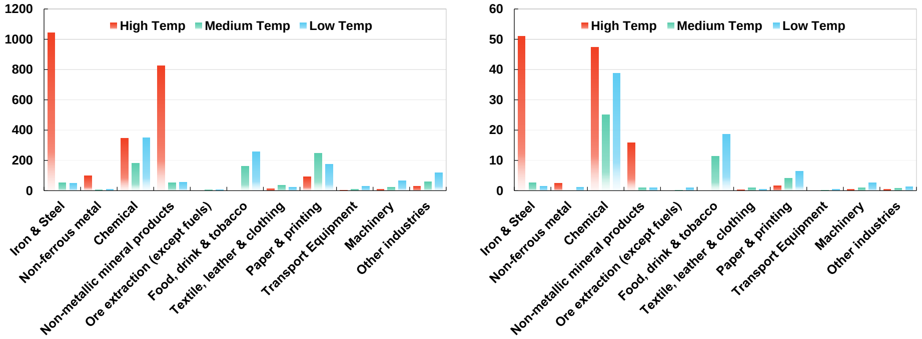

(a) (b)

Figure 1.2: Breakdown of useful heat demand (in PJ) for the industry in (a) the European Union and (b) the Netherlands in 2009. Data was taken from Ref. [6].

shows the typical subsectors.

Beyond the large heating demands for the iron & steel and chemical industry, the food, drink & tobacco industry also shows large heating demands, especially at the medium and low temperature ranges (below 100 °C). The food, drink and tobacco sectors, as one of the important industries in the Netherlands, accounted for about 9% of the final industrial energy demand, 15% of the industrial employment, and 23% of the industrial added value [7]. The broad range of products in these industries also requires specific strategies of energy supply due to their distinctive and complicated manufacturing processes [6].

For the agriculture and fisheries sectors, heating is mainly used for pasteurization, cleaning purposes, and space heating in production facilities (stables), greenhouses and drying of the crops. Cooling in agriculture and fisheries is used for preserving products such as milk and seafood. For instance, in fishing vessels for pelagic seas, the refrigeration plant is one of the largest electricity consumers onboard, typically using 50% of the total power requirement [8]. Meanwhile, the consumption of energy for heating and cooling in agriculture occurs in all European countries, while energy consumption in fisheries is limited mainly to the Northern and Mediterranean countries [9].

As for the Netherlands, Fig. 1.3 shows breakdowns of final heating and cooling demands into different temperature levels and sectors in 2009. It indicates that a majority of the energy consumption for heating was at temperatures below 100°C, and at least half of energy demands for cooling were not for a very low temperature range.

Heating and cooling constitute a large share of energy needs in both the EU and in the Netherlands, as summarized above for the residential, food & drink in-

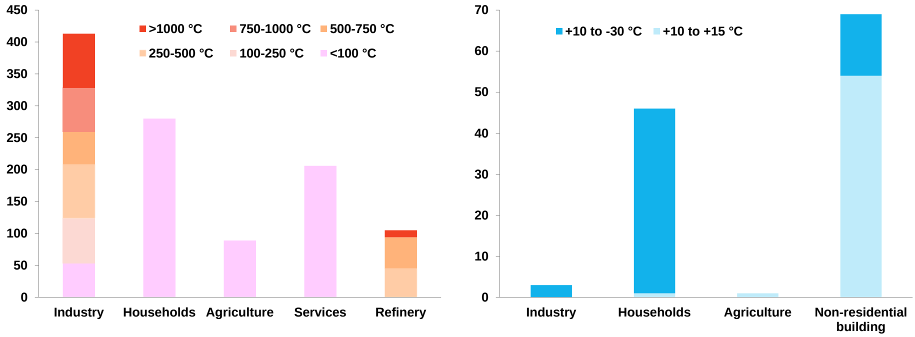

(a) (b)

Figure 1.3: Breakdown of final heating (a) and cooling (b) demands (in PJ) in the Netherlands for the year 2006, broken down into sector and temperature level. Data was taken from Ref. [10].

dustry, and agriculture sectors. The conventional option for heating is using boilers, and for cooling by using chillers with compressors. Absorption heat pumps and chillers provide alternatives to meet the demands. These systems have been frequently recommended as highly efficient technologies by the EU [9], the IEA [11, 12], and the IIR [13].

One of the highlighted features of these absorption systems is that they are driven mainly by heat and only need very limited electricity input. This feature makes a number of heat sources applicable for highly efficient heating or cooling. As shown in Fig. 1.4(a), rather than directly making use of fuels for heating in a boiler, the absorption cycle can additionally reclaim the low temperature heat from the environment (cooling water or air), allowing the total heating efficiency to be more than one. Some advanced cycle configurations, such as the double-effect system, could even make the efficiency higher than 2. This is more than twice the efficiency of boilers.

Using heat to separate the refrigerant (here the ammonia) from the working fluid, the absorption chiller can achieve the cooling effect without consuming a lot of electricity (Fig. 1.4(b)). The only needed electricity is for the pump to circulate the working fluids, which is normally negligible. Some special designs, for example the diffusion-absorption chiller, require no electricity input at all. This is an advantage compared with the frequently used vapor compression chiller with a compressor, especially in scenarios where a high temperature heat source is abundant.

Moreover, absorption technologies also provide opportunities to use clean and sustainable energy, for example low-grade thermal energy and energy from renewable sources, for efficient heating and cooling. The practices and studies

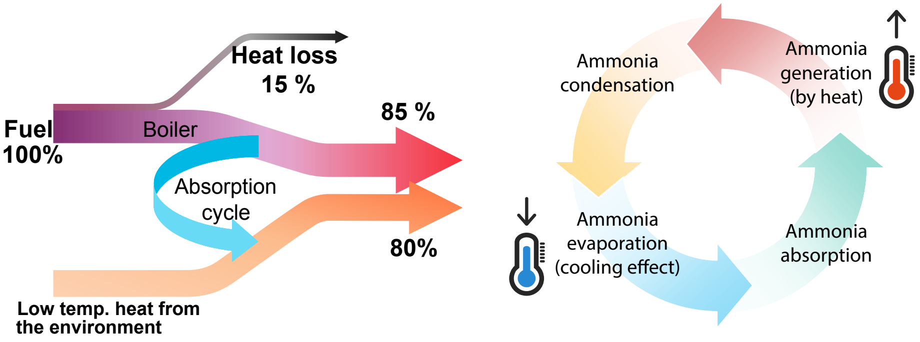

(a) (b)

Figure 1.4: Efficient approaches of heating and cooling by using absorption technologies. (a) Heat driven absorption cycles perform better than boilers by reclaiming low temperature heat from the environment; (b) Absorption refrigeration systems achieve cooling effects with a very limited amount of electricity consumption.

include bio-gas [14], geothermal hot water [15], concentrated solar thermal energy [16, 17], and waste heat from industry [18], engines [19], fuel cells [20, 21], and data centers [22, 23]. Absorption systems can also be applied in combination with electricity generation technologies. This results in combined cold and power (CCP) cogeneration systems, and combined cold, heat, and power (CCHP) trigeneration systems [13].

1.2. ABSORPTION REFRIGERATION/HEAT PUMP SYSTEMS

1.2.1. ABSORPTION CYCLES

The above background information reveals that there is an immense potential to apply absorption refrigeration and heat pump systems, which provide opportunities for a clean and efficient way of thermal energy utilization. In this section, the absorption cycles are briefly introduced.

Fig. 1.5(a) shows the principle of the vapor absorption refrigeration (VAR) cycle.

The pure refrigerant vapor from the evaporator (EVA) is absorbed by the solution in the absorber (ABS). The strong solution (high NH_3 concentration, the same for the following text) is then pumped to the vapor generator (GEN) through the solution heat exchanger (SHX), where it is preheated by the hot side in which the weak solution coming from the GEN flows. The pump circulates the solution. In the GEN, heat is added by an external heat source so that the refrigerant boils out of the solution, reducing the solution concentration. The weak solution flows

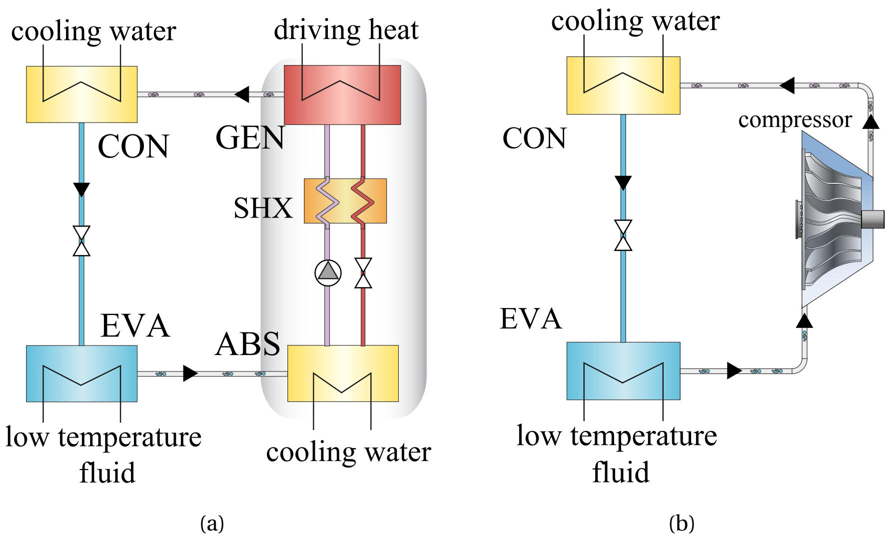

Figure 1.5: Schematic representations of (a) vapor absorption refrigeration cycle (VAR) and (b) vapor compression refrigeration (VCR) cycle. These two cycles share the same refrigerant condensation, expansion and evaporation processes. The compression process is different: the VAR cycle uses a "thermal compressor", which consists of an ABS, an GEN, an SHX and a throttling valve, while the VCR uses a mechanical compressor.

back to the ABS passing the SHX and a throttling valve. The valve maintains the pressure in the GEN at a higher level. The refrigerant vapor generated in the GEN flows to the condenser (CON) where it is condensed. The condensed liquid then flows through a throttling valve before entering the EVA. The refrigerant experiences the same process as in the vapor compression refrigeration (VCR) cycle (Fig. 1.5(b)). Functionally similar, the VAR cycle also achieves the cooling effect with the latent heat during the liquid-vapor phase change.

By comparing the VAR with the popularly applied VCR cycle, its characteristics can be highlighted:

- Instead of a mechanical compressor used in the VCR cycle, the VAR cycle uses a "thermal compressor" which consists of an ABS, an GEN, an SHX, a solution pump and a throttling valve (highlighted in Fig. 1.5(a)).
- The heat input to the GEN boils refrigerant vapor off and the pump circulates the solution. The low pressure, low temperature solution absorbs the refrigerant vapor in the ABS, which is cooled down by an external cooling flow.
- The driving energy of the VAR is the heat input to the GEN. Besides a small

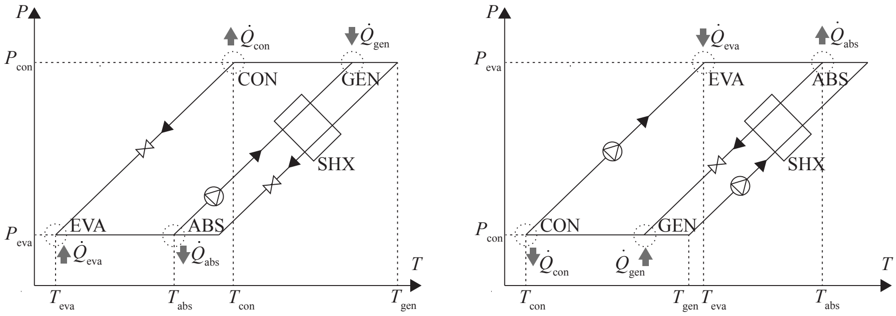

(a) (b)

Figure 1.6: Two types of AHP cycles. (a) AHP Type 1 cycle: The high temperature heat added to the GEN drives the cycle. The intermediate temperature heat is released in the CON and ABS, and cooling effect is achieved in the EVA. (b) AHP Type 2 (heat transformer) cycle: it is driven by heat at an intermediate temperature via the GEN and EVA, and rejects heat at low temperature surroundings (CON). The useful high temperature heat is achieved at the high pressure ABS.

amount of electricity required by the pump, the VAR cycle does not consume any other mechanical work.

In a refrigeration cycle, the cooling effect is achieved in the EVA, which is at a low temperature, and the surrounding is at an intermediate temperature level. The absorption heat pump (AHP) cycle shares the same principle as the VAR cycle, while the only difference is that the useful heat transfer is at an intermediate temperature, i.e. the heat exchanged in the ABS and CON for a heating purpose. The surroundings are regarded as the low temperature reservoir. Because they share an identical working principle, the VAR and AHP cycles are also classified as the AHP Type 1.

Fig. 1.6(a) qualitatively illustrates the temperature and pressure levels of each component in a ln P - $1/T$ diagram for the AHP Type 1 (VAR and AHP) cycles. Another type of AHP (Type 2) is schematically shown in Fig. 1.6(b), and is also known as the absorption heat transformer (AHT). The AHT cycle shares the same components as the AHP type 1 cycle, but works under different conditions. It is driven by heat at an intermediate temperature via the GEN and EVA, and rejects heat at low temperature surroundings (CON). The useful heating effect is achieved at the highest temperature level via the ABS.

Because the AHT or AHP Type 2 cycle is not the focus in this study, the term AHP discussed in this thesis will only refer to the AHP Type 1 cycle. Besides, the VAR and AHP cycles are identical in terms of the working principle. When generally talking about them without identifying a certain application, the term

"VAR" will be used.

The VAR cycle is a technology which relies on the working fluids flowing through heat exchangers within a cyclic process. The performance of VARs is significantly affected by the working fluid, cycle configuration and heat & mass transfer in the components. In fact, these three aspects are also the most frequently researched directions in the VAR field.

1.2.2. WORKING FLUIDS

NH_3-BASED WORKING FLUIDS

NH_3/H_2O and $H_2O/LiBr$ are the most applied working fluids in the currently commercialized VAR systems. VAR systems with $H_2O/LiBr$ are known for its high performance. However, there are also some challenges. For instance, $H_2O/LiBr$ pair may solidify at the inlet of the ABS when applied with a high temperature heat source and a low temperature heat sink; the working fluid $H_2O/LiBr$ also has a risk of corroding devices; moreover, H_2O can not be used for cooling below 0 °C.

In this study, we focus on NH_3 as the refrigerant. NH_3 is a promising natural refrigerant, with the values of ODP and GWP both 0. It is intensively used in large scale refrigeration plants for low temperature applications. NH_3 has relatively large latent heats (comparable to some alcohols), and small viscosities and heat capacities, allowing it to obtain superior performance in respect to thermodynamics and heat transfer. The levels of operating pressure of NH_3 in the VAR system are always higher than the atmospheric pressure, what makes VAR systems easy from a maintenance point of view.

Using the working fluid NH_3/H_2O in VAR systems started earlier than the use of $H_2O/LiBr$. Some later replacements were mainly due to the complexity of the NH_3/H_2O systems. H_2O has a saturation temperature value close to that of the refrigerant NH_3. As a consequence, the vapor stream will partially contain H_2O vapor. The H_2O vapor will deteriorate the cooling effect in the EVA. To ensure the purity of the refrigerant, H_2O has to be separated before entering the condenser, thus additional distillation and rectification sections are required. Unfortunately, these extra sections, in one hand, add complexity and investments to the systems, and in the other hand, reduce the cycle performance because extra heat is required in the GEN since cooling is required in the separation section [24].

To overcome these problems, salts, such as $LiNO_3$ and NaSCN, were proposed to be used with NH_3 in VAR cycles in the past decades, because these salts have good affinities with NH_3, and their vapor pressures are negligible. Infante Ferreira [25] presented a series of thermo-physical properties equations for the $NH_3/LiNO_3$ and NH_3/NaSCN pairs. Sun [26]'s thermodynamic analysis showed that the performance of the $NH_3/LiNO_3$ and $NH_3/NaSCN$ pairs is better than that of the NH_3/H_2O pair, while the $NH_3/NaSCN$ pair cannot operate for cooling below -10 °C because of crystallization. Garousi Farshi *et al.* [27] reported that the $NH_3/LiNO_3$ pair is able to achieve higher performance at low GEN temperature, while for high GEN temperature, the $NH_3/NaSCN$ pair is superior. These facts make $NH_3/LiNO_3$ more appropriate for using low temperature heat sources such as solar thermal energy. Moreover, a theoretical study of a solar driven double-effect VAR system with $NH_3/LiNO_3$ pair was conducted by Vasilescu and Infante Ferreira [17] by coupling the cooling cycle with a parabolic trough solar collector for cooling under 0 °C.

Because they are free of rectification sections and able to reach a lower heat sink temperature, NH_3/salt pairs have also been explored in VAR systems with air cooling. A pre-industrial prototype of a new $NH_3/LiNO_3$ VAR chiller was developed and experimentally characterized by Zamora *et al.* [28]. At a condition of 15 °C chilled water, 90 °C hot water and 35 °C ambient air temperature, the electrical cooling coefficient of performance (COP) was 6.5. Llamas-Guillén *et al.* [29] reported experimental work with a direct air-cooled $NH_3/LiNO_3$ system. It achieved thermal COP of 0.3-0.4. The operating conditions were ambient temperature of 25-35 °C and cooling at 10 °C.

However, the VAR systems with NH_3/salt binary working fluids still encounter challenges, such as the possibilities of crystallization [25, 26], lower heat & mass transfer during absorption due to the higher viscosity of the working fluids, especially for the $NH_3/LiNO_3$ pair [30], and high operating pressure. There are quite a lot of other attempts to solve these challenges in researches, as for instance applying ternary NH_3-salt fluids [31–35], and using ionic liquids (ILs) as absorbents.

ILs are a family of room-temperature molten salts. They hold the strength of non-solidification at room-temperature due to their molecular structures with long alkyl chains, which is a superiority to the previously proposed salts. Apart from that, they also show advantages such as high boiling point, good affinity with refrigerants and high chemical and thermal stabilities [36]. Moreover, the properties of the IL can be adjusted by the design of anion and cation combinations for a task-specified purpose [37]. ILs have drawn considerable attention in the past years, for the sake of overcoming drawbacks of the traditional working fluids in the VAR cycle [24, 38].

As for NH_3-based working fluids, Yokozeki and Shiflett [39, 40] explored vapor-liquid equilibrium (VLE) properties of NH_3 with eight different ILs. The studied ILs include [bmim][PF_6], [hmim][Cl], [emim][Tf_2N], [bmim][BF_4], [emim][Ac], [emim][SCN], [emim][$EtOSO_3$] and [DMEA][Ac]. Most of them are imidazolium-based ones, which are currently well commercialized. Other imidazolium ILs that have been studied with NH_3 vapor includes [mmim][DMP] [41], [emim][BF_4],

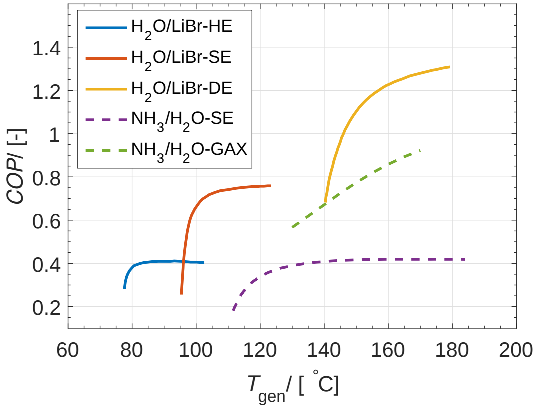

Figure 1.7: *COP* levels of some typical cycles at an environment temperature of 30-35°C. For cycles with H_2O/LiBr, the cooling temperature is 5°C [48], while it is set -5°C for cycles with NH_3/H_2O. HE, SE, DE and GAX stand, respectively, for half-effect, single-effect, double-effect and generator/absorber heat exchange.

[hmim][BF_4] and [omim][BF_4] [42]. There were also some studies in terms of functionalized ILs with NH_3 for absorption cycles, for instance, [bmim][Zn_2Cl_5] studied by Chen *et al.* [43], [EtOHmim][BF_4], [choline][Tf_2N], [MTEOA][$MeOSO_3$] and [EtOHmim][DCA] investigated by Ruiz *et al.* [44], and [N112(2OH)][TfO], [N112(2OH)][Tf_2N], [N111(2OH)][Tf_2N], [N1113][Tf_2N], [EtOHmim][BF_4] along with [EtOHmim][Tf_2N] studied by Cera-Manjarres [45].

In respect to the cycle performance, Wang and Infante Ferreira [24] updated Yokozeki and Shiflett [39, 40]'s VLE properties data and experimental heat capacities data, analyzed eight NH_3/IL working pairs for heat pump applications, and identified [emim][SCN] as a good absorbent to be used with NH_3 in a VAR driven by heat under 130 °C, by considering cycle and heat transfer performance. Chen *et al.* [46]'s thermodynamic studies show the NH_3/[bmim][Zn_2Cl_5] fluids can obtain a slightly better performance than NH_3/NaSCN. Additionally, EtOHmim-based ILs have also been evaluated holding better NH_3 solubilities [47] and lower viscosities [45].

1.2.3. ADVANCED VAR CYCLE CONFIGURATIONS

Considering the conditions under which the VAR systems are to be applied, different cycle configurations can reach different performance. Fig. 1.7 gives approximate *COP* levels of some typical VAR cycles.

The cycles with H_2O/LiBr are able to reach relatively high *COP*s, while they can not be used for cooling below 0°C. Besides, the frequently used single-effect

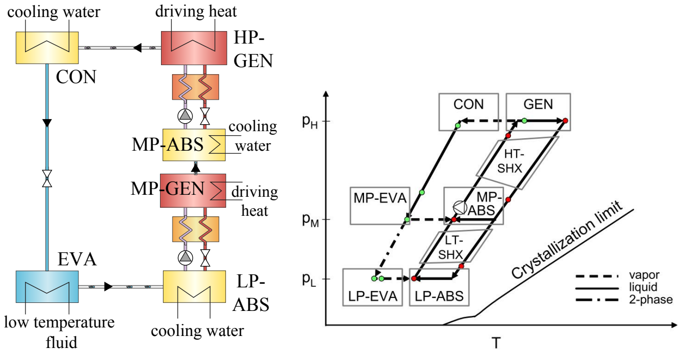

(a) (b)

Figure 1.8: Half-effect VAR cycles. (a) The most common one: a heat coupling between middle-pressure generator and absorber. (b) The heat-coupled one proposed by Kim and Infante Ferreira [52].

(SE) cycle can not achieve a good performance under either lower or higher driving temperature conditions. Alternatives are the half-effect (HE) and double-effect (DE) cycles, respectively. The cycles with NH_3/H_2O are appropriate for cooling below 0°C, but the efficiencies are lower than for the cycles with H_2O/LiBr. Frequently studied alternative to the NH_3/H_2O cycle is the generator-absorber heat exchanger (GAX) cycle, which is able to perform well at high driving temperatures. Most of the advanced schemes are realized by internal heat (or mass) coupling.

Table 1.1 introduces the basic configurations of some typical advanced VAR cycles. They are selected because the author considers each of them representing a simple but basic way to make the VAR cycles superior. More sophisticated cycles can be developed, such as the multi-stage and multi-effect ones [49–51].

There are also some cycles combining VAR cycles with other refrigeration techniques, such as separators, compressors and ejectors, for various purposes. They are also included in Table 1.1.

Even though these advanced cycles have been studied thoroughly with the traditional working fluids, there are still some limitations: (1) Except the double-effect and the Robur VAR cycles, most of others are still far from commercialization. (2) The majority of the current studies of the IL-based VAR systems focus on the basic SE-VAR cycle.

Table 1.1: Summary of some typical and simple ways to make the VAR cycles superior.

	Figure	Driving heat	Cooling *COP* range	Feature	Proper application
Half-effect	1.8(a)	lower T	0.4 ($H_2O/LiBr$) [51]	mass-coupling: vapor from the MP-GEN absorbed in the MP-ABS	with low temperature heat source
	1.8(b)	60-70 °C	0.3-0.4 ($H_2O/LiBr$) [52]	heat-coupling: MP-EVA and LP-ABS	
Double-effect	1.9(a)	150-170 °C	1.2-1.3 ($H_2O/LiBr$); 0.7-0.9 ($NH_3/LiNO_3$)	heat-coupling: HP-CON and MP-GEN	with high temperature heat source.
	1.9(b)	higher T	1.3 ($NH_3/LiNO_3$)	heat-coupling: HT-ABS and LT-GEN	
GAX	1.10(a)	higher T	0.8-1.0 (NH_3/H_2O) [51]	heat-coupling: ABS and GEN	with high temperature heat source; for sub-zero degree cooling
Robur cycle	1.10(b)	gas-fired	0.3-0.5 (NH_3/H_2O) [53, 54]	heat-coupling: solution leaving the ABS is used to cool down the rectifier and pre-vapor-absorption	with air-cooling
Auto-cascade VAR	1.11(a)	150-170 °C	0.01-0.02 (R23+R134a/DMF) [55]	mass coupling: refrigerant is split into vapor and liquid streams; heat-coupling: in the condenser-evaporator	low-temperature cooling
VAR-C*	1.11(b)	-	-	pressure coupling: compressor boosts the pressure in ABS, or decrease it in the GEN	with air-cooling ABS; with low-temperature heat source
VAR-E*	1.11(c)	190-230 °C	0.9-1.0 ($H_2O/LiBr$) [56]	substitution of the valve by an ejector helps to boost the pressure of the ABS	with air-cooling ABS
	-	70-100 °C	0.5-0.7 ($NH_3/LiNO_3$) [57]	the ejector linking the GEN, CON and a bypass from EVA, decreases the pressure level of the GEN	with low-temperature heat source

* C stands for compressor; E stands for ejector.

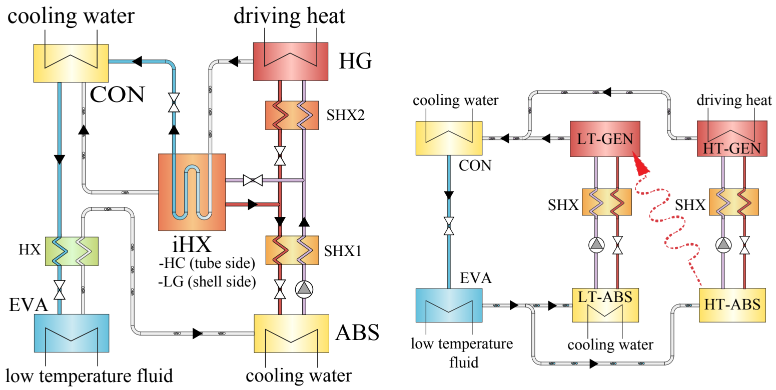

(a) (b)

Figure 1.9: The double-effect VAR cycles. (a) The most common DE-VAR cycle: a heat coupling between high-temperature condenser and low-temperature generator. (b) The two-stage DE-VAR cycle: a heat coupling between high-temperature absorber and low-temperature generator.

1.3. IONIC LIQUIDS ADOPTED IN ABSORPTION REFRIGERATION CYCLES

1.3.1. VLE PROPERTIES

VLE MEASUREMENTS

As the most fundamental thermophysical properties in relevant applications, such as absorption and separation, the VLE data is needed to provide the relationship between pressure, temperature and concentration of working fluids.

According to the author's statistics from the NIST ILThermo database [58, 59], 1221 VLE measurements of IL-based binary mixtures have been executed before August 7, 2017, including the measurements of the equilibrium pressure, temperature and composition. Here "one measurement" means one group of reported data-points of a certain mixture containing vapor/IL binary components. The amount of them reflects the interest in specific mixtures. These measurements of vapor-components/IL based binary mixtures are categorized into several groups by featuring the vapor-components, as shown in Fig. 1.12.

VLE investigations on CO_2 with ILs take up the largest portion, followed by the binary mixtures with alcohols and H_2O. These three systems correspond to more than half of the total measurements. Despite they have an even broader spectrum of applications, using these three fluids as refrigerants is also popular in the refrigeration and heat pump fields. Besides, measurements of the group "other refrigerants/IL mixtures" accounts for 19% of the total investigations. Specifically speaking for this group, the VLE measurements of the HCs and

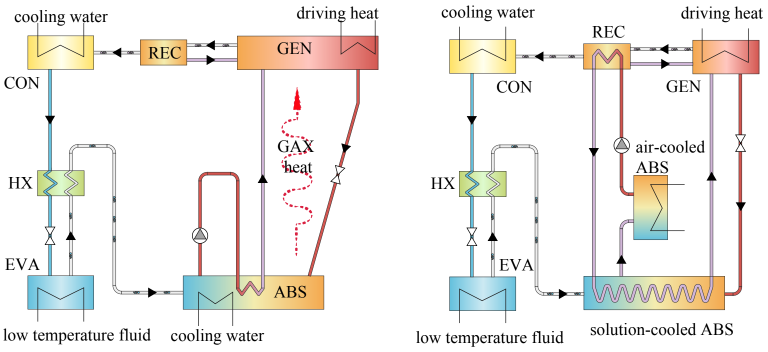

(a) (b)

Figure 1.10: The GAX cycles. (a) The most common one: heat coupled between parts of the generator and absorber. (b) The Robur one [54]: the absorber is split into sections realizing a heat coupling with the REC.

HFCs take up the majority. The phased-out refrigerants CFCs and HCFCs, and the recently popularized HFOs only take quite small percentages.

As the focus of this study, the natural refrigerant NH_3 has nine VLE measurements in this database which represent less than 1% of the total measurements. This is not as large as other natural refrigerants (CO_2, H_2O and HCs). A limited amount of studies has been dedicated to NH_3/IL mixtures. This fact also indicates that the scientific potential of this refrigerant for an IL-based VAR cycle is still worth exploring, especially when appropriate practical scenarios are identified.

On the other hand, making use of other methodologies, apart from experimental methods, to determine the VLE properties might be attractive. Molecular simulations provide a relevant alternative method.

EXCESS ENTHALPIES

Enthalpy is another fundamental property required in the VAR cycles for energetic evaluation purposes. For the enthalpy of a mixture, besides contributions from the pure components, an excess contribution due to the gas absorption (or mixing) is also an essential part to the total enthalpy.

In the same database, there are 402 measurements of the excess enthalpy. The excess enthalpy of the vapor-phase component with ILs has not been frequently reported. Among the 402 measurements, only 173 are for the mixtures of which the VLE properties have been reported (the rest apply for liquid-liquid equilibrium), which implies that with these two properties, the energetic performance of the mixtures can be quantified in processes. Brief statistics are shown

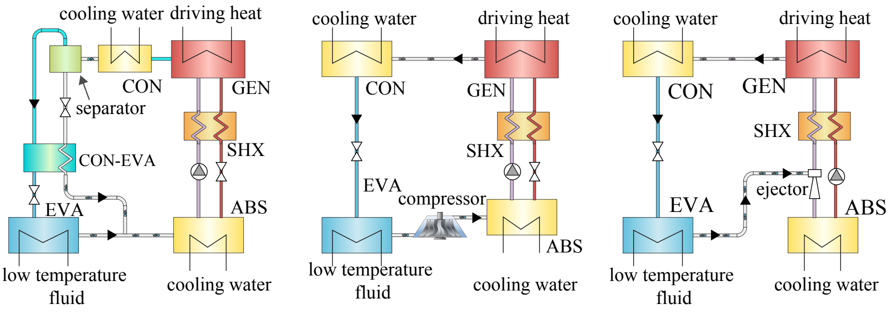

(a) (b) (c)

Figure 1.11: Advanced cycles on the basis of VAR by combining devices. (a) Auto-cascade VAR cycle, (b) VAR with compressor (-C) cycle, and (c) VAR with ejector (-E) cycle

in Fig. 1.13.

It is obvious that a majority of the measurements of the excess enthalpies are focused on H_2O or alcohols with ILs. There are no measurements reported of natural refrigerants, NH_3 or CO_2, with ILs.

Other way to obtain the excess enthalpy is to use the Gibbs-Helmholtz relations [60], which bridge the phase equilibrium with the enthalpy change. By using this approach, VLE models are also needed to correlate the VLE data. Previous, frequently applied, VLE models for the IL-based working fluids with NH_3 or H_2O are summarized in Chapter 2.

However, the feasibility of using the different models for this specified purpose has been rarely investigated, especially for what concerns NH_3/IL pairs. In recent publications, only Shiflett and Yokozeki [61] mentioned that an accurate prediction of the mixing enthalpy with NRTL model was difficult, because the excess enthalpy is derived from the temperature derivative of the activity coefficient, and the temperature-dependency in any activity model is always in a purely empirical form.

Thus, a thorough assessment of these VLE models is of significance for the NH_3/IL working fluids.

1.3.2. PRACTICAL CONSIDERATIONS

In terms of the VAR system evaluation, most of the studies were just based on system performance predictions, which maybe due to the relatively high cost of ILs [24]. In the recent decade, there were some experimental studies of IL-based VAR systems. For instance, Radspieler and Schweigler [62], Schneider *et al.* [63] and Wasserscheid and Seiler [64] experimentally studied H_2O/ILs pairs in a

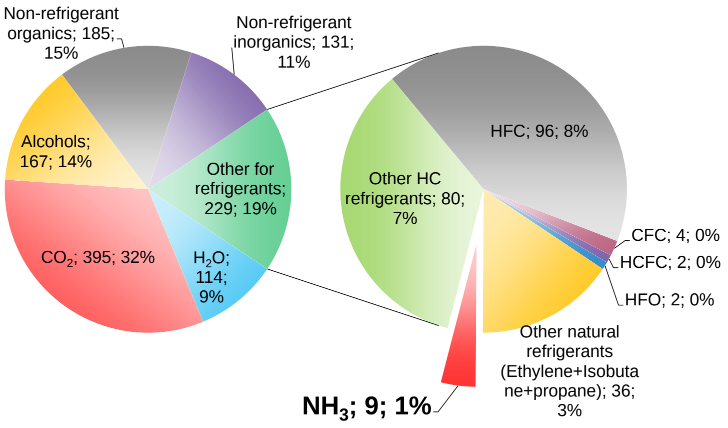

Figure 1.12: Statistics of measurements of VLE properties (including the measurements of the equilibrium pressure, temperature and composition) for the gas-component/IL-components binary mixtures. Data have been acquired from the NIST ILThermo database [58, 59] before August 7, 2017.

commercial system by substituting the working pairs. Kim *et al.* [65] studied a VAR system with R134a/[bmim][PF_6] in a small scale system obtaining a cooling COP of 0.35. Merkel *et al.* [66] ran an absorption heat transformer with most of the components of the set-up constructed with plate heat exchangers. Besides those, there were also works aiming at understanding the heat and mass transfer of the IL-based working fluids. Meyer *et al.* [67] studied the combined heat and mass transfer phenomena of H_2O/[emim][DEP] pairs in an absorption refrigeration system by using analytical functions. Ariyadi and Coronas [68] developed a measurement setup to study the absorption capacity of NH_3 vapor in ILs in a pool type absorber. Wadekar [69] simulated the heat transfer behavior of IL [bmim][Tf_2N] in different heat exchangers (HXs). The results showed that the heat transfer performance was not particularly attractive, but heat transfer enhancement technology can improve it effectively. Boman *et al.* [70] screened working pairs including the IL-based ones for a single-effect AHP based on both thermodynamic and heat transfer principles. The shell-and-tube HXs of IL-based AHP systems need more heat exchanger area due to the poor heat transfer performance of the ILs. Chugh *et al.* [71] implemented a membrane-based semi-open absorption system using IL for heating, dehumidification and cooling applica-

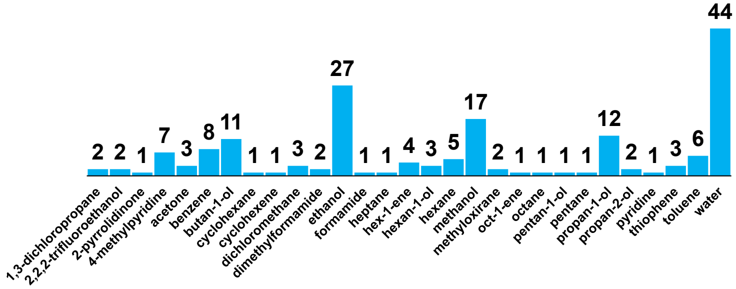

Figure 1.13: Statistics of measurements of excess enthalpies for the IL-based binary mixtures, whose VLE were also reported. Data have been acquired from the NIST ILThermo database [58, 59] before August 7, 2017.

tion. The experimental test achieved a heating coefficient of performance (COP) of 1.4.

Besides the mentioned experimental investigations, studies with more practical considerations are still limited. Studies of NH_3/IL working fluid in closed loops have not been reported yet. Also heat and mass transfer studies of this type of working fluids in appropriate geometries have not been reported yet.

1.4. SCOPE AND OUTLINE OF THIS THESIS

1.4.1. LIMITATIONS OF PREVIOUS STUDIES

The previous sections introduced knowledge of the NH_3-based VAR cycles and reviewed current research on NH_3/IL working fluids applied in VAR cycles. As a summary, some limitations of the previous relevant studies are:

Research related to NH_3/IL working pairs is limited. Most of the IL-based VAR cycles studied were based on CO_2, H_2O and HCs and HFCs as refrigerants. As a highly performing natural refrigerant, feasible for both industrial and residual heating and cooling, NH_3 based working fluids in VAR cycle need further investigation.

The estimations of mixing enthalpies for the IL-based working pairs used for VAR cycles were not thoroughly evaluated. Except for some binary systems containing H_2O or some alcohols, measured mixing enthalpies are practically not available. For NH_3, no data has been reported for the mixing enthalpies as far as the author is aware of. The suitability of VLE models for estimating the mixing enthalpies has still not been comprehensively investigated.

The potential of more advanced NH_3-based VAR systems needs to be explored since the complexity of these systems could be reduced a lot by using ILs. Advanced cycles, for instance the double-effect ones which achieve high performance, are worth investigating for appropriate applications. The feasibility of applying the proposed systems from techno-economic and environmental points of view needs to be investigated, so that the benefits of applying NH_3/IL based VAR cycles can be quantified.

The relatively high viscosity of ILs has always been considered as a disadvantage when applying ILs in practice due to its negative influence on the heat & mass transfer processes. Only a limited amount of studies was carried out for the proposed working fluids for what concerns the heat & mass transfer. Appropriate geometries for vapor absorption are rarely suggested either. As a consequence, knowledge on the design of appropriate equipment with the novel fluids is limited.

1.4.2. SCOPE AND METHODOLOGY OF THIS STUDY

The main focus of this study is to evaluate the application of NH_3/IL working pairs in VAR cycles. The author bridges the knowledge of the new absorbents, ILs, with the absorption refrigeration field. To answer the aforementioned challenging questions and fill-in some scientific gaps on this topic, the content of this thesis covers aspects going from properties, to systems/applications, and to equipment. Correspondingly, various methodologies are involved.

For what concerns properties, various VLE models are correlated using experimental VLE data and their performance in reproducing vapor pressure is evaluated. By using thermodynamically consistent equations, the mixing enthalpies are also estimated with different VLE models. These properties influence the calculation of the cycle performance. The overall effects are evaluated by applying different VLE models for the evaluation of a single-effect VAR cycle. In addition, an optimization work based on a genetic algorithm (GA) is developed to determine the properties of ideal absorbents required for an optimum cycle performance. In addition, outside the range of available experimental VLE, Monte Carlo (MC) simulations are carried out to predict the VLE data at high temperature and high pressure conditions. These results are needed to allow for the prediction of the performance of NH_3/IL working fluids in double-effect VAR cycles.

For what concerns system aspect, the performances of single-effect and double-effect cycles are evaluated using the first law of thermodynamics. Experimental data of VLE and heat capacities are the basis of the analysis, while for the double-effect cycle, VLE data from MC simulations are also applied. Additionally, the technical and economic performance and environmental impacts of these cycles are investigated when applied to specific applications.

For what concerns system component, plate heat exchangers (PHXs) are proposed to be used with the NH_3/IL working fluids in the vapor absorption systems. A theoretical method is employed to model the local heat and mass transfer processes within the absorber. The two-resistance theory is applied to describe the vapor-liquid interface behavior during absorption. Experimental data of the heat and mass transfer processes are used to develop correlations which are used in the model to describe the transport phenomena.

1.4.3. OUTLINE OF THIS THESIS

The sequence of chapters in this thesis reflects that the investigation of NH_3/IL absorption heat pump and refrigerations systems gradually moves from conceptual to detailed level. Fig. 1.14 provides the topics and highlights of the chapters.

Thermodynamic properties of the new working fluids provide a foundation to carry out other studies in evaluating their applications for specific purposes. However, before being capable of doing it, the thermodynamic properties models, based on which, the properties are modeled, should be carefully selected for the newly studied working pairs. The VLE models are systematically assessed in Chapter 2, to investigate their performance in correlating and reproducing the corresponding experimental VLE data, and in estimating the mixing enthalpies.

In Chapters 3 and 4, the studies of thermodynamic cycles allow to determine which working fluids are most suitable to be used in single- and double-effect absorption cycles, respectively, and which ones are most promising. The performance of a single-effect cycle was evaluated for eight NH_3/IL working pairs. Chapter 3 also contains an optimization of the single-effect cycle, which provides the required properties of the working fluids to obtain optimum performance in NH_3/IL single-effect cycles, and assists in the selection of ILs as absorbents. Chapter 4 discusses the application of double-effect VAR cycles driven by waste heat for cooling of fishing vessels. One of the features in this chapter is the use of molecular simulations to predict the VLE data at high temperature levels, which helps to prevent errors by directly extrapolating the VLE data. Techno-economic and environmental studies in the two chapters identify benefits of applying these novel working pairs for certain applications.

After answering the capabilities of the working pairs, Chapter 5 studies the heat & mass transfer performance of the selected working fluids. A theoretical study is carried out by using a model which takes simultaneous heat and mass transfer of NH_3 absorption into NH_3/IL mixtures in plate heat exchangers into account. The transport phenomena are derived from an experimental study of NH_3 absorption into an NH_3/$LiNO_3$ mixture in a corrugated plate heat exchanger.

Chapter 6 summarizes the main conclusions of the study. Further efforts in terms of investigating and applying ILs within absorption systems are also outlooked.

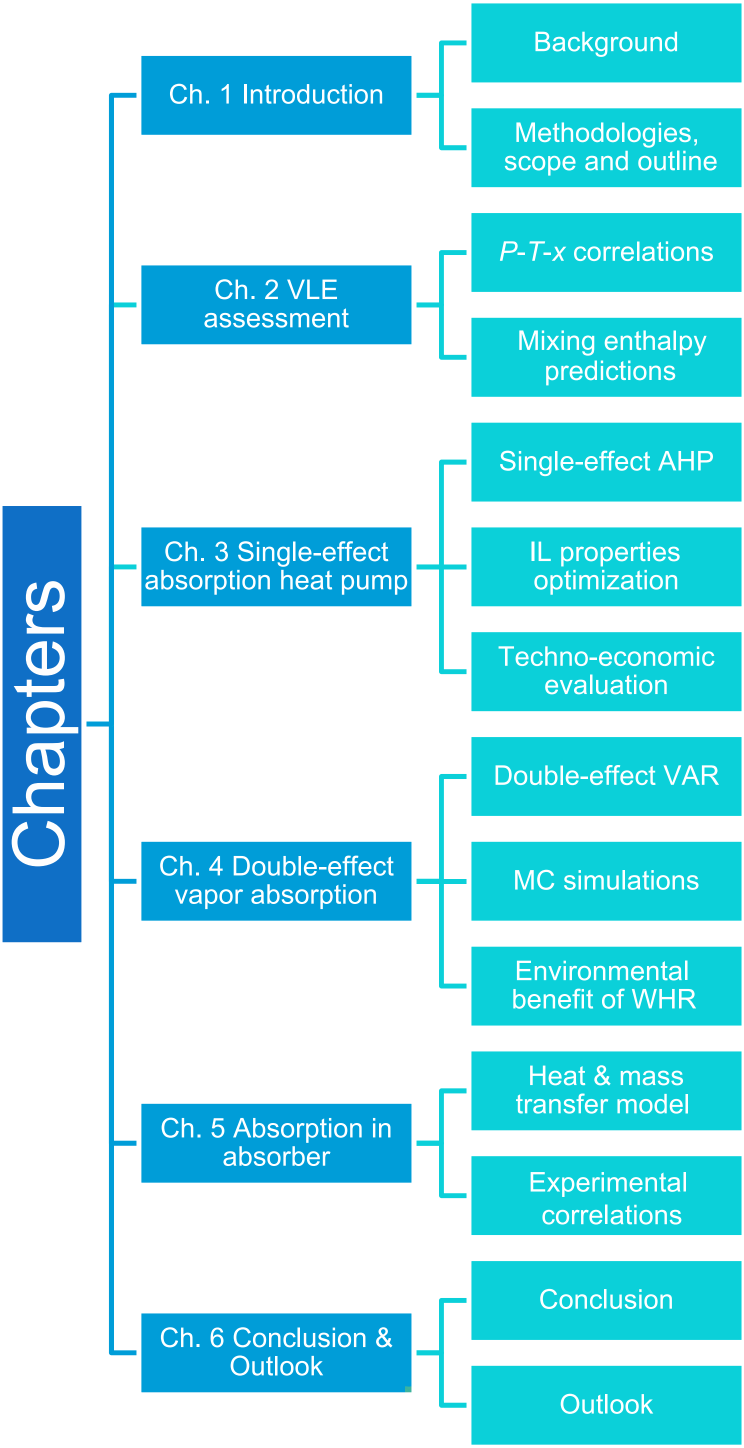

Figure 1.14: Scope of this thesis: topics and highlights of chapters.

2

ASSESSMENT OF VAPOR-LIQUID EQUILIBRIUM MODELS FOR IONIC LIQUID BASED WORKING PAIRS IN ABSORPTION CYCLES

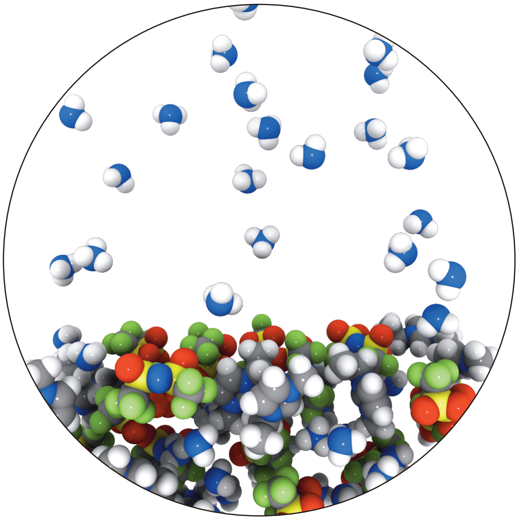

This chapter assesses the performance of vapor-liquid equilibrium (VLE) models in ionic liquid based absorption cycles with natural refrigerants. Frequently used equation-of-state (EOS) based models, activity coefficient based models, and generic Clausius-Clapeyron relations are evaluated. Working pairs considered are H_2O*/[emim][DMP] and* NH_3*/[bmim][*BF_4*]. Firstly, experimental VLE data of those working pairs are correlated by using the models. Mixing enthalpies are then estimated using the models and corresponding correlated parameters. Performances of the different models in reproducing VLE data and estimating mixing enthalpies are compared with each other. Subsequently, total enthalpies and thermodynamic performances of absorption refrigeration cycles are predicted based on the different models. The assessment reveals that the RK-EOS and the NRTL model perform best in reproducing VLE data. In addition, the RK-EOS and the UNIFAC model show the best performance in estimating mixing enthalpies. Hence, the RK-EOS is recommended in correlating VLE data and estimating mixing enthalpies in absorption cycles.*

Parts of this chapter have been published in: International Journal of Refrigeration, **87**, 10-25 (2018) [72].

2.1. INTRODUCTION

Vapor-liquid equilibrium (VLE) properties and their models play significant roles in the performance analysis of absorption cycles with novel ionic liquid-based working pairs. Firstly, they are used to correlate and predict the relationship between pressure, temperature and composition of working pairs. This is usually applied as the first step in performance evaluations, such as working pair screening, and determination of state point conditions. The correlated VLE models can also be used to estimate the mixing enthalpy of the working pair, which is an essential part of the total enthalpy. The term mixing enthalpy quantifies the heat effect during mixing of liquid components, which is defined as the difference between the total enthalpy of the solution and its ideal counterpart [73],

$$\Delta\bar{h}_{\text{mix}} = \bar{h}^{\text{sol}} - \sum_{i} x_{\text{i}}\bar{h}_{\text{i}} \tag{2.1}$$

VLE models applied in absorption cycles in recent studies are reviewed as follows. For the H_2O based pair H_2O/[emim][DMP], Yokozeki and Shiflett [74] measured and analyzed VLE data of plentiful H_2O/ILs working pairs using the generic Redlich-Kwong (RK) equation of state (EOS) model and applied this model in the absorption cycle analysis. Wang *et al.* [75], Wu *et al.* [76], Ren *et al.* [77], Nie *et al.* [78] measured and correlated vapor pressure data for other H_2O/ILs pairs with the NRTL model. The correlated NRTL model of Ren *et al.* [77] has also been used to study the performance of absorption chillers [79] and absorption heat transformers [80]. Dong *et al.* [38] used their own correlated NRTL model for the estimation of mixing enthalpy in an investigation of an absorption refrigeration cycle with the H_2O/[dmim][DMP] pair. Kim *et al.* [81] explored a miniature absorption refrigeration cycle with working pairs consisting of different refrigerants and imidazolium-based ILs, including H_2O/[emim][Tf_2N] and H_2O/[emim][BF_4] working pairs. The correlated NRTL model was used for VLE determination and mixing enthalpy estimation. However, in their following work [65, 82], the NRTL model was replaced by the generic RK-EOS model, which is the same model Yokozeki and Shiflett [39, 40, 74] previously used. Since 2013, the group of Zheng started using the UNIFAC model. They examined the previous VLE experimental data of H_2O/ILs pairs [83, 84] with the UNIFAC model to quantify the interaction parameters. In terms of NH_3, Yokozeki and Shiflett [39, 40] applied the generic RK-EOS model in their work to correlate experimental VLE data and to estimate the mixing enthalpy for ammonia based pairs, after they pointed out that an accurate estimation of the mixing enthalpy with the NRTL model is difficult [61]. Additionally, Chen *et al.* [46] implemented a self-correlated UNIFAC model [43] to estimate the mixing enthalpy for an NH_3/IL-based absorption cycle. Ruiz *et al.* [44] modeled NH_3/ILs absorption cycles making use of the COSMO-based Aspen thermodynamic properties estimation. The COSMO-RS model was used to estimate properties of non-database components. An overview of previous studies which used VLE models to estimate the mixing enthalpies for H_2O/IL and NH_3/IL working pairs is summarized in Table 2.1.

It is obvious that the NRTL, RK-EOS and UNIFAC models have been frequently used to correlate experimental VLE data and to estimate the mixing enthalpies of working pairs for absorption cycles. All these mentioned models can be regarded as thermodynamically consistent models (TCMs). They were also classified into a family of Gibbs-Helmholtz (G-H) equations by Mathias and O'Connell [60], Mathias [87], which bridges the phase equilibrium with the enthalpy change.

$$\frac{\bar{h}}{R} = \left.\frac{d\left(\bar{g}/RT\right)}{d\left(1/T\right)}\right|_p \tag{2.2}$$

Depending on the certain equation applied in the description of the equilibrium, the forms can be different. The current methods of mixing enthalpy estimation can be sorted into the following groups: EOS methods (Eq. 2.3), activity coefficient, G^e, (Eq. 2.4) method and C-C method (Eq. 2.5), the general forms of them are as follows, respectively,

$$\frac{\bar{h}_{\mathrm{i}}^{\mathrm{res}}}{R} = -\left.\frac{\partial \ln \hat{f}_{\mathrm{i}}}{\partial\left(1/T\right)}\right|_{p,x} \tag{2.3}$$

$$\frac{\bar{h}^{\mathrm{e}}}{R} = \left.\frac{d\left(g^{\mathrm{e}}/RT\right)}{d\left(1/T\right)}\right|_{p,x} \tag{2.4}$$

$$\frac{\Delta\bar{h}}{R} = \frac{\partial \ln P}{\partial\left(1/T\right)} \tag{2.5}$$

They are mathematically derived from the fundamental thermodynamic relations, see details in Mathias and O'Connell [60] and Mathias [87]. The right sides of these TCMs are related to the equilibrium properties, and the left sides provide enthalpy changes. Functionally similar to the Gibbs-Duhem equation, these TCMs can be used for:

1. Property estimation, when having the VLE data to predict energy data or vice versa.
2. Consistency analysis, when having both VLE and excess enthalpy data.

In this work, various thermodynamic models are used to correlate the same experimental VLE data of two refrigerant/IL working pairs, H_2O/[emim][DMP]

Table 2.1: VLE models applied for the estimation of mixing enthalpy in H_2O/IL and NH_3/IL-based absorption cycles.

Working fluids*	**Application**	**Model for the excess enthalpy**	**Researcher**	**Source of VLE data**
H_2O/[emim][DMP]	absorption refrigeration cycle absorption heat transformer cycle	NRTL NRTL	Zhang and Hu [79] Zhang and Hu [80]	Ren *et al.* [77]
H_2O/[dmim][DMP]	absorption refrigeration cycle	NRTL	Dong *et al.* [38]	Dong *et al.* [38]
H_2O/[emim][Tf_2N] H_2O/[emim][BF_4]	absorption refrigeration cycle absorption refrigeration cycle	NRTL NRTL	Kim *et al.* [81]	Kato and Gmehling [85] Seiler *et al.* [86]
H_2O/[bmim][BF_4] H_2O/[emim][BF_4] H_2O/[emim][$C_2H_5SO_4$] H_2O/[mmim][$(CH_3)_2PO_4$] H_2O/[bmim][I] H_2O/[choline][Gly] H_2O/[choline][CH_3SO_3] H_2O/[choline][Lac] H_2O/[bmim][$(C_4H_9)_2PO_4$] H_2O/[eeim][$(C_2H_5)_2PO_4$] H_2O/[emim][$(C_2H_5)_2PO_4$] H_2O/[emim][$(CH_3)_2PO_4$]	absorption refrigeration cycle	RK EOS	Yokozeki and Shiflett [74]	Yokozeki and Shiflett [74]
NH_3/[bmim][PF_6] NH_3/[hmim][Cl] NH_3/[emim][Tf_2N] NH_3/[bmim][BF_4]	absorption refrigeration cycle	RK EOS	Yokozeki and Shiflett [39]	Yokozeki and Shiflett [39]
NH_3/[emim][Ac] NH_3/[emim][SCN] NH_3/[emim][$EtOSO_3$] NH_3/[DMEA][Ac]	absorption refrigeration cycle	RK EOS	Yokozeki and Shiflett [40]	Yokozeki and Shiflett [40]
NH_3/[bmim]Zn_2Cl_5	absorption refrigeration cycle	UNIFAC	Chen *et al.* [46]	Chen *et al.* [43]
NH_3/[choline][NTf_2] NH_3/[emim][Ac] NH_3/[emim][$EtSO_4$] NH_3/[emim][SCN] NH_3/[HOemim][BF_4] NH_3/[hmim][Cl]	absorption refrigeration cycle	COSMO-RS	Ruiz *et al.* [44]	N/A

* Nomenclature of ILs is according to the original works.

and NH_3/[bmim][BF_4]. The performance of these models is examined. The models considered here include EOS models, activity coefficient models and the general Clausius-Clapeyron relations. Following the thermodynamic consistency, performances of different models in estimating mixing enthalpies and total enthalpies are also evaluated. The estimated values from different models are compared with each other. For H_2O/[emim][DMP], experimental values are also included. Finally, these VLE models are applied to calculate the performance of an absorption cycle, to test how the precision of the model influences the prediction of the cycle performance. This systematic assessment of VLE models is intended to provide essential information for the selection of models in IL-based absorption cycles.

2.2. APPROACHES AND VLE MODELS

The procedure of the assessment in this study can be summarized as follows:

1. Reliable VLE data are applied to correlate the corresponding VLE models. The correlation performance is evaluated by comparing the deviations. The preferred model gives a low value for the root-mean-square deviation ($RMSD$) between experimental data and predicted values. A high value of the squared correlation coefficient (r^2) would confirm the quality of the correlations.

2. VLE data from independent sources of the same working pairs are adopted to verify the reproducibility of the correlations, and to allow for an uncertainty analysis of the experimental VLE data.

3. Using corresponding models, mixing enthalpies are estimated based on the correlated interaction parameters obtained previously in Step 1.

As mentioned in the introduction in Section 2.1, there are 3 different alternative methods for the estimation of $\Delta\bar{h}_{\mathrm{mix}}$ from VLE data by VLE models. In contrast to the method based on the C-C relation, the EOS and G^e methods rely on interaction parameters correlated from VLE data. Thus, the method of VLE calculation is first introduced.

2.2.1. VLE CALCULATIONS

The equilibrium criterion is the starting point of VLE calculations. Its general form can be expressed by using the fugacities of both liquid and vapor phases [88],

$$\hat{f}_{\mathrm{i}}^{\mathrm{L}}(T, P, x_{\mathrm{i}}) = \hat{f}_{\mathrm{i}}^{\mathrm{V}}\left(T, P, y_{\mathrm{i}}\right) \tag{2.6}$$

When using EOS methods, the equilibrium criterion can be stated as in Eq. 2.7. This procedure is also referred to as ϕ-ϕ method,

$$x_i\hat{\phi}_i^L(T,P,x_i) = y_i\hat{\phi}_i^V(T,P,y_i) \tag{2.7}$$

The fugacity coefficients ϕ for both phases can be obtained from the EOS.

Another description of VLE uses an activity coefficient for the liquid phase and an EOS for the vapor phase. This method is usually referred to as the γ-ϕ method.

$$x_i\gamma_i(T,P,x_i)P_i^{sat}(T)\Phi_i = y_iP\hat{\phi}_i^V(T,P,y_i) \tag{2.8}$$

In the case of refrigerant/IL systems, due to the non-volatility of IL, its fraction in the vapor phase can be neglected, i.e. $y_1 = 1$. The equilibrium pressure of the binary system is relatively low, especially compared with the critical pressure of refrigerants. Therefore, the Poynting correction Φ can be considered to be unity. The fugacity coefficient of the refrigerant component in the vapor phase, $\bar{\phi}_1^V$, can also be approximated to be 1 due to the ideal behavior of the vapor at low pressure. Following these assumptions, Wang *et al.* [75] and Ren *et al.* [77] implemented the equilibrium criterion as,

$$\gamma_1 = \frac{P}{x_1P_1^{sat}} \tag{2.9}$$

For the VLE models discussed in this work, the same set of experimental data are used to regress the unknown interaction parameters. The nonlinear-least-square method is implemented to correlate the data. The objective function F in Eq. 2.10 is chosen as the difference between experimental liquid phase fugacity values and calculated ones using the models.

$$F = \sum_{i=1}^{N}\left(\hat{f}_{1,i}^{exp,L} - \hat{f}_{1,i}^{calc,L}\right)^2 \tag{2.10}$$

2.2.2. MIXING ENTHALPY ESTIMATION

MIXING ENTHALPY ESTIMATED FROM EOS MODELS

The first method for the estimation of $\Delta\bar{h}_{mix}$ is to use a specific EOS model. After obtaining the interaction parameters in the mixing rules, the general form of residual enthalpy, $\bar{h}^{res}$, can be expressed as Eq. 2.11,

$$\bar{h}^{res} = RT^2\int_{P_0}^{P}\left(\frac{\partial Z}{\partial T}\right)_P \frac{dP}{P} \tag{2.11}$$

where Z is the compressibility factor, the form of which depends on the certain EOS. Residual enthalpy, $\bar{h}^{res}$, is defined as the difference between the ideal gas enthalpy and the real one.

$$\bar{h}^{\text{res}} = \bar{h}^{\text{ig}} - \bar{h}^{\text{real}} \tag{2.12}$$

With the residual enthalpies of the mixture and of both pure components at liquid state, the mixing enthalpy can be calculated via

$$\Delta\bar{h}_{\text{mix}} = \sum_{i=1}^{N} x_{\text{i}}\bar{h}_{\text{i}}^{\text{res}} - \bar{h}_{\text{sol}}^{\text{res}} \tag{2.13}$$

In this study, the PR-EOS with van der Waals mixing rules (PRVdW) [89], PR-EOS with Wong-Sandler mixing rules (PRWS) [90] and a modified RK-EOS [40] were included in the evaluation. The details of these models can be found in Appendix B.

MIXING ENTHALPY ESTIMATED FROM G$^{\text{e}}$ MODELS

The second method is to use G$^{\text{e}}$ models. With a G$^{\text{e}}$ model and the corresponding regressed binary interaction VLE parameters, the excess Gibbs energy can be obtained by

$$\frac{\bar{g}^{\text{e}}}{RT} = \sum_{i=1}^{N} x_{\text{i}} \ln \gamma_{\text{i}} \tag{2.14}$$

The relationship between excess enthalpy and excess Gibbs energy is defined by Eq. 2.4. Together with Eq. 2.14, the excess enthalpy can be obtained.

G$^{\text{e}}$ models only work for solutions, thus, the excess enthalpy calculated by Eq. 2.4 is actually the mixing heat [38, 46]. G$^{\text{e}}$ models considered here are the NRTL [38] and the UNIFAC [83] models. The details of these models can also be found in Chapter 3 and in Appendix B.

MIXING ENTHALPY ESTIMATED FROM C-C EQUATION

The third method to estimate the $\Delta\bar{h}_{\text{con}}$ is to use the C-C equation. In a $\ln P$-(-$1/T$) diagram, the slope of the curve reflects the heat effect during phase-change:

$$\frac{d \ln P}{d(1/T)} = -\frac{\Delta\bar{h}}{R} \tag{2.15}$$

For the vapor pressure curve of a pure fluid, $\bar{\Delta} h$ is the latent heat $\Delta\bar{h}_{\text{con}}$ [91]. When it concerns the vapor pressure of a mixture with fixed fraction, $\Delta\bar{h}$ is the absorption heat $\Delta\bar{h}_{\text{abs}}$ [67]. Note that the mixing enthalpy is the heat effect during the mixing of two liquid components, it can be obtained by removing the latent heat from the absorption heat,

$$\Delta\bar{h}_{\text{mix}} = \Delta\bar{h}_{\text{abs}} - \Delta\bar{h}_{\text{con}} \tag{2.16}$$

Table 2.2: Inputs to the PR-EOS for the studied working pairs*.

Compound	T_c [K]	P_c [MPa]	ω [-]
H_2O	647.1	22.06	0.3443
[emim][DMP]	836.85	2.50	0.6383
NH_3	406.15	11.42	0.25601
[bmim][BF_4]	643.18	2.04	0.8877

* PRVdW and PRWS models are discussed in Peng and Robinson [89] and Wong and Sandler [90], respectively. Critical points and acentric factors are predicted using the group-function method proposed by Valderrama and Robles [92].

Table 2.3: Inputs to the RK-EOS for the studied working pairs*.

Compound	T_c [K]	P_c [MPa]	β_0 [-]	β_1 [K]	β_2 [MPa]	β_3 [-]
H_2O	647.1	22.06	1.00236	0.54254	-0.08667	0.00525
[emim][DMP]	852.21	1.81	1	to be correlated	0	0
NH_3	406.15	11.42	1.00027	0.45689	-0.05772	0
[bmim][BF_4]	894.9	3.02	1	to be correlated	0	0

* The RK-EOS studied in this work and its input parameters are discussed in Yokozeki and Shiflett [39, 74].

2.2.3. PARAMETERS IN VLE MODELS

Except for the NRTL model, the application of VLE models in VLE calculation and the estimation of the $\Delta\bar{h}_{\text{mix}}$ require input information. For instance, the critical information and acentric factors are required for the EOS based models. In the case of UNIFAC models, group volumes, area parameters and some interaction parameters of/between split functional groups are needed. H_2O/[emim][DMP] and NH_3/[bmim][BF_4] working pairs were selected because the required input information of these pairs is available in literature. Tables 2.2, 2.3, 2.4 and 2.5 list the needed information and the corresponding references for each model discussed in this study. Note that all the inputs of the studied ILs in PR-EOS (Tables 2.2) are predicted using the group-function method proposed by Valderrama and Robles [92]. However in the studied RK-EOS, acentric factors are not required inputs. The critical information follows the ones used in the original works [39, 74].

2.3. RESULTS AND DISCUSSION

2.3.1. PERFORMANCE IN CORRELATING AND REPRODUCING VLE DATA

H_2O/[EMIM][DMP] PAIR

H_2O/[emim][DMP] pair is one of the few working pairs for which experimental mixing enthalpy data have been published. For this working pair, the VLE data

Table 2.4: Group volumes and area parameters used in the UNIFAC model for the studied working pairs*.

Group	**Volumes** [-]	**Surface area** [-]
H_2O	0.92	1.4
NH_3	1.4397	2.0918
CH_2	0.6744	0.54
CH_3	0.9011	0.848
[mim][DMP]	6.2609	4.996
[mim][BF_4]	6.5669	4.005

* Group division of working fluids is discussed in Dong *et al.* [83], Lei *et al.* [93].

Table 2.5: Group interaction parameters used in the UNIFAC model for the studied working pairs*.

Group 1	**Group 2**	a_{12} [-]	a_{21} [-]
H_2O	CH_2/CH_3	300	1318
H_2O	[mim][DMP]	to be correlated $gi_1(1)$	to be correlated $gi_3(1)$
CH_2/CH_3	[mim][DMP]	to be correlated $gi_2(1)$	to be correlated $gi_4(1)$
NH_3	CH_2/CH_3	to be correlated $gi_1(2)$	to be correlated $gi_3(2)$
NH_3	[mim][BF_4]	to be correlated $gi_2(2)$	to be correlated $gi_4(2)$
CH_2/CH_3	[mim][BF_4]	1108.51	588.74

* Group division of working fluids is discussed in Dong *et al.* [83], Lei *et al.* [93].

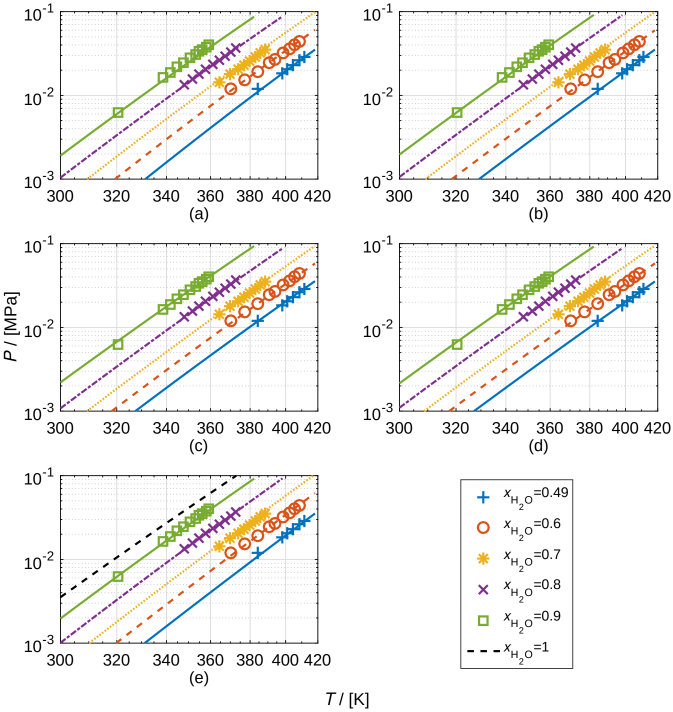

Figure 2.1: Experimental VLE data of the H_2O/[emim][DMP] pair as reported by Ren *et al.* [77] and the correlated VLE curves at constant H_2O fraction via different models. (a) PRVdW, (b) PRWS, (c) RK, (d) NRTL and (e) UNIFAC.

reported by Ren *et al.* [77] are used for the correlation. The authors collected the experimental data at 5 different H_2O fractions, see Fig. 2.1.

Different VLE models are correlated based on the VLE data. The correlated interaction parameters and the qualities of the correlations of different models are listed in Table 2.6. The qualities are quantified using the root-mean-square deviation ($RMSD$), the maximum relative deviation ($Max.\ Dev.$) of data points, and by the squared correlation coefficient (r^2) between the measured and correlated pressures (which reflect the degree of linearity of the correlations). The predicted VLE curves of the H_2O/[emim][DMP] pair are also illustrated in Fig. 2.1 from (a) to (e) for the corresponding VLE models.

The studied models seem to be able to reproduce the VLE data of the working pair H_2O/[emim][DMP]. The prefered models, RK-EOS and NRTL models, perform the best because they give low values for the *RMSD* between data and predicted values.

Table 2.6: Correlation results and performances of different models by using VLE data reported by Ren *et al.* [77] of H_2O/[emim][DMP] pair

	Correlated coefficients*	**Correlation performance****		
		$RMSD$	$Max. Dev.$	r^2
PRVdW	-0.796; -0.282	5.53%	11.35%	0.970
PRWS	0.576; 0.591; -15.080; -2.679	3.99%	7.14%	0.986
RK	0.174; -17.584; 0.038; 0.015; 0.608	2.43%	9.21%	0.997
NRTL	0.434; 0.454; 350.924; -2.261; -388.387	2.63%	7.08%	0.996
UNIFAC	-590.684; -686.639; -460.958; 1780.121	4.55%	10.17%	0.983

* Coefficients of PRVdW are k_{12} (=k_{21}) and l_{12} (=l_{21}) respectively [91]; Coefficients of PRWS are k_{12}, α, $\tau_{12}^{(0)}$ and $\tau_{21}^{(0)}$ respectively [94]; Coefficients of RK are β_1, τ_{12} (=τ_{21}), l_{12}, l_{21} and m_{12} (=m_{21}) respectively [40]; Coefficients of NRTL are α, $\tau_{12}^{(0)}$, $\tau_{12}^{(1)}$, $\tau_{21}^{(0)}$ and $\tau_{21}^{(1)}$ respectively [38]; Coefficients of UNIFAC are the group interaction parameters ($gi_1(1)$-$gi_4(1)$) mentioned in Table 2.5.

** $RMSD(P) = \sqrt{\frac{\sum_N (P_{\text{calc}}/P_{\text{exp}}-1)^2}{N}}$, represents the root-mean-square deviation. $Max. Dev.$ is the maximum relative deviation of data points. r^2 is the squared correlation coefficient between the measured and correlated pressures.

Table 2.7: VLE data reproducibility of the H_2O/[emim][DMP] pair [95] by using the correlated models based on VLE data reported by Ren *et al.* [77]

	$RMSD$	r^2
PRVdW	14.08%	0.976
PRWS	12.49%	0.982
RK	9.16%	0.965
NRTL	9.56%	0.965
UNIFAC	10.60%	0.966

The previous correlations were only based on the VLE data reported by Ren *et al.* [77]. VLE data from other, independent, source [95] are also applied to check the uncertainly of the previous correlations. Similarly, the root-mean-square deviation ($RMSD$) and the squared correlation coefficient (r^2) are adopted to verify the reproduction qualities, as listed in Table 2.7.

Even though the reproducibility of the independent data is worse then reproducing the same data used for the correlation, the performances of most models are still acceptable, especially for the RK and NRTL models with lower $RMSD$ values.

NH_3/[BMIM][BF_4] PAIR

VLE data of the NH_3/[bmim][BF_4] pair for 5 isothermal conditions are plotted in Fig. 2.2, as reported by Yokozeki and Shiflett [39]. The correlated interaction parameters and the correlations performances of the different models for this pair are listed in Table 2.8. Generally, the errors are larger than those for the

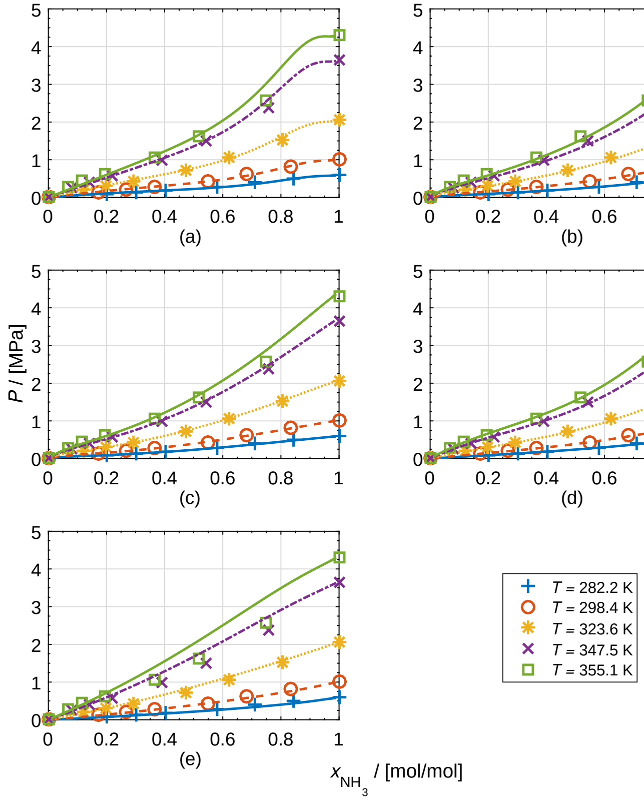

Figure 2.2: Experimental VLE data of the NH_3/[bmim][BF_4] pair as reported by Yokozeki and Shiflett [39] and the correlated VLE isotherms via different models. (a) PRVdW, (b) PRWS, (c) RK, (d) NRTL and (e) UNIFAC.

H_2O/[emim][DMP] pair. However, the RK-EOS and NRTL models still show the best performance. While the performance of the UNIFAC model is the worst. The predicted isotherms of the NH_3/[bmim][BF_4] pair are also illustrated in Fig. 2.2 from (a) to (e) for the corresponding VLE models.

VLE data reported by Li *et al.* [42] are applied here as an independent source to verify the reproducibility of the previous correlations based only on data of Yokozeki and Shiflett [39]. As listed in Table 2.9, the reproducibility of this pair is not as good as the previous checking for the H_2O/[emim][DMP] pair. Nevertheless, the reproduction qualities, especially of the ones based on NRTL and UNIFAC models, are still acceptable.

Table 2.8: Correlation results and performances of different models by using VLE data reported by Yokozeki and Shiflett [39] of NH_3/[bmim][BF_4] pair.

	Correlated coefficients *	**Correlation performance ****		
		$RMSD$	$Max. Dev.$	r^2
PRVdW	-0.036; 0.517	10.32%	25.52%	0.992
PRWS	0.633; -7.206; 0.233; 0.363	5.06%	11.79%	0.998
RK-EOS	0.771; -3.104; -0.017; -0.074; 0.028	4.68%	11.72%	0.997
NRTL	-0.011; -52.253; 9597.721; 36.085; -6024.139	2.82%	7.87%	0.997
UNIFAC	296.011; 210.119; -316.806; -316.844	14.64%	16.45%	0.987

* Coefficients of PRVdW are k_{12} (=k_{21}) and l_{12} (=l_{21}) respectively [91]; Coefficients of PRWS are k_{12}, α, $\tau_{12}^{(0)}$ and $\tau_{21}^{(0)}$ respectively [94]; Coefficients of RK are β_1, τ_{12} (=τ_{21}), l_{12}, l_{21} and m_{12} (=m_{21}) respectively [40]; Coefficients of NRTL are α, $\tau_{12}^{(0)}$, $\tau_{12}^{(1)}$, $\tau_{21}^{(0)}$ and $\tau_{21}^{(1)}$ respectively [38]; Coefficients of UNIFAC are the group interaction parameters ($gi_1(2)$-$gi_4(2)$) mentioned in Table 2.5.

** $RMSD(P) = \sqrt{\frac{\sum_N (P_{\text{calc}}/P_{\text{exp}}-1)^2}{N}}$, represents the root-mean-square deviation. $Max. Dev.$ is the maximum relative deviation of data points. r^2 is the squared correlation coefficient between the measured and correlated pressures.

Table 2.9: VLE data reproducibility of the NH_3/[bmim][BF_4] pair [42] by using the correlated models based on VLE data reported by Yokozeki and Shiflett [39]

	$RMSD$	r^2
PRVdW	29.4%	0.963
PRWS	36.8%	0.972
RK	37.9%	0.974
NRTL	27.3%	0.971
UNIFAC	23.6%	0.952

2.3.2. PERFORMANCE IN THE ESTIMATION OF MIXING ENTHALPIES

H_2O/[EMIM][DMP] PAIR

For the H_2O/[emim][DMP] working pair, the estimated mixing enthalpies using the different models at T = 298.15 K and P = 0.1 MPa (for G^e and C-C methods, only T = 298.15 K is required) are shown in Fig. 2.3 along with the experimentally measured ones [77, 96].

All estimated values show obvious deviations from the measured ones. The RK-EOS, UNIFAC and NRTL models estimate the experimental data the best. The mixing enthalpies estimated with the PRVdW model are positive while the other models show negative values. For conditions $x_{H_2O} < 0.5$, the results estimated with the C-C relation require extrapolation of the experimental data. This results in an outlier for $x_{H_2O} = 0.18$.

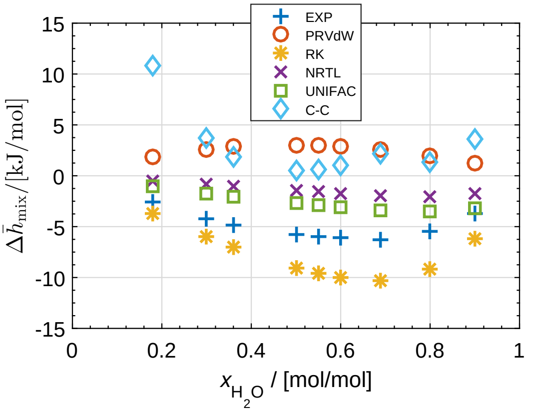

Figure 2.3: Comparison of the experimental and the estimated Δh_{mix} values for the H_2O/[emim][DMP] pair at T = 298.15 K and P = 0.1 MPa.

NH_3/[BMIM][BF_4] PAIR

The VLE data of the NH_3/[bmim][BF_4] pair were measured at 5 isothermal conditions. When using the C-C method, an additional step is required to obtain the data at different concentrations. Fig. 2.4 shows how the data have been processed. The experimental VLE data including the vapor pressure data of pure NH_3 are first fitted to a polynomial. Vapor pressure data at constant fractions (0.1-0.9 of NH_3 molar fraction) were then interpolated, see Fig. 2.4(a). The interpolated data are again plotted in a ln$P$-(-1/T) diagram, see Fig. 2.4(b), for the experimental temperature range. The slopes of these curves are used to estimate the absorption and mixing heat with Eq. 2.15 and 2.16. This data processing inevitably introduces additional errors.

Estimated $\Delta\bar{h}_{\mathrm{mix}}$ values at T = 298.15 K and P = 1.1 MPa (for G^e and C-C methods, only T = 298.15 K is required) are shown in Fig. 2.5. Note that for the given conditions, the pure NH_3 is at a liquid state, the latent heat is not taken into account here. The values for the PRVdW and PRWS models are significantly larger than the others, and are not presented. The two G^e models, i.e.: NRTL and UNIFAC, produce contradicting trends. The RK-EOS model and the C-C relation show intermediate values. $\Delta\bar{h}_{\mathrm{mix}}$ values estimated from C-C and RK-EOS change from positive to negative. This behavior indicates that the mixing of the two liquid components is exothermic at low ammonia fractions while endothermic at high fractions. The differences in the estimated $\Delta\bar{h}_{\mathrm{mix}}$ values at the same condition are significant.

To the best of the author's knowledge, the measurement of the mixing enthalpy for the solution NH_3/[bmim][BF_4] has not been reported currently, thus

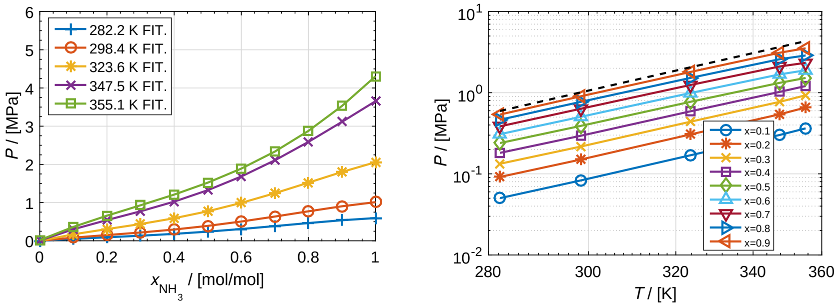

(a) (b)

Figure 2.4: VLE data processing before using Clausius-Clapeyron relations. (a) Interpolation at constant NH_3 fractions. (b) The interpolated data shown in a $\ln P$-$(-1/T)$ diagram (dash line represents the saturated pressure of pure NH_3).

the judgment of which model is more accurate for this pair is not available. Nevertheless, compared with $\Delta\bar{h}_{\mathrm{mix}}$ values of the H_2O/[emim][DMP] pair, absolute values of $\Delta\bar{h}_{\mathrm{mix}}$ for the NH_3/[bmim][BF_4] pair are generally much lower. This indicates smaller heat effects during the mixing of liquid NH_3 with [bmim][BF_4].

Table 2.10 summarizes the key information of the models considered in this study and their performances in respect to the estimation of $\Delta\bar{h}_{\mathrm{mix}}$.

OUTLOOK OF MOLECULAR SIMULATION

Besides the discussed models here, molecular simulations can be used to predict the mixing enthalpy of IL working pairs. In molecular simulations, thermodynamic properties are calculated based on a potential which describes the molecular interactions. These potentials are often correlated to experimental VLE data similar to the models discussed in this work, but can also be used to extrapolate mixture properties from pure component data. Previously, Maginn explored these methods to calculate the mixing enthalpy of H_2O/[emim][$EtSO_4$] [97] and NH_3/[emim][Tf_2N] [98]. While the initial results for H_2O/[emim][$EtSO_4$] did not agree well with experimental measurements, these authors slightly adjusted the potential to better reproduce experimental results. Moreover, these authors suggested more sophisticated potentials to further improve the accuracy of molecular simulations. Hence, we see molecular simulations as an alternative approach.

2.3.3. TOTAL ENTHALPY CALCULATIONS

H_2O/[EMIM][DMP] SOLUTION

Depending on the availability of the heat capacities of the IL-based solutions, there are two alternative methods to calculate the total enthalpy. If the heat ca-

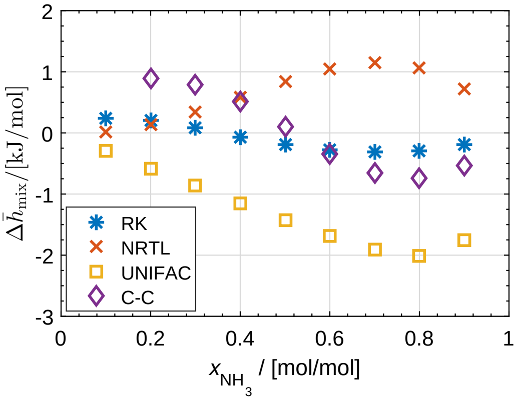

Figure 2.5: Comparison between the $\Delta\bar{h}_{\mathrm{mix}}$ estimated with the different estimation methods for the NH_3/[bmim][BF_4] working pair at T = 298.15 K and P = 1.1 MPa.

pacity of the solution, $\bar{c}_{\mathrm{p}}^{\mathrm{sol}}$, is known, its total enthalpy at a specified temperature and concentration can be calculated from

$$\bar{h}^{\mathrm{sol}}(T, x_1) = \bar{h}^{\mathrm{sol}}(298.15, x_1) + \int_{298.15}^{T} \bar{c}_{\mathrm{p}}^{\mathrm{sol}}(x_1)\, dT \tag{2.17}$$

where $\bar{h}^{\mathrm{sol}}(298.15, x_1)$ is the solution enthalpy at 298.15 K and an H_2O fraction of x_1. Based on an arbitrarily chosen reference state, here at 273.15 K, this enthalpy can be calculated via,

$$\bar{h}^{\mathrm{sol}}(298.15, x_1) = \Delta\bar{h}_{\mathrm{mix}}(298.15, x_1) + (1 - x_1) \int_{273.15}^{298.15} \bar{c}_{\mathrm{p}}^{\mathrm{IL}}\, dT + x_1 \int_{273.15}^{298.15} \bar{c}_{\mathrm{p}}^{\mathrm{H_2O}}\, dT \tag{2.18}$$

For the H_2O/[emim][DMP] working pair, total enthalpies at 328.15 K are calculated using $\Delta\bar{h}_{\mathrm{mix}}(298.15, x_1)$ from different models. The results are presented in Fig. 2.6. Heat capacities of pure IL and solutions reported by Zhang and Hu [79] were also used in the calculation. The properties of H_2O were taken from the NIST database [99].

The ideal solution, IS, in which the effects of mixing enthalpy are neglected is also shown in Fig. 2.6. Only mixing enthalpies calculated by the PR-EOS and the C-C relation, see Fig. 2.3, have positive deviations. Compared with the total enthalpy calculated using the experimental mixing enthalpies, the UNIFAC and RK models agree the best, while the comparable deviations are in opposite directions. The largest deviation occurs at a fraction around x_1 = 0.7-0.8.

Table 2.10: Summary of $\Delta\bar{h}_{\mathrm{mix}}$ estimation using the different VLE models for the H_2O/[emim][DMP] pair.

Type	**Model**	$\Delta\bar{h}_{\mathrm{mix}}$ **estimation method**	**Remarks**
EOS	PRVdW	$\ln\hat{f}_{\mathrm{i}} \rightarrow \bar{h}_{\mathrm{i}}^{\mathrm{res}} \rightarrow \Delta\bar{h}_{\mathrm{mix}}$	Critical information and acentric factors needed Sign of heat effect does not agree with experiments
	PRWS		Critical information and acentric factors needed Large deviations from experiments
	RK		Critical information needed, one the two best performing models
G^e	NRTL	$\ln\gamma_{\mathrm{i}} \rightarrow \bar{g}^{\mathrm{e}} \rightarrow \bar{h}^{\mathrm{e}}(\Delta\bar{h}_{\mathrm{mix}})$	No input needed, close to UNIFAC model
	UNIFAC		Group information needed, one of the best performing methods
	C-C	$\ln P_{\mathrm{i}} \rightarrow \Delta\bar{h}_{\mathrm{abs}} \rightarrow \Delta\bar{h}_{\mathrm{mix}}$	No input needed, second largest deviation

The previous method of the total enthalpy calculation only requires mixing enthalpy data at one temperature condition, while it also needs heat capacities of the solution. For most IL-based pairs, especially in the absorbent screening phase, the heat capacities of the solutions are not available. Therefore, the previously presented total enthalpy calculation method is not applicable. As an alternative, the following method which directly uses the mixing enthalpy and the enthalpy of the ideal solution can be applied [46, 65].

$$\bar{h}^{\mathrm{sol}}(T,x) = \Delta\bar{h}_{\mathrm{mix}}(T,x) + (1-x_1)\int_{T_0}^{T} \bar{c}_{\mathrm{p}}^{\mathrm{IL}}\,dT + x_1\int_{T_0}^{T} \bar{c}_{\mathrm{p}}^{\mathrm{H_2O}}\,dT \tag{2.19}$$

In Fig. 2.7, the total enthalpies calculated using both methods are displayed along the horizontal axis and the vertical axis, respectively. All points are displayed along the $x = y$ line. This indicates that the two methods can be used alternatively to calculate the total enthalpies for the H_2O/[emim][DMP] solution. Furthermore, this implies that the excess heat capacity of the solution, i.e. the difference between the heat capacity of the real solution and its ideal counterparts, has a very limited influence, because Eq. 2.19 neglects the excess heat capacity part.

NH_3/[BMIM][BF_4] SOLUTION

Fig. 2.8 shows the results of total enthalpies of the NH_3/[bmim][BF_4] solution when the mixing enthalpies obtained by the different sources are used. Eq. 2.19 has been used because there is no published heat capacity data for this solution. In comparison to the H_2O/[emim][DMP] solution, a smaller deviation can be observed between the ideal solution and the enthalpy values obtained with

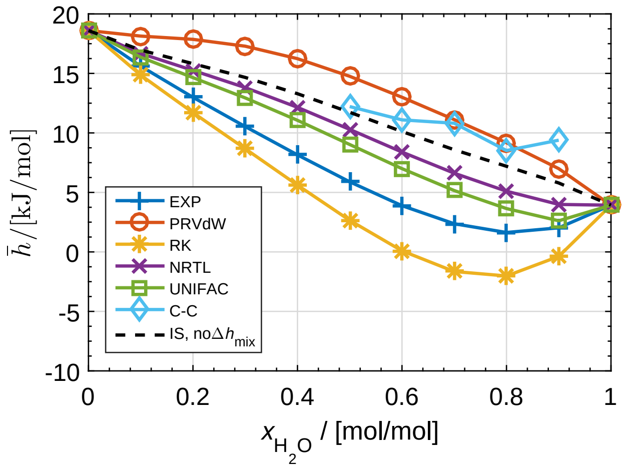

Figure 2.6: Comparison of the total enthalpies of the H_2O/[emim][DMP] solution at 328.15 K as estimated by the different VLE models. The lines distinguish sources of the mixing enthalpies for the estimation of total enthalpies.

the different models. This is because the $\Delta\bar{h}_{\mathrm{mix}}$ of the NH_3/[bmim][BF_4] pair is smaller.

2.3.4. INFLUENCE ON THE ABSORPTION CYCLE PERFORMANCE

Two factors resulting from VLE models can lead to different predictions of the performance of an absorption cycle. One is the influence of the models on the determination of operating conditions. If the solubility is incorrectly predicted, the cycle performance will be inaccurate. The second aspect is the mixing enthalpy estimation, which is of significance for the estimation of the total enthalpy. The circulation ratio, f, one of the performance criteria reflects solely the effect of the VLE correlation, while the coefficient of performance (COP) reflects the effects of both factors. In the following, the comparison of these two performance criteria is presented when the different models are used.

The cycle configuration and its thermodynamical description will be introduced in Chapter 3. In this study, both working pairs are applied in an absorption refrigeration system operating under the conditions $T_{\mathrm{con}}/T_{\mathrm{abs}}/T_{\mathrm{eva}} = 45/30/5\,°\mathrm{C}$. The heat source temperature T_{gen} varies from 85 to 100 °C.

The circulation ratio, f, which is defined as the mass flow ratio between the pump stream and the refrigerant stream can be obtained using mass and species balances,

$$f = \frac{\dot{m}_{\mathrm{s}}}{\dot{m}_{\mathrm{r}}} = \frac{1 - w_{\mathrm{w}}}{w_{\mathrm{s}} - w_{\mathrm{w}}} \tag{2.20}$$

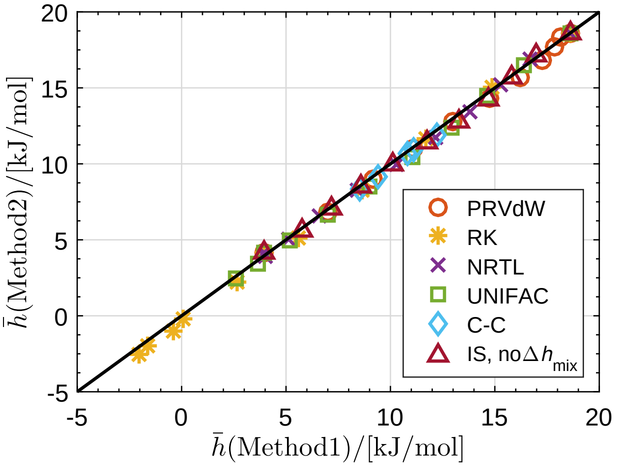

Figure 2.7: Comparison of the two methods for the calculation of the total enthalpies of H_2O/[emim][DMP] solution at 328.15 K. h-Method1 is based on Eq. 2.17 and 2.18, while h-Method2 is based on Eq. 2.19 The symbols distinguish sources of the mixing enthalpies for the estimation of total enthalpies.

Fig. 2.9 presents the results of circulation raio, f, for the absorption cycle with H_2O/[emim][DMP] working pair. These results are obtained when applying the different VLE models. f is solely quantified by the solubilities obtained from the VLE data. The results of f do not show large differences, because they are based on the same set of VLE experimental data.

Using the enthalpy calculation methods discussed in Section 2.3.3, the COP, defined as a ratio between the cooling effect obtained in the evaporator and the heat input to the generator, can be calculated. Fig. 2.10 shows the estimated COP for varying levels of heat source temperature. Since there is no sensible difference in f, the difference in the predicted COPs is mainly due to the difference in mixing enthalpies. Results based on ideal solutions and experimental mixing enthalpy data are also plotted as references.

Generally, the models that estimate higher mixing enthalpies lead to a higher predicted COP. This relationship implies that a less exothermic effect during mixing is preferable for the absorption cycle. The highest COP is attained when using the C-C model. Thereby, it is shown that a steep change of the mixing enthalpy can lead to an overestimated performance.

Similar to the mixing enthalpy estimation, RK-EOS and UNIFAC models also present the closest predictions for COP values compared with the one using experimental data. However, the COP values predicted using these two models are distributed on both sides of the experimental predicted COP.

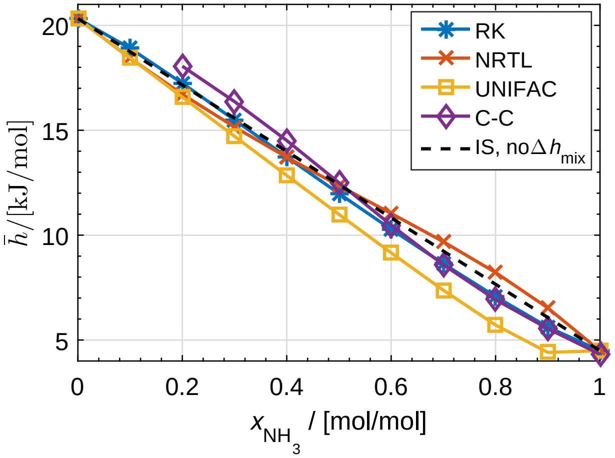

Figure 2.8: Comparison of the total enthalpies at 328.15 K of the NH_3/[bmim][BF_4] solution estimated by different VLE models. The lines distinguish sources of the mixing enthalpies for the estimation of total enthalpies.

For the NH_3/[bmim][BF_4] working pair, the values of f and COP of the absorption refrigeration cycle are also calculated, see Figs. 2.11 and 2.12. Large differences for f can be observed at a lower generation temperature (85 °C): The UNIFAC model gives a lower value of f, which leads to a higher estimation of COP. This is mainly due to the relatively poor performance in reproducing the VLE data, as listed in Table 2.8. For high generation temperatures, RK-EOS, UNIFAC and C-C models show similar values for the COP, while all results are lower than the ones for the ideal solution. The NRTL model overestimates the COP. The relation between the cycle performance and the estimated values of Δh_{mix} agrees with the previous observations for the cycle using H_2O/[emim][DMP] as working pair. Additionally, the COP values of the cycle with NH_3/[bmim][BF_4] working pair are lower than the ones for the H_2O/[emim][DMP] pair.

2.4. CONCLUSIONS

The performance of different VLE models applied to ionic liquid based absorption refrigeration cycles has been evaluated, for the two investigated working pairs (H_2O/[emim][DMP] and NH_3/[bmim][BF_4]). Specifically:

- For the sake of analyzing absorption cycles when no experimental data is available for the mixing enthalpy, the Redlich-Kwong equation of state performs best in both correlating VLE data and estimating mixing enthalpies. Besides, the NRTL model is also suitable for the correlation of VLE data and

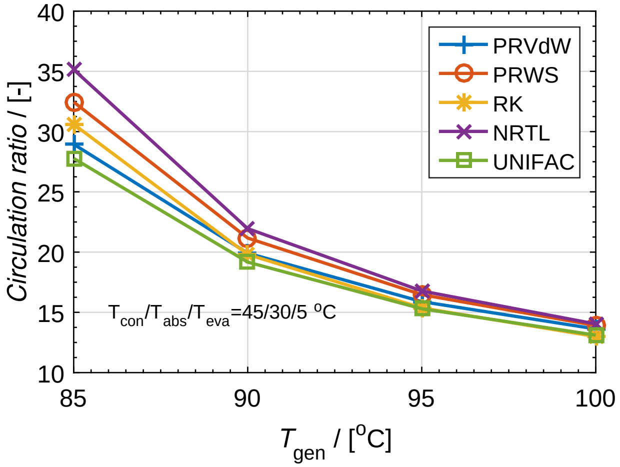

Figure 2.9: Calculated circulation ratio of the H_2O/[emim][DMP] working pair in an absorption refrigeration cycle by different VLE models. The lines distinguish sources of the VLE prediction.

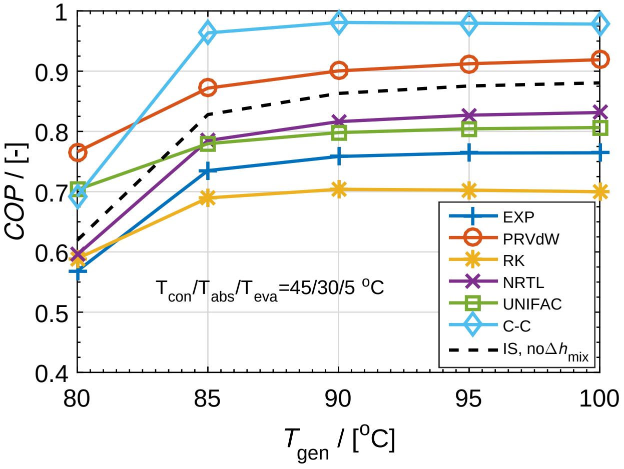

Figure 2.10: Calculated coefficient of performance of the H_2O/[emim][DMP] working pair in an absorption refrigeration cycle when the different VLE models are applied. The lines distinguish sources of the VLE prediction and the mixing enthalpy estimation.

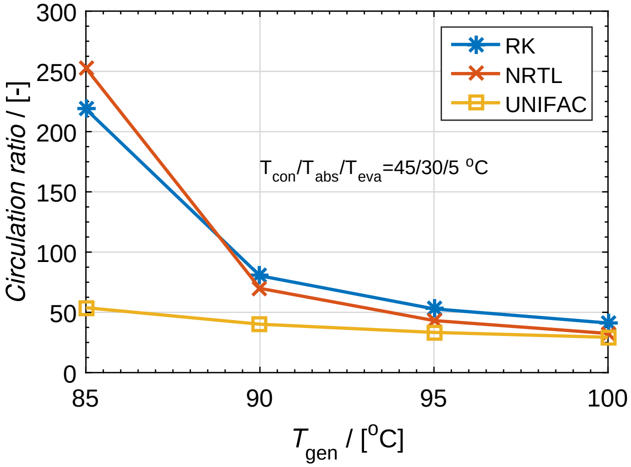

Figure 2.11: Calculated circulation ratio of the NH_3/[bmim][BF_4] working pair in an absorption refrigeration cycle by different VLE models. The lines distinguish sources of the VLE prediction.

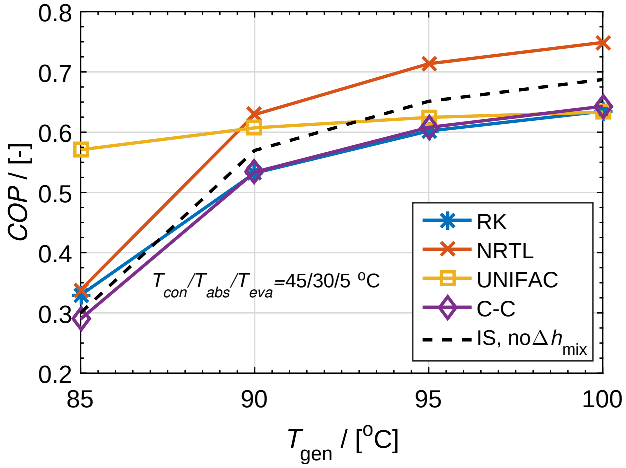

Figure 2.12: Calculated coefficient of performance of the NH_3/[bmim][BF_4] working pair in an absorption refrigeration cycle when the different VLE models are applied. The lines distinguish sources of the VLE prediction and the mixing enthalpy estimation.

the UNIFAC model can be applied for estimating mixing enthalpies.

- The mixing of liquid NH_3 with [bmim][BF_4] is less exothermic since the absolute values of $\Delta\bar{h}_{\mathrm{mix}}$ for this pair are smaller than those of the working pair H_2O/[emim][DMP].
- The results of total enthalpies for the H_2O/[emim][DMP] solution are more sensitive to the VLE models compared to the NH_3/[bmim][BF_4] solution.
- Excess effects in the heat capacity of solutions are not dominant. This has been shown by comparing two alternative methods for the calculation of total enthalpies for the H_2O/[emim][DMP] solution.
- Performance parameters (f and COP) of the absorption refrigeration cycle vary when using different VLE models. The variation of COP is larger for the cycle with the H_2O/[emim][DMP] pair. For the same working pair, a model estimating a smaller Δh_{mix} (larger exothermic effect) would underestimate the COP.

3

AMMONIA/IONIC LIQUID-BASED SINGLE-EFFECT ABSORPTION HEAT PUMPS

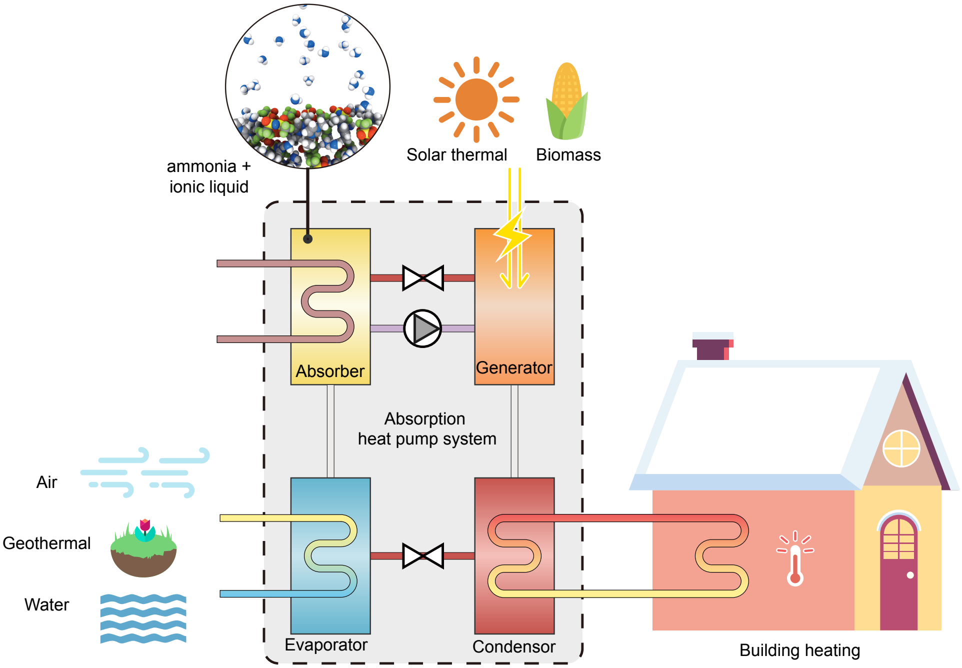

In this chapter, performances of 9 currently investigated NH_3*/ILs pairs are calculated and compared in terms of their applications in the single-effect absorption heat pumps (AHPs) for the floor heating of buildings. Among them, 4 pairs were reported for the first time in absorption cycles (including one which cannot operate for this specific heat pump application). The highest coefficient of performance (COP) was found for the working pair using [mmim][DMP] (1.79), and pairs with [emim][*Tf_2N*] (1.74), [emim][SCN] (1.73) and [bmim][*BF_4*] (1.70) also had better performances than that of the* NH_3/H_2O *pair (1.61). Furthermore, an optimization was conducted to investigate the performance of an ideal* NH_3*/IL pair. The COP of the optimized mixture could reach 1.84. Discussions on the contributions of the generator heat and optimization results revealed some factors that could affect the performance. It could be concluded that the ideal IL candidates should show high absorption capabilities, large solubility difference between inlet and outlet of the generator, low molecular weights and low heat capacities. In addition, an economic analysis of the AHP using* NH_3*/[emim][SCN] working pair with plate heat exchangers was carried out based on heat transfer calculations. The results indicated that the* NH_3*/IL AHP is economically feasible. The efforts of heat transfer optimization in the solution heat exchanger and a low expense of ILs can help the IL-based AHP systems to become more promising.*

Parts of this chapter have been published in: Applied Energy, **204**, 819-830 (2017) [24].

3.1. INTRODUCTION

In order to preselect promising ionic liquid to be used in absorption systems, many researchers did performance investigations. The majority of investigations were focused on performance predictions, in which the frequently studied refrigerants include H_2O [38, 100], hydrocarbons [101], hydrofluorocarbons (HFC) [102, 103] and CO_2 [104]. Since NH_3 based absorption systems hold strengths such as sub-zero degree applications and free of air infiltration, research related to these mixtures is most relevant. Nevertheless, there is only limited work which has been reported. Yokozeki and Shiflett [39, 40] measured solubility data for NH_3 with a set of ILs, and calculated the thermodynamic performance of these mixtures in a single-effect cycle. Kotenko [105] also developed thermodynamic simulations for absorption heat pumps (AHPs) with 4 NH_3/ILs mixtures in Aspen Plus, and compared their performances with that of the NH_3/H_2O system. Their results showed that the efficiency of some of the investigated NH_3/IL AHP processes, at specified operating conditions, was higher than that of conventional NH_3/H_2O systems. Chen *et al.* [43, 46] investigated vapor-liquid equilibria (VLE) for metal ion-containing ionic liquid [bmim][Zn_2Cl_5] with NH_3, and compared the thermodynamic performance of this mixture with that of the NH_3/NaSCN pair. The performance of the former system is better than that of the latter one when the generator temperature is high and the absorber and the condenser temperatures are low. Ruiz *et al.* [44] modeled NH_3/IL absorption using COSMO-based Aspen simulations and analyzed cycle performance for conventional and task-specific ILs.

In these performance prediction studies of absorption systems, the enthalpy of the NH_3/IL solution is always an essential thermodynamic property. Most researchers obtained this property by adding an excess enthalpy to the weighted sum of enthalpies of the two pure components. The excess enthalpy could be obtained from the VLE data via a variety of models. Some researchers [38, 61, 81] used the non-random two-liquid (NRTL) activity coefficient model to predict it. However, Shiflett and Yokozeki [61] found that accurate prediction of mixing enthalpy with NRTL is very difficult, because excess enthalpy is derived from the temperature derivative of the activity coefficient, and the temperature-dependency in any activity model is always in a purely empirical form. Therefore then they turned to a cubic equation of state (EOS) method for excess enthalpy predictions [39, 40]. Meanwhile, for the pure components part, one of the challenges is the heat capacity of the IL. In the work of Yokozeki and Shiflett [39, 40], this part was obtained from a group function contribution method [106]. But Cai *et al.* [104] pointed out that this group function contribution method is not always accurate. In the prediction work of Chen *et al.* [46], experimental heat capacity data of ILs were employed in the enthalpy predictions. Therefore, according to the previous studies, the combination of EOS based method for the excess enthalpy with the experimental heat capacity data of ILs may provide a more accurate way for the performance prediction of AHPs.

Previous experimental studies were carried out either by substituting the working pairs in a traditional commercial system [62–64] with H_2O/ILs pairs, or restricted to small scale systems [65]. Apart from these studies, the understanding of ILs in more practical aspects, for example the heat and mass transfer aspects, is still limited. However, researches of IL-based working pairs is emerging recently taking more practical aspects into account. Meyer *et al.* [67] studied the combined heat and mass transfer phenomena of H_2O/[emim][DEP] pairs in an absorption refrigeration system by using analytical functions. Ariyadi and Coronas [68] developed a measurement setup to study the absorption capacity of the NH_3 vapor in ILs in a pool type absorber. Wadekar [69] simulated the heat transfer behavior of IL [bmim][Tf_2N] in different heat exchangers (HXs). The results showed that the heat transfer performance was not particularly attractive, but heat transfer enhancement technology can improve it effectively. Boman *et al.* [70] screened working pairs including the IL-based ones for a single-effect AHP based on both thermodynamic and heat transfer principles. The shell-and-tube HXs of IL-based AHP systems need more heat exchanger area due to the poor heat transfer performance of the ILs. Chugh *et al.* [71] implemented a membrane-based semi-open absorption system using IL for heating, dehumidification and cooling application. The experimental test achieved a heating coefficient of performance (COP) of 1.4.

In this chapter, a thermodynamic model of single-effect AHPs is first proposed accompanied with an accurate method to estimate enthalpies of solutions. With this model, the performance behaviors of 9 commercialized ILs with NH_3 are investigated along with that of the conventional NH_3/H_2O pair. Considering previous studies, the 9 working pairs cover all the ILs which have sufficient published data (VLE data with NH_3 and pure heat capacities of ILs) for this calculation. The performance of four of these pairs in absorption systems is reported for the first time. The influence of the GEN temperatures on the circulation ratio (f) and on the COP is also studied. As one of the most original parts of this chapter, the developed NRTL and heat capacity models have been made generic, by integrating them with a genetic algorithm (GA) in the thermodynamic AHP model, to determine the maximum COP of the AHP cycle and explore how the thermodynamic properties of the ideal ILs should show. In addition, the heat transfer calculations for each heat exchanger of an AHP are carried out considering all heat exchangers are plate heat exchangers (PHXs). Based on that, the feasibility of applying IL in an AHP system is analyzed by investigating its economic performance.

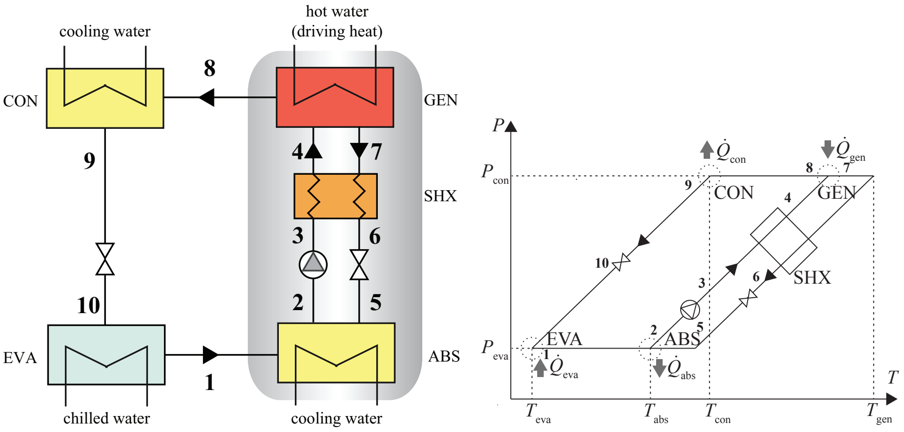

(a) (b)

Figure 3.1: Schematic diagrams of a single-effect AHP system using IL based working pair. (a) Flow diagram of the cycle; (b) State points of the cycle on a ln P-(-1/T) diagram. The arrows show directions of flows. The corresponding numbers denote state points in both diagrams.

3.2. METHODS

3.2.1. THERMODYNAMIC MODEL OF THE CYCLE

Thermodynamic models of the single-effect AHP systems have been frequently reported in the literature, see for instance Kiss and Infante Ferreira [91]. In this section, only the details required for the following steps of this chapter will be discussed.

Fig. 3.1(a) depicts a schematic diagram of a single-effect absorption refrigeration/heat pump cycle. The system is mainly composed of an absorber (ABS), a generator (GEN), a condenser (CON), an evaporator (EVA), along with a solution heat exchanger (SHX), a pump and two throttle valves.

To qualitatively illustrate the temperature and pressure relationship of each state, the process is also plotted in a ln P-(-1/T) diagram in Fig. 3.1(b). In the ABS, the weak NH_3/IL solution 5 (weak in the refrigerant, NH_3) absorbs the saturated pure NH_3 refrigerant vapor 1 from the EVA, and then it turns into strong solution 2. The heat $\dot{Q}_{abs}$ is delivered to the heating system by the ABS. The outlet solution 2 from the ABS is then pumped to a high pressure level and enters the SHX as a cold flow. The outlet flow of the cold side, stream 4, then goes into the GEN, where the driving heat $\dot{Q}_{gen}$ is input. With the heat input, strong solution 4 releases some refrigerant vapor 8, then becomes the poor solution 7 and enters the SHX. In the SHX, the weak solution 7 is cooled by the cold side to state 6 and then throttled to a low pressure level through a valve, before going back to the ABS. The superheated refrigerant vapor 8 from the GEN is condensed to a saturated pure liquid refrigerant in the CON, where the heat $\dot{Q}_{\mathrm{con}}$ is delivered to the heating system. After that, the saturated liquid refrigerant 9 expands to a low pressure level through a valve, and extracts heat $\dot{Q}_{\mathrm{eva}}$ from the surrounding in the EVA. The outlet vapor 1 goes back to the ABS and finishes the cycle.

In order to create an integrated model for the thermodynamic analysis of the absorption process with NH_3/ILs pairs, several assumptions are made to simplify the calculations:

- The system operates in a steady state.
- The heat losses, pressure losses and pumping work are neglected. The throttling is an isenthalpic process.
- The operating pressures of the EVA and the ABS are the same, and similarly, the pressures of the GEN and the CON are also equal.
- The minimum temperature approach of the solution heat exchanger, SHX, is set to 5 K.
- The refrigerant stream is saturated liquid or saturated vapor at the outlet of the CON or the EVA, respectively. The solution is at equilibrium state when leaving the GEN. While the solution leaving the ABS is subcooled, with a subcooling of 3 K.
- Vapor leaving the GEN is pure NH_3 which has the same temperature as the inlet solution (Fig. 3.2 (a)).

The AHP system with an NH_3/H_2O pair is also modeled in this study for reference purposes. For it, an additional column and a rectifier are needed to purify the outlet vapor, as shown in Fig. 3.2 (b). The reflux ratio must be iterated until an acceptable purity of the vapor outlet is obtained. Thus, additional simplification is taken into account,

- Vapor leaving the rectifier is pure enough (99.99% NH_3), and has a saturated temperature corresponding to the operating pressure (Fig. 3.2 (b)). After the rectifier, it is treated as a pure fluid.

With the enthalpy of each state point, the heat exchanged, for instance, in the EVA and the GEN is,

$$\dot{Q}_{\mathrm{eva}}/\dot{m}_{\mathrm{r}} = h_1 - h_9 \tag{3.1}$$

$$\dot{Q}_{\mathrm{gen}}/\dot{m}_{\mathrm{r}} = h_8 + f\,(h_7 - h_4) - h_7 \tag{3.2}$$

From the mass balance of refrigerant in the solution,

$$\dot{m}_{\mathrm{s}}\,(1 - w_4) = (\dot{m}_{\mathrm{s}} - \dot{m}_{\mathrm{r}})\,(1 - w_7) \tag{3.3}$$

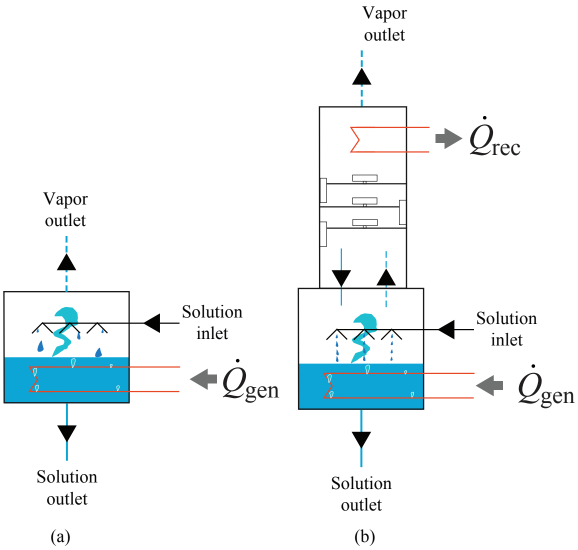

Figure 3.2: Two constructions of the generator. (a) The generator for working pairs using absorbents with a negligible vapor pressure at operating temperature, say NH_3/ILs in this study. (b) The generator with purification section above it (distillation column and rectifier) for working pairs using absorbents with a non-negligible vapor pressure at operating temperature, say NH_3/H_2O in this study.

The performance parameters, i.e. circulation ratio (f) and COP can be calculated as,

$$f = \frac{\dot{m}_s}{\dot{m}_r} = \frac{1 - w_7}{w_4 - w_7} \tag{3.4}$$

$$COP = \frac{\dot{Q}_{con} + \dot{Q}_{abs}}{\dot{Q}_{gen}} \tag{3.5}$$

3.2.2. PROPERTIES

VAPOR-LIQUID EQUILIBRIA FOR THE NH_3/ILS BINARY SOLUTIONS

Vapor-liquid equilibrium describes the relationships between parameters P-T-x, which can be used to identify the state points in the cycle. Non-random two-liquids (NRTL) models for the prediction of vapor liquid equilibrium of mixtures have been frequently reported in the literature, see for instance [91]. In this section, only the details required for the following steps of this chapter will be discussed.

For the NH_3/IL system, due to the non-volatility of ILs, the equilibrium criterion is simplified as,

$$P = \gamma_{NH_3} x_{NH_3} P^{sat}_{NH_3} \tag{3.6}$$

here, $P_{\mathrm{NH_3}}^{\mathrm{sat}}$ can be obtained from NIST Refprop [99]. The activity coefficient $\gamma_{\mathrm{NH_3}}$ can be obtained by the NRTL activity coefficient model after correlations of VLE data,

$$\ln\gamma_{\mathrm{NH_3}} = x_2^2\left[\tau_{21}\left(\frac{G_{21}}{x_1 + x_2 G_{21}}\right)^2 + \frac{G_{12}\tau_{12}}{(x_2 + x_1 G_{12})^2}\right] \tag{3.7}$$

where,

$$\begin{cases} G_{12} = \exp(-\alpha\tau_{12}) \\ G_{21} = \exp(-\alpha\tau_{21}) \\ \tau_{12} = \tau_{12}^{(0)} + \dfrac{\tau_{12}^{(1)}}{T} \\ \tau_{21} = \tau_{21}^{(0)} + \dfrac{\tau_{21}^{(1)}}{T} \end{cases} \tag{3.8}$$

ENTHALPIES OF THE REFRIGERANT AND SOLUTIONS

The enthalpy data of pure NH_3 is directly obtained from NIST's Refprop [99]. For a real solution, the total enthalpy can be estimated using the following method, depending on its state.

For a saturated solution at an equilibrium condition T, P and $w_{\mathrm{NH_3}}$, the total enthalpy is,

$$h^{\mathrm{sol}}\left(T, P, w_{\mathrm{NH_3}}\right) = w_{\mathrm{NH_3}} h_{\mathrm{NH_3}}(T) + w_{\mathrm{IL}} h_{\mathrm{IL}}(T) + h^{\mathrm{e}}\left(T, P, w_{\mathrm{NH_3}}\right) \tag{3.9}$$

where the enthalpies of NH_3 are chosen at their saturated liquid states. For the ILs, the enthalpies are calculated with the help of their pure heat capacities $c_{\mathrm{p}}^{\mathrm{IL}}$,

$$h_{\mathrm{IL}}(T) = h_0(T_0) + \int_{T_0}^{T} c_{\mathrm{p}}^{\mathrm{IL}}\, dT \tag{3.10}$$

The calculation of the excess enthalpy, h^{e}, can be obtained using an equation of state (EOS) and mixing rules. Yokozeki and Shiflett [39, 40, 74] employed a generic Redlich-Kwong (RK) type of cubic EOS to fit the vapor pressure data and to predict the excess enthalpy. This method is also used for the prediction of the mixing heat in the present work. The detailed approach has been reported in the mentioned references. The values of the critical temperature and pressure of ILs needed for the following calculations, along with their molecular weights, are listed in Table 3.1.

For subcooled solutions at condition T, P and $w_{\mathrm{NH_3}}$, its enthalpy can be obtained by subtracting the subcooled part from a corresponding saturated solution,

$$h^{\mathrm{sol}}\left(T, P, w_{\mathrm{NH_3}}\right) = h^{\mathrm{sol}}\left(T_{\mathrm{sat}}, P, w_{\mathrm{NH_3}}\right) - \int_{T}^{T_{\mathrm{sat}}} c_{\mathrm{p}}^{\mathrm{sol}}\, dT \tag{3.11}$$

Table 3.1: Molecular weight and critical data of the investigated ILs.

ILs	M_w [kg/kmol]	T_c* [K]	P_c* [MPa]
[mmim][DMP]	222.18	816.8	2.72
[emim][BF_4]	197.97	596.2	2.36
[hmim][BF_4]	254.08	690.0	1.79
[omim][BF_4]	282.13	737.0	1.60
[bmim][BF_4]	226.02	643.2	2.04
[bmim][PF_6]	284.18	719.4	1.73
[emim][Tf_2N]	391.31	1249.3	3.27
[emim][$EtSO_4$]	236.29	1067.5	4.05
[emim][SCN]	169.25	1013.6	2.23

*The critical data are obtained using the group-contribution-function method [92].

In this study, the weighted average heat capacity of both components has been implemented to express $c_\mathrm{p}^\mathrm{sol}$.

$$c_\mathrm{p}^\mathrm{sol}\left(w_{\mathrm{NH_3}}\right) = w_{\mathrm{NH_3}}\, c_\mathrm{p}^{\mathrm{NH_3}} + \left(1 - w_{\mathrm{NH_3}}\right) c_\mathrm{p}^\mathrm{IL} \tag{3.12}$$

This treatment has been verified for H_2O/[mmim][DMP] with $c_\mathrm{p}^\mathrm{sol}$ data in [38], showing that the relative deviation is always smaller than 4%.

If T of a stream is higher than T_sat, part of the NH_3 in the solution will be boiled off. For this case, the total enthalpy can be expressed as,

$$h^\mathrm{sol}\left(T, P, w_{\mathrm{NH_3}}\right) = \left(1 - q\right) h_\mathrm{sat}^\mathrm{sol} + q h^\mathrm{V} \tag{3.13}$$

where, $h_\mathrm{sat}^\mathrm{sol}$ and h^V are the specific enthalpies for the saturated solution part and the vapor part, respectively. q is the quality, which can be identified as,

$$q = \frac{w - w_\mathrm{sat}}{1 - w_\mathrm{sat}} \tag{3.14}$$

3.2.3. OPTIMIZATION PROBLEM

The properties of ILs can be adjusted by the design of anion and cation combinations for a task-specified purpose. However, because of the large number of anions and cations, the number of possible combinations is considerable. In this chapter, the determination of screen criteria of task-specific ILs for AHPs will also be discussed. These criteria are identified by the optimization of the performance.

In the optimization, the objective is the maximization of the *COP* which depends on solubility (mass fractions of weak and strong solutions) and enthalpy values as will be discussed in Section 3.3.5. Making use of an NRTL model, a total of eight parameters are identified which affects the attained COP value. They are α, $\tau_{12}^{(0)}$, $\tau_{12}^{(1)}$, $\tau_{21}^{(0)}$ and $\tau_{21}^{(1)}$ of the NRTL model for VLE, $\bar{c}_0$, $\bar{c}_1$ in linear molar $\bar{c}_\mathrm{p}$ expression and the molecular weight M_w. Once the COP reaches the optimal value, corresponding optimal variables can be determined for the optimum IL and mixture. Meanwhile, in order to obtain a practical and reasonable result, constraints of these optimal variables are needed. They are determined in terms of experimental data which are collected and discussed in Section 3.3.1.

Genetic algorithm is better at finding global solutions than gradient-based solvers. GA selectively generates new candidate points to evaluate based upon a method that is similar to breeding between two "parents" to generate a "child". They are useful for problems that are highly nonlinear, such as the present problem. One of the concerns is the computational efficiency. To check a large amount of individuals from generation to generation is time-consuming. Luckily, the present optimization problem is not so CPU-intensive. In addition, the selection of individuals in the current generation is random, which can also lead to local minima. To overcome this drawback, instead of using GA for only one optimization, we try thousands of optimizations based on GA independently to remove local minima. The non-physical optimization results will be rejected. Finally, the optimum value for the objective function can be identified. The GA toolbox of Matlab has been used to identify the optimum combination of parameters. The effect of the settings for what concerns population size, elicit count, crossover fraction and generations has been investigated by studying the effect of variations and finally the settings proposed in the Matlab toolbox, respectively, 200, 10, 0.8 and 500, have been adopted.

3.3. RESULTS AND DISCUSSION

3.3.1. CORRELATIONS AND SUMMARIES OF PROPERTIES

VAPOR LIQUID EQUILIBRIUM

With the experimental VLE data of binary NH_3/ILs, the binary parameters, α, $\tau_{12}^{(0)}$, $\tau_{12}^{(1)}$, $\tau_{21}^{(0)}$ and $\tau_{21}^{(1)}$ of the NRTL model (Eq. 3.7 and 3.8), can be correlated and will allow for the determination of the operating concentrations. The correlated results and accuracies are listed in Table 3.2. In this work, most of the data have been correlated with a root-mean-square deviation ($RMSD$) smaller than 5.62% as shown in Table 3.2. Only the model for the pair NH_3/[omim][BF_4] showed slightly larger deviation: 8.7%.

HEAT CAPACITIES

Experimental heat capacity (c_p) data of 61 ILs at 298.15 K, reviewed by Paulechka [108], are plotted in Fig. 3.3 in mole-based and mass-based units, respectively. It

Table 3.2: Correlated binary parameters in the NRTL model for the investigated working pairs.

Working pairs*	α	$\tau_{12}^{(0)}$	$\tau_{12}^{(1)}$	$\tau_{21}^{(0)}$	$\tau_{21}^{(1)}$	**Data points**	*RMSD***
NH_3/[mmim][DMP][1]	0.24032	7.82	-2300.68	-4.43	1000.39	30	3.31%
NH_3/[emim][BF_4][2]	0.99952	-0.01	236.41	-1.26	164.59	25	5.14%
NH_3/[hmim][BF_4][3]	0.99998	-14.8	5081.74	-2.67	478.85	25	4.29%
NH_3/[omim][BF_4][4]	0.90702	-7.01	2690.74	-2.4	283.17	25	8.71%
NH_3/[bmim][BF_4][5]	-0.01285	-48.23	8961.06	32.62	-5490.64	30	2.62%
NH_3/[bmim][PF_6][6]	0.33411	3.73	-509.57	-4.19	643.5	29	2.98%
NH_3/[emim][Tf_2N][7]	-0.00422	-100	14710.17	71.51	-9046.21	30	5.62%
NH_3/[emim][$EtSO_4$][8]	0.71604	11.17	-4089.25	-7.53	2451.46	29	4.32%
NH_3/[emim][SCN][9]	-0.27082	-10.66	3120.01	5.6	-1967.71	36	4.59%
NH_3/H_2O[10]	-0.24355	24.17	-18636.43	7.26	-3370.40	111	3.24%

*The experimental VLE data used are from, [1] [41], [2], [3] and [4] [42], [5], [6] and [7] [39], [8] and [9] [40], and [10] [107]. Data of the NH_3/H_2O pair are used as a reference.

***RMSD* is obtained based on the deviations between the correlated and experimental pressure data by $RMSD\ (P) = \sqrt{\frac{\sum_N (P_{\mathrm{calc}}/P_{\mathrm{exp}}-1)^2}{N}}$.

is quite interesting to see that the mole-based $\bar{c}_p$ data are distributed in a linear trend with respect to the molecular weight. The mass-based c_p data are centralized near 1.44 kJ/(kg·K) in a nearly constant range between 1-2 kJ/(kg·K). This trend provides a general relationship between $\bar{c}_p$ and M_w for ILs, which will be used in the property optimization as a constraint. Even though the relationship is not very accurate, it still can be helpful to identify how this property impacts on the performance of the mixture in the AHP.

For the same ILs involved in the NRTL correlation in Table 3.2, the mole-based c_p values are also plotted as a function of temperature in Fig. 3.4. With respect to the temperature, the $\bar{c}_p$ values of different ILs also show approximately linear trends. Thus, the molar $\bar{c}_p$ value of each IL is represented by a linear expression. Table 3.3 lists the correlated parameters of the linear expression and is based on the experimental c_p data from literature [109–115]. The accuracies of all correlations are also listed. Notice that for most fluids the available data are limited to 100 °C, so that the relation is extrapolated when calculating values up to 130 °C. This may lead to larger errors than reported in Table 3.3.

3.3.2. PERFORMANCE COMPARISON

To compare the performances in detail, some calculated results are listed in Table 3.4 at a specific condition ($T_{gen}/T_{con}/T_{abs}/T_{eva}$ = 120/45/45/10 °C). This operating conditions range is specified based on applications in floor heating.

Under these operating conditions, the circulation ratio, f, of the working

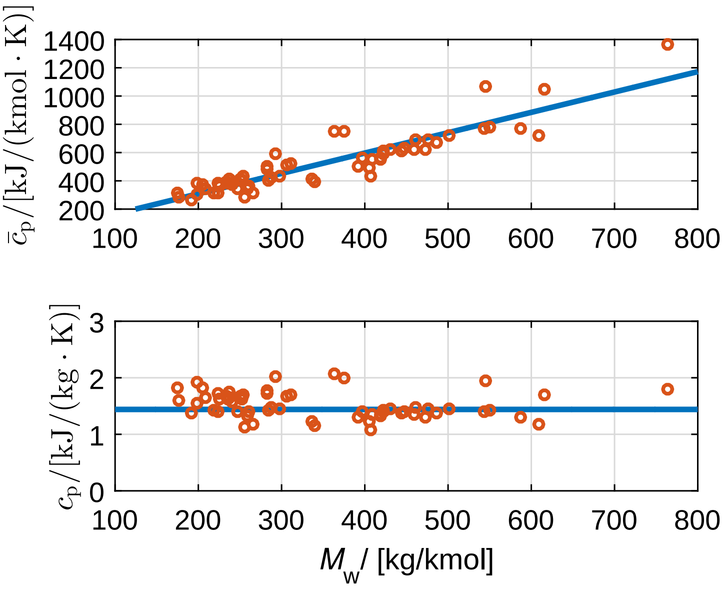

Figure 3.3: Specified heat capacity values of 61 ILs at 298.15 K (upper: mole-based $\bar{c}_p$, lower: mass-based c_p). These 61 data points have been collected from experimental c_p data reviewed by Paulechka [108]. They are selected because they are the only ones having c_p data at 298.15 K with uncertainties lower than 15%.

pair, NH$_3$/[hmim][BF$_4$], always has a negative value, what means this pair can not be used in an AHP which operates under the imposed conditions. Thus, it is not included in the following discussions.

Apart from the solubility levels of the in- and outlet of the ABS and performance parameters f and COP, the conditions at the GEN inlet (state point 4) are also checked. Qualities q_4 are listed to show if there is vapor boiled-off before entering the GEN. The table also includes the results for the NH$_3$/H$_2$O system and optimum results obtained in Section 3.3.5. The single-effect AHP cycle with NH$_3$/H$_2$O as working fluids, reported by Kotenko [105], operates at similar conditions as applied in the current work. His predicted heating COP for a system with a rectifier and slightly lower evaporating temperature ($T_{\text{eva}} = 5\,^\circ$C) is around 1.59, which is quite similar to the values obtained in the current work of 1.61.

Two facts resulting from the circulation ratio, f, can influence the cycle performance. One is its impact on the pumping power. A higher value of f means a larger mass flow rate through the pump (at the same flow of refrigerant stream), which can increase the power consumption of the solution pump. The second one is due to the relationship between f and the energy and mass balances for the GEN and for the ABS, which will be discussed in detail in Section 3.3.3. In all,

Table 3.3: Correlated parameters in $\bar{c}_\mathrm{p}$ [kJ/(kmol·K)] = $\bar{c}_0 + \bar{c}_1 T$ [K] (mole-based) for the investigated ILs.

ILs*	$\bar{c}_0$	$\bar{c}_1$	**Data points**	*RMSD*
[mmim][DMP][1]	-153.898	1.476	4	0.94%
[emim][BF_4][2]	214.067	0.308	12	0.18%
[hmim][BF_4][3]	275.962	0.520	9	0.00%
[omim][BF_4][4]	323.894	0.588	100	0.21%
[bmim][BF_4][5]	250.201	0.397	20	0.68%
[bmim][PF_6][6]	282.070	0.452	1528	0.91%
[emim][Tf_2N][7]	363.188	0.478	16	0.01%
[emim][$EtSO_4$][8]	245.526	0.462	146	0.60%
[emim][SCN][9]	116.474	0.547	20	0.61%

*The experimental c_p data used are from, [1] [109], [2] [110], [3] [111], [4], [5] and [8] [112], [6] [113], [7] [114] and [9] [115].

a small f is preferable. Because of the significant difference in molecular weights between NH_3 and ILs, the mass fractions of NH_3/ILs pairs are much lower than that of the NH_3/H_2O system. As a result, the circulation ratios of NH_3/ILs mixtures (29.3 - 112.4) are significantly higher than that of conventional NH_3/H_2O (4.6). Promisingly, four ILs based systems hold higher *COP* values than that for the NH_3/H_2O system (1.61). These ILs are [mmim][DMP] (1.79), [emim][Tf_2N] (1.74), [emim][SCN] (1.73) and [bmim][BF_4] (1.70). Although the performance of the NH_3/H_2O system could be improved by implementing advanced cycles, such as the generator/absorber heat exchanger (GAX) cycle, that would also increase the complexity and investment of the system. These promising results show the potential of NH_3/ILs working pairs which can be executed with a simple cycle, making these pairs superior alternatives.

Previously Yokozeki and Shiflett [39, 40] have compared the performance of some of the investigated mixtures in single-effect absorption refrigeration cycles. Their results are also included in Table 3.4 for reference. At their considered operations conditions, the NH_3/H_2O pair has been identified to perform better than the considered NH_3/ILs pairs. This is different from the current work, in which the NH_3/H_2O pair is not identified as the superior one for a heat pump operation. Yokozeki and Shiflett [39, 40] did not include the effect of the rectifier when calculating the performance of the NH_3/H_2O pair. The rectifier is essential to guarantee the purity of the produced refrigerant. This is the main reason why their *COP* of the NH_3/H_2O pair was overestimated. Besides, although the experimental data of Yokozeki and Shiflett [39, 40] have been used for these fluids in the present work, the NRTL parameters have been independently correlated.

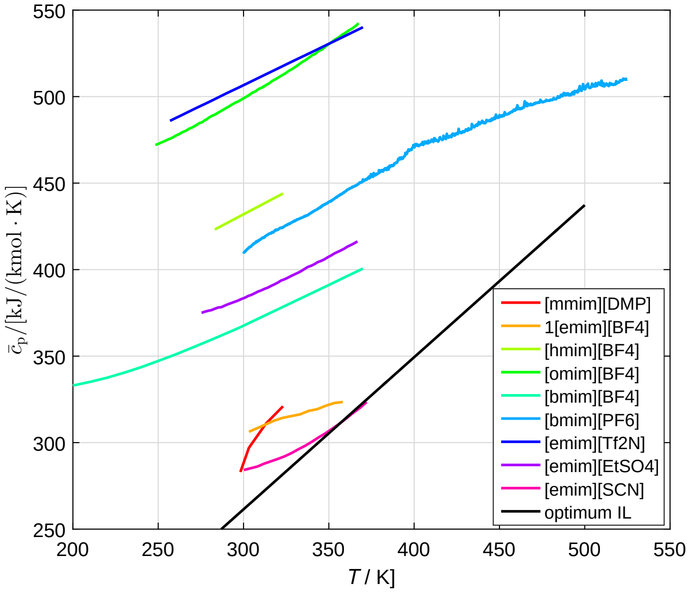

Figure 3.4: Experimental $\bar{c}_p$ (mole-based) values of the investigated ILs as a function of temperature.

The fitted VLE behaviors are not identical but quite similar to the ones reported by Yokozeki and Shiflett [39, 40]. The difference in *COP* results for the NH_3/IL pairs is mainly due to the method used to predict the specific heat of the working pairs. For example, Yokozeki and Shiflett [39, 40] made use of the group contribution function method to predict these values, while in this study the reported experimental values have been used as discussed in Section 3.3.1. Problems encountered when using the group contribution function method for the prediction of the specific heat of ionic liquids have previously been reported by Cai *et al.* [104], as already discussed in Section 3.1.

3.3.3. CONTRIBUTIONS TO THE GENERATION HEAT

Considering the energy balance of the 4 main devices, the *COP* of a heat pump system can also be expressed as,

$$COP = \frac{\dot{Q}_{\mathrm{abs}} + \dot{Q}_{\mathrm{con}}}{\dot{Q}_{\mathrm{gen}}} = \frac{Q_{\mathrm{eva}} + \dot{Q}_{\mathrm{gen}}}{\dot{Q}_{\mathrm{gen}}} = 1 + \frac{\dot{Q}_{\mathrm{eva}}}{\dot{Q}_{\mathrm{gen}}} \tag{3.15}$$

The EVA heat, $\dot{Q}_{\mathrm{eva}}$, is equal for all fluids. Thus, the difference in *COP* results from the GEN heat, $\dot{Q}_{\mathrm{gen}}$: A higher $\dot{Q}_{\mathrm{gen}}$ leads to a lower heat pump *COP*.

Table 3.4: Performance comparison when different working pairs are used in the AHP cycle ($T_{gen}/T_{con}/T_{abs}/T_{eva}$ = 120/45/45/10 °C) and the refrigeration COP ($T_{gen}/T_{con}/T_{abs}/T_{eva}$ = 100/40/30/10 °C) of corresponding pairs as reported by Yokozeki and Shiflett [39, 40].

Working pairs	**Heat pump performance**					**Refrigeration performance**	
	w_2 [kg/kg]	w_7 [kg/kg]	q_4 [kg/kg]	f [-]	COP [-]	f [-]	COP [-]
NH_3/[mmim][DMP]	0.057	0.031	0.017	36.61	1.785	-	-
NH_3/[emim][BF$_4$]	0.054	0.034	0.011	46.82	1.609	-	-
NH_3/[omim][BF$_4$]	0.080	0.072	0.002	112.4	1.381	-	-
NH_3/[bmim][BF$_4$]	0.057	0.023	0.014	29.28	1.695	12.98	0.557
NH_3/[bmim][PF$_6$]	0.061	0.046	0.006	63.08	1.461	17.27	0.575
NH_3/[emim][Tf$_2$N]	0.043	0.025	0.007	54.30	1.736	24.57	0.525
NH_3/[emim][EtSO$_4$]	0.056	0.039	0.010	55.54	1.509	17.55	0.485
NH_3/[emim][SCN]	0.082	0.049	0.015	29.24	1.732	12.42	0.557
NH_3/H_2O	0.481	0.335	0.024	4.56	1.612	2.54	0.646
NH_3/optimum IL	0.908	0.013	-	1.102	1.84	-	-

*Mass fraction data are all for the NH_3 component. The subscript 2 and 7 represent outlet conditions of the ABS and the GEN, respectively, which are locations with strong and weak solution flows. The subscript 4 represents the inlet conditions of the GEN.

To make this clear, relevant expressions of the total enthalpies in Section 3.2.2 along with Eq. 3.4 and 3.14 are substituted into Eq. 3.2. Taking into account the heat and mass balances of the GEN, the heat input in the GEN, $\dot{Q}_{gen}$, can be rewritten as,

$$\begin{aligned}\dot{Q}_{gen}/\dot{m}_r = {} & (1-fq)\left[h_8-(h_{NH_3})_{4,sat}\right] + \left[(f-1)(h^e)_7 - f(1-q)(h^e)_{4,sat}\right] \\ & + (f-1)(w_{NH_3})_7\left[(h_{NH_3})_7-(h_{NH_3})_{4,sat}\right] + (f-1)(w_{IL})_7\left[(h_{IL})_7-(h_{IL})_{4,sat}\right]\end{aligned} \tag{3.16}$$

$\dot{Q}_{gen}$ is split into 4 terms in this expression. The first term is the latent heat effect from the condensation of NH_3 vapor (while also includes the sensible heat associated with the superheated state). The second one denotes the excess heat. The other two terms represent the contributions of sensible heat, in which, the third term is the sensible heat change of the NH_3 component while the last term is that of the IL component.

In order to analyze the performance, each of the above contributions to the GEN heat, for the operating conditions $T_{gen}/T_{con}/T_{abs}/T_{eva}$=120/45/45/10 °C, is depicted in Fig. 3.5 for all the NH_3/ILs working pairs.

The values of T_4 are almost identical for all the cases, indicating that the latent heats per unit mass flow, $h_8-(h_{NH_3})_{4,sat}$, are more or less the same for all

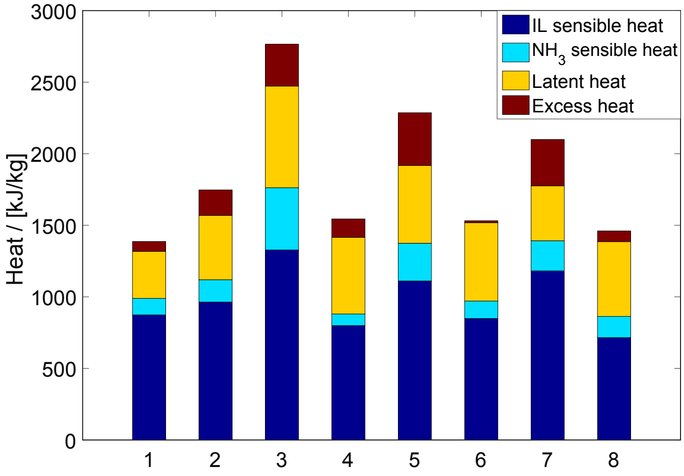

Figure 3.5: Contributions to the GEN heat $\dot{Q}_{\text{gen}}$ by the 4 terms of Eq. 3.16. The 4 terms are latent heat, absorption heat and sensible heats of both components. 1 - 8 denotes NH_3 based working fluids with [mmim][DMP], [emim][BF_4], [omim][BF_4], [bmim][BF_4], [bmim][PF_6], [emim][Tf_2N], [emim][$EtSO_4$] and [emim][SCN].

cases. The difference in latent heat in Fig. 3.5 is due to the different mass flows, $1-fq$. Large values of f or q can lead to a low value of the latent heat contribution. The q has an obvious negative correlation with the latent heat contribution, which can be observed in Fig. 3.5, e.g. pairs with [omim][BF_4] and [bmim][PF_6]. A higher q implies more vapor is boiled off before the flow enters the GEN. In this way, the heat duty of the GEN is reduced. The q value results mainly from the VLE properties of the NH_3/ILs systems.

Again, due to the almost equal values of T_4, the sensible heats per unit mass flow from NH_3 component are identical for all the mixtures. The difference in NH_3 sensible heats is mainly caused by the factor, $(f-1)\left(w_{\mathrm{NH_3}}\right)_7$. Also the circulation ratio, f, has a stronger impact compared with $(w_{\mathrm{NH_3}})_7$. This is also true for the contribution of the sensible heat of the ILs: Since the mass-based c_{p} values of ILs and temperature differences between inlet and outlet ΔT are approximately the same, the sensible heat of the ILs per unit mass flow, $c_{\mathrm{p}}\Delta T$, are similar for all the ILs. The difference in sensible heat contributions is mainly due to the required circulation ratio, f. Smaller f of pairs with [bmim][BF_4], [emim][Tf_2N] and [emim][SCN] lead to smaller sensible heat contributions and correspondingly higher COPs. This indicates that the circulation ratio f is dominant in this case. The solubility difference at the in- and outlet of the ABS will determine the f values.

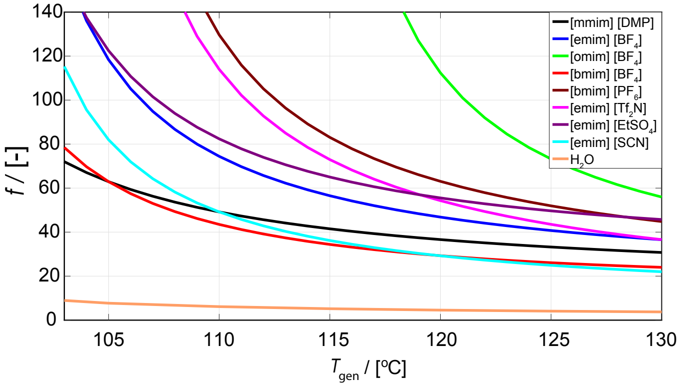

Figure 3.6: Circulation ratios, fs, with respect to generation temperature for the NH_3/IL based working pairs in the single-effect AHP cycles at the condition of $T_{con}/T_{abs}/T_{eva}$ = 45/45/10 °C.

Since the VLE properties are usually studied with mole-based units, when considering mass-based properties, say f here, M_w also plays a role. For the NH_3 absorption system, a larger molecular weight of the absorbent leads to a smaller mass fraction change when the molar change is maintained. This also implies that smaller molecular weight of the absorbent is preferable in terms of performance.

The contribution of excess heat will be discussed in Section 3.3.4.

3.3.4. INFLUENCE OF HEAT SOURCE TEMPERATURE ON THE PERFORMANCE

To investigate the influence of heat source temperature on the performance, condensing temperature T_{con}, absorbing temperature T_{abs} and evaporating temperature T_{eva} are set to be 45 °C, 45 °C and 10 °C, respectively, while the temperature of the heat source, T_{gen}, varies in a range from 100 °C to 130 °C. Because all the experimental VLE conditions are lower than 130 °C, T_{gen} is maintained below 130 °C in all calculations.

Fig. 3.6 and 3.7 only show the circulation ratio f and COP variation, respectively, for the other 8 NH_3/ILs pairs which can be operated and NH_3/H_2O pair. All the working pairs, considered for the proposed AHP system, show similar trends. With increase of T_{gen}, f first decreases rapidly and then reduces to a more constant value. On the contrary, the COPs increase first sharply and then rise to a practically constant value. At the higher temperature range, the values of f and COP are quite close for most NH_3/ILs pairs. f falls in the range of 20 - 60 and COPs reach 1.4 - 1.8. It looks like these trends will be maintained when T_{gen} increases above 130 °C.

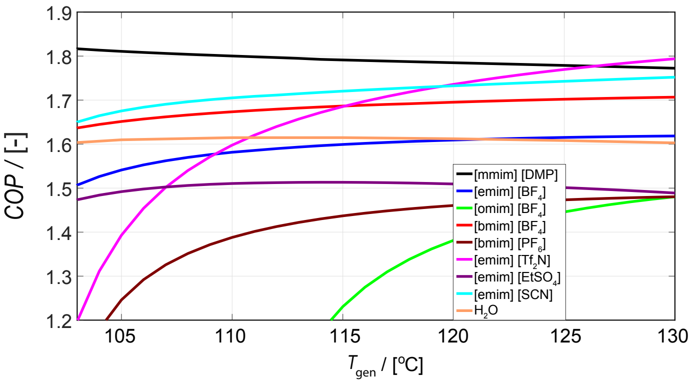

Figure 3.7: *COP*s with respect to generation temperature for different NH_3/IL based working pairs in the single-effect AHP cycles at the condition of $T_{con}/T_{abs}/T_{eva}$ = 45/45/10 °C.

The performances of working pairs of NH_3 with [mmim] [DMP], [bmim] [BF_4], [emim] [Tf_2N] and [emim] [SCN] are outstanding, just as shown in Section 3.3.2 at a constant condition. Even though the fs of these fluids are larger than that of the NH_3/H_2O, when T_{gen} is high enough, the *COP*s are still higher. In addition, the NH_3/[mmim] [DMP] pair has the highest *COP*.

As for the NH_3/H_2O pair, it holds the lowest f and relatively high *COP* values when compared with the NH_3/ILs pairs. With an increase of T_{gen}, the *COP* slightly rises, and after 105 °C, it becomes more or less constant.

Because an accurate prediction of the excess enthalpy is difficult as discussed in Section 3.1, and to assess the sensitivity of excess enthalpy on the performance, *COP*s calculated based on ideal solutions (without taking account the excess enthalpy) are presented in Fig. 3.8.

In most of cases, the range of the *COP* is smaller than when the excess enthalpy is taken into account. This is not true for the NH_3/[bmim] [BF_4] mixture at higher T_{gen} of Figs. 3.7 and 3.8. Despite the *COP* values are different, the working pairs, which show a better performance than that of NH_3/H_2O pair in Fig. 3.7, still perform better when the excess enthalpy contribution is neglected. An accurate measurement is still needed for a good assessment of the excess enthalpy of NH_3/IL pairs in AHPs. However, even when its effect is not taken into account, the expected performance is still higher for some of the IL pairs when compared to the performance of NH_3/H_2O.

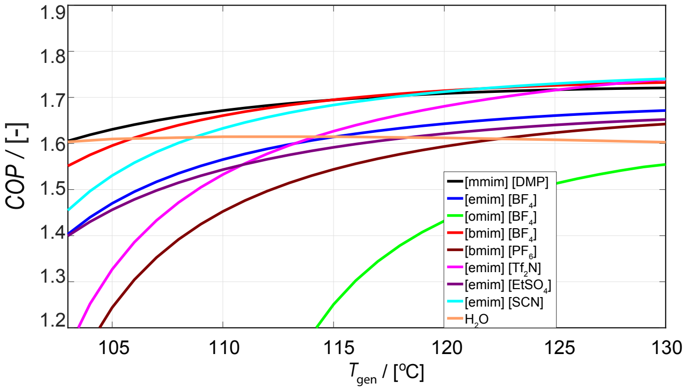

Figure 3.8: *COP*s with respect to generation temperature for different NH3/IL based working pairs in the single-effect AHP cycles when the excess enthalpy is not taken into account, at the condition of $T_{\text{con}}/T_{\text{abs}}/T_{\text{eva}}$ = 45/45/10 °C.

Table 3.5: Limits of optimization variables and properties used in the optimization problem.

Variable	α	$\tau_{12}^{(0)}$	$\tau_{12}^{(1)}$	$\tau_{21}^{(0)}$	$\tau_{21}^{(1)}$	$\bar{c}_0$	$\bar{c}_1$	$\bar{c}_p$ [kJ/(kmol·K)] at 298.15 K	M_w [kg/kmol]
Lower limit	-1	-200	-5000	-10	-10000	-1000	0	1.3	170
Upper limit	2	100	15000	100	2500	100	1000	2	400

3.3.5. OPTIMUM PERFORMANCE AND CORRESPONDING PROPERTIES

In the optimization work, the molecular weight is assumed in a range 170 - 400 kg/kmol. Taking the previous results into account, the upper and lower limits of the thermodynamic model parameters are summarized in Table 3.5. Based on this, and the linear relationships of c_p with both molecular weight and temperature as discussed in Section 3.3.1, the constraints of the search domain have been defined.

The property optimization work is conducted under the same operating conditions as discussed in Section 3.3.2, i.e. $T_{\text{gen}}/T_{\text{con}}/T_{\text{abs}}/T_{\text{eva}}$=120/45/45/10 °C, for the application of building's floor heating.

Using the GA method, the optimized performance and corresponding optimum variables are obtained and listed in Table 3.6. The maximum *COP* under above constraints could reach 1.836 and the circulation ratio 1.102.

The *P*-*T*-*x* diagram of the optimum IL/NH3 mixture described by the parameters of the NRTL model is shown in Fig. 3.9. As a comparison, the *P*-*T*-*x* diagram of NH3/[emim][SCN] is also plotted. Generally, the vapor pressure of the optimum pair has a large deviation between the low and high temperature

Table 3.6: Optimized performance & optimum variables of the working fluids in the single-effect AHP at a condition of $T_{\text{gen}}/T_{\text{con}}/T_{\text{abs}}/T_{\text{eva}}$ = 120/45/45/10 °C.

Performance		**NRTL**					$\bar{c}_p$ [kJ/(kmol·K)]		M_w
COP	*f*	α	$\tau_{12}^{(0)}$	$\tau_{12}^{(1)}$	$\tau_{21}^{(0)}$	$\tau_{21}^{(1)}$	$\bar{c}_0$	$\bar{c}_1$	[kg/kmol]
1.836	1.102	1.171	8.898	14147.7	23.557	-8759.68	-39.966	0.875	170

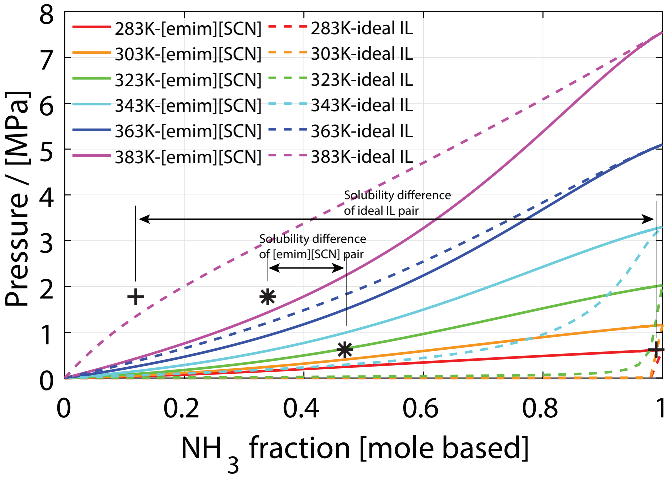

Figure 3.9: Comparison of the P-T-x behavior between the optimized NH_3/IL pair and the real pair (NH_3/[emim][SCN]).

range. For the optimum working pair, there is a negative deviation effect from the Raoult's law at the low temperature range while a positive deviation applies at the high temperature range. This absorption capability difference causes a large difference of NH_3 fractions between in and outlet of the ABS, what will lead to a smaller f, and a higher *COP*.

The optimum molecular weight M_w is exactly its lowest limit, 170. For the same molar solubility difference, a lower value of M_w will lead to a higher value of mass solubility difference which will then lead to a lower f and a higher *COP*. Besides, since the molecular weight M_w has a linear ascending relationship with mole-based $\bar{c}_p$, correspondingly, a lower mole-based $\bar{c}_p$ is observed for the optimum IL, which is depicted in the lowest position in Fig. 3.4.

The optimum properties including vapor pressure, $\bar{c}_p$ and M_w allow us to screen the ideal ILs for AHP cycles. The challenge for future work is identifying ILs which show properties close to the M_w, $\bar{c}_p$ and vapor pressure of the optimized ideal mixture. It is clear that a low molecular weight, low $\bar{c}_p$ and large

Table 3.7: Viscosities and prices of the most promising commercialized ILs for single-effect AHPs in this study.

ILs*	**Viscosity at 25 °C** [Pa·s]	**Viscosity at 90 °C** [Pa·s]	**Price** [€/kg]
[mmim][DMP][1]	0.291	-	910
[bmim][BF_4][2]	0.106	0.0099	846
[emim][Tf_2N][3]	0.0339	0.0056	1265
[emim][SCN][4]	0.0245	0.0055	703/172**
58.5 wt% LiBr aqueous solution[5]	0.0068	0.0022	-

*Price data are collected from vendors of ILs. The data of viscosities are from: [1] [96], [2] [116], [3] [117], [4] [118] and [5] [119].

**Different prices are offered by two different vendors.

fraction difference between in- and outlet of the ABS are essential requirements.

3.3.6. OUTLOOK OF TECHNICAL AND ECONOMIC FEASIBILITIES

In an economic analysis, the *COP* values are related to the operational costs of the AHP while the capital costs are related to the investment in equipment and working fluid. To determine the size of the main components, which are the heat exchangers, the duty and overall heat transfer coefficient of each main heat exchanger are first estimated taking the local flow and fluid properties into account. A conventional NH_3/H_2O AHP with shell-and-tube HXs is compared with an NH_3/IL AHP. IL [emim][SCN] is selected as absorbent for the NH_3/IL AHP since it is one of the best performing ILs and because its viscosity and current price are the lowest among the studied ILs as shown in Table 3.7.

Boman *et al.* [70] have recently shown that the IL-based AHP systems need more heat exchanger area due to the poor heat transfer performance of the ILs, caused by their higher viscosity, lower thermal conductivity and heat capacity. In this section, PHXs are considered in the IL based absorption systems in the roles of GEN, ABS, SHX, CON and EVA. The PHX is selected mainly due to its compact size and good performance of heat and mass transfer. The compact design of PHXs keeps the system volume small so that a smaller amount of expensive working fluid is sufficient to fill the system.

EQUIPMENT SIZING

The floor heating system for a building in a moderate climate area, for example, the Netherlands, is taken for the economic comparison of the AHPs. The heating load will generally not exceed 60 W/m^2 [120]. A 3750 m^2 building will have a heating capacity of 225 kW and its yearly heating requirement will be, approximately, 337.5 MWh.

Table 3.8: Overall heat transfer performance and equipment size for components used in two AHP systems with different working fluids. The calculations are based on the operating condition $T_{gen}/T_{con}/T_{abs}/T_{eva}$ = 120/45/45/10 °C).

Component	**NH_3/[emim][SCN]**				**NH_3/H_2O**		
	Heat duty [kW]	U [W/(m^2·K)]	**Area** [m^2]	**Number of plates** [-]	**Heat duty** [kW]	U [W/(m^2·K)]	**Area** [m^2]
GEN	129.9	2390	2.7	39	138.4	1700	4.1
ABS	111.7	3010	2.3	33	138.3	880	6.8
REC	-	-	-	-	21.2	800	2.2
EVA	95.1	6980	2.1	31	85.5	820	16.2
CON	113.3	5870	1.4	21	86.7	700	8.9
SHX (option 1)**	354.8	300	134.7	856	87.6	610	11.7
SHX (option 2)	292.6	400	53.9	233	-	-	-

*Option 1 denotes a SHX with a minimum temperature approach of 5 K. Option 2 denotes a SHX with a minimum temperature approach of 16 K.

PHX with plate sizes 0.191 × 0.618 m (width× length) and plate spacing of 1.5 mm have been considered for all heat exchangers except for the SHX. The dimensions of the SHX were 0.390 × 0.990 m with an identical plate spacing.

The overall heat transfer coefficient for each heat exchanger has been obtained by summing the heat transfer resistances on both sides of the heat exchangers. The local heat transfer coefficient for single phase flows (both of external fluid and working fluid) has been predicted making use of the correlation proposed by Yan *et al.* [121]. Similarly, for the evaporation processes the correlation proposed by Khan *et al.* [122] and for the condensation processes the correlation proposed by Thonon and Bontemps [123] have been used. For the GEN and ABS the smallest value obtained considering single phase flow or, respectively, evaporation and condensation have been adopted so that mass transfer resistance is taken into account. The required heat exchanger area follows from the heat exchanger duty, its overall heat transfer coefficient and the logarithmic mean temperature difference between the two fluids.

The properties of the external fluid (water) and of NH_3 have been obtained from Lemmon *et al.* [99]. The properties of [emim][SCN] have been obtained from Freire *et al.* [118] (density and dynamic viscosity), Navarro *et al.* [115] (heat capacity) and Tenney *et al.* [124] (thermal conductivity). Table 3.8 shows the calculated areas for the different heat exchangers. For the SHX of the NH_3/IL system two options have been considered: a minimum temperature approach of 5 K (option 1) and a minimum temperature approach of 16 K (option 2). In this case the *COP* drops from 1.73 (option 1) to 1.54 (option 2) while the required PHX area significantly reduces.

ECONOMIC ANALYSIS

For the economic calculation, a cost equation based on DACE [125] PHX costs has been applied to the areas reported in Table 3.8:

$$C_{\mathrm{phx}} = 1.934A^{0.6233} \tag{3.17}$$

with C_{phx} expressed in k€ and A expressed in m^2, for the SS316 PHX in the area range of 40 to 300 m^2. The cost of SS316 shell-and-tube HXs is taken from the same source for the area range of 30 to 200 m^2.

$$C_{\mathrm{sthx}} = 3.743A^{0.5948} \tag{3.18}$$

The yearly HX and fluids costs take into account a (linear) depreciation time of 15 years. The price of natural gas for households and commercial consumers has been taken as 55 €/MWh [126]. A boiler efficiency of 85% has been adopted, which has also been taken into account for the other AHP systems. The price of IL varies significantly depending both on production amounts and manufacturing technique. The prices of [emim][SCN] listed in Table 3.7 are based on quotations for a lab scale production. It is also reported that, in large scale production, some ILs' cost will reduce to 3.00 $/kg [127]. Honeywell UOP [128] reports the use of ILs to produce high-octane motor fuels and claims it is a "cost-effective solution". This indicates that the application of ILs at an industrial scale does make their price economically more competitive. The values from the current vendors and the expected low value (3.00 $/kg) have been adopted in the present calculations. Table 3.9 shows the results of the economic comparison between the different AHP solutions and the use of a conventional boiler. The heating efficiency is obtained by multiplying the COP with the boiler efficiency. All considered AHP options lead to both energy savings (42%) and costs savings (29%), when the cost of IL is at a reasonable level (industrial scale production). The influence of the IL price is also shown. The NH_3/IL AHP with a large minimum temperature approach in the SHX performs economically the best for current IL prices.

OTHER TECHNICAL CONCERNS

Other concerns on the application of ILs includes their stability and volatility.

STABILITY Most ILs have been reported as being stable as liquids over a very wide temperature range. It has also been reported for some NH_3/IL mixtures that chemical reactions take place [43]. Chemical reactions make the cycles less reversible. The long term operation of these fluids might be a concern but NH_3/IL mixtures which do not undergo chemical reactions are expected to be capable of realizing a large number of operational cycles in a reliable way.

Table 3.9: Yearly energy requirements and yearly capital costs of the different AHP systems in comparison to a conventional boiler.

	Heating efficiency [-]	Primary energy demand [MWh]	Primary energy cost [k€]	Yearly HX cost [k€]	Yearly working fluid cost* [k€]	Total yearly cost [k€]	Yearly savings** [%]
Boiler	0.85	397	21.8	-	-	21.8	-
AHP NH_3/IL (option 1)	1.47	229	12.7	2.8	29.3/ 7.2/ 0.1	44.7/ 22.6/ 15.5	-105.0/ -3.6/ 28.9
AHP NH_3/IL (option 2)	1.31	258	14.3	1.6	8.1/ 2.0/ 0	23.8/ 17.7/ 15.7	-9.2/ 18.8/ 28.0
AHP NH_3/H_2O	1.37	246	13.7	2.5	-	16.0	26.6

*Three different costs in the case of NH_3/[emim][SCN] pairs corresponding to three prices (two prices from vendors listed in Table 3.7, and an estimation reported by Chen *et al.* [127]) adopted in the analysis.

**The negative of the yearly saving indicates extra costs.

VOLATILITY There have also been concerns about the negligible vapor pressure of ionic liquids [129]. Although being small, very small concentrations of IL vapor may leave the generator and enter the condenser. After a large number of cycles, IL may accumulate in the evaporator requiring additional actions to bring it back to the absorbent loop. Since no long term operation with these cycles has been reported, the practical performance of these mixtures still needs to be confirmed.

3.4. CONCLUSIONS

After a review of methods and a summary of available experimental properties, a thermodynamic model has been proposed to investigate single-effect AHPs with NH_3/ILs working pairs as working fluids for the purpose of the floor heating of buildings. With this model, the performance of the AHPs has been calculated for all 8 feasible NH_3/ILs pairs (one additional pair cannot operate under the considered conditions) and also for NH_3/H_2O. Additionally, a properties optimization work and economic analysis have been executed. Based on the work, the following conclusions could be drawn:

- The circulation ratio f decreases and COP increases with an increase of generator temperature (up to 130 °C).
- Under the considered conditions, the COP of the NH_3/[mmim][DMP] pair reaches the best performance (COP of 1.79), and along with NH_3/[bmim][BF_4], NH_3/[emim][Tf_2N], NH_3/[emim][SCN] all showing a higher COP than that of the NH_3/H_2O pair. Nevertheless, the circulation ratio f is significantly higher than that for the NH_3/H_2O pair.
- The analysis of the generator heat requirement revealed that, high vapor quality values at the inlet of the GEN resulted in a high COP because of a lower latent heat contribution. The influence of circulation ratio, f, is mainly associated with the two sensible contributions (the sensible heat of both components), and a low f would lead to a high COP.
- Neglecting the excess enthalpy, the performance changes, but the better working pairs still beat NH_3/H_2O pair in terms of COP.
- The optimum COP of this type of working pairs and for the condition considered can be expected to reach 1.84 as demonstrated by the property-optimization study.
- To realize an ideal performance, the optimum IL candidates should show high absorption capabilities, large solubility differences between in- and outlet of the generator, low molecular weights and low heat capacities. The optimization study shows its potential to assist in the selection of IL as absorbents.

- Large circulation ratio combined with worse heat transfer performance in the solution heat exchanger lead to large demand of heat transfer area, which additionally requires a large amount of expensive ILs.
- An economic feasibility analysis indicates that, when the [emim][SCN] would be produced at industrial scales, this NH_3/IL AHPs lead to both significant energy (42%) and economic (29%) savings.

4

Ammonia/Ionic Liquid-based Double-Effect Absorption Chillers

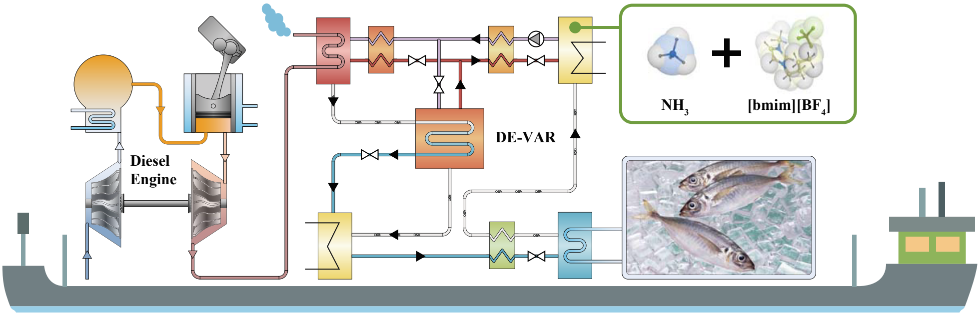

An ammonia-based double-effect vapor absorption refrigeration cycle is proposed to recover high-temperature waste heat generated by diesel engines on board of fishing vessels. Non-volatile ionic liquids are applied as absorbents in the double-effect absorption system. In comparison to systems using ammonia/water fluid, the complexity of the system can be reduced by preventing the use of rectification sections. In this chapter, a multi-scale method is implemented to study the proposed system, including Monte Carlo molecular simulations for computing vapor-liquid equilibrium properties at high temperatures and pressures, thermodynamic modeling of the double-effect absorption cycles, and system evaluations by considering practical integration. The Monte Carlo simulations provide reasonable vapor-liquid equilibrium predictions. [bmim][BF$_4$] is found to be the best performing candidate among the investigated ionic liquids. In the proposed cycle, the best working fluid achieves a coefficient of performance of 1.1 at a cooling temperature of -5 °C, which is slightly higher than that obtained with generator-absorber cycles. Integrated with the exhaust gas from diesel engines, the cooling capacity of the system is sufficient to operate two refrigeration seawater plants for most of engine operating modes in high-latitude areas. Thereby, the carbon emission of onboard refrigeration of the considered fishing vessel could be reduced by 1633.5 tons per year compared to the current practice.

Parts of this chapter have been published in: Energy Conversion and Management **174**, 829-843 (2018) [130].

4.1. INTRODUCTION

Global warming is one of the critical issues of the society in this age. According to the International Maritime Organization [131], maritime transport emits around 1000 million tons of carbon dioxide (CO_2) annually and is responsible for about 2.5% of global greenhouse gas emissions along with 15% and 13% of global NO_x and SO_x emissions. Fishery is one of the major parts of the maritime transport sector. Vessels for pelagic seas usually demand refrigeration plants, which consume fuel or electricity onboard [132]. The refrigeration plant is one of the largest electricity consumers onboard of fishing vessels, typically using 50% of the total power [8]. Diesel engines are normally used for propulsion and onboard electricity generation in trawlers. The engines also produce a significant amount of waste heat [19]. A study [133] shows that a large 2-stroke marine diesel engine may waste 50% of total fuel energy and 25.5% of the total energy is wasted through the exhaust gas (250 - 500 °C) [132].

Heat activated vapor absorption refrigeration (VAR) systems provide opportunities to recover waste heat and to use it to cool down fish and onboard space. Fernández-Seara *et al.* [134] designed, modeled, and analysed a gas-to-thermal fluid waste heat recovery system based on an ammonia/water (NH_3/H_2O) cycle for onboard cooling applications. Cao *et al.* [135] carried out a study on a water/lithium bromide ($H_2O/LiBr$) VAR system powered by waste heat for space cooling in a cargo ship. In their study, the cooling COP is 0.6 and an electricity-based coefficient of performance (COP) could be up to 9.4. Thereby, fuel consumption and CO_2 emission for the cooling system are reduced by 62%. Recently, Salmi *et al.* [19] modeled both an $H_2O/LiBr$ single-effect (SE) VAR cycle and an NH_3/H_2O refined cycle for cooling on a bulk carrier ship with waste heat recovered from exhaust gases, jacket water and scavenge air cooler. The VAR system has a theoretical potential to save 70% of electricity in comparison to a compression air-conditioning system. They also pointed out that the $H_2O/LiBr$ cycle is more efficient (COP of 0.75-0.85) and NH_3/H_2O is more suitable for below-freezing-point cooling (COP of 0.5).

Exhaust gases seem to be the best source of waste heat onboard to drive absorption chillers, even though they cannot be cooled down below 167 °C because of a risk of sulfur corrosion [19]. At temperatures above 150 °C, double-effect vapor absorption refrigeration (DE-VAR) cycles, in which the refrigerant is generated twice, are able to achieve higher thermal efficiencies by taking advantage of the higher temperature of the heat sources [51]. However, these cycles usually utilize the working fluid $H_2O/LiBr$, which cannot meet the demand of below-freezing-point cooling. With NH_3/H_2O, the DE-VAR is not feasible because of the need of rectifiers which introduce a higher complexity.

To use higher temperature exhaust gases for below-freezing-point cooling onboard, NH_3 with ionic liquids (ILs) working fluids is proposed to be used in DE-VAR systems. ILs, a family of room-temperature molten salts, have been intensively studied due to their potential in replacing the absorbents in conventional absorption refrigeration and heat pump technology [36]. ILs show strengths such as high boiling points, strong affinities with refrigerants and high chemical and thermal stabilities [36]. Moreover, NH_3 based absorption systems have strengths such as below-freezing-point cooling, free of air infiltration and low impact on the environment (zero for both ozone depletion and global warming potentials).

NH_3/ILs working fluids in absorption cycles have received significant attentions in the past decade. Yokozeki and Shiflett [39] reported the first vapor-liquid equilibrium (VLE) data of four NH_3/ILs working pairs. By including measurements and correlations of the other four NH_3/ILs pairs, the performance of the eight NH_3/ILs fluids in an SE absorption cycle was compared in Ref. [40]. Most of their studied imidazolium ILs are currently well commercialized. Functional ILs with NH_3 in SE absorption cycles were also investigated. For instance, Chen *et al.* [43] investigated the VLE property of NH_3 with a metal ion-containing imidazolium IL. A thermodynamic performance of a VAR cycle using the studied fluids was conducted in a sequential work by the same authors [46]. Ruiz *et al.* [44] studied some ammonium ILs. Cera-Manjarres [45] explored six other ILs including imidazolium and ammonium ILs with a hydroxyl group (-OH). By applying more reliable mixing enthalpies and experimental heat capacities, Wang and Infante Ferreira [24] explored the performance of nine NH_3/ILs fluids in SE absorption cycles for heat pump systems. The authors identified promising absorbents which work with NH_3 in absorption cycles under 130 °C heating.

Nevertheless, the above studies were all applied at temperature and pressure ranges available for SE-VAR cycles. The DE-VAR cycle requires VLE data at higher temperatures and higher pressures, which have not been measured experimentally. Previously, Wang and Infante Ferreira [136] investigated nine NH_3/ILs working fluids in DE absorption cycles for application in refrigeration and heat pump systems. The used VLE properties were obtained by simply extrapolating the ones at temperatures and pressures available for SE-VAR cycles. Schouten [137] used the same extrapolated properties for a DE-VAR in a series design. In this context, Becker *et al.* [138] showed that molecular simulation is able to predict relevant thermophysical properties for temperatures and pressures applied in SE-VAR cycles. These authors also pointed out that improved force fields are needed for an accurate prediction of the cycle performance.

In this chapter, a DE-VAR in parallel configuration using NH_3/ILs fluids is proposed for refrigeration applications in fishing vessels, driven by heat recovered from diesel engines. A multi-scale method is applied to study its perfor-

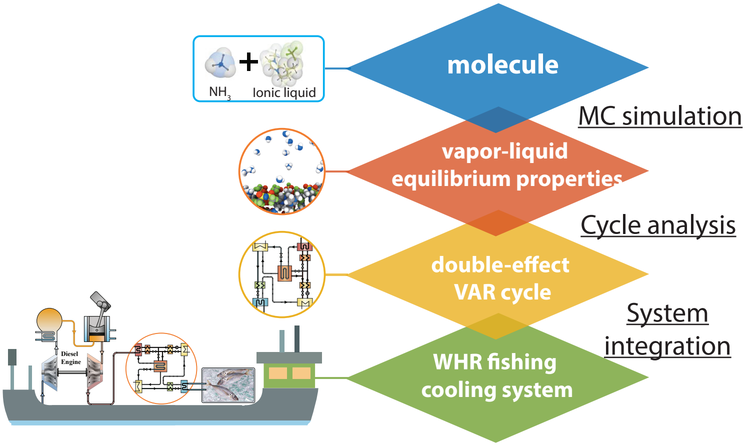

Figure 4.1: Outline of this chapter showing different levels of details considered: Monte Carlo molecular simulations for computing VLE properties, thermodynamic modeling of the VAR cycle, and evaluation of the system integrating the VAR cycle with the diesel engine for fishing cooling.

mance, from a molecular level to a system integration level, as shown in Fig. 4.1. First, an adjusted force field is used in Monte Carlo (MC) simulations to predict VLE properties in high temperature and high pressure conditions of the three selected NH_3/IL pairs. Together with the experimental VLE and heat capacities, the VLE data are correlated and mixture enthalpies are predicted. These thermophysical properties are then used for the evaluation of the DE-VAR cycles. After considering practical concerns, a case study based on a real vessel operating in high-latitude conditions is carried out to check the techno-economic feasibility of the integrated system in practice.

4.2. PROPERTIES OF WORKING FLUIDS

In this chapter, the ILs under consideration are [emim][SCN], [bmim][BF_4], and [emim][Tf_2N]. The corresponding NH_3/IL working fluids were identified showing higher *COP*s than NH_3/H_2O in SE absorption cycles [24]. Additionally, as commercialized ILs, their thermophysical properties and force fields required in this chapter are accessible. Hence, they are selected as the investigated ILs.

4.2.1. VLE PROPERTIES FOR THE BINARY SOLUTIONS

For the three studied NH_3/IL working fluids, experimental VLE data measured by Yokozeki and Shiflett [39, 40] only cover the conditions suitable for SE-VAR cycles. To extend the VLE data of these fluids for DE-VAR cycle at higher temperature and pressure conditions, Monte Carlo simulations are conducted. The data from experimental sources together with the simulated ones are correlated with the NRTL model for usage in the studied cycle.

MONTE CARLO METHOD

Molecular simulation is a powerful tool to predict the behavior of materials [139]. In this type of simulation, thermodynamic properties are computed based on force fields which describe interactions between molecules [140]. Comparable to the previously discussed models, these force fields are often developed by correlating experimental data. However, the potential to predict properties outside the correlated data is often better than with traditional models and hence molecular simulations can be used to extend existing experimental data [141]. Here, MC simulations were performed to obtain solubility data of NH_3 in 3 different ILs at higher temperatures than measured experimentally.

As shown in a previous publication by the author [138], the osmotic ensemble [142] can be applied to compute the uptake of gases in ILs. Thereby, the temperature, the pressure, the number of solvent molecules, and the fugacity of the solute are fixed, while the volume of the system, and the number of solute molecules can fluctuate. Here, the Continuous Fractional Component Monte Carlo method is applied to insert and delete solute molecules [142–145]. After the equilibration phase, the total amount of solute molecules in the system determines the gas uptake at the chosen conditions. The details of the conducted simulations can be found in the previous work by the author [138].

All force fields considered in this chapter were taken from literature. The force fields for the ILs were taken from the work of Tenney *et al.* [124] (for cation [emim$^+$] and anion [SCN$^-$]), Liu *et al.* [146] (for cation [bmim$^+$] and anion [Tf_2N^-]), and Canongia Lopes and Pádua [147] (for anion [$BF_4{}^-$]). For NH_3, the TraPPE force field was used [148]. In the simulations, parts of the cations and NH_3 molecules are considered to be rigid while the alkyl part and the anions are flexible. A summary of the force field parameters is provided in Appendix C. The Ewald summation technique with a relative precision of 10^{-5} [139] is used to calculate electrostatic interactions. Lennard-Jones interactions are truncated and shifted at 12 Å without applying tail corrections. Polarization is not explicitly considered in the simulations. The simulations are conducted with the RASPA software package [149, 150].

Unfortunately, commonly used force fields do not predict the solubility of NH_3 in ILs accurately [138]. To overcome this limitation, the binary mixing rule of the Lennard-Jones energy parameters, ψ, between NH_3 and ILs in MC simulations has been scaled to fit the experimental solubility for available conditions.

The applied mixing rule is:

$$\psi = k \cdot \sqrt{\psi_{\mathrm{NH_3}} \cdot \psi_{\mathrm{IL}}} \tag{4.1}$$

By adjusting ψ, the interaction strength between NH_3 and the ILs is changed. Different interaction strengths between the molecules were tested to find the one that predicts the best behavior in regard to the experimental data. The applied scaling parameter, k, is respectively 0.78, 0.15, and 0.78 for [emim][SCN], [bmim][BF_4] and [emim][Tf_2N]. To validate the quality of the adjusted force field, a comparison between the computed solubilities (dashed curves) with the adjusted force fields and the experimental data [39, 40] (solid curves) is provided in Fig. 4.2.

In the case of [bmim][BF_4] (Fig. 4.2(b)), the computed solubility without adjusting force field is also shown (dotted curves). It can be observed that the qualitative trend of the gas uptake of these simulations is similar, while the absolute values are significantly overestimated. After the scaling of the mixing rule, the simulation results agree well with the experimental data for all investigated ILs and for varying temperatures. The average 95% confidence interval for the computed solubilities for [emim][SCN], [bmim][BF_4], and [emim][Tf_2N] used in the cycle calculations is 2.8%, 1.7%, and 2.9%, respectively.

CORRELATIONS OF VAPOR-LIQUID EQUILIBRIUM PROPERTIES

The non-random two-liquid (NRTL) model has been shown as a suitable model to correlate and predict VLE of ILs-based working fluids [72]. The experimental vapor pressures of NH_3/IL binary systems have been regressed to the NRTL model as explained in Chapter 3. Subsequently the operating concentrations of solutions can be determined. The form of the NRTL model can be found in Chapter 3. Note that for the data points at temperatures above the critical point of NH_3, an extrapolation of the vapor pressure equation is used for an easy processing of the data [46]. In particular, an extrapolation of the Antoine equation is applied. This processing will somehow influence the solid physical basis of the NRTL model.

4.2.2. DENSITIES AND HEAT CAPACITIES

Densities of pure [emim][SCN], [bmim][BF_4] and [emim][Tf_2N] have been reported by Matkowska and Hofman [151], Ficke *et al.* [152], Tariq *et al.* [153] respectively. Specific heat capacities of [emim][SCN] are from the work of Navarro *et al.* [115]. The data reported by Paulechka *et al.* [112] and Nieto de Castro *et al.* [154] are used together for the specific heat capacities of [bmim][BF_4]. For [emim][Tf_2N], the data of specific heat capacities were reported by Paulechka *et al.* [114] and Ferreira *et al.* [155] for different temperature ranges. These data

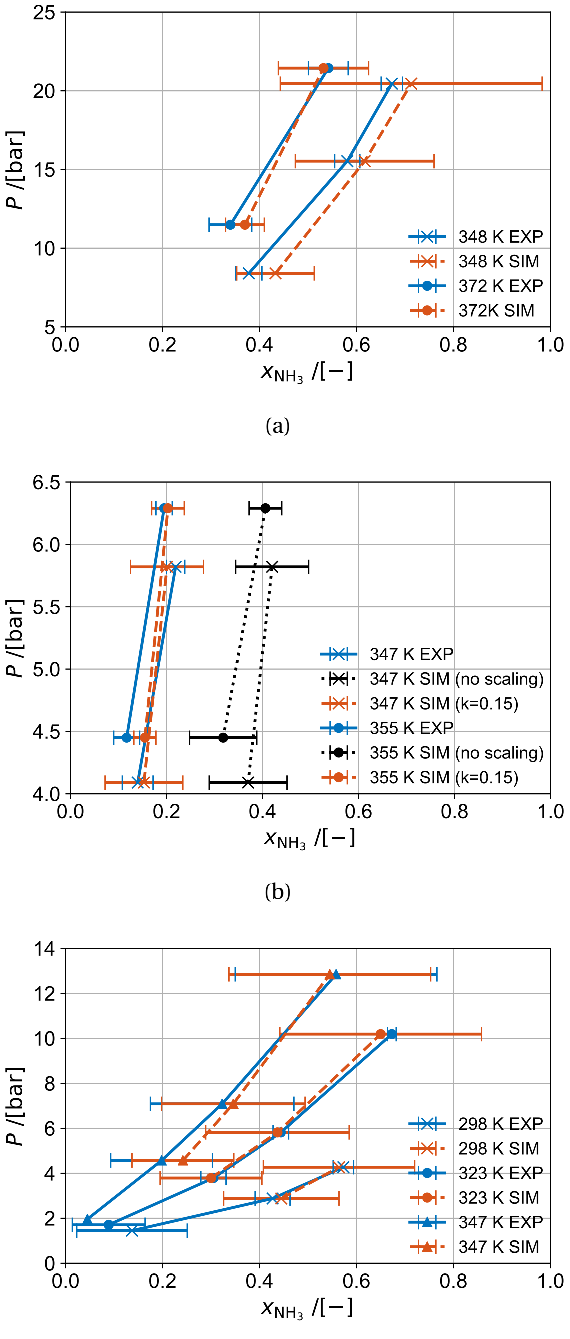

(a)

(b)

(c)

Figure 4.2: Comparison between the simulated (SIM) and experimental (EXP) VLE data [39, 40] with error bars for the working pairs: (a) NH_3/[emim][SCN], (b) NH_3/[bmim][BF_4] and (c) NH_3/[emim][Tf_2N]. The shown error bars of the simulated data represent the 95% confidence interval.

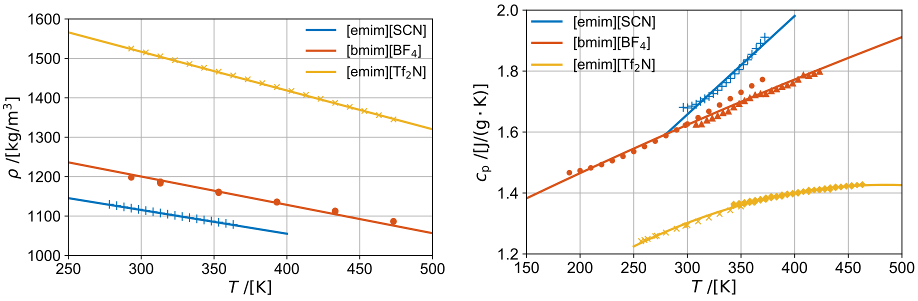

(a) (b)

Figure 4.3: Experimental data and the correlations of (a) densities [151–153], and (b) heat capacities [112, 114, 115, 154, 155] of the three studied ILs.

Table 4.1: Molecular weights (M_w) and correlations of relevant thermophysical properties for the 3 investigated ILs at 1 bar *.

IL	M_w [kg/kmol]	ρ [kg/m^3]	c_p [kJ/(kg·K)]
[emim][SCN]	169.25	$\rho = 1296 - 0.602 \times T$	$c_p = 0.6882 + 0.0032 \times T$
[bmim][BF$_4$]	226.02	$\rho = 1416 - 0.719 \times T$	$c_p = 1.119 + 1.83 \times 10^{-3} \times T - 4.879 \times 10^{-7} \times T^2$
[emim][Tf$_2$N]	391.31	$\rho = 1812 - 0.9837 \times T$	$c_p = 0.5644 + 3.56 \times 10^{-3} \times T - 3.674 \times 10^{-6} \times T^2$

* T in K.

are plotted in Fig. 4.3, as functions of temperature. Correlations of the data are listed in Table 4.1.

Currently, densities and heat capacities of the studied NH_3/IL mixtures have not been reported. Eq. 4.2 provides a general form of ideal solution properties, which is based on weighted average of properties from both components. This form is used to estimate the densities and heat capacities for the investigated mixtures:

$$M_{sol} = w_{NH_3} M_{NH_3} + w_{IL} M_{IL} \tag{4.2}$$

This simplification is verified with the density data of six NH_3/IL mixtures reported by Cera-Manjarres [45]. The maximum relative deviation is 6.5%. Moreover, the simplification for the heat capacities has been verified with data of H_2O/[mmim][DMP] from Dong *et al.* [38]. The relative deviation is smaller than 4% [24]. This treatment has also been checked for the H_2O/[emim][DMP] solution, for predicting the solution enthalpy and cycle performance. No obvious difference has been observed in comparison to using the heat capacity of the real solutions [72] .

4.2.3. ENTHALPIES

The enthalpy of pure NH_3 is directly obtained from NIST's Refprop [99].

For a saturated solution at T, P and with an NH_3 mass fraction of w_{NH_3}, the total enthalpy of the solution, h_{sat}^{sol}, is provided by,

$$h_{sat}^{sol}\left(T, P, w_{NH_3}\right) = w_{NH_3} h_{NH_3}(T) + w_{IL} h_{IL}(T) + \Delta h_{mix}\left(T, P, w_{NH_3}\right) \tag{4.3}$$

where the enthalpies of NH_3 are chosen at their saturated liquid states for the cases below the critical temperature. For the cases at temperature above the critical point of NH_3, an additional effect of ideal gas enthalpy is added to the enthalpy at the critical point, following the work of Chen *et al.* [46]:

$$h_{NH_3}(T)|_{T>T_c} = h_{NH_3}(T_c) + \int_{T_c}^{T} c_{p,ig}^{NH_3}\, dT \tag{4.4}$$

For the ILs, enthalpies are calculated based on their pure heat capacities c_p^{IL},

$$h_{IL}(T) = h_0(T_0) + \int_{T_0}^{T} c_p^{IL}\, dT \tag{4.5}$$

The experimental mixing enthalpy Δh_{mix} used in Eq. 4.3 has not been reported for the studied NH_3/IL working fluids. For an alternative NH_3/IL working fluid, the author has quantified this term using various thermodynamic models [72]. The calculation has shown that the exothermic effect of mixing NH_3/IL is less than that of mixing H_2O/IL. Furthermore, it has been shown that neglecting Δh_{mix} does not significantly change the total enthalpy and the *COP* in an SE-VAR cycle with NH_3/IL pairs [72]. Therefore, in the following calculations, the effect of the mixing enthalpy is neglected.

For solutions at a subcooled condition T, P and w_{NH_3}, enthalpies can be obtained by subtracting the subcooled part from corresponding saturated solution,

$$h_{sub}^{sol}\left(T, P, w_{NH_3}\right) = h_{sat}\left(T_{sat}, P, w_{NH_3}\right) - \int_{T}^{T_{sat}} c_p^{sol}\, dT \tag{4.6}$$

4.3. CONFIGURATIONS OF CYCLES AND MODELING METHODS

The configuration and modeling method of the studied DE-VAR cycle are presented. Besides, an alternative choice, the generator-absorber heat exchange (GAX) cycle with NH_3/H_2O, is introduced for a sake of comparison, since it is promising with high temperature heat sources [51].

4.3.1. DOUBLE-EFFECT ABSORPTION REFRIGERATION CYCLE

Fig. 4.4 depicts a schematic representation of a double-effect absorption system in parallel configuration. The main feature of the parallel DE-VAR cycle is that the strong solution (strong in refrigerant NH_3), pumped from the absorber (ABS), is divided into two parallel streams after being heated in the solution heat exchanger (SHX1).

Two sub-streams are heated in two generators (GENs) to generate refrigerant vapor: One of the sub-streams is heated in the high pressure generator (HG) by the external heat source at a high temperature. Superheated refrigerant vapor is generated there and then continues to the high pressure condenser (HC). The other sub-stream is heated in the low pressure generator (LG) to generate the other refrigerant vapor. The heat is from the condensation of the superheated refrigerant vapor in the HC. The HC and LG are coupled in an intermediate heat exchanger (iHX).

Key state points of the solutions are illustrated qualitatively in both ln P-(-1/T) and h-w diagrams in Fig. 4.5. The cycle 5-8-9-11a-11-13-5 shows the sub-stream passing the HG and cycle 5-7c-11b-11-13-5 represents the other sub-stream passing the LG.

The mass flows of the two sub-streams of the solution can be quantified with the distribution ratio (DR), which is defined as the mass flow ratio between the sub-stream of the solution passing the HG and the total mass flow:

$$DR = \frac{\dot{m}_8}{\dot{m}_5} \tag{4.7}$$

4.3.2. MODELING METHODOLOGY OF THE CYCLE

To create an integrated model for the thermodynamic analysis of the DE-VAR system, several assumptions are made to simplify the calculations:

- The system operates in a steady state.
- The operating pressures of the absorber and the evaporator are identical, and similarly the pressure of each generator is equal to its directly linked condenser.
- In the outlets of the two condensers and evaporator, the refrigerant stream is in a saturated liquid or saturated vapor state, respectively. The solution is in equilibrium state while leaving two generators and the ABS.
- The pinch temperature of the SHXs is assumed as 10 K. The pinch temperature of the iHX is set to 5 K. The effectiveness of the HX1 is assumed to be 75%.
- Heat losses and pressure losses are neglected.
- Throttling is an isenthalpic process.

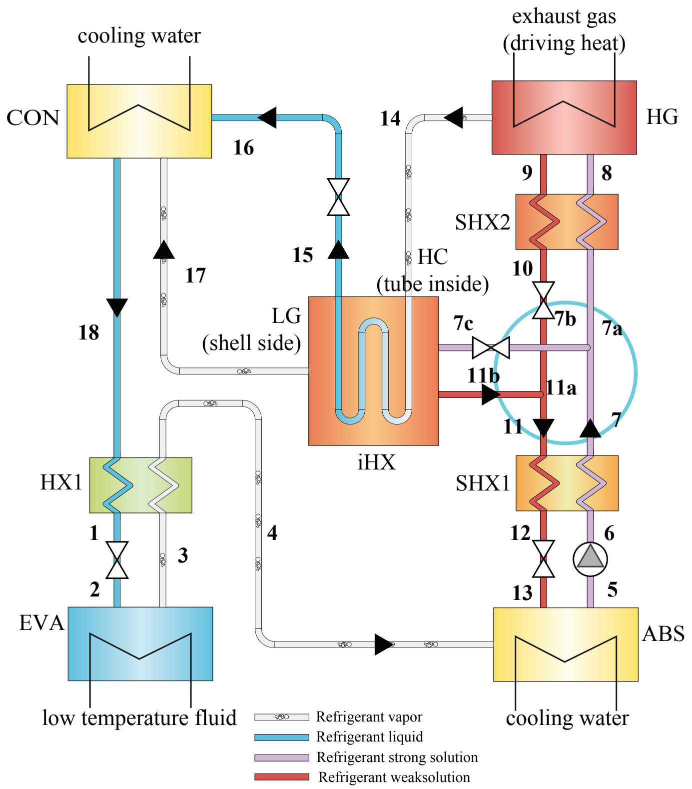

Figure 4.4: Schematic diagram of the studied DE-VAR system in parallel configuration. Non-volatile absorbents absorb refrigerant in the absorber (ABS). The solutions are then pumped parallelly to the high and low pressure generators (HG and LG) for refrigerants generation. A blue circle identifies the parallel sub-streams leaving and returning the ABS. The refrigerant vapors generated in the HG are used for heating the LG. The two refrigerant streams are mixed in the condenser (CON) and then go through the valve and the evaporator (EVA) to generate cooling effects.

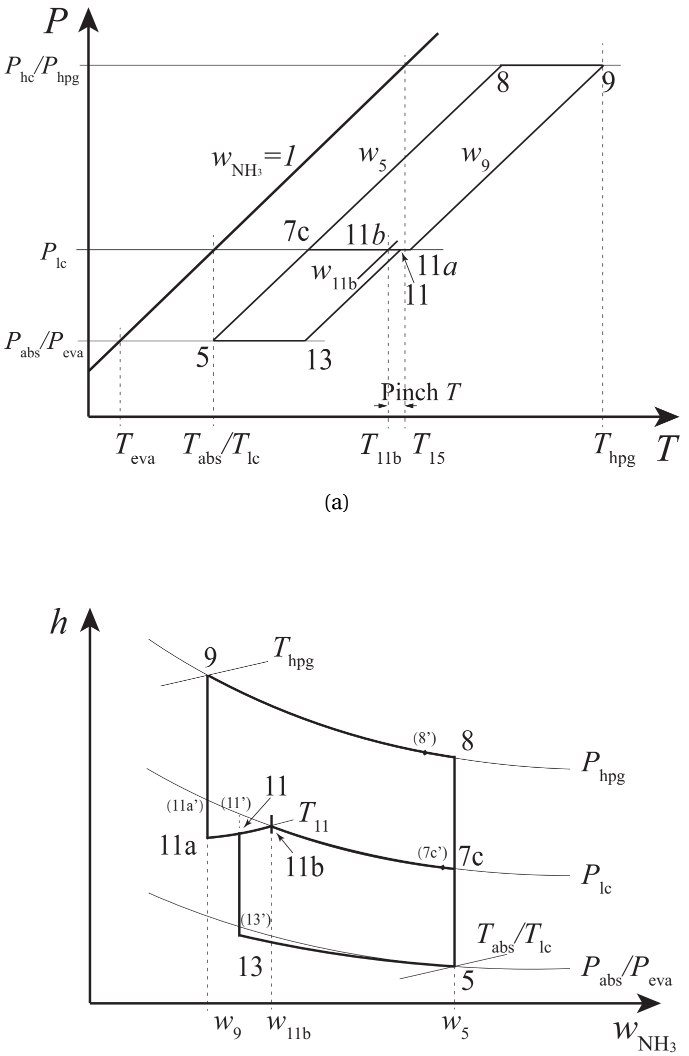

(a)

(b)

Figure 4.5: The state points (referring to the points shown in Fig 4.4) of the solution stream plotted in a $\ln P - (-1/T)$ diagram (a) and an $h - w$ diagram (b). Points 11, 11a and 13 sharing the same pressure and fraction with points 11', 11a', and 13', respectively, are at subcooled conditions. Points 7c and 8 have a possibility of refrigerant boil off, the portions of saturated solutions are denoted as 7c' and 8', respectively.

For each component shown in Fig. 4.4, the mass, species and energy balances are implemented. For instance, for the ABS shown in Fig. 4.4, the balances are:

$$\begin{cases} \dot{m}_4 + \dot{m}_{13} = \dot{m}_5 \\ \dot{m}_4 + w_{13}\dot{m}_{13} = w_5\dot{m}_5 \\ \dot{m}_4 h_4 + \dot{m}_{13} h_{13} = \dot{m}_5 h_5 + \dot{Q}_{\mathrm{abs}} \end{cases} \tag{4.8}$$

The power consumption of the solution pump, $\dot{W}_{\mathrm{p}}$, can be calculated by,

$$\dot{W}_{\mathrm{p}} = \frac{\dot{m}_5}{\rho_{\mathrm{sol}}} \frac{P_{\mathrm{hpg}} - P_{\mathrm{eva}}}{\eta_{\mathrm{p}}} \tag{4.9}$$

The calculation procedure for the cycle is illustrated in Fig. 4.6. The temperature of state point 7, which is between two SHXs, is obtained iteratively to reach the energy balances of both the SHXs. The other iteration is required to determine the temperature of state point 15, which is based on the energy balance of the iHX.

With the heat duties and the pump power consumption, the coefficient of performance, COP, of a cycle for cooling is defined as,

$$COP = \frac{\dot{Q}_{\mathrm{eva}}}{\dot{Q}_{\mathrm{hpg}} + \dot{W}_{\mathrm{p}}} \tag{4.10}$$

The circulation ratio, f, defined as the required mass flow of pump stream for generating a unit mass flow of refrigerant, is also taken into account in this chapter. f can be obtained via mass and species balances around the ABS as,

$$f = \frac{\dot{m}_5}{\dot{m}_4} = \frac{1 - w_{13}}{w_5 - w_{13}} \tag{4.11}$$

This model was previously validated by Vasilescu and Infante Ferreira [156] for an air-conditioning application with an LiBr/H_2O working pair.

4.3.3. GENERATOR-ABSORBER HEAT EXCHANGE CYCLE

NH_3/H_2O GAX cycles have been claimed to be suitable for applications with higher temperature driving heat [51]. As shown in Fig. 4.7, the promising thermal performance of this cycle is achieved by couping the heat between partial sections of the GEN and the ABS.

A perfect operation of the GAX cycle relies on the accurate identifying of temperature profiles of sections in ABS and GEN where the heat can be coupled. This kind of heat coupling is difficult to achieve in practice. However, the GAX cycle represents “a compelling theoretical possibility” [51]. Therefore it is used as a benchmark to compare the DE-VAR cycle with.

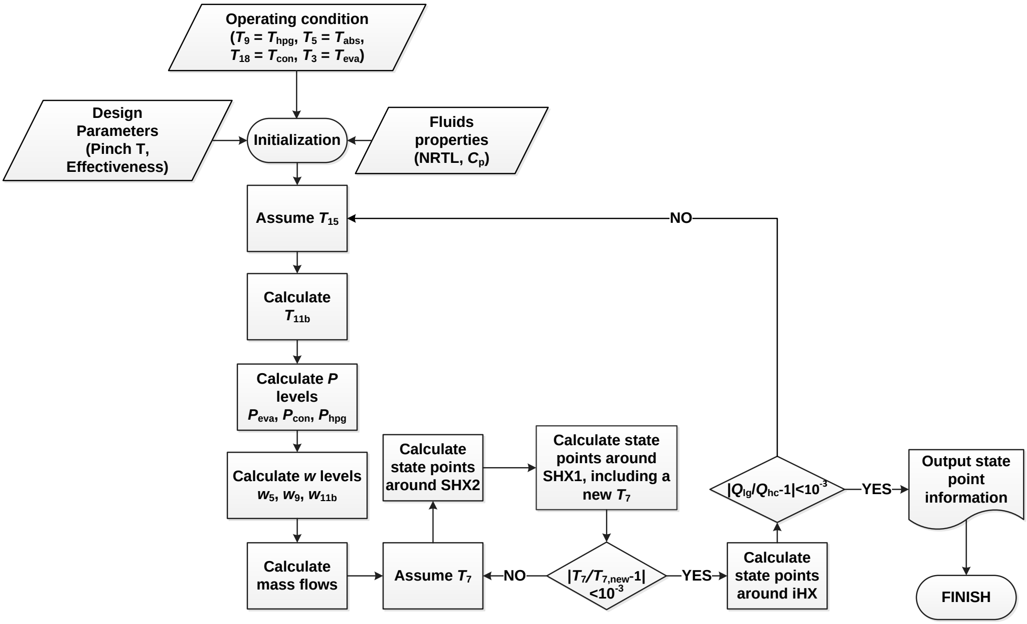

Figure 4.6: Flow-chart for the thermodynamic modeling of the DE-VAR in parallel configuration. Mass, species and energy balances are applied in each component. Iterations of T_{15} and T_7 are implemented to reach the balances of the iHX and two SHXs.

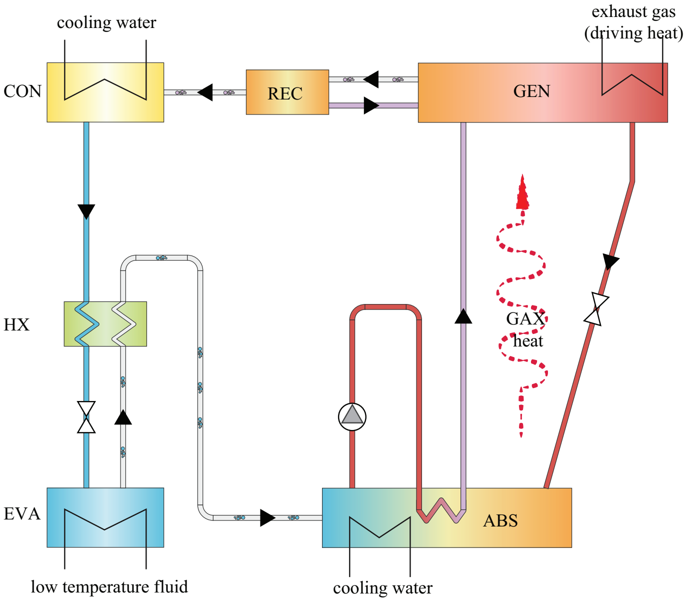

Figure 4.7: Schematic diagram of a standard NH_3/H_2O GAX system [51]. The main feature of the GAX cycle is that the final stages of its ABS have higher temperatures than the flow in the first stages of the GEN. The heat from the ABS can be recycled to heat up those stages in the GEN. The weak NH_3/H_2O solutions absorb NH_3 vapors from the EVA and experience an internal heat recycling in the ABS before they are pumped into the GEN. Vapors leaving the GEN are mixtures of NH_3/H_2O, which are purified in the rectifier (REC). The NH_3 vapors then experience a similar process as the DE-VAR cycle for generating cooling effects.

Table 4.2: Cooling capacities, temperatures and power consumptions of the refrigeration plants (RSW, CWP and the NH_3 circuits of FP) used in the studied trawler vessel, in two typical climate cases.

	$\dot{Q}_{\text{eva}}$ [kW]	T_{eva} [°C]	$\dot{W}$ [kW]	
RSW plant	2×1416	-5	2×414	
CWP	2×880	-5	2×222	32 °C heat sink
FP (NH_3 circuits)	2×900	-5	2×253	
RSW plant	2×1556	-5	2×271	
CWP	2×954	-5	2×152	16 °C heat sink
FP (NH_3 circuits)	-	-	-	

The modeling of the GAX cycle is based on the method introduced by Herold *et al.* [51]. During the heat coupling, both the available heat in the ABS and the required heat in the GEN can be obtained through mass and energy balances. The GAX heat really transferred is the minimum between the available and required heat of vapor generation. The rectifier is analyzed as an ideal device that produces vapor with 99.5% NH_3.

4.4. THE INTEGRATED FISHING VESSEL

A trawler vessel is taken into consideration for the following case studies.

The required cooling capacity in this vessel is provided by the refrigeration seawater (RSW) plant, chilled water plant (CWP), and freezing plant (FP). Currently, the plants are all configured with vapor compression refrigeration systems. The RSW and CWP apply NH_3 as a refrigerant, while FP is an NH_3/CO_2 cascade system (NH_3 is used in the high temperature circuits). The technical characteristics are listed in Table 4.2. It is investigated if the proposed IL-based DE-VAR system has the potential to replace the current plants entirely or partially.

Scavenge air, jacket water, and exhaust gas are among the main waste heat sources from the diesel engines as illustrated in Fig. 4.8. The heat released via the exhaust gas takes up approximately 50% of total wasted heat [133]. In this chapter, the exhaust gas after the turbine is used.

The studied ship is equipped with a Wärtsilä diesel engine of type 12V38 for propulsion [157]. The properties of the exhaust gas after the turbine from this engine are shown in Fig. 4.9, which are taken from the official project guide [157]. Note that the data for 40% load are based on extrapolations.

Operations of the engine can be classified into the five typical modes, which are listed in Table 4.3. Corresponding exhaust gas properties are identified from Fig. 4.9.

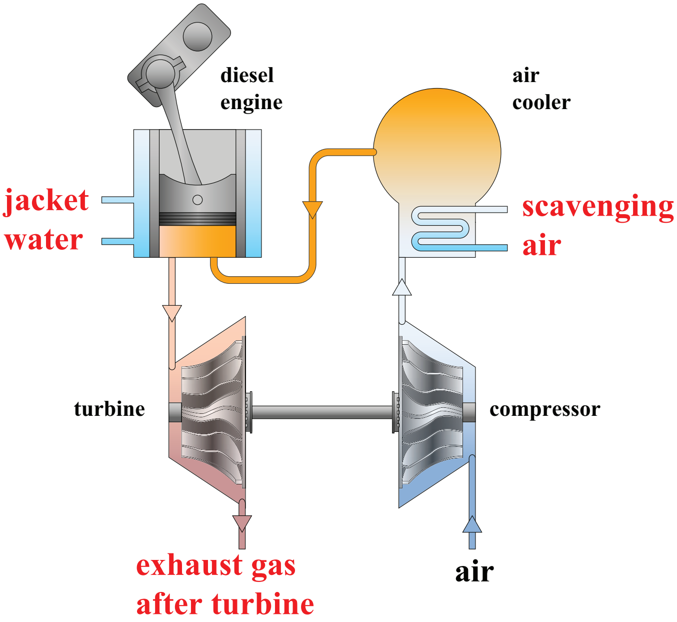

Figure 4.8: Main waste heat sources of a two-stroke diesel engine: Scavenge air is used to cool down the compressed air before going to the engine. Jacket water is applied to maintain the temperature of the engine where the combustion of fuels takes place. Exhaust gas, a mix of air and fuel at high temperature, is released with 50% of the total waste heat.

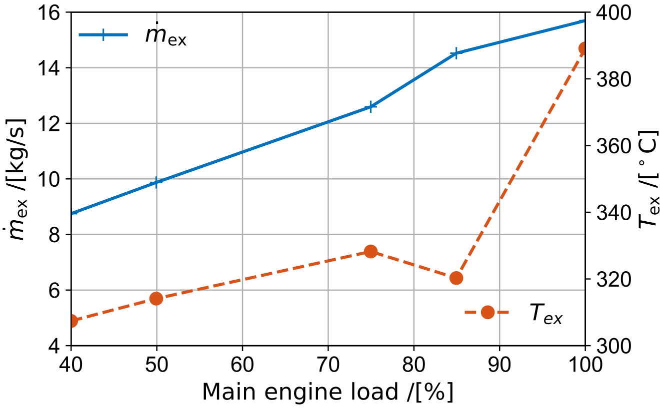

Figure 4.9: Exhaust gas flow and temperature (after the turbine) of the studied diesel engine 12V38 for different engine loads [157]. The solid curve denotes the flow rate of the exhaust gas and the dashed curve denotes its temperature after the turbine.

Table 4.3: Typical operating modes of the fishing vessel, main engine loads and the corresponding flow and temperature of the exhaust flue gas flow.

	Operation mode	Duration per year [hour]	Main engine load [-]	Exhaust gas flow [kg/s]	T of exhaust gas [°C]
Mode 1	Fishing with production	5400	90%	15	340
Mode 2	Fishing without production	400	90%	15	340
Mode 3	Sailing to fishing zone and pre-cooling	320	70%	12	326.5
Mode 4	Placing or retrieving nets, pumping fish on board	1200	40%	8.75	307.4
Mode 5	Unloading or out of service	1440	0%	-	-

Table 4.4: Fitted interaction parameters in the NRTL model (following the same notations in Ref. [24]) for the studied NH_3/IL working pairs.

IL	α [-]	$\tau_{12}^{(0)}$ [-]	$\tau_{12}^{(1)}$ [K]	$\tau_{21}^{(0)}$ [-]	$\tau_{21}^{(1)}$ [K]
[emim][SCN]	-0.0320	-20.18	4342.10	11.07	-2084.20
[bmim][BF_4]	-0.0001	-481.23	2740.10	456.75	-2297.27
[emim][Tf_2N]	-0.0024	-107.90	8969.70	82.95	-5276.93

4.5. RESULTS AND DISCUSSION

Following the proposed multi-scale method, the result of the property level, cycle level, and integrated system level are discussed in this section.

4.5.1. SIMULATION OF VAPOR-LIQUID EQUILIBRIUM PROPERTIES AND THEIR CORRELATIONS

The experimental VLE data and the ones from Monte Carlo simulations are plotted together in Fig. 4.10 for the three studied NH_3/IL working fluids.

The fitted parameters of the NRTL model based on the shown data are listed in Table 4.4. These parameters follow the same notations introduced Chapter 3.

Based on the NRTL model, predicted vapor pressures of the three studied fluids are shown in Fig. 4.11. To show the influence of the additional data provided by the Monte Carlo simulations, the results are compared with and without the inclusion of the computed data. Vapor pressures shown in Figs. 4.11(a), 4.11(c) and 4.11(e) are obtained by only fitting experimental VLE data at low temperatures and low pressures (interaction parameters can be found in Chapter 3). The vertical and horizontal dashed lines represent temperature and pressure boundaries, respectively, of EXP data. The other three diagrams are based on both the experimental VLE data and the computed ones. In each diagram of Fig. 4.11, NH_3 fractions represented by the various curves cover the conditions applied in

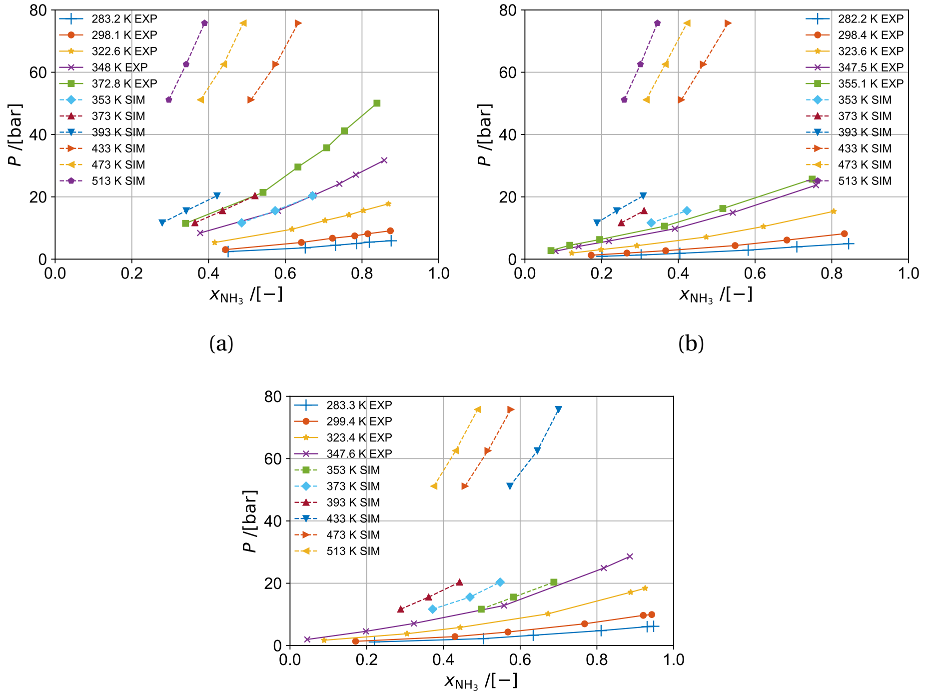

(a)

(b)

(c)

Figure 4.10: VLE data of working pairs (a) NH_3/[emim][SCN], (b) NH_3/[bmim][BF_4] and (c) NH_3/[emim][Tf_2N]. Solid curves denote the experimental data from Yokozeki and Shiflett [39, 40] (denoting as EXP), and dashed curves denote the simulated results by the author (denoting as SIM).

the DE-VAR cycle.

Vapor pressures fitted only with the VLE data at low temperatures and low pressures (Figs. 4.11(a),4.11(c) and 4.11(e)) show linear behavior inside the experimental temperature and pressure ranges. However, out of the range of the experimental data, the vapor pressures increase rapidly with an increase of temperature. This behavior fails to follow the physical basis indicated by the Clausius-Clapeyron equation (Eq. 4.12): for which the vapor pressures are approximately linear, because the term $-\Delta h/(R\Delta Z)$ depends only slightly on temperature [158].

$$\frac{d\ln P}{d(1/T)} = -\frac{\Delta h}{R\Delta Z} \tag{4.12}$$

The nonlinear shape of vapor pressures curves is pronounced at relatively low NH_3 mass fractions, which are crucial for the studied cycle. The influence of using exclusively the experimental based VLE properties on estimating the cycle performance will be discussed in detail in Section 4.5.3.

By including the computed data (right-hand side), the trends of vapor pressures, especially for the cases with low NH_3 fractions at high temperatures, become more reasonable. This indicates that the simulation helps to improve the description of the behavior. The reasonable extension of the VLE data for NH_3/IL mixtures, confirms the added value and need for MC simulations to extend the range of VLE properties of NH_3/IL mixtures.

4.5.2. DIAGRAMS OF THERMOPHYSICAL PROPERTIES

Based on the thermal property methods discussed in Section 4.2, the diagrams of the studied working fluids are generated for using them in thermal applications including VAR cycles. The corresponding diagrams are provided in Appendix D.

4.5.3. CYCLE PERFORMANCE

With the thermo-physical properties, the performance of the DE-VAR cycle can be predicted. The influences of operation conditions and different sources of properties are investigated. The comparison of its performance with the GAX cycle is also presented.

THE INFLUENCE OF VARYING OPERATION CONDITIONS

Parametric studies are carried out to explore the performance of the DE-VAR for different operating conditions. The investigated parameters are the DR, the heat source temperature, the cooling temperature and the environmental temperature.

As shown in Fig. 4.12, optimum performances for different conditions (heat source temperature, T_{hpg}, of 160 and 220 °C, respectively) of the three working

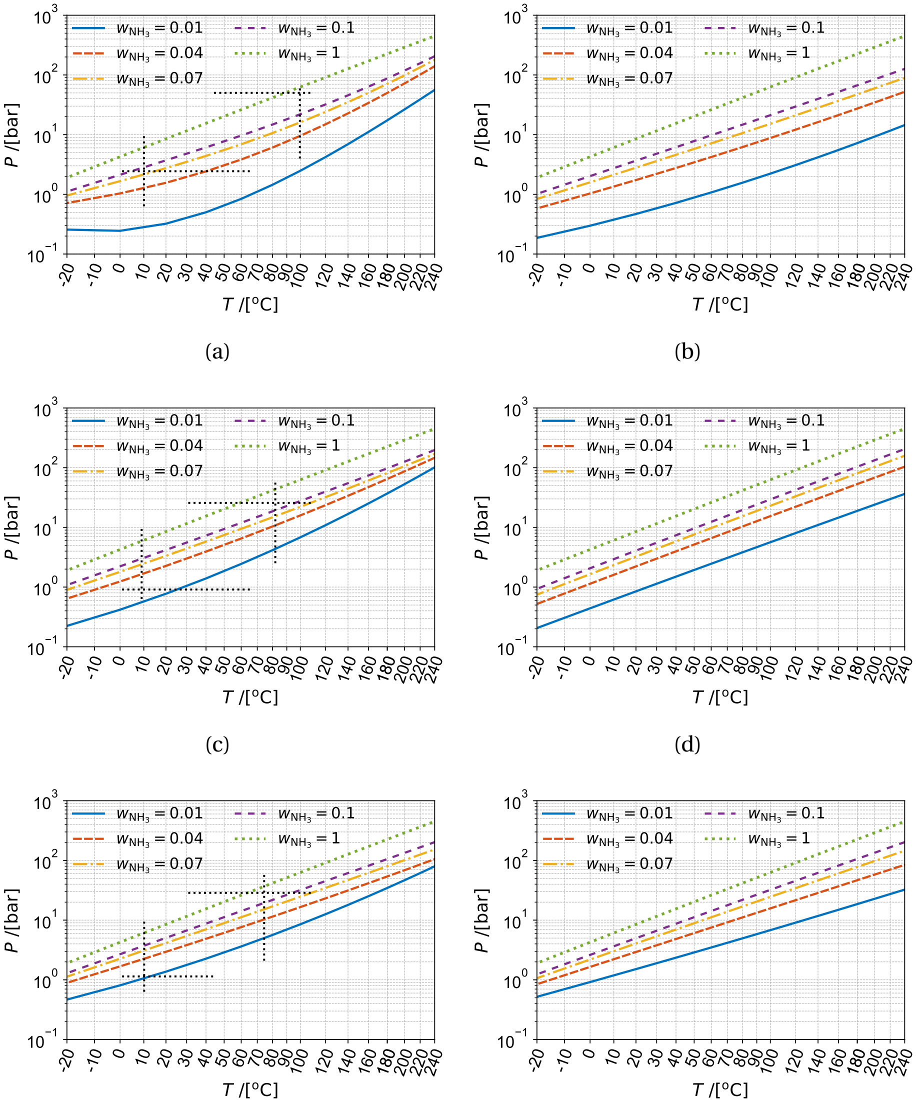

(a) (b)

(c) (d)

(e) (f)

Figure 4.11: Comparison of the vapor pressure curves generated only using the experimental VLE data (EXP) and the ones together using the experimental and simulated VLE data (SIM) for the studied NH_3/IL working pairs: (a) NH_3/[emim][SCN] pair (EXP [40]), (b) NH_3/[emim][SCN] pair (EXP [40] + SIM) (c) NH_3/[bmim][BF_4] pair (EXP [39]), (d) NH_3/[bmim][BF_4] pair (EXP [39] + SIM), (e) NH_3/[emim][Tf_2N] pair (EXP [39]), (f) NH_3/[emim][Tf_2N] pair (EXP [39] + SIM). Vertical and horizontal dashed lines represent temperature and pressure boundaries of EXP data.

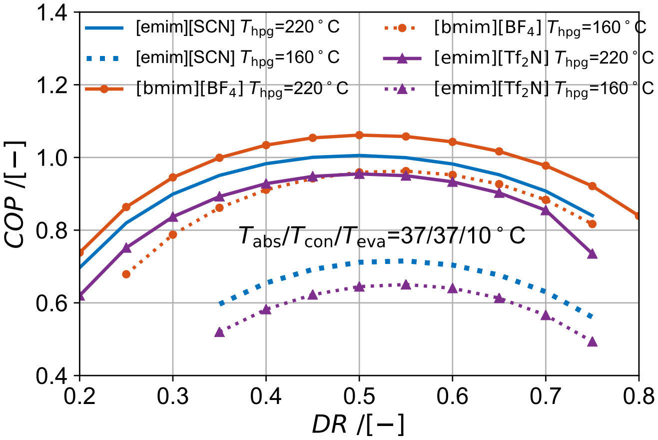

Figure 4.12: Influence of the Distribution Ratio on the Coefficient of Performance of the DE-VAR with working pair NH_3/[emim][SCN], NH_3/[bmim][BF_4] and NH_3/[emim][Tf_2N]. The performance is calculated at the conditions T_{hpg} are 220 or 160 °C, and $T_{abs}/T_{con}/T_{eva}$ are kept constant at 37/37/10 °C.

fluids are always obtained when the *DRs* are close to 0.5. This indicates that two sub-streams which are comparable in flow are preferable, which would allow for simplifications in constructing pipelines and controlling valves in a real system. In the following calculations, the value of *DR* will be kept constant at 0.5.

Fig. 4.12 also indicates that a higher temperature of the heat source, T_{hpg}, contributes to a better performance for the studied conditions. Similar trends can be observed for the other cases in Figs. 4.13(a) and 4.13(b) for which the cooling temperature, T_{eva}, is at a relatively low level or the heat sink temperature, T_{con} and T_{abs}, is at a relatively high level. However, when T_{eva} is higher and T_{con} or T_{abs} is lower, an increase of T_{hpg} can lead to constant trends of the *COP*. This is, for instance, the case in Fig. 4.13(a), when T_{eva} = 10 °C, for the working pair NH_3/[bmim][BF_4]. A decreasing trend can also be observed in Fig. 4.13(b), when T_{eva} = 0 °C, for the same working pair.

Figs. 4.13(a) and 4.13(b) indicate that a lower temperature of the cooling demand leads to an inferior performance for all working pairs. Moreover, for the same operating condition, the NH_3/[bmim][BF_4] pair performs better than the other two pairs.

The influence of the temperature of the seawater on the performance can be understood by comparing Figs. 4.13(a) and 4.13(b). Fig. 4.13(a) applies for cases in which the seawater temperature is 32 °C, corresponding to an application in tropical areas. The temperature of the working fluid side is 5 K higher than the cooling medium, the seawater (T_{abs} = T_{con} = 37 °C). Fig. 4.13(b) corresponds to

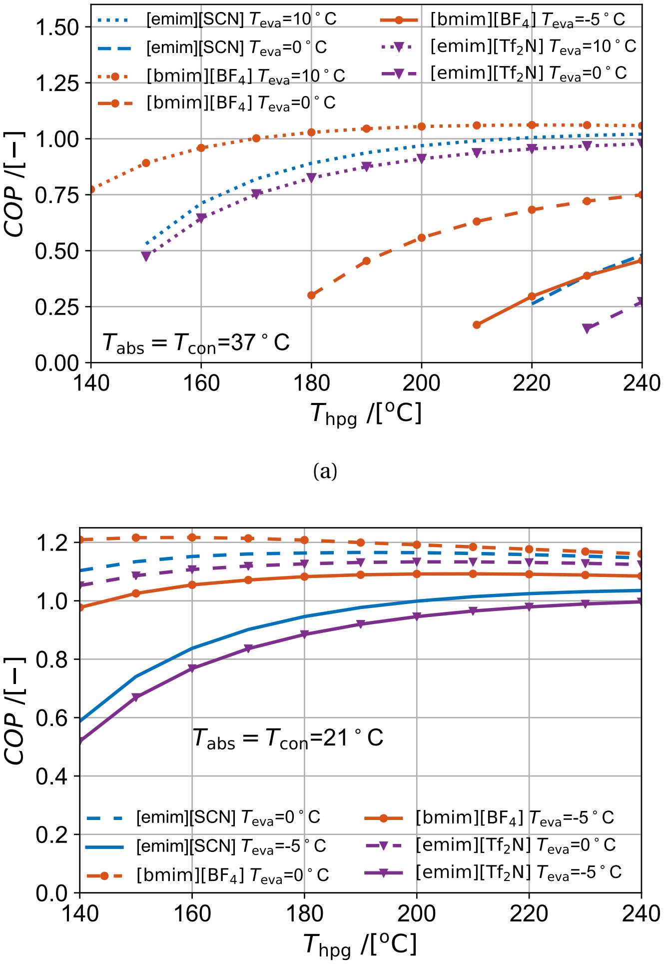

(b)

Figure 4.13: Influence of the cooling temperature, T_{eva}, on the Coefficient of Performance of the DE-VAR with working pairs NH_3/[emim][SCN] (smooth curves), NH_3/[bmim][BF$_4$] (curves with round symbols) and NH_3/[emim][Tf$_2$N] (curves with triangle symbols) for applications in: (a) tropical areas ($T_{con} = T_{abs} = 37$ °C) and (b) high-latitude areas ($T_{con} = T_{abs} = 21$ °C).

Table 4.5: Comparison of the effect of different VLE properties sources for NH_3/[bmim][BF_4] on the DE-VAR cycle performance at the condition of $T_{hpg}/T_{abs}/T_{con}/T_{eva}$ = 240/37/37/-5 °C (DR = 0.5).

Relevant parameters		EXP [39] VLE (Fig. 4.11(c))	EXP [39] + SIM VLE (Fig. 4.11(d))
w_5	[-]	0.0387	0.0383
w_{11b}	[-]	0.0245	0.0290
w_9	[-]	0.0064	0.0285
w_{13}	[-]	0.0156	0.0287
f	[-]	42.49	101.72
specific $\dot{Q}_{eva}$	[kJ/kg]	1158.32	1158.32
specific $\dot{Q}_{hpg}$	[kJ/kg]	1204.01	1638.62
specific $\dot{W}_p$	[kJ/kg]	321.80	772.49
COP	[-]	0.759	0.480

an application in high-latitude areas, for instance, the North Sea adjoining the Netherlands, where the seawater temperature is on average 16 °C (T_{con} = T_{abs} = 21 °C).

The comparison of Figs. 4.13(a) and 4.13(b) shows that both working fluids have higher performances at lower T_{abs} and T_{con}. Unfortunately, for the application in tropical areas, the DE-VAR cycle with working pairs NH_3/[emim][SCN] and NH_3/[emim][Tf_2N] cannot operate at a cooling temperature of −5 °C. The NH_3/[bmim][BF_4] working fluid does not show very promising performance, either. Hence, the following analysis will only focus on high-latitude areas.

The DE-VAR cycle with NH_3/IL pairs shows similar performances, in respect to the operating conditions, as the cycle with the traditional H_2O/LiBr working pair [159] or other investigated working pairs, such as NH_3/$LiNO_3$ [17].

THE INFLUENCE OF DIFFERENT VAPOR-LIQUID EQUILIBRIUM PROPERTIES ON THE CYCLE PERFORMANCE

To investigate the influence of excluding the simulated VLE data, the DE-VAR cycle with NH_3/[bmim][BF_4] in the condition of $T_{hpg}/T_{abs}/T_{con}/T_{eva}$ = 240/37/37/-5 °C is studied. Relevant parameters which can help to indicate the influences of different VLE sources on the cycle performance are listed in Table 4.5.

The NH_3 mass fractions of state point 5 (solution outlet of the ABS), 11b (solution outlet of the LG) and 9 (solution outlet of the HG) are determined by the temperatures and pressures at saturated conditions. The NH_3 fractions estimated based on solely extrapolating EXP VLE data are lower than those based on VLE data including SIM data (only for point 5, they are almost identical). From point 5 to 11b and to 9, temperatures and pressures increase. The deviation of saturated NH_3 fractions from the one obtained including SIM data also show an increasing trend.

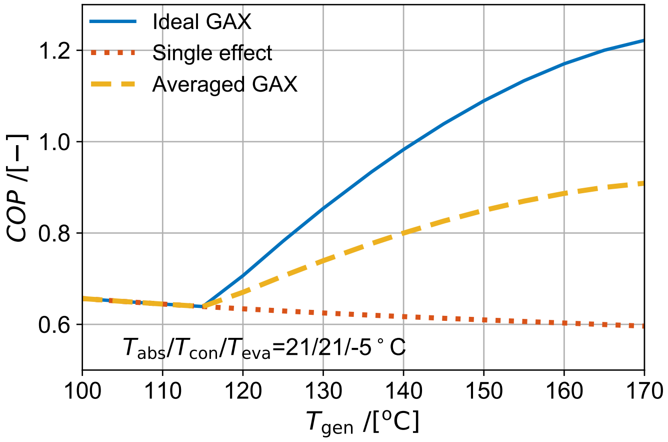

Figure 4.14: Comparison of performance between the ideal NH_3/H_2O GAX cycle and the single-stage NH_3/H_2O cycle at various T_{gen} conditions ($T_{abs}/T_{con}/T_{eva} = 21/21/-5$ °C). Solid curve indicates the “ideal” GAX performance and the dotted curve indicates the “degraded” GAX, i.e. the single-effect cycle. The dashed curve denotes the expected performance of a real system.

Two streams with an NH_3 mass fractions of w_9 and w_{11b} are mixed before state point 13. Consequently, state point 13 also shows a lower value of NH_3 fraction when obtained without using the simulation VLE data. Due to the underestimation of the change in NH_3 fraction between points 5 and 13, the circulation ratio, f, which is based on w_{13} and w_5 (Eq. 4.11), is lower than the one obtained using the SIM VLE. This indicates that the required pump flow is lower.

In terms of cycle performance, the specific heat duties and pump power are listed in Table 4.5, as well. They are the corresponding heat and power loads for 1 kg/s refrigerant flow. The estimated demands of heat and pump power by using exclusively EXP VLE data is underestimated compared with the ones using SIM VLE data. This is consistent with the underestimation of the circulation ratio. As a result, the COP is remarkably overestimated.

COMPARISON WITH THE GENERATOR-ABSORBER HEAT EXCHANGE CYCLE

Fig. 4.14 shows how the *COP* of a GAX cycle changes with the temperature of the heat source, T_{gen}, at the condition of $T_{abs}/T_{con}/T_{eva} = 21/21/-5$ °C. Due to the limitation of the thermophysical properties database [99] of the NH_3/H_2O mixture, the calculated performance of the GAX cycle can only be obtained for T_{gen} below 170 °C.

It can be seen in Fig. 4.14 that when T_{gen} is below 116 °C, there is no possibility for heat coupling. Thus, the GAX performs as a single-stage cycle, showing a decreasing trend with rising T_{gen}. Above 116 °C, the solid curve indicates the

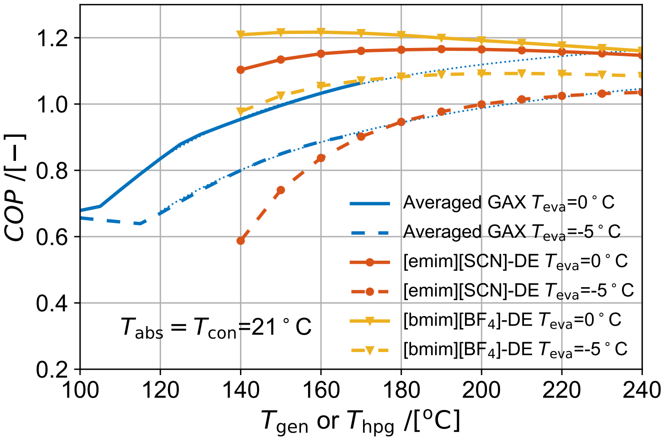

Figure 4.15: Comparison of the performance of the DE-VAR with working pairs NH_3/[bmim][BF$_4$], NH_3/[emim][SCN] and the NH_3/H_2O GAX cycle at condition $T_{abs} = T_{con} =$ 21 °C. Smooth curves indicate the GAX performance and the dotted curves are extrapolations of their trend lines. The solid curves denote the performance of cooling at $T_{eva} = 0$ °C and the dashed curves denote the performance of cooling at $T_{eva} = -5$ °C.

performance of the ideal GAX cycle, which is increasing as T_{gen} rises. The GAX cycle is entitled “ideal” because the calculation of it is based on the perfect heat coupling between the ABS and GEN. Hence, the solid curve shows the upper limit of the GAX cycle. The dotted curve represents the results of the single-stage (or single-effect) NH_3/H_2O VAR cycle, which gives the lower limit of the GAX cycle if the heat is not perfectly coupled. A practical system is supposed to perform between these two limits. The dashed curve represents the average of these two limits, which is an expected estimation of the actual performance.

Fig. 4.15 shows a comparison of the performance of the NH_3/H_2O GAX cycle and the DE-VAR cycle with the NH_3/[bmim][BF$_4$] and NH_3/[emim][SCN] pairs at the condition of $T_{abs} = T_{con} = 21$ °C, indicating applications at high-latitude areas. T_{eva} is set to -5 and 0 °C. The temperature of the driving heat is varied to investigate its influence. Note that the performance of the GAX cycle is represented by the average value between the ideal GAX and normal SE-VAR performance. The data of T_{gen} above 170 ° are based on extrapolation.

As shown in Fig. 4.15, the GAX cycle is able to reach a high performance even when the driving temperature is relatively low. With the T_{gen} increasing, the performance of this cycle is increasing less rapidly. The DE-VAR cycle with working pair NH_3/[emim][SCN] shows a poor performance around 150 °C for a −5 °C cooling application. After a sharp initial increase, *COP* values of the DE-VAR increase only slightly when T_{hpg} is above 180 °C. The *COP* value of the proposed cycle with NH_3/[bmim][BF_4] is approximately 10% higher than that of the averaged GAX cycle when they are driven by heat at 200 °C. In the higher temperature range, these two cycles show a similar performance. Considering the proposed DE-VAR applying ILs, there is no special need for a control strategy of the internal heat coupling, and the utilization of the ILs prevents the need for rectification of the refrigerant flow.

4.5.4. SYSTEM INTEGRATION OF THE DOUBLE-EFFECT VAPOR ABSORPTION CYCLE WITH THE EXHAUST GAS

Direct heat exchange is assumed between the exhaust gas and the strong NH_3/IL solution. DE-VAR cycles are designed for high temperature applications and a direct coupling could take full advantage of the high temperature exhaust gas. Thus, the waste heat recovery (WHR) exchanger, i.e. the flue gas cooler, also plays the role of a high pressure generator.

RECOVERABLE HEAT AND CORRESPONDING COOLING CAPACITIES

For the exhaust gas stream associated with the WHR heat exchanger applied in typical modes, the inlet temperature, $T_{\mathrm{ex}}^{\mathrm{in}}$, and the flow rate, $\dot{m}_{\mathrm{ex}}$, are listed in Table 4.3. The outlet temperature, $T_{\mathrm{ex}}^{\mathrm{out}}$, cannot be cooled down below 167 °C to prevent the risk of sulfur corrosion [19]. With these constraints, the driving heat of the DE-VAR system is the recovered heat from the exhaust gas, $\dot{Q}_{\mathrm{whr}}$, which is expressed as,

$$\dot{Q}_{\mathrm{whr}} = c_{\mathrm{p}}^{\mathrm{ex}} \dot{m}_{\mathrm{ex}} \left(T_{\mathrm{ex}}^{\mathrm{in}} - T_{\mathrm{ex}}^{\mathrm{out}} \right) \tag{4.13}$$

where the specific heat of the exhaust gas, $c_{\mathrm{p}}^{\mathrm{ex}}$, is taken as 1.08 kJ/(kg·K) [160].

In the design phase, a pinch temperature of 10 K is assumed in this HX. T_8 cannot be below 157 °C to prevent corrosion problems. The value of T_8 is also influenced by the operation of the cycle. Hence, the pumping flow, which is easy to adjust by changing the pump settings, is studied to explore its influence on the cooling capacity and on the heat recycling performance.

Fig. 4.16 depicts a case in which the inlet exhaust gas stream is at 340 °C and 15 kg/s (which corresponds to the majority of the operating cases: Mode 1 and 2 in Table 4.3), in high-latitude areas ($T_{\mathrm{abs}} = T_{\mathrm{con}} = 21$ °C) and for a $T_{\mathrm{eva}} = -5$ °C cooling application.

In the proposed DE-VAR, a higher driving temperature leads to a higher T_8. To maintain a fixed temperature difference of heat transfer, a higher $T_{\mathrm{ex}}^{\mathrm{out}}$ is required. Accordingly, the exhaust gas has a smaller temperature range over which it can be cooled and a smaller waste heat can be recovered. While a higher driving temperature also results in a higher *COP*. These dependencies influence the cooling capacity $\dot{Q}_{\mathrm{eva}}$ (round symbols), and lead to an initial increase, and then to a constant value as a function of the pump flow.

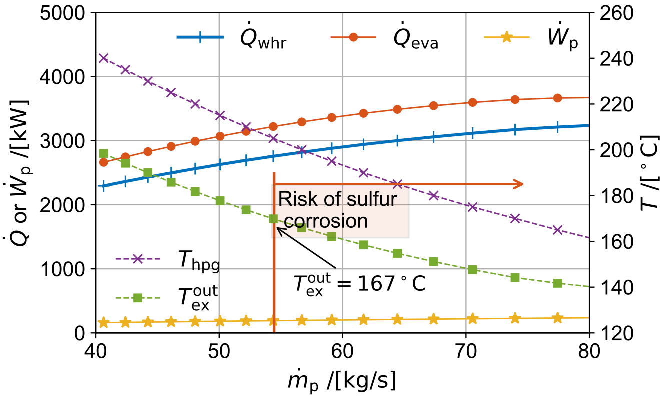

Figure 4.16: The influence of the designed pump flow, $\dot{m}_p$, on operating parameters of the exhaust gas driven DE-VAR system with NH_3/[bmim][BF_4]. The case is based on a 90% diesel engine load, in high-latitude areas for a −5 °C cooling temperature. Note that for pump flows above 54.4 kg/s, the exhaust gas might condensate and cause sulfur corrosion.

However for the studied case, when the pump flow of the solution, $\dot{m}_p$, is higher than 54.4 kg/s, the exhaust gas will be cooled below 167 °C as shown in Fig. 4.16. Even though cooling and heat recovery performances are better in this range, the DE-VAR system cannot be operated due to the risk of sulfur corrosion. Therefore, the optimum performance is achieved at a pump flow of 54.4 kg/s. The corresponding cooling capacity is 3220 kW.

Table 4.6 summarizes the operating parameters and optimum cooling performance when using the DE-VAR with the studied three working fluids for different engine loads.

The cooling capacity of the exhaust gas-driven DE-VAR system with working pair NH_3/[bmim][BF_4] is always larger than 1518 kW in the high-latitude environment, which has the largest cooling capacity among the three studied working pairs. For an engine load of 90%, the cooling capacity is able to reach 3220 kW. It has the potential to substitute at least one of the RSW plants in the studied fishing vessel (Table 4.2) for most of the operating condition. The solution pump flow, $\dot{m}_p$, of the NH_3/[bmim][BF_4] working pair is also lower than the ones of the other two pairs.

STATE INFORMATION

The state point information for the working fluid, NH_3/[bmim][BF_4] in the DE-VAR system, is listed in Table 4.7, for the above studied case in a condition of $T_{hpg}/T_{abs}/T_{con}/T_{eva} = 205/21/21/\text{-}5$ °C.

Due to the pressure drop in the valve and heating in the SHXs, solutions at

Table 4.6: The optimum cooling performance ($\dot{Q}_{\mathrm{eva}}$), corresponding recovered waste heat ($\dot{Q}_{\mathrm{whr}}$), DE-VAR cycle performance (f and COP, $\dot{m}_{\mathrm{p}}$, and $\dot{W}_{\mathrm{p}}$), and operating conditions ($T_{\mathrm{ex}}^{\mathrm{in}}$, $T_{\mathrm{ex}}^{\mathrm{out}}$, T_8, and T_{hpg}) for different diesel engine loads with the working pair NH_3/[emim][SCN], NH_3/[bmim][BF$_4$], and NH_3/[emim][Tf$_2$N] in high latitude areas.

	NH_3/[emim][SCN]			**NH_3/[bmim][BF$_4$]**			**NH_3/[emim][Tf$_2$N]**		
Engine load	90%	70%	40%	90%	70%	40%	90%	70%	40%
$T_{\mathrm{ex}}^{\mathrm{in}}$ [°C]	340	326.5	307.4	340	326.5	307.4	340	326.5	307.4
$T_{\mathrm{ex}}^{\mathrm{out}}$ [°C]	170.4	170.4	170.4	169.8	169.8	169.8	179.6	179.6	179.6
T_8 [°C]	160.4	160.4	160.4	159.8	159.8	159.8	169.6	169.6	169.6
T_{hpg} [°C]	190	190	190	205	205	205	200	200	200
f [-]	28.7	28.7	28.7	20.4	20.4	20.4	22.8	22.8	22.8
COP [-]	0.977	0.977	0.977	1.092	1.092	1.092	0.946	0.946	0.946
$\dot{m}_{\mathrm{p}}$ [kg/s]	69.8	51.4	32.9	54.4	40.1	25.6	94.5	69.2	43.9
$\dot{W}_{\mathrm{p}}$ [kW]	257	189	121	191	141	90	257	188	120
$\dot{Q}_{\mathrm{whr}}$ [kW]	2748	2023	1295	2756	2030	1300	2599	1904	1208
$\dot{Q}_{\mathrm{eva}}$ [kW]	2936	2162	1383	3220	2372	1518	2701	1979	1255

state points 7c and 8 may have NH_3 vapor generated [24]. A close investigation reveals that only small amounts of NH_3 vapor are generated before entering the generators. Results of NH_3 fractions and specific enthalpies of these two points in Table 4.7 are the data for bulk streams (saturated solution with NH_3 vapor). Specific enthalpies of the bulk stream are obtained via,

$$h^{\mathrm{sol}}\left(T, P, w_{\mathrm{NH_3}}\right) = \left(1-q\right) h_{\mathrm{sat}}^{\mathrm{sol}} + q h^{\mathrm{V}} \tag{4.14}$$

where, $h_{\mathrm{sat}}^{\mathrm{sol}}$ and h^{V} are the specific enthalpies for the saturated solution part and the vapor part, respectively. q is the quality, which is identified as,

$$q = \frac{w - w_{\mathrm{sat}}}{1 - w_{\mathrm{sat}}} \tag{4.15}$$

The qualities and saturated NH_3 fractions in solution of these two points are additionally listed in the footnote of Table 4.7.

4.5.5. FEASIBILITY CONSIDERATION

The above studied IL-based working pairs show a promising technical performance in the DE-VAR at high-temperature applications. Before implementing the cycle, thermal stabilities of the investigated ILs and the potential economic benefits must be considered.

THERMAL STABILITIES

It has been reported that imidazolium ILs have high thermal stabilities [161]. The short and long-term thermal stabilities of [emim][SCN] have been studied

Table 4.7: State points of the DE-VAR in a condition of $T_{hpg}/T_{abs}/T_{con}/T_{eva}$ = 205/21/21/-5 °C) with the working fluid pair of NH_3/[bmim][BF_4] (DR = 0.5, $\dot{m}_p$ = 54.4 [kg/s]).

Point	ṁ[kg/s]	T [°C]	P [bar]	w_{NH_3} [-]	h * [kJ/kg]
1	2.67	10.6	8.85	1	146.90
2	2.67	-5.0	3.55	1	146.90
3	2.67	-5.0	3.55	1	1353.86
4	2.67	14.5	3.55	1	1402.69
5	54.40	21.0	3.55	0.0766	79.38
6	54.40	21.0	39.53	0.0766	82.37
7	54.40	57.2	39.53	0.0766	148.41
7a	27.20	57.2	39.53	0.0766	148.41
7b	27.20	57.2	39.53	0.0766	148.41
7c **	27.20	57.2	8.85	0.0766	148.41
8 **	27.20	159.8	39.53	0.0766	393.02
9	25.57	205.0	39.53	0.0179	411.84
10	25.57	67.2	39.53	0.0179	151.64
11	51.73	70.1	8.85	0.0290	160.09
11a	25.57	67.2	8.85	0.0179	151.64
11b	26.16	72.9	8.85	0.0399	168.34
12	51.73	31.0	8.85	0.0290	90.64
13	51.73	31.0	3.55	0.0290	90.64
14	1.63	205.0	39.53	1	1791.27
15	1.63	77.9	39.53	1	485.50
16	1.63	21.0	8.85	1	485.50
17	1.04	72.9	8.85	1	1517.54
18	2.67	21.0	8.85	1	195.73

* Specific enthalpies are calculated based on an arbitrarily chosen reference state of T = -23 °C and P = 10 bar.

** At state points 7c and 8, the NH_3 may boil off from the solution. Saturated fractions and qualities of state points 7c and 8 are: w_{sat}^{7c} = 0.0672, q_{7c} = 0.01. w_{sat}^{8} = 0.0384, q_8 = 0.04.

by Navarro *et al.* [115]. Liu *et al.* [162] investigated short and long-term thermal stability of [bmim][BF_4]. Feng *et al.* [163] also carried out thermal analysis of [bmim][BF_4]. Heym *et al.* [164] measured the thermal decomposition of [emim][Tf_2N]. The work of Villanueva *et al.* [165] included the long-term stabilities of [emim][Tf_2N]. The key findings of these studies are summarized in Table 4.8.

It can be seen that the thermal stability of [bmim][BF_4] and [emim][Tf_2N] is better than that of [emim][SCN] regarding both short and long-term stability. The two ILs have also been classified into the group of "most stable" ILs by Cao and Mu [161]. The conducted long-term tests have shown the applicability of [bmim][BF_4] below 250 °C. [emim][SCN] has shown obvious mass loss above 160 °C and for this reason it cannot be applied in DE-VAR systems.

ECONOMIC AND ENVIRONMENTAL BENEFITS

It can be concluded that the proposed DE-VAR system with NH_3/[bmim][BF_4] is promising for the application in high-latitude areas. An accurate estimation of the initial cost and the system size relies on a thorough understanding of the heat and mass transfer of the newly-proposed working fluids and further investigation is required. Nevertheless, the operational cost can be estimated based on the analysis in this chapter. Table 4.9 shows the two options of replacing RSW plants with the proposed exhaust gas driven DE-VAR system.

The first option is to replace one RSW plant. The exhaust gas for all 5 engine operating modes (Mode 1-5 shown in Table 4.3) is able to drive the proposed DE-VAR system to produce the equivalent cooling capacity of one RSW. For these operating time (7320 hour per year), a saved primary energy can be obtained via the difference in power consumption of the proposed system and the existing compression one, which is 4.77 TJ/year. If the CO_2 emission of diesel oil is taken as 778 g/kWh$_e$ (diesel) [166], the CO_2 emission during fishing can be reduced by 1031 tons/year. Option 2 concerns replacing two RSW plants with one DE-VAR system, while this option is able to provide an equivalent cooling capacity of two RSW plants only when the engine operates at a 90% load. For this case, by operating it 5800 hours/year, the saved energy is 7.56 TJ/year and the corresponding reduced CO_2 emission is 1633.5 tons/year.

4.6. CONCLUSIONS

A waste heat recovery cooling system is proposed which uses ammonia/ionic liquid mixtures as working fluids in a double-effect vapor absorption refrigeration (DE-VAR) system. A multi-scale analysis is carried out to study its performance in a fishing vessel. The analysis includes Monte Carlo simulation to predict vapor-liquid equilibria at high temperatures and pressures, thermodynamic modeling

Table 4.8: A summary of assessment for the thermal stabilities of the studied ILs [115, 162–165].

	[emim][SCN][115]	[bmim][BF_4]	[emim][Tf_2N]
T_{onset} *	525.5 (5 K/min) 538.6 (10 K/min) 553.7 (20 K/min)	630 K (10 K/min) [162]	692 K (10 K/min) [164]
long-term stability	≥ 433.2 K for 48 hours: obvious mass loss ≤ 393.2 K for 48 hours: no obvious mass loss	513 K for 5 hours: No obvious mass loss [162]. Mass losses rates 1.30% and 2.60% for 453 K and 573 K, for 10 hours. No change in Fourier Transform Infrared Spectroscopy analysis [163].	533 K for 5 hours: mass losses rates ≥ 2% [165].

* T_{onset} is an extrapolated and reproducible temperature that denotes a point at which the weight loss begins. A graphic explanation can be found from literature, for instance, Navarro *et al.* [115].

Table 4.9: Economic and environmental benefits of replacing refrigeration seawater plants with the proposed system applied in high-latitude areas.

	in substitute of	operating hours [hrs/year]	saved energy [TJ/year]	reduced CO_2 [tons/year]
Option 1	RSW×1	7320	4.77	1030.8
Option 2	RSW×2	5800	7.56	1633.5

for cooling cycle analysis, and system evaluation when integrated with engine exhaust gas. Based on the work, the following conclusions could be drawn:

- Monte Carlo simulations are capable to extend the vapor-liquid equilibrium data of the working fluids. The inclusion of the computed solubilities improves the quality of the extension of the NRTL model to high temperature and pressure conditions in comparison to solely using experimental data obtained at low temperatures and pressures.
- The ranking of the coefficient of performance (*COP*) for the three studied ILs within NH_3-based DE-VAR cycle is: [bmim][BF_4] > [emim][SCN] > [emim][Tf_2N]. The best IL candidate achieves a *COP* above 1.1 for -5 °C cooling in a fishing vessel operating in high-latitude areas.
- DE-VAR cycles show approximately 10% higher performance than GAX cycles with NH_3/H_2O for applications with high temperature driving heat.
- Because of stability problems at high temperatures, [emim][SCN] is not suitable for high-temperature applications of a double-effect vapor absorption refrigeration cycle.
- The proposed system with NH_3/[bmim][BF_4] can provide the cooling capacity of one refrigeration seawater (RSW) plant for all operating modes of the diesel engine, when driven by its exhaust gas (*COP* of 1.1, cooling capacity of 1518 kW). Thereby, 4.8 TJ of energy can be saved and 1030 tons of CO_2 emission can be avoided annually per fishing vessel. Alternatively, the proposed system can provide the cooling capacity of two RSW plants for most of the operating modes (cooling capacity of 3200 kW). Annually saved energy and reduced CO_2 emissions are 7.6 TJ and 1634 tons, respectively.

5

ABSORPTION OF AMMONIA VAPOR BY AMMONIA/NON-VOLATILE COMPONENT MIXTURES IN PLATE HEAT EXCHANGERS

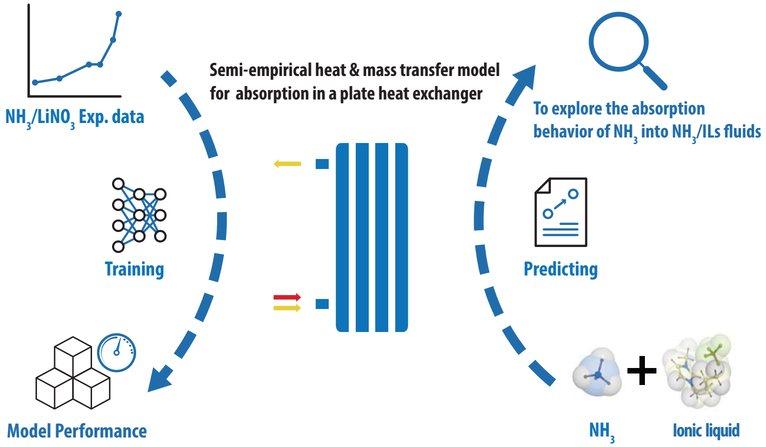

Unfavorable transport properties have always been pointed out as the key factors that hinder the application of ammonia/ionic liquids (NH$_3$/ILs) in absorption cycles, while heat and mass transfer of these new fluids in components have been rarely reported. In this chapter, a corrugated plate heat exchanger is selected as the geometry for exploring the absorption of NH$_3$ in the proposed NH$_3$/ILs working fluids. The process is studied making use of a semi-empirical framework: experimental data is needed to determine unknown information of heat and mass transfer, and a numerical model is developed making use of frequently applied theories. In addition, relevant transport properties of the NH$_3$/ILs working fluids are modeled based on collected experimental data. The proposed model is used to study the heat and mass transfer performance during the absorption of NH$_3$ vapor into NH$_3$/ILs fluids. Distribution of local parameters and overall heat and mass transfer characteristics are obtained. The performance of absorption of NH$_3$ into different working fluids is investigated as well. The highest overall heat transfer coefficient is obtained for the NH$_3$/[emim][SCN] mixture.

Parts of this chapter have been published in: International Journal of Heat and Mass Transfer, **134**, 1302-1302 (2019) [167].

5.1. INTRODUCTION

Thermally driven vapor absorption heat pumps and refrigeration systems provide energy-efficient ways of heating and cooling for the industry, agriculture, residential and transport sectors. Recently more and more investigations have been carried out to explore the application of ionic liquids (ILs), a type of room-temperature molten salts, as absorbents in vapor absorption systems. Some ILs have been found with high boiling points, strong affinities with refrigerants and favorable thermal and chemical stabilities. They provide an alternative way to prevent the risks of corrosion and crystallization of H_2O/LiBr pair and weaknesses of low efficiency and complexity of systems with NH_3/H_2O pair. In particular, working pairs of NH_3/ILs have been proposed as working fluids in absorption cycles to remove rectification and distillation sections, and to improve cycles' thermal efficiency. Applications of these fluids used in cycles for heating and cooling introduced in previous chapters also confirm their promising potentials.

In the past decade, investigations of ILs for applications in absorption cycles were mainly based on thermodynamic analysis for screening suitable working fluids [36]. Recent studied refrigerants with ILs include water [38, 100], hydrofluorocarbon [61, 103], carbon dioxide [104] and ammonia [39, 40]. In these analyses, only thermodynamic properties, for instance the vapor-liquid equilibria, enthalpies and densities, are sufficient. Besides, limited experimental work to evaluate the practical performance on a systematic level was also reported [64–66].

Currently, the number of reported studies about the heat and mass transfer processes of IL-based fluids is limited. However these processes are important in sizing the systems in practice. Boman *et al.* [70] examined plenty of refrigerant/ILs fluids making use of a general heat transfer evaluation. Vertical, flat plate, falling-film heat exchangers were proposed to be used as the main heat and mass transfer components. Wang and Infante Ferreira [24] proposed using plate heat exchangers (PHXs) as absorber, generator, evaporator, condenser and solution heat exchanger in an NH_3/IL single-effect absorption heat pump, considering their compact sizes and superior performance of heat and mass transfer. Brief estimations of sizes and costs of the devices, and of charge of working fluids were carried out based on selected heat transfer correlations. For other application, Wadekar [69] simulated the heat transfer behavior of pure IL, [bmim][Tf_2N], as a heat transfer fluid in different heat exchangers including PHX.

Studies containing mass transfer for the ILs-based working fluids are even fewer. Meyer *et al.* [67, 168] made use of the analytical functions to describe the combined heat and mass transfer of working fluids ethanol/[emim][DEP] inside the absorber and generator, for which horizontal shell-and-tube heat exchangers were used. Because of the large areas required for the solution heat exchanger, a PHX was implemented. Besides, work on measuring absorption/desorption kinetics and key transport properties, such as mass diffusivity, was also reported for the application of absorption refrigeration cycles, for instance by Ariyadi and Coronas [68], Bedia *et al.* [169], Ariyadi *et al.* [170] and Chen *et al.* [171].

Previous work demonstrated that PHX can be a promising heat and mass exchanger in the IL-based absorption systems. A recent operation of absorption heat transformer using H_2O/[emim][OMs] fluids reported by Merkel *et al.* [66] brought this idea into practice. They implemented PHXs as evaporator, condenser and solution heat exchanger, a modified PHX with a liquid distributor was used as absorber. However, the heat and mass transfer performance of the IL-based working fluids inside plate heat exchangers was not studied in a detailed way.

On the other hand, plate heat exchangers have been frequently studied for NH_3 absorption systems. Kang *et al.* [172] compared the NH_3/H_2O absorption inside PHX with two different modes: falling film absorption and bubble absorption, with a control volume analysis. Cerezo *et al.* [173] reported an experimental study of an NH_3/H_2O bubble absorber using a PHX. A comparison with a numerical model was also presented in the work of Cerezo *et al.* [174]. Cerezo *et al.* [30] compared the performance of the bubble absorber using a PHX for the working fluids NH_3/H_2O, NH_3/$LiNO_3$ and NH_3/NaSCN with a similar numerical model previously introduced and concluded that the NH_3/$LiNO_3$'s high viscosity weakens its performance in the absorber. Experimental work was then carried out to compare the effect of adding H_2O into NH_3/$LiNO_3$ in a PHX used as a bubble absorber by Oronel *et al.* [175]. Recently Triché *et al.* [176] presented an experimental and numerical study of heat and mass transfer in a falling film absorber with the fluids NH_3/H_2O. Tao *et al.* [177] reviewed work on two-phase downward flow within PHX and proposed flow pattern maps. These maps are instructive to distinguish different mechanisms of NH_3 absorption or condensation in the PHX.

The literature review indicates that heat and mass transfer research regarding NH_3/IL working fluids has not been reported yet. In this chapter, a numerical study about heat and mass transfer during absorption of NH_3 into NH_3/IL solution will be carried out. A corrugated PHX is selected as the geometry of the absorber. The outline of this chapter is illustrated in Fig. 5.1.

A semi-empirical model is proposed to describe the heat and mass transfer performance of the vapor absorption inside PHX. The model is called "semi-empirical" because parts of it are based on frequently applied theories, such as the two-resistance theory with a gas-liquid interface; void-fraction for a prediction of the liquid film thickness; and Chilton-Colburn analogy to couple the heat

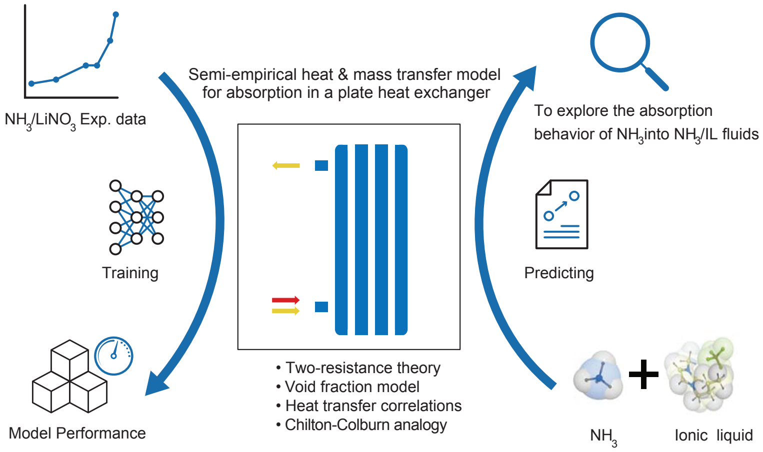

Figure 5.1: Outline of this chapter.

and mass transfer. On the other hand, undetermined parameters describing the heat and mass transfer characteristics are obtained from a similar experimental investigation - NH_3 absorption by $NH_3/LiNO_3$ fluids. Also, relevant thermodynamic and transport properties of the studied NH_3/IL fluids are modeled based on the collected experimental data. With these thermophysical properties, heat and mass transfer performances are investigated during NH_3 absorption by different NH_3/ILs fluids inside the PHX.

5.2. HEAT AND MASS TRANSFER FRAMEWORK FOR THE VAPOR ABSORBER

5.2.1. GENERAL DESCRIPTION

In the working fluid side of the PHX absorber, there are two different flow regimes considered in this study: the two-phase vapor-liquid flow and the single-phase subcooled liquid flow. The model of the subcooled single-phase flow (only heat transfer occurs) can be derived from the other one, thus here only the modeling of the two-phase vapor-liquid flow is introduced.

As shown in Fig. 5.2, taking advantage of the symmetry feature of the plate heat exchanger, only a plate with its surrounding two streams are studied in this model. Distribution of parameters is considered by numerically dividing the plate heat exchanger into small control volumes along the bulk streams (the length of the plates). The heat and mass transfer of the three flow streams, i.e., the cooling water, the solution and the NH_3 vapor, are studied in each control volume. Regarding the vapor absorption, the two-resistance theory with an interface is applied to describe the heat and mass transport between the vapor-liquid interface with its surroundings (the vapor and solution bulk streams, respectively). Heat and mass transfer fluxes are calculated using empirical correlations. This modeling method has been successfully adopted to investigate overall two-phase heat and mass transfer processes with complex geometrical structures in previously studies [174, 176, 178].

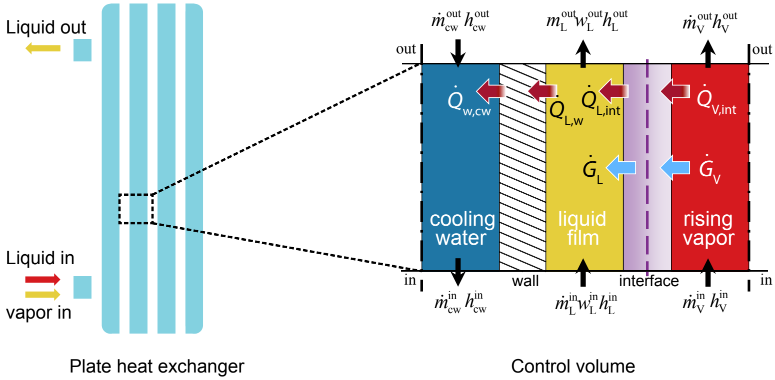

Figure 5.2: Schematic representation of the modeled absorber (left), and the split control volume (right). The corrugated surface of plates is not shown.

These general simplifications are adopted to develop the heat and mass transfer model of absorption:

- Absorption is assumed at a steady state.
- The liquid film is assumed to have a symmetrical thin feature contacting with plates.
- Interface is in equilibrium at saturated conditions.
- The distribution along the width of plates is taken as uniform.
- Properties and conditions at the inlet of a control volume are used to represent the local ones.
- Absorbents are regarded as non-volatile, thus no mass transfer of it occurs in the vapor phase.
- Thermal boundary layers between the two-phase and single-phase regions show a smooth transition.
- Heat conduction along the thickness of plates is negligible.
- Longitudinal conduction of plates and fluids are negligible.
- No heat loss to the environment.

The implementation of the calculation is shown in the Fig. 5.3. In this study, the calculation is carried out from the bottom of the plate heat exchanger to its top. Control volumes are discretized according to their lengths, which are identical in the current setting. For each control volume, conditions (flow, temperature, pressure and composition) in the bottom are taken as the input. Subroutines for obtaining other thermophysical properties, film thicknesses and dimensionless numbers are used before starting the conservation calculations. An iteration is carried out based on the heat and mass balances to obtain the interface temperature, T_{int}.

Calculated results are heat and mass transfer properties and the outlet parameters. The latter ones will be used as the input for the next control volume. For the studied cases, the number of the control volume is taken as 400 after a grid dependency evaluation.

5.2.2. FILM THICKNESS

Symmetrical thin films on plates can be used to represent the liquid flow of various flow patterns, such as film and slug flow, for vapor-liquid two phase flow in PHXs. In this chapter, the solution streams are also simplified as liquid films. The simplification is verified in the Section. 5.6.1.

The thickness of the liquid film is obtained with the help of the void-fraction. NH_3 vapor is assumed surrounded with liquid films between plates, as shown in Fig. 5.2. Void-fraction is applied to estimate the fraction of the channel cross-sectional area that is occupied by the gas phase. With it, the film thickness is expressed as,

$$\delta_{\mathrm{f}} = (1-\epsilon)\,\frac{L_{\mathrm{g}}}{2} \tag{5.1}$$

where, L_{g} is the gap between plates.

The void-fraction, ϵ, is obtained according to the frequently used Eq. 5.2, which has been proposed by Zivi [179] based on the principle of minimum entropy production for annular two-phase flow:

$$\frac{1}{\epsilon} = 1 + \left(\frac{1-q}{q}\right)\left(\frac{\rho_{\mathrm{V}}}{\rho_{\mathrm{L}}}\right)^{2/3} \tag{5.2}$$

One of the advantages of applying the void-fraction to predict the film thickness is that the thickness is related with the vapor quality (q), ensuring that the thickness turns to the gap dimension when vapor is fully absorbed.

5.2.3. PRESSURE DROP

The frictional pressure drop of a stream along a channel is estimated using Eq. 5.3:

$$\frac{\mathrm{d}P}{\mathrm{d}L} = \xi\,\frac{\rho \bar{v}^2}{2 d_{\mathrm{h}}} \tag{5.3}$$

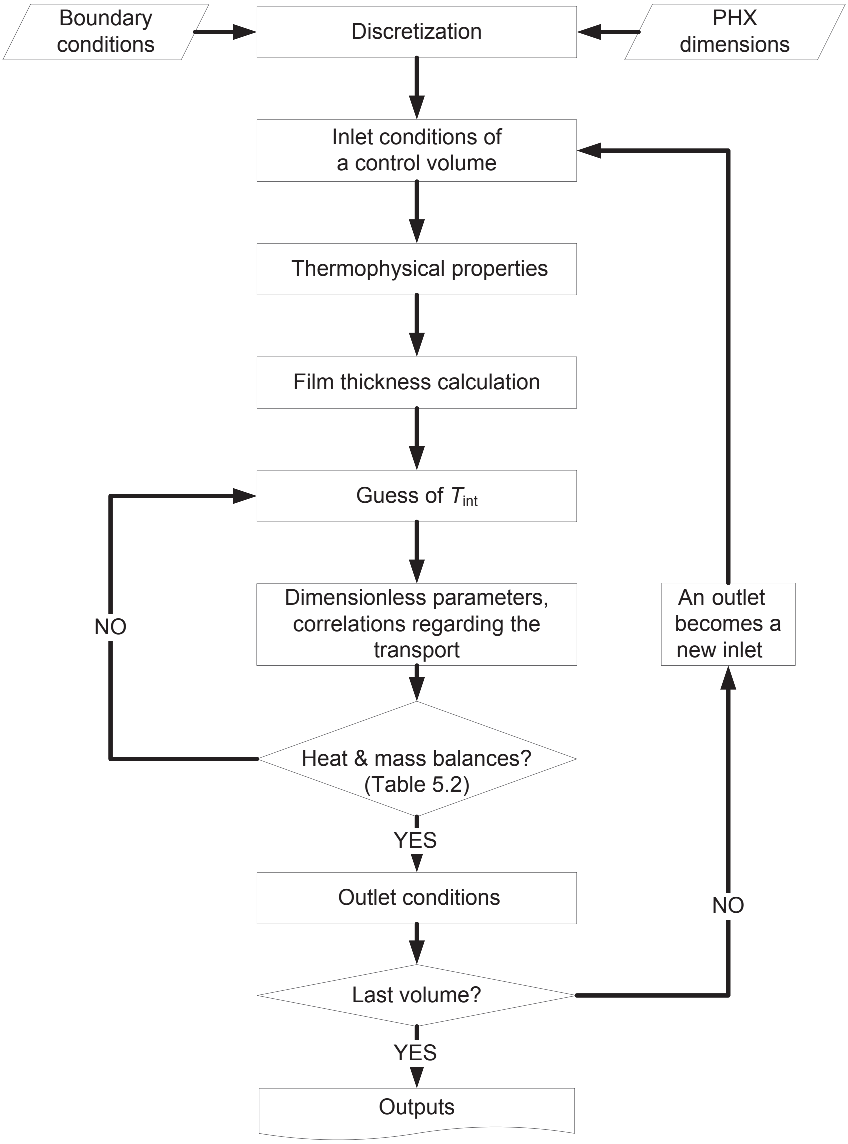

Figure 5.3: Calculation procedure of the model: A set of transport conservation equations are carried out in each discretized control volume. Sub-routines regarding the thermophysical properties, film thicknesses and dimensionless numbers are implemented. An iteration is carried out to obtain the interface temperature based on the heat and mass transport conservation equations. The outlet of each volume is used as the input to the next one.

where, $d_h = 2L_g$.

For the plate heat exchanger, the friction factor, ξ, is obtained from the experimental data of Amaris Castilla [180].

5.2.4. HEAT TRANSFER

The heat transfer characteristics of the two single-phase flows: cooling water, and NH_3 vapor (heat transfer to the interface), are described using correlations as summarized in Table 5.1.

Table 5.1: Correlations of heat transfers used in this study.

	Cooling water	Vapor with the interface
Correlation	$\mathrm{Nu} = 0.858\mathrm{Re}^{0.555}\mathrm{Pr}^{1/3}$	$\mathrm{Nu} = 8.23$
Source	Amaris Castilla [180]	Bergman *et al.* [181]

Characteristic lengths of dimensionless numbers are the hydraulic diameters for both cases.

Previous work conducted by peers distinguished the heat transfer between liquid film bulk and the wall with that between the interface and the film bulk [176, 182]. Analytic work by Grossman [183] and Brauner [184] also confirms the need of separately considering the two heat transfer layers within liquid films.

However, the thin feature of the film makes its heat transfer characteristic more difficult to describe than other streams. Additionally, the interface which is introduced for a convenience to study absorption problems does not naturally exist. The heat and mass transfer related to it cannot be practically detected. In this work, with the help of the proposed model, the Nusselt numbers of the liquid film, $\mathrm{Nu}_{\mathrm{L,w}}$ and $\mathrm{Nu}_{\mathrm{L,int}}$, will be determined using the experimental data by Amaris Castilla [180].

The heat transfer of the solution stream to the wall should smoothly go from the vapor-liquid two-phase region to the single-phase one. Considering this natural fact, the heat transfer of solution to the wall in the two-phase region and that in the single-phase region should have comparable characteristics. This is realized by assuming the heat transfer boundary layers share the same thicknesses in the two consecutive control volumes during the regime transition.

5.2.5. MASS TRANSFER

For the studied problem with absorption controlled by the liquid phase, the only mass transfer takes place from the interface to the solution bulk stream. The Chilton-Colburn analogy is applied to obtain the mass transfer coefficient between them, which is based on the boundary layers analogy.

The analogy is expressed simply for heat and mass transfer as,

$$\frac{\mathrm{Sh}}{\mathrm{Nu}_{\mathrm{L,int}}} \approx \left(\frac{\mathrm{Sc}}{\mathrm{Pr}}\right)^{1/3} \tag{5.4}$$

The characteristic lengths of the dimensionless numbers for the liquid film in the two-phase region are selected as the film thickness.

5.2.6. TRANSPORT CONSERVATION EQUATIONS

The heat and mass transport conservation equations of the liquid-vapor two-phase flow during absorption are listed in Table 5.2.

Table 5.2: Transport conservation equations describing the absorber section with two-phase flow.

	Equation
Energy balance of the cooling water stream	$\dot{Q}_{\mathrm{w,cw}} - \dot{m}_{\mathrm{cw}}^{\mathrm{in}} h_{\mathrm{cw}}^{\mathrm{in}} + \dot{m}_{\mathrm{cw}}^{\mathrm{in}} h_{\mathrm{cw}}^{\mathrm{out}} = 0$
Energy balance of the solution stream	$\dot{G}_{\mathrm{int}} \hat{h}_{\mathrm{L}} + \dot{Q}_{\mathrm{int,L}} - \dot{Q}_{\mathrm{L,w}} + \dot{m}_{\mathrm{L}}^{\mathrm{in}} h_{\mathrm{L}}^{\mathrm{in}} - \dot{m}_{\mathrm{L}}^{\mathrm{out}} h_{\mathrm{L}}^{\mathrm{out}} = 0$
Energy balance of the vapor stream	$-\dot{G}_{\mathrm{int}} \hat{h}_{\mathrm{V}} - \dot{Q}_{\mathrm{V,int}} + \dot{m}_{\mathrm{V}}^{\mathrm{in}} h_{\mathrm{V}}^{\mathrm{in}} - \dot{m}_{\mathrm{V}}^{\mathrm{out}} h_{\mathrm{V}}^{\mathrm{out}} = 0$
Energy balance through the wall	$\dot{Q}_{\mathrm{L,w}} = \dot{Q}_{\mathrm{w,cw}}$ $\dot{Q}_{\mathrm{w,cw}} = \bar{\alpha}_{\mathrm{w,cw}} \left(T_{\mathrm{w}} - T_{\mathrm{cw}}^{\mathrm{in}}\right) A_{\mathrm{int}}$ $\dot{Q}_{\mathrm{L,w}} = \bar{\alpha}_{\mathrm{L,w}} \left(T_{\mathrm{L}}^{\mathrm{in}} - T_{\mathrm{w}}\right) A_{\mathrm{int}}$
Energy balance through the interface	$\dot{G}_{\mathrm{int}} A_{\mathrm{int}} \hat{h}_{\mathrm{V}} + \dot{Q}_{\mathrm{V,int}} = \dot{G}_{\mathrm{int}} A_{\mathrm{int}} \hat{h}_{\mathrm{L}} + \dot{Q}_{\mathrm{int,L}}$ $\dot{Q}_{\mathrm{int,L}} = \bar{\alpha}_{\mathrm{int,L}} \left(T_{\mathrm{int}} - T_{\mathrm{L}}^{\mathrm{in}}\right) A_{\mathrm{int}}$ $\dot{Q}_{\mathrm{int,V}} = \bar{\alpha}_{\mathrm{int,V}} \left(T_{\mathrm{V}}^{\mathrm{in}} - T_{\mathrm{int}}\right) A_{\mathrm{int}}$
Mass balance of the solution stream	$\dot{G}_{\mathrm{int}} A_{\mathrm{int}} + \dot{m}_{\mathrm{L}}^{\mathrm{in}} - \dot{m}_{\mathrm{L}}^{\mathrm{out}} = 0$ $\dot{G}_{\mathrm{int}} = M_{\mathrm{w}} \beta (c_{\mathrm{int}} - c_{\mathrm{L}})$
Mass balance of the vapor stream	$-\dot{G}_{\mathrm{int}} A_{\mathrm{int}} + \dot{m}_{\mathrm{V}}^{\mathrm{in}} - \dot{m}_{\mathrm{V}}^{\mathrm{out}} = 0$
NH_3 species balance in the liquid stream	$\dot{G}_{\mathrm{int}} A_{\mathrm{int}} + \dot{m}_{\mathrm{L}}^{\mathrm{in}} w^{\mathrm{in}} - \dot{m}_{\mathrm{L}}^{\mathrm{out}} w^{\mathrm{out}} = 0$

Regarding these equations, parameters with superscripts are inputs or outputs of a calculation: “in” denotes the input in the bottom of a control volume, and “out” denotes the output on top.

The amount of unknown parameters and that of the equations equals with each other, indicating the problem is solvable. For an easy solving, an iteration of the unknown interface temperature, T_{int}, is conducted until the assumed value guarantees that the heat and mass balances of the control volume are satisfied.

5.3. PARAMETERS DETERMINATION AND MODEL PERFORMANCE

Amaris Castilla [180] experimentally investigated the absorption of NH_3 in an $NH_3/LiNO_3$ solution inside a plate heat exchanger. The working fluids flow from the bottom of the PHX to its top in a counter-current direction with the cooling water stream, which is identical with the studied problem. The geometrical parameters of the tested PHX are listed in Table 5.3.

Table 5.3: The geometrical parameters of the studied PHX.

Length	[m]	0.53
Width	[m]	0.112
Amount of channels	[-]	3
Space between plates	[m]	0.002
Total heat transfer area	[m^2]	0.1

The required properties of fluid $NH_3/LiNO_3$, are listed in Table 5.4 with their sources.

Table 5.4: Thermo-physical properties of $NH_3/LiNO_3$ studied in this work.

	Property	Source
ρ	Density	Infante Ferreira [25]
P-T-w	Vapor-liquid equilibrium	Libotean *et al.* [185]
c_p	Heat capacity	Infante Ferreira [25]
h	Enthalpy	Infante Ferreira [25]
μ	Viscosity	Libotean *et al.* [186]
λ	Thermal conductivity	Cuenca *et al.* [187]
D	Mass diffusivity	Venegas *et al.* [188]
σ	Surface tension	Venegas *et al.* [188]

5.3.1. PARAMETERS DETERMINATION

In the proposed framework described in Section 5.2, determination of the performance of the absorber requires the friction factors and heat and mass transfer coefficients for the liquid film. 14 sets of experimental data at different solution flow conditions, as shown in Table 5.5, are used to obtain the unknown parameters in the proposed heat and mass transfer framework: Nu numbers of the liquid film and the frictional factor. Correlations of these parameters with solution flows are also presented.

Firstly, to obtain the friction factor, ξ, data of inlet and outlet pressures in the working fluids side are used with Eq. 5.3. The values of ξ from 14 independent cases present a relation to the solution Re_L at the entrance, which is based on the hydraulic diameter of the PHX (d_h), as shown in Fig. 5.4.

Table 5.5: Experimental data used to obtain unknown parameters in the proposed heat and mass transfer framework and the performance of parameters determination.

Case	$\dot{m}_{\mathrm{L}}^{\mathrm{in}}$	$T_{\mathrm{L}}^{\mathrm{in}}$	$w_{\mathrm{L}}^{\mathrm{in}}$	$\dot{m}_{\mathrm{V}}^{\mathrm{in}}$	$P_{\mathrm{L}}^{\mathrm{in}}$	$P_{\mathrm{L}}^{\mathrm{out}}$	$\dot{m}_{\mathrm{cw}}^{\mathrm{in}}$	$T_{\mathrm{cw}}^{\mathrm{in}}$	$\dot{Q}/A$ [kW/m^2]			U [W/(m^2·K)]		
	[kg/h]	[°C]	[-]	[kg/h]	[kPa]	[kPa]	[kg/h]	[°C]	EXP	SIM	RD[-]	EXP	SIM	RD [-]
1	10.39	44.93	0.4524	1.56	521.24	516.06	271.54	37.48	4.84	4.82	-0.003	1512.1	1504.7	-0.005
2	15.38	45.70	0.4500	1.88	513.86	507.94	270.66	38.23	6.97	7.00	0.004	1585.3	1606.9	0.014
3	20.45	45.63	0.4538	1.93	516.14	509.3	264.19	38.14	8.12	8.13	0.002	1800.4	1803.9	0.002
4	25.34	45.69	0.4497	2.20	510.34	502.24	267.19	38.63	9.69	9.49	-0.020	1867.9	1896.1	0.015
5	40.24	44.71	0.4528	2.80	517.38	505.08	275.38	38.80	12.18	12.19	0.001	2242.4	2383.1	0.063
6	30.88	45.64	0.4526	2.09	519.63	510.55	266.64	38.98	10.47	9.55	-0.088	2042.0	2303.2	0.128
7	50.01	46.15	0.4533	2.54	509.85	495.5	266.13	39.61	13.08	12.27	-0.062	2246.4	2471.9	0.100
8	10.57	45.39	0.4519	1.34	521.39	516.67	266.62	41.46	3.38	3.38	0.000	1531.9	1532.0	0.000
9	15.33	45.39	0.4530	1.01	514.77	509.4	268.39	41.73	4.34	4.03	-0.072	1772.2	1724.3	-0.027
10	20.55	45.85	0.4528	1.25	515.8	509.62	267.93	41.92	5.3	5.12	-0.035	1846.8	1871.9	0.014
11	25.33	46.10	0.4523	1.52	518.95	511.82	267.62	42.18	6.08	6.07	-0.001	1977.7	1991.9	0.007
12	30.25	45.00	0.4527	1.65	518.21	509.97	267.09	42.25	6.25	6.25	0.000	2406.5	2566.7	0.067
13	48.85	45.87	0.4518	1.45	513.26	501.43	269.16	43.23	7.56	6.57	-0.131	2707.6	3182.8	0.176
14	40.59	45.32	0.4496	1.74	515.08	504.69	269.02	42.68	7.08	7.09	0.001	2535.7	2545.0	0.004

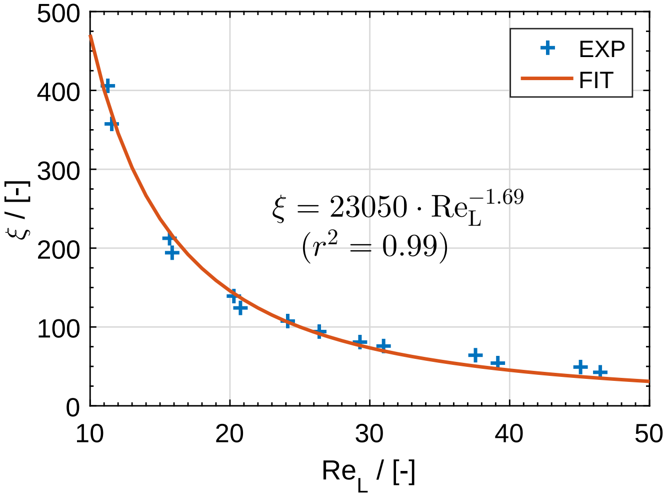

Figure 5.4: Values of frictional factor, ξ, of the experimental cases with their correlations to $\mathrm{Re_L}$.

The inlet conditions of solution, vapor and cooling water streams are used as inputs in the proposed heat and mass transfer model. Since the cooling water enters at the top of the absorber, the outlet temperature needs to be iterated. With the heat transfer area specified, the heat duty and temperature distributions are the calculation results.

To find the suitable $\mathrm{Nu_{L,w}}$ and $\mathrm{Nu_{L,int}}$ to be used in the model to describe the absorption problem, optimizations are carried out based on the 14 experimental cases.

For each experiment from Amaris Castilla [180], an optimization work is conducted in which the two Nu numbers have been optimized. The objective function of the optimization is the minimization of the following function,

$$F = \sqrt{\left[\frac{(\dot{Q}/A)_\mathrm{exp} - (\dot{Q}/A)_\mathrm{sim}}{(\dot{Q}/A)_\mathrm{exp}}\right]^2} + \sqrt{\left[\frac{(U)_\mathrm{exp} - (U)_\mathrm{sim}}{(U)_\mathrm{exp}}\right]^2} \tag{5.5}$$

Beside using heat flux, $\dot{Q}/A$, as an indication to ensure the energy balance, the overall heat transfer coefficient, U, is applied to take into account the heat transfer performance. Both the mean square deviations of them have been considered so that the effect of different temperature driving forces is taken into account. For each experiment, implementation in the model of the obtained Nu numbers resulted in an accurate prediction of the system performance.

The optimization and correlation procedures are illustrated in Fig. 5.5.

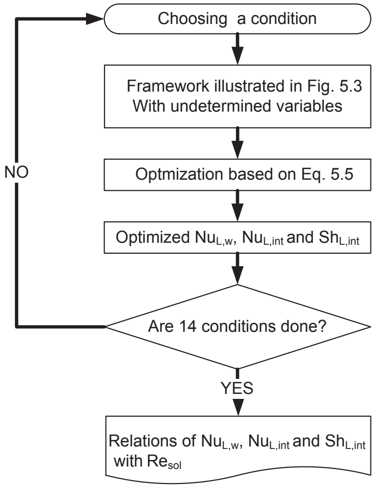

Figure 5.5: Steps to determine unknown heat and mass transfer characteristics and their relations with flow rates.

The values of $\mathrm{Nu}_{\mathrm{L,w}}$ and $\mathrm{Nu}_{\mathrm{L,int}}$ from the 14 independent optimizations are presented in Table 5.6 and Fig. 5.6. The comparison of optimized results of $\dot{Q}/A$ and U with the experimental ones is listed in Table 5.5. The deviations are acceptable at an overall device level.

As shown in Fig 5.6, the values of optimized $\mathrm{Nu}_{\mathrm{L,w}}$ and $\mathrm{Nu}_{\mathrm{L,int}}$ show clear relations with the liquid Reynolds number. By correlating these data to a frequently used form of $\mathrm{Nu} = a\mathrm{Re}^b\mathrm{Pr}^{1/3}$, coefficients can be determined, as shown in Fig. 5.6.

To confirm the validity of the correlations, the additional 16 independent experiments also reported by Amaris Castilla [180], which were not used in the generation of the correlations, are used to check the reliability of obtained Nu numbers. The relative deviations between experimental and simulation results for $\dot{Q}/A$ and U are 5.6% and 1.8% in average. Conditions of these experiments and comparisons of experimental and predicted values are listed in a table provided in Appendix E.

The heat transfer boundary layers can be estimated using $\frac{\delta_\mathrm{f}}{\mathrm{Nu}_\mathrm{L}}$ (Note that the film thickness is used as the characteristic length for the heat and mass transfer of the liquid film). The obtained Nusselt numbers in this work provide a relation: $\frac{\delta_\mathrm{f}}{\mathrm{Nu}_{\mathrm{L,w}}} + \frac{\delta_\mathrm{f}}{\mathrm{Nu}_{\mathrm{L,int}}} < \delta_\mathrm{f}$. It reflects the heat transfer on the liquid film is not only dominated by conduction within a heat transfer boundary layer. The additional convection effects on the heat transfer can be enhanced by the corrugated plates surface and the coupled mass transfer.

Table 5.6: Determined Nusselt numbers of liquid film from experimental data.

Case	Re_L^{in}	$\mathrm{Nu}_{L,w}$	$\mathrm{Nu}_{L,int}$
1	11.27	2.49	17.60
2	15.72	2.25	46.25
3	20.33	3.65	50.20
4	24.13	3.41	67.08
5	37.60	4.53	85.95
6	29.29	4.94	55.64
7	45.05	5.32	93.50
8	11.58	1.61	17.82
9	15.89	3.38	35.06
10	20.75	3.97	43.27
11	26.35	3.90	52.62
12	31.03	4.86	47.30
13	46.48	5.87	78.06
14	39.17	4.42	70.93

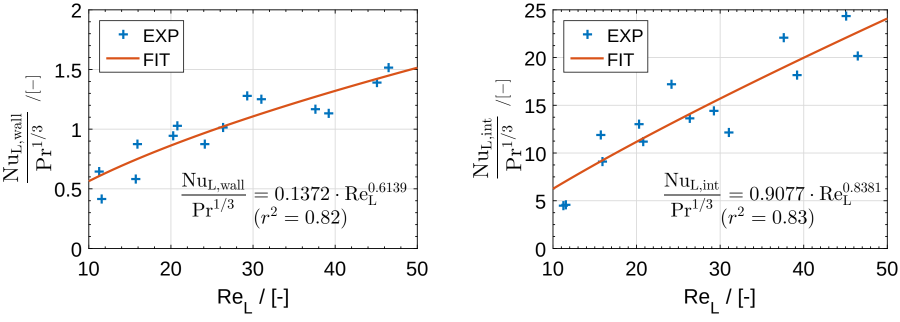

(a) (b)

Figure 5.6: Results of the independently optimized Nusselt numbers of the solution film with their correlations to the solution Reynolds numbers. (a) Nusselt numbers of the solution film to the wall; (b) Nusselt numbers of the solution film to the interface.

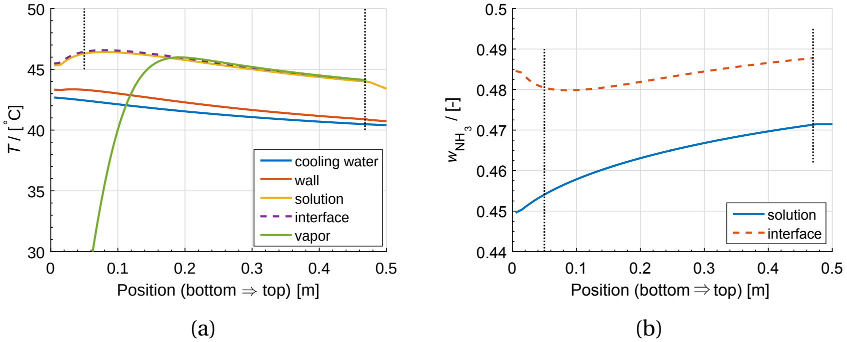

(a) (b)

Figure 5.7: Distributions of (a) temperature, and (b) NH_3 mass fraction of the experimental absorption Case 14 (Table 5.5).

5.3.2. MODEL PERFORMANCE

The proposed model is capable of capturing variable distributions, for instance for temperatures and NH_3 mass fractions as shown in Fig 5.7, for a typical absorption case.

For the working fluids side, temperature of NH_3 vapor increases rapidly at the beginning of the absorption. Then it reaches a peak which is at a comparable level with the local temperature of the solution, and drops until it is completely absorbed.

The curve of solution temperature shows a trend with three obvious sections. It firstly raises at the entrance of the absorber, and then decreases moderately until the vapor absorption completes. After that, the temperature drops more rapidly. For convenience, as divided by the vertical dashed lines, the three sections are named as entrance of absorption, absorption and non-absorption regions.

The temperature of interface is close to that of the liquid, since the heat resistance between interface and liquid film is small. On the other hand, the NH_3 fraction difference between them is larger at the entrance. It drives a high rate of NH_3 mass transfer from the interface to the liquid. The large transfer of mass also leads to the release of a large amount of absorption heat, which in turn increases the liquid temperature. An increase of interface temperature causes the equilibrium fraction of NH_3 to drop, leading to a reduction of the absorption rate. In the no-absorption region, since no absorption heat is released, the solution temperature drops sharply.

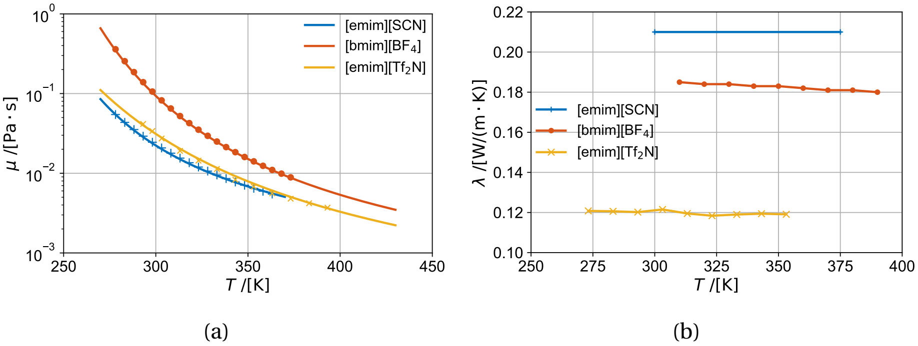

Figure 5.8: Experimental data and trends (Table 5.7) of (a) viscosities [116, 117, 152] and (b) thermal conductivities [124, 189, 190] of the three studied ILs.

5.4. THERMOPHYSICAL PROPERTIES OF STUDIED AMMONIA / IONIC LIQUIDS FLUIDS

The properties of pure ammonia are from NIST database refprop 9.1 [99].

The three ionic liquids under consideration for the ammonia absorption are the ones investigated in Chapter 4. Vapor-liquid equilibrium (VLE) properties, densities, heat capacities and enthalpies of the studied ILs and their NH_3 mixtures, and the relevant modeling methods have been reported in previous chapters. In this section, only the relevant transport properties of the studied working fluids are introduced, for length and simplicity reasons.

For the pure ILs, the correlations for their relevant experimental properties are summarized in Fig. 5.8 and Table 5.7.

5.4.1. VISCOSITY

High viscosity is always mentioned as the main weakness which prevents applications of the ILs in absorption systems. Viscosity data of pure [emim][SCN] [152], [bmim][BF$_4$] [116] and [emim][Tf$_2$N] [117] are plotted in Fig. 5.8(a).

Three-parameter Vogel equations are used to correlate these viscosity data, which are shown in Table 5.7. The viscosity of [bmim][BF$_4$] is higher than the one of the other two ILs. This will lead to a negative influence on its heat transfer performance.

Previously reported viscosity data of NH_3/IL solutions measured by Cera-Manjarres [45] indicate that adding NH_3 reduces the viscosity of the mixture. Even though viscosities of solutions containing NH_3 and the considered three ILs have not been reported yet, Eq. 5.6 is used in this study. The excess term is neglected here, which has been discussed in literature, for instance in the work

Table 5.7: Molecular weights and correlations of relevant thermo-physical properties for the three investigated ILs*.

	[emim][SCN]	[bmim][BF_4]	[emim][Tf_2N]
M_w [kg/kmol]	169.25	226.02	391.31
μ [Pa·s]	$\ln\mu = -7.839 + \frac{486}{T-179.6}$	$\ln\mu = -8.99 + \frac{871.1}{T-168.4}$	$\ln\mu = -9.717 + \frac{1111}{T-122.2}$
λ [W/(m·K)]	0.21	0.183	0.12
σ [N/m]	$\sigma = 7.926 \times 10^{-2} - 8.709 \times 10^{-5} \times T$	$\sigma = 6.031 \times 10^{-2} - 5.639 \times 10^{-5} \times T$	$\sigma = 5.114 \times 10^{-2} - 5.145 \times 10^{-5} \times T$
D_{NH_3} [m^2/s]	-	$D_{NH_3} = -1.502 \times 10^{-8} + 5.2 \times 10^{-11} \times T$	-

* T in K.

of Gao and Wagner [191].

$$\ln \mu_{\mathrm{is}} = x_{\mathrm{A}} \ln \mu_{\mathrm{A}} + x_{\mathrm{B}} \ln \mu_{\mathrm{B}} \tag{5.6}$$

The deviation of solution viscosities predicted with Eq. 5.6 in relation to their real values has also been checked using the reported viscosities of 6 NH_3/IL mixtures by Cera-Manjarres [45], as listed in Table 5.8. Neglecting the excess viscosity term may introduce at worst over -90% deviations (which are underestimated of real values), nevertheless it is still the best one compared with other weight-average methods (mass fraction based, or absolute viscosity based).

Table 5.8: Deviations of the predicted values of viscosities (by using Eq. 5.6) from the real values using the data reported by Cera-Manjarres [45].

Working fluids*	ARD	max RD
NH_3/[N112(2OH)][TfO]	-0.450	-0.871
NH_3/[N112(2OH)][NTf_2]	-0.547	-0.917
NH_3/[N111(2OH)][NTf_2]	-0.556	-0.904
NH_3/[N1113][NTf_2]	-0.503	-0.901
NH_3/[EtOHmim][BF_4]	-0.582	-0.964
NH_3/[EtOHmim][NTf_2]	-0.560	-0.917

* Nomenclature of ILs is according to the original work of Cera-Manjarres [45].

5.4.2. THERMAL CONDUCTIVITY

Reported thermal conductivities of pure [emim][SCN] [124], [bmim][BF_4] [189] and [emim][Tf_2N] [190] all indicate almost constant trends in the relevant temperature range as 0.21, 0.183 and 0.12 W/(m·K), respectively (Fig. 5.8(b)). The thermal conductivities of [emim][SCN] and [bmim][BF_4] are significantly larger than the one of [emim][Tf_2N]. No data for the thermal conductivity of the 3 ILs mixed with NH_3 solutions have been reported in literature. Eq. 5.7, which is based on weighted average of properties from both components with weights of their mass concentrations, is applied for solutions' thermal conductivities.

$$M_{\mathrm{sol}} = w_{\mathrm{A}} M_{\mathrm{A}} + w_{\mathrm{B}} M_{\mathrm{B}} \tag{5.7}$$

5.4.3. SURFACE TENSION

Surface tensions of pure [emim][SCN], [bmim][BF_4] and [emim][Tf_2N], have been reported respectively by Almeida *et al.* [192], Ghatee and Zolghadr [193] and Tariq *et al.* [153]. They show linear trends with the temperature change. For the NH_3/IL mixtures, its values are estimated using the weight-averaged value based on the pure components (Eq. 5.7).

5.4.4. MASS DIFFUSIVITY

Effective mass diffusivities of NH_3 in [bmim][BF_4] have been reported by Bedia *et al.* [169] for 3 temperature levels. The values of NH_3 in [emim][Tf_2N] have been reported by Ariyadi *et al.* [170] for 3 pressure levels at 30 °C.

As a new proposed working fluid for the absorption cycle, the mass diffusivity of NH_3 in [emim][SCN] has not been reported yet. Nevertheless the relation of it with the viscosity can be used for an estimation.

Stokes-Einstein equation provides a relation of the mass diffusivity of a solute A into a stationary component B with the viscosity of component B, which is based on the Nernst-Einstein relation and Stokes' law [194]:

$$\frac{D_{\mathrm{AB}}\mu_{\mathrm{B}}}{\kappa T} = \frac{1}{4\pi \bar{R}_{\mathrm{A}}} \tag{5.8}$$

where κ is the Boltzmann constant and $\bar{R}_{\mathrm{A}}$ is the radius of the spherical particle A.

The underlying theory of Stokes-Einstein equation has been developed to a number of empirical correlations, which permit an estimation of diffusivities in terms of more easily measured properties such as viscosity and molar volume. For instance for the IL-based fluids, Morgan *et al.* [195] proposed correlations for different pure vapor components in imidazolium-based ILs with a different exponent of the viscosity of ILs ($D_{\mathrm{V,IL}} \propto \mu_{\mathrm{IL}}^{-0.6}$). However, these authors did not include NH_3.

In this work, a different dependence is found using the limited mass diffusivity data of NH_3 in ILs reported in the work of Bedia *et al.* [169] and Ariyadi *et al.* [170], with the available viscosity data from Cera-Manjarres [45], Salgado *et al.* [116] and Hofmann *et al.* [117], for the cases of NH_3 absorption.

The mass diffusivity data of NH_3 with different imidazolium-based ILs are shown in Fig. 5.9. Data in Fig. 5.9(a) were measured at different temperature levels, while data in Fig. 5.9(b) show mass diffusivities at different pressure levels at 30 °C.

As shown in Fig. 5.9, the mass diffusivity of NH_3 in ILs as a function of the viscosity of ILs presents a slope of -1.45 in loglog diagrams. Therefore, with a known NH_3 mass diffusivity and viscosities of a known IL, the trend can be applied to estimate NH_3 mass diffusivity in the other IL via,

$$D_{\mathrm{NH_3,ILB}} = \left(\frac{\mu_{\mathrm{ILB}}}{\mu_{\mathrm{ILA}}}\right)^{-1.45} \cdot D_{\mathrm{NH_3,ILA}} \tag{5.9}$$

The averaged relative deviations of correlations for the current data are 41.76% and 38.99%, respectively for cases in Fig. 5.9(a) and 5.9(b). Nevertheless, the cor-

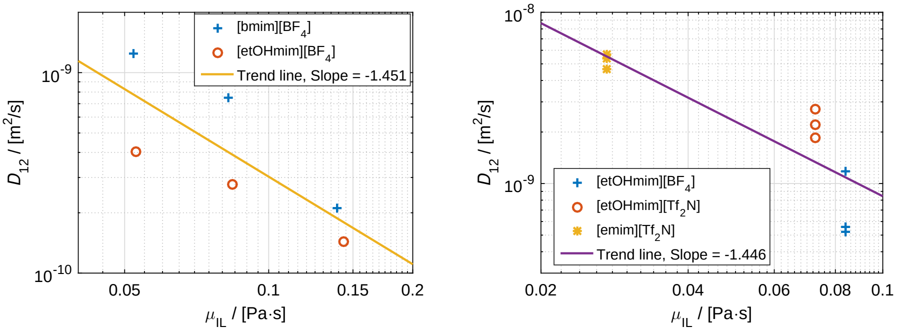

(a) (b)

Figure 5.9: The relations of effective mass diffusivities of NH_3 in ILs with respect to viscosities of corresponding pure ILs. (a) Effective mass diffusivities at different temperature levels reported by Bedia *et al.* [169] (ARD of 41.76%); (b) Effective mass diffusivities at different pressure levels reported by Ariyadi *et al.* [170] (ARD of 38.99%). The information about the ILs shown can be found in the original studies.

relation is simple and clear. The only unknown mass diffusivity is for [emim][SCN] and is obtained using Eq. 5.9.

5.5. PREDICTION USING THE MODEL FOR AMMONIA/IONIC LIQUID ABSORPTION IN PHX

The exploration of heat and mass transfer performance of NH_3/ILs absorption is based on the application of NH_3 absorption heat pumps in an operation condition of $T_{\mathrm{gen}}/T_{\mathrm{con}}/T_{\mathrm{abs}}/T_{\mathrm{eva}}$ = 120/45/45/10 °C as indicated in Chapter 3. Some conditional parameters in the working fluid side have already been determined referring to the thermodynamic analysis, such as the circulation ratio (corresponds to the term, $\dot{m}_{\mathrm{L}}^{\mathrm{in}}/\dot{m}_{\mathrm{V}}^{\mathrm{in}}+1$), the mass fraction and the temperature at the solution inlet, $w_{\mathrm{L}}^{\mathrm{in}}$, $T_{\mathrm{L}}^{\mathrm{in}}$, the solution outlet temperature, $T_{\mathrm{L}}^{\mathrm{out}}$, and the vapor inlet temperature, $T_{\mathrm{V}}^{\mathrm{in}}$. They are part of boundary conditions in the following discussion. Their values for the three studied NH_3/IL working fluids are listed in Table 5.9.

The heat and mass transfer performance of $NH_3/LiNO_3$ for an absorption heat pump application is also calculated for reference purposes. Following the same method introduced in Chapter 3, the circulation ratio and coefficient of performance (for heating) of the $NH_3/LiNO_3$ fluid in absorption heat pumps are found to be 4.64 and 1.63, respectively, at the same operating conditions. The boundary conditions of these fluids are listed in Table 5.9 as well.

The geometrical parameters of the PHX are the same as the ones listed in

Table 5.9: Determined boundary conditions in the NH_3/IL working fluids side of the absorber, for an absorption heat pump application*.

Working fluid	$\dot{m}_L^{in}/\dot{m}_V^{in}$ [-]	w_L^{in} [kg/kg]	T_L^{in} [°C]	T_V^{in} [°C]
NH_3/[bmim][BF_4]	29.09	0.030	56	10
NH_3/[emim][SCN]	34.34	0.059	56	10
NH_3/[emim][Tf_2N]	55.92	0.031	56	10
NH_3/$LiNO_3$	3.64	0.374	56	10

* Boundary conditions are determined based on a heat pump cycle with operation conditions of $T_{gen}/T_{con}/T_{abs}/T_{eva}$ = 120/45/45/10 °C. The method can be referred to Chapter 3. VLE properties of the IL-based fluids can be found in Appendix D. It is assumed that the temperature pinch of the solution heat exchanger is 11 K, which is related to the solution inlet condition. The subcooling degrees at the solution inlet are 8.5, 2.8, 1.4 and 25.3 K for the four fluids. The coefficient of performance (for heating) of absorption heat pumps with these fluids are estimated as around 1.6.

Table 5.3. For an easy comparison, the vapor flow and cooling water inlet conditions are kept the same for all cases, which are $\dot{m}_V = 3.89\times10^{-4}$ kg/s, $T_{cw}^{in} = 40$ °C and $\dot{m}_{cw} = 1.41\times10^{-2}$ kg/s.

5.5.1. DISTRIBUTIONS OF PARAMETERS

Temperature distributions during absorption of the studied cases are provided in Fig. 5.10.

As shown in Fig. 5.10, the temperature distributions along PHXs of two studied ILs cases share similar trend with that found in the experimental cases, except for the case with [bmim][BF_4], see Fig. 5.7. Three sections are also clearly detected for the temperature distribution of the solution streams. For the reference case (Fig. 5.10(d)), the absorption is not finished, thus the single-phase convection region is not there. Compared with the ILs cases, the reference case shows a less rapid increasing of vapor temperature. The temperature rise of the solution stream is more obvious at the entrance.

Changes of NH_3 mass fraction in the interface and bulk solution for the 3 studied ILs cases along with the reference case are illustrated in Fig 5.11.

The levels of interface NH_3 fractions reflect the ILs' solubilities of NH_3. The case with NH_3/[emim][SCN] shows the highest level of NH_3 solubility among the three ILs cases, as expected in previous discussions. The fraction differences between the interface and the bulk solution are related to the mass transfer potentials during NH_3 absorption. As indicated, the fluid NH_3/[emim][Tf_2N] provides the least difference and NH_3/[bmim][BF_4] shows a quite large one. Compared with the ILs cases, the NH_3/$LiNO_3$ case has the highest level of NH_3 fractions.

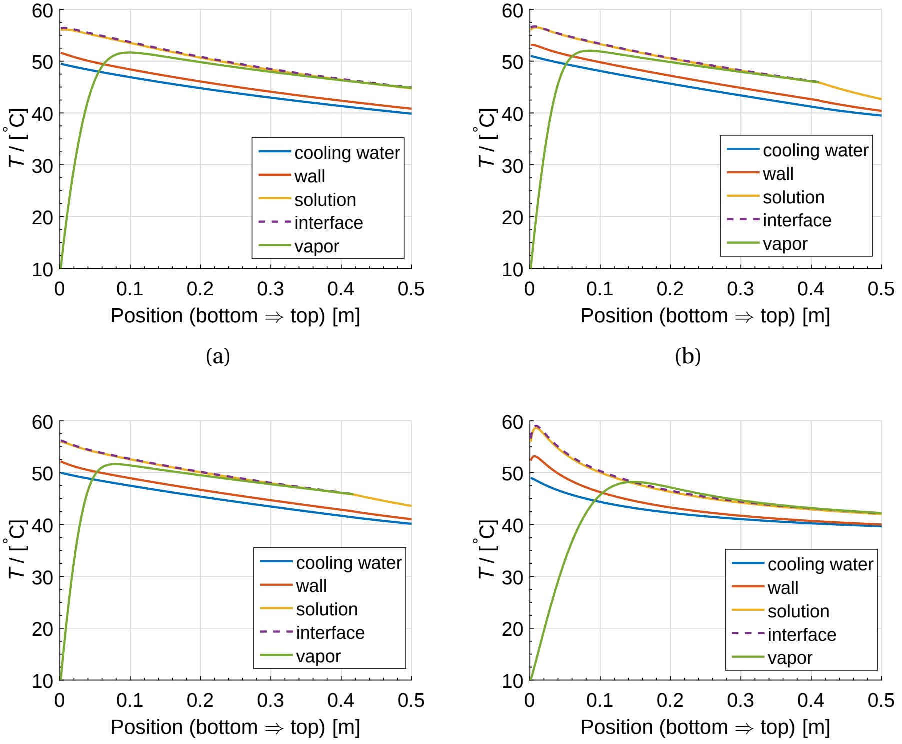

(a) (b)

(c) (d)

Figure 5.10: Temperatures distributions of the studied absorption cases: (a) NH_3/[bmim][BF_4] case, (b) NH_3/[emim][SCN] case, (c) NH_3/[emim][Tf_2N] case, and (d) NH_3/$LiNO_3$ case.

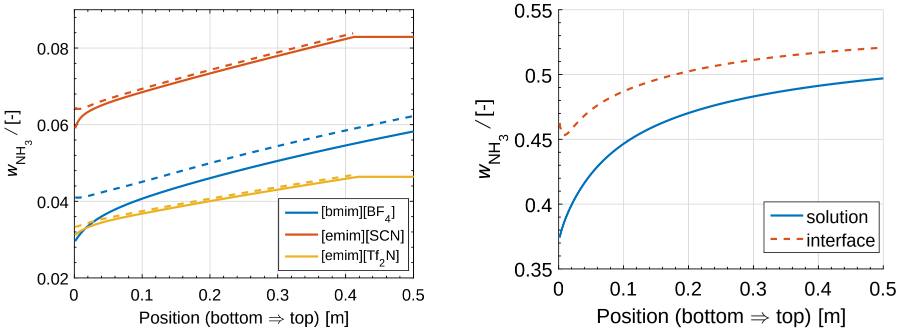

(a) (b)

Figure 5.11: NH_3 mass fraction distributions of the studied absorption cases: (a) NH_3/ILs cases (dashed curves: interface properties), (b) NH_3/$LiNO_3$ case.

Because it has a lower solution flow, the increase of NH_3 fraction in solution of the $NH_3/LiNO_3$ case is also larger than that of the NH_3/ILs cases.

5.5.2. OVERALL PERFORMANCE

Parameters concerning the heat transfer, mass transfer and pressure drop are summarized to evaluate the overall performance of the studied fluids in the PHX absorber.

The term $\dot{Q}/A$ is the heat transfer flux across the plate. Using the logarithmic mean temperature difference, $LMTD$, defined in Eq. 5.10, the overall heat transfer coefficient, U, can be obtained to evaluate the heat transfer performance of different fluids in the studied PHX.

$$LMTD = \frac{(T_{\text{L,out}} - T_{\text{cw,in}}) - (T_{\text{L,in}} - T_{\text{cw,out}})}{\ln\left[(T_{\text{L,out}} - T_{\text{cw,in}})/(T_{\text{L,in}} - T_{\text{cw,out}})\right]} \tag{5.10}$$

$$U = \frac{\dot{Q}/A}{LMTD} \tag{5.11}$$

However, an application of the $LMTD$, which is only making use of the temperature values in the inlet and outlet of the solution and cooling water streams, may neglect the influence of obvious segments of temperature change, for instance the solution temperature change in this study. Considering it, an integrated averaged temperature difference between the solution and cooling water streams in each control volume, ΔT_{ave}, is used as an alternative to evaluate the overall temperature difference, as defined in Eq. 5.12. The corresponding overall heat transfer coefficient, U', as provided in Eq. 5.13 is considered as well.

$$\Delta T_{\text{ave}} = \frac{1}{L}\int \Delta T \cdot dL \tag{5.12}$$

$$U' = \frac{\dot{Q}/A}{\Delta T_{\text{ave}}} \tag{5.13}$$

As for the mass transfer, the term, A_{mt}/A, quantifies the ratio of the effective mass transfer area to the total one. $\dot{G}$ provides the mass flux in the quantified mass transfer area. Subcooling degree of the solution at the outlet, defined as Eq. 5.14, indicates the mass transfer potential for the solution stream at the outlet.

$$\Delta T_{\text{L,out}}^{\text{sub}} = T_{\text{L}}^{\text{sat}}(P_{\text{out},\text{w}_{\text{out}}}) - T_{\text{L,out}} \tag{5.14}$$

Results of these parameters are obtained and listed in Table 5.10.

To achieve the same amount of NH_3 absorption with the same cooling medium, the studied cases show more or less similar heat transfer fluxes, $\dot{Q}/A$, which

Table 5.10: Comparison of results on heat transfer, mass transfer and pressure drop of the studied four working fluids in the PHX absorber, in the operating condition of $T_{cw}^{in} = 40$ °C, $\dot{m}_{cw} = 1.41\times10^{-2}$ kg/s, and $\dot{m}_V = 3.89\times10^{-4}$ kg/s.

absorbent		[bmim][BF_4]	[emim][SCN]	[emim][Tf_2N]	$LiNO_3$
$\dot{Q}/A$	[kW/(m^2)]	5.65	6.74	5.77	5.45
$LMTD$	[K]	5.78	4.34	4.61	4.26
U	[W/(m^2·K)]	977	1552	1253	1280
ΔT_{ave}	[K]	5.77	4.83	4.66	4.27
U'	[W/(m^2·K)]	980	1396	1238	1275
A_{mt}/A	[-]	1	0.83	0.84	1
$\dot{G}$	[$\times10^{-3}$ kg/(m^2·s)]	3.44	4.71	4.64	3.46
$\Delta T_{L,out}^{sub}$	[K]	1.88	3.69	2.69	5.74
P_{out}	[kPa]	613.4	615.0	615.0	613.1

is around 6 kW/m^2. For this specific operating condition, NH_3/[emim][SCN] solution shows the best heat transfer performance among the IL-based fluids. Using the $LMTD$ for a rating, it reaches an overall heat transfer coefficient of 1550 W/(m^2·K). The alternative overall heat transfer coefficient, U' is around 1400 W/(m^2·K), which is still the highest among the fluids. NH_3/[emim][SCN] also allows for a promising mass transfer performance. The effective mass transfer area, A_{mt}, takes 83% of the total heat transfer area.

The heat transfer and mass performance of NH_3/[emim][Tf_2N] for the NH_3 absorption comes similar to that of the NH_3/[emim][SCN]. Note that the plate areas in these two fluids cases are not fully used for the vapor absorption. It indicates there is still room to enhance the mass transfer duty at working fluids side. A discussion of operation conditions in the working fluid side is presented in Section 5.6.2 based on a sensitivity analysis.

The fluid NH_3/[bmim][BF_4] presents the lowest heat transfer performance of over 970 [W/(m^2·K)], because of its unfavorable transport properties. For the studied absorption condition, the area of the proposed PHX is not enough to accomplish the gas absorption duty. Nevertheless, the subcooling degree, ΔT_{sub}, of the fluid in the solution outlet is 1.88 K, which indicates it still has sufficient margin for the NH_3 absorption.

The reference fluid, NH_3/$LiNO_3$ shows similar heat transfer performance as these best NH_3/IL fluids. However, the provided area is not sufficient to accomplish the vapor absorption.

For a closer examination of the absorption performance of NH_3 with different working fluids, typical thermophysical properties, parameters related to heat and mass transfer, and relevant dimensionless numbers of the solution stream at the middle position of PHXs are listed in Table 5.11.

Table 5.11: Comparison of relevant thermophysical properties and dimensionless numbers in the middle position of the PHX.

absorbent		[bmim][BF_4]	[emim][SCN]	[emim][Tf_2N]	$LiNO_3$
T	[°C]	49.4	49.3	49.0	45.1
P	[kPa]	614.3	615.1	615.1	614.2
w	[kg/kg]	0.048	0.076	0.042	0.478
ρ	[kg/m^3]	1154	1061	1456	1003
c_p	[J/(kg·K)]	1823	1972	1484	3084
λ	[mW/(m·K)]	194	226	132	301
D	[$\times 10^{-9}$ m^2/s]	1.75	8.63	5.82	0.74
μ	[$\times 10^{-3}$ Pa·s]	3.39	1.42	1.28	4.60
σ	[$\times 10^{-2}$ N/m]	4.08	4.84	3.38	5.20
δ_f	[$\times 10^{-4}$ m]	7.96	8.44	8.73	2.86
$\bar{\alpha}_{Lw}$	[$W/(m^2 \cdot K)$]	1219	2010	1699	1287
$\bar{\alpha}_{Lint}$	[$W/(m^2 \cdot K)$]	18553	41273	39366	11113
$\bar{\beta}$	[$\times 10^{-4}$ m/s]	6.28	36.61	37.91	1.39
Nu_{Lw}	[-]	4.99	7.52	11.20	1.22
Nu_{Lint}	[-]	75.98	154.39	259.49	10.56
Pr	[-]	31.76 (52*)	12.38 (15*)	14.40 (18*)	47.09 (80*)
Sh	[-]	284.77	358.30	568.66	53.71
Sc	[-]	1672 (2265*)	155 (175*)	152 (172*)	6190 (10649*)

* Solution Prandtl or Schmidt numbers at the entrance of PHX are shown inside brackets. They, together with the entrance Reynolds numbers as shown in Fig. 5.12, are used to quantify the solution Nusselt and Sherwood number, respectively.

Since the interface heat transfer coefficient cannot be measured directly, the heat and mass transfer analogy is here used to confirm the obtained transfer coefficients are reasonable. The mass transfer coefficient for the $NH_3/LiNO_3$ cases is 1.39×10^{-4} m/s. For a similar mass transfer problem (liquid-phase-controlled case) reported by Olujić and Seibert [196], the liquid phase mass transfer coefficients of structured packing, which applies thin corrugated metal plates sharing similar features as the plates in the studied plate heat exchanger, are of the same magnitude as the ones reported in this work. Besides, liquid mass transfer coefficients from H_2O vapor into a falling film of $H_2O/LiBr$ along a vertical tube reported by Miller and Keyhani [197] are also in a similar range. These studies confirm the reasonable prediction of mass transfer coefficient, and consequently, through the heat and mass transfer analogy, confirm the reasonable prediction of the heat transfer coefficients.

The values of mass transfer coefficients, $\bar{\beta}$, for the proposed IL-based fluids are higher than the one for the fluid $NH_3/LiNO_3$. This can be expected since the mass diffusivity, D, of the new proposed fluids is 2.4 times to 12 times larger than the mass diffusivity for the $NH_3/LiNO_3$ mixture (0.74×10^{-9} m^2/s). Notice that the mass diffusivity of the mixture NH_3/[emim][Tf_2N], which is one of the highest, has been obtained from experiments, see Fig. 5.9(a). The higher mass diffusivity of ILs-based mixture could be explained by the differences of molecule sizes and structures between the gas and the IL-based solvent which are obviously greater than those between gas and $LiNO_3$. Additionally, the higher mass diffusivity of IL-based mixture has also been reported by Chen *et al.* [171] which they measured and obtained significantly higher mass diffusivities of H_2O in the mixture H_2O/[mmim][DMP] than in the mixture H_2O/LiBr.

The fluids NH_3/[bmim][BF_4] and NH_3/[emim][SCN] share similar operating conditions of the absorber in heat pump cycles. Most of the thermophysical properties are also quite close, except for their viscosities and mass diffusivities. Even though the relatively higher viscosity can lead to a higher Pr ($\propto \mu^{0.33}$), its impact on Reynolds numbers is more dominant in the Nusselt numbers ($\propto \mu^{-0.6139}$ and $\propto \mu^{-0.8381}$), which leads to a worse heat transfer performance. Together with the relatively lower mass diffusivity of NH_3/[bmim][BF_4], its mass transfer performance is not promising.

The fluid NH_3/[emim][SCN] has similar values of Pr and Sc with those of the NH_3/[emim][Tf_2N] fluid. It implies that these two fluids share comparable ratios of thermal and mass diffusivities to the viscous diffusivity. However, the large solution flow for the fluid NH_3/[emim][Tf_2N] (see Table 5.9) leads to a large Re_L, and hence the flow convection promotes heat and mass transfer. Note that the large flow also requires a significant consumption of pump work, which is not negligible in large pressure drop applications, for instance the double-effect cycle discussed in Chapter 4. The selection of ILs for the absorption system requires a trade-off between operational and initial costs.

5.6. DISCUSSIONS

5.6.1. VALIDATIONS OF THE PROPOSED FLOW PATTERNS

The thin film feature of the solution flow inside the PHX has been re-examined in the following two ways for the cases considered in this study.

The work of Tao *et al.* [177] presents three different maps to distinguish flow patterns of downward condensation and absorption two-phase flow inside PHXs. The recommended one is a pair of dimensionless numbers: Re_L and Fr/Λ^2. Re_L represents flow characteristics of the liquid phase. Fr number accounts for the influence of vapor flow. Λ is a correction factor of fluid properties, which is de-

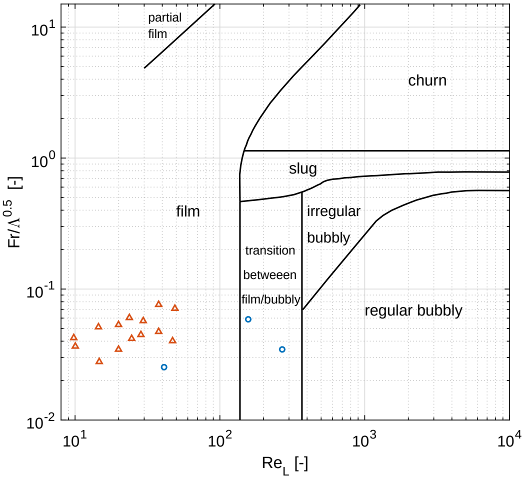

Figure 5.12: The studied cases shown in the flow pattern map proposed in Tao *et al.* [177]. Triangle symbols represent the cases with the fluid $NH_3/LiNO_3$, round ones represent the cases with NH_3/IL fluids.

5

fined as,

$$\Lambda = \frac{\mu_L/\mu_{H_2O}}{\left[\frac{\rho_L}{\rho_{H_2O}}\left(\frac{\sigma_L}{\sigma_{H_2O}}\right)^3\right]^{1/4}} \tag{5.15}$$

Even though the map is not derived for the flow direction studied in this work, these two parameters can however give an indication of the expected vapor and liquid distribution along the flow through the heat exchanger. In Fig. 5.12, the studied cases are represented inside the map according to the relevant dimensionless numbers.

As shown in Fig 5.12, values of Re_L and Fr/Λ^2 of most cases in this study fall into the film flow region. Only for two IL-based fluids, the flow may transit from film to bubbly region, this is mainly due to the large liquid flow required.

The other examination is carried out by assuming a bubble flow is dominant for the investigated cases.

Fig. 5.13 shows visualization results of flow patterns in $NH_3/LiNO_3$ vertical tubular absorbers with cocurrent upward flows of liquid and vapor phases reported by Infante Ferreira [198].

As the flow passage area reduces from right (diameter = 25 mm) to left (diameter = 10 mm), the vapor slugs become longer and a thin film of solution is formed between the slug and the wall. The authors expect that, with an even narrower flow passage area in plate heat exchangers, the vapour slugs become

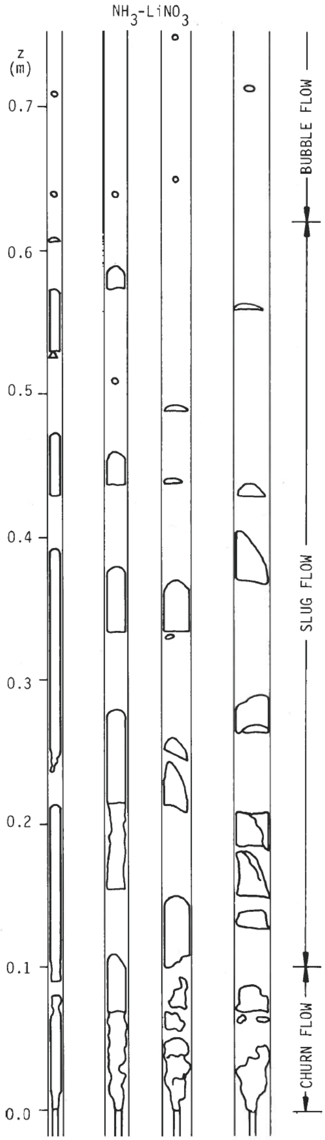

Figure 5.13: Visualizations of flow patterns in $NH_3/LiNO_3$ vertical tubular absorbers with cocurrent upward flows [198]. The ammonia vapor flow is in average 72.5×10^{-6} kg/s, the solution flow 5.5×10^{-3} kg/s.

even longer so that film flow is predominant in the absorber.

Furthermore, diameters of initial bubbles leaving the orifice can also be estimated based on equations provided by Treybal [199]. Considering an orifice of 1 mm diameter, the orifice Reynolds numbers, $\mathrm{Re}_{\mathrm{ori}}$,

$$\mathrm{Re}_{\mathrm{ori}} = \frac{d_{\mathrm{ori}} \cdot v_{\mathrm{ori}} \cdot \rho_{\mathrm{V}}}{\mu_{\mathrm{V}}} \tag{5.16}$$

which are based on the vapor velocity through the orifice and the orifice diameter as the characteristic length, show values larger than 10^5 for the studied cases.

It indicates that the selected gas rate in simulations and also the NH_3/$LiNO_3$ experimental conditions all have large vapor velocities through the orifice. The corresponding estimation of initial bubble diameters is provided by Eq. 5.17, which is only related to the NH_3 vapor flow.

$$d_{\mathrm{ini}} = 0.0071 \cdot \mathrm{Re}_{\mathrm{ori}}^{-0.05} \tag{5.17}$$

For the studied NH_3/$LiNO_3$ cases, the values of initial bubble diameters are in the range of 4.0-4.7 mm. For all the NH_3/ILs cases, the initial bubble diameters are 4.0 mm identically.

The estimated initial bubble diameters of these cases are all larger than the gap between plates (2 mm), which implies a deformed bubble would pass through the channel. These facts indicate that the assumption of a thin film flow for the solution stream is sufficiently accurate to represent the physics of the liquid phase of vapor-liquid absorption inside the PHX.

5.6.2. SENSITIVITY ANALYSIS OF TRANSPORT PROPERTIES AND OPERATION CONDITIONS

The availability of transport properties for NH_3-IL mixtures is limited. The current property method, which is based on very few reported property data may introduce errors on the overall heat and mass transfer calculation. Here a sensitivity analysis is carried out to investigate the influence of the uncertainty of two fundamental transport properties, mass diffusivity of NH_3 into the NH_3/IL mixture and viscosities of the mixture, on the heat and mass transfer performance estimated by the proposed framework.

Fig. 5.14 illustrates an evaluation of scaled properties on the two overall heat transfer coefficients (U and U'), mass transfer flux on the effective mass transfer area ($\dot{G}$) and the area ratio of the plates needed for mass transfer (A_{mt}) for the working pair NH_3/[emim][Tf_2N]. The operating conditions are the same as introduced in Secion 5.5.

A lower value of mass diffusivity has a limited influence on the heat transfer as shown in Fig. 5.14(a). It mainly affects the mass transfer. A 90% decrease of D

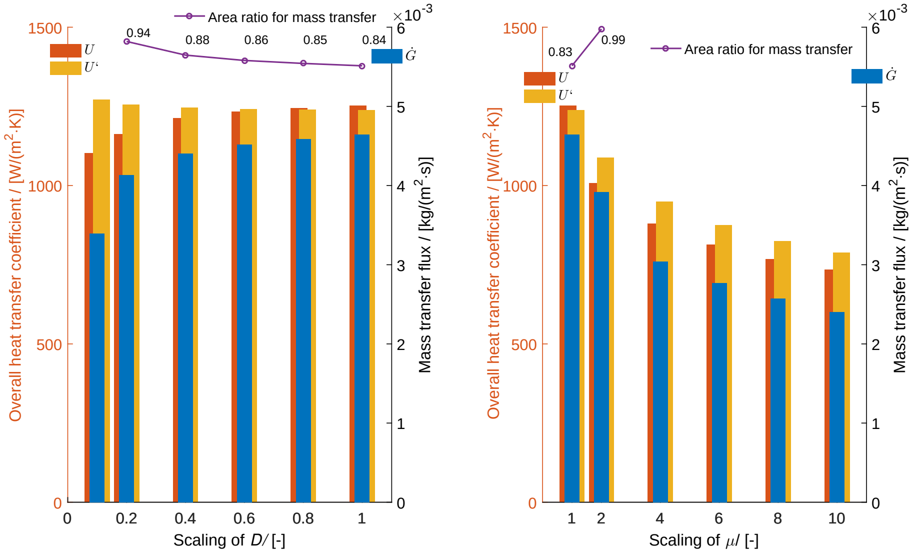

(a) (b)

Figure 5.14: Sensitivity analysis of (a) mass diffusivity and (b) mixture viscosity on the overall heat and mass transfer performance of NH_3's absorption into NH_3 / [emim][Tf_2N] solution.

(maximum deviation) can introduce a drop of mass transfer coefficient of 18%. In that case, the current PHX can not complete the mass transfer duty. Notice that the experimental data is predicted in average with a deviation smaller than -50%. For such decrease, the reduction of the mass transfer flux is around 5%.

The current method used to predict the mixture viscosity may underestimate it for a real solution. As the method may introduce an average error of -50%, it can cause a 12-20% decrease of overall heat transfer coefficients and a 15% decrease of the mass transfer flux. For an extreme case when the mixture viscosity is 10 times larger than the predicted one, heat and mass transfer will be deteriorated significantly. In that case, overall heat transfer performance and total mass transfer flux both drop 40%.

Moreover, operating conditions in the working fluid side, the solution inlet temperature, $T_{\mathrm{L}}^{\mathrm{in}}$, and the flow, $\dot{m}_{\mathrm{V}}$, are also studied to evaluate their influences on the heat and mass transfer performance, as presented in Fig. 5.15. Notice that except for the studied variable, other operating conditions are the same as introduced in Section 5.5, including the ratio of $\dot{m}_{\mathrm{L}}$ to $\dot{m}_{\mathrm{V}}$.

As shown in Fig. 5.15(a), a lower inlet solution temperature can enhance the NH_3 absorption, thus the mass transfer flux improves and the area needed for mass transfer decreases. The heat duty is reduced at lower $T_{\mathrm{L}}^{\mathrm{in}}$ cases, causing the

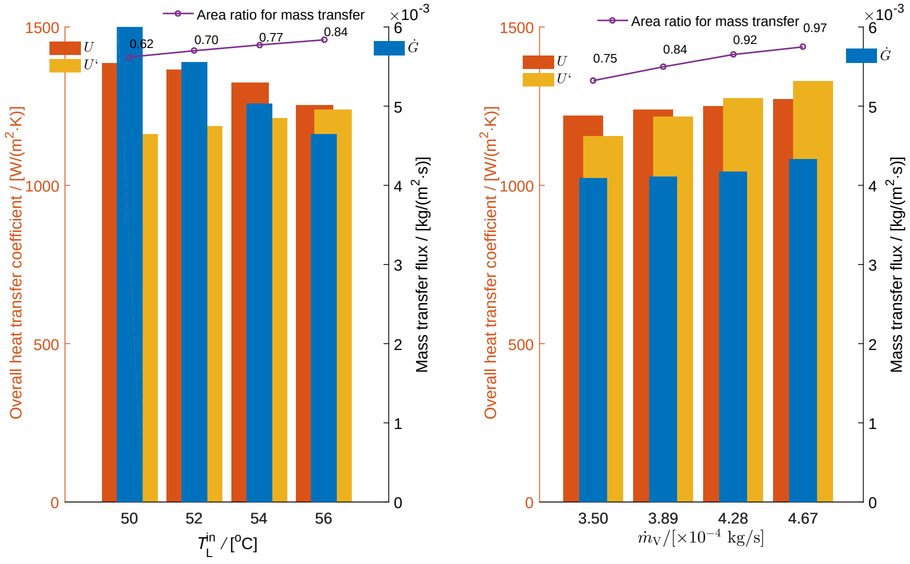

(a) (b)

Figure 5.15: Sensitivity analysis of (a) solution inlet temperature and (b) vapor flow rate on the overall heat and mass transfer performance of NH_3's absorption into NH_3/[emim][Tf_2N] solution.

overall heat transfer coefficient, U', predicted using Eqs. 5.12 and 5.13, to drop. The deviation of its behavior from the standard overall heat transfer coefficient, U, estimated using Eqs. 5.10 and 5.11, is due to the large temperature rise at the inlet of working fluids, which is a result of a larger amount of absorption heat released.

Fig .5.15(b) shows that an increase of the working fluid flows can enhance both the heat and mass transfer performance. At the best design point when the vapor flow, $\dot{m}_V$, is 4.67 $\times 10^{-4}$kg/s, the current PHX is almost fully used for the absorption duty.

5.7. CONCLUSIONS

This work aims at providing knowledge on the absorber design for IL-based absorption systems. A semi-empirical framework is proposed to study the heat and mass transfer during the absorption of NH_3 into NH_3/non-volatile salts solutions inside corrugated plate heat exchangers. Experimental data of $NH_3/LiNO_3$ absorption is applied to determine unknown information concerning the heat and mass transfer performance of the solution film. The identified relations are then used in combination with the thermophysical data of NH_3/ILs, to predict the performance of the absorber of an NH_3/ILs absorption heat pump cycle.

- The friction factors of the $NH_3/LiNO_3$ absorption in the studied PHX have been correlated as a function of solution Reynolds number: $\xi = 23050 \cdot \mathrm{Re}_L^{-1.69}$.
- Nusselt numbers of the liquid film to the wall and interface are determined, showing relations with the solution Reynolds number:
  $\mathrm{Nu}_{L,w} = 0.1372 \cdot \mathrm{Re}_L^{0.6139} \cdot \mathrm{Pr}^{1/3}$ and $\mathrm{Nu}_{L,int} = 0.9077 \cdot \mathrm{Re}_L^{0.8381} \cdot \mathrm{Pr}^{1/3}$.
  The Nusselt number of the liquid film at the interface side is much larger than the one at the wall side.
- A stronger absorption is detected in the entrance of the absorber, which may cause a rapid temperature rise.
- The effective mass diffusivity of NH_3 in ILs is proposed as an exponential relation to the pure IL's viscosity with an exponent of -1.45.
- The ranking of the heat transfer performance for the NH_3/ILs is: [emim][SCN] > [emim][Tf_2N] > [bmim][BF_4]. An absorber with the studied geometry can achieve an overall heat transfer coefficient of around 1.4 kW/(m^2K) under the studied condition, which is slightly better than the performance of $NH_3/LiNO_3$'s absorber.
- The averaged uncertainties of the mass diffusivity and viscosity predicted using the current property methods will cause less than 20% reductions to the overall heat and mass transfer performance under the studied conditions.

6

CONCLUSIONS AND RECOMMENDATIONS

6.1. CONCLUSIONS

This work has demonstrated that ammonia absorption systems with the novel absorbents, ionic liquids, are capable to provide high-efficient heating and cooling. In this thesis, ammonia/ionic liquid based working pairs for application in absorption refrigeration and heat pump systems have been investigated considering both fundamental and application perspectives. The study covers multi-scale considerations from properties, components, cycles and system-integration aspects, and also discusses the feasibility of practical applications.

6.1.1. PROPERTIES ASPECTS

The performance of various vapor-liquid equilibrium models applied in absorption refrigeration cycles has been evaluated, making use of experimental equilibrium data of the working pairs (H_2O/[emim][DMP] pair and NH_3/[bmim][BF_4] pair). The Redlich-Kwong equation of state performs best in both correlating equilibrium data and estimating mixing enthalpies. The Non-Random Two Liquid model is also suitable for correlating and reproducing experimental vapor-liquid equilibrium data. The UNIFAC model can be applied for estimating mixing enthalpies. All studied models indicate that the mixing of liquid H_2O with an IL is significantly more exothermic than that mixing of NH_3 with an IL. Moreover, the obtained total enthalpies for the H_2O/[emim][DMP] solution are more sensitive to the vapor-liquid equilibrium models than the total enthalpies for the NH_3/[bmim][BF_4] solution. This has a large impact into the calculation of the *coefficient of performance* (COP) of the VAR cycle.

Most thermophysical properties can be predicted with sufficient accuracy by considering the solution as ideal and neglecting the excess effects. Density and heat capacity of NH_3/IL solutions can be predicted making use of mass-fraction averaged properties of the pure components. Predictions are within 6.5% and 4% accuracies respectively. The specific heat capacities of 61 ILs at room temperature have been found between 1-2 kJ/(kg·K) and concentrated near 1.44 kJ/(kg·K). Neglecting the mixing enthalpy does not show remarkable difference when calculating the total enthalpies of the studied IL-based mixtures. The viscosity of these solutions can be estimated making use of the molar fraction averaged logarithmic properties of the pure components. The effective diffusivity of NH_3 in ILs is found has an exponential relation to the IL's viscosity with an exponent of -1.45.

Making use of a genetic algorithm, the properties of NH_3/IL mixtures leading to the highest performance have been identified. The optimum IL candidates should show high absorption capabilities, large solubility differences between in- and outlet of the generator, low molecular weights and low heat capacities.

Monte Carlo simulations have been demonstrated to be advantageous methods to extend the vapor-liquid equilibrium data for what concerns cost and time consumed. For instance in the studied cases at a high temperature and high pressure range, where there is no experimental VLE data available, simulation is a feasible way to fill in the gap for the three investigated NH_3/IL working fluids. The addition of the computed VLE to the experimental ones improves the quality of the VLE extension when the NRTL model is used, making vapor pressure curves follow trends as expected by the Clausius-Clapeyron equation.

6.1.2. COMPONENT ASPECTS

For an NH_3 absorption with NH_3/IL-based fluids in a corrugated plate heat exchanger, the following ranking of the heat transfer performance has been found: [emim][SCN] > [emim][Tf_2N] > [bmim][BF_4]. An absorber with the studied geometry is able to achieve an overall heat transfer coefficient of 1.4 kW/(m^2·K) in the studied conditions, which is comparable with the performance of $NH_3/LiNO_3$. In addition, friction factors of NH_3/salt fluids in the plate heat exchangers have been obtained as a function of solution Reynolds numbers: $\xi = 23050 \cdot Re_L^{-1.69}$. Nusselt numbers for the liquid film to wall heat transfer and for the interface to film heat transfer have shown to be related to solution Reynolds numbers: $Nu_{L,wall} = 0.1372 \cdot Re_L^{0.6139} \cdot Pr^{1/3}$, and $Nu_{L,int} = 0.9077 \cdot Re_L^{0.8381} \cdot Pr^{1/3}$. The Nusselt number at the interface side of the liquid film is much larger than the one at the wall side. The heat and mass transfer model detects a strong absorption in the entrance of the absorber, which may cause a rapid temperature rise.

6.1.3. CYCLE AND IMPLEMENTATION ASPECT

In a single-effect absorption heat pump application, the circulation ratio f decreases and the heating coefficient of performance, COP, increases with an increase of generator temperature. The working pair NH_3/[mmim][DMP] obtains the best performance (COP of 1.79). The working pairs NH_3/[bmim][BF_4], NH_3/[emim][Tf_2N], NH_3/[emim][SCN] also show a higher COP than that of the NH_3/H_2O pair. Nevertheless, the circulation ratio f is significantly higher than that of a cycle with the NH_3/H_2O pair. In a closer examination of the generator heat requirement, it has been revealed that partial boiling of the solution at the entrance of the generator results in a higher COP for the cycle.

The optimization of the cycle performance making use of a genetic algorithm has indicated that single-effect absorption heat pumps with NH_3/IL working pairs could reach a heating COP of 1.84.

A brief heat transfer calculation has revealed that large circulation ratios combined with unfavorable transport properties cause extremely large areas for heat exchangers, which would additionally require a large amount of expensive ILs to charge the system. An economic feasibility analysis indicates that, if [emim][SCN] would be produced at industrial scales, AHPs with this NH_3/IL fluid would lead to both significant energy (42%) and economic (29%) savings in comparison with conventional boilers.

For the double-effect absorption cycle driven by a high temperature heat source (around 250 °C), the ranking of COP for the three studied ILs is: [bmim][BF_4] > [emim][SCN] > [emim][Tf_2N]. The best IL candidate achieves a COP above 1.1 for -5 °C cooling with cooling water at 16 °C. In addition, double-effect absorption cycles for cooling show approximately 10% higher performance than the generator-absorber heat exchange cycles with NH_3/H_2O fluids for applications with high temperature driving heat.

[Emim][SCN] is not suitable for high temperature applications. Its thermal stability is the worst among the three studied ILs for high temperature refrigeration cycles.

The waste heat from the flue gases of diesel engines can be used to drive double-effect VAR cycles. The proposed system with NH_3/[bmim][BF_4] can provide at least a cooling capacity of 1500 kW, more than one refrigeration seawater (RSW) plant, for all the diesel engine operating modes. It recovers 1300 kW waste heat and consumes 90 kW pump work. As a result, per fishing vessel, 4.8 TJ of energy can be saved and 1030 tons of CO_2 emissions can be avoided annually. Alternatively, the proposed system is able to provide at most a cooling capacity of 3200 kW (comparable to two RSW plants), when the diesel engine operates at 90% load (5800 hours/year). It then recovers 2756 kW waste heat and consumes 191 kW pump work. Annually saved energy and reduced CO_2 emissions are 7.6

TJ and 1634 tons, respectively.

6.2. RECOMMENDATIONS

Many scientific and practical challenges have to be addressed before IL-based absorption technologies become suitable for industrial applications. Regarding the research experience on this topic, the author believes the following issues are urgent to be figured out:

- Experimental research of an NH_3/IL absorption at system level has never been reported to the best of the author's knowledge. Relevant experience with these systems has only rarely been discussed. A continuously operated absorption-desorption set-up has been designed by the author to gain experience with its operation. Details of the setup and working fluids are briefly provided in Appendix F.
- The claim of high thermal stability of ILs is questionable. The mechanism of the decomposition is complicated: evaporation and/or chemical decomposition. The influence of these issues on IL-based absorption systems should be avoided or dealt with to ensure reliable operating.
- Additives aiming at improving the transport performance of NH_3/IL systems should be identified to be used with IL-based fluids. The transport phenomena, for instance the wetting behavior of IL-based fluids, is worth investing in depth.
- The pump work becomes significant for multi-effect applications, especially when using ammonia as the refrigerant which has a large vapor pressure difference for the temperature lifts used in these applications. The circulation ratio should be reduced. Screening better fluids or optimizing cycle configuration could be directions to address this disadvantage.
- To address the major challenges that hinder large scale applications of IL-based absorption systems, inter-discipline, cooperative, work is always welcome. Cooperation between stakeholders with expertises regarding synthesis, thermodynamics, refrigeration and equipment development, both in academia and industry should be intensified.

APPENDIX A

Ionic liquids considered in this study

Name in this thesis	CAS No.	IUPAC name	Chemical formula	M_w [kg/kmol]
[mmim][DMP]	654058-04-5	1,3-dimethylimidazolium dimethyl phosphate	$C_7H_{15}N_2O_4P$	222.18
[emim][BF$_4$]	143314-16-3	1-ethyl-3-methylimidazolium tetrafluoroborate	$C_6H_{11}BF_4N_2$	197.97
[hmim][BF$_4$]	244193-50-8	1-hexyl-3-methylimidazolium tetrafluoroborate	$C_{10}H_{19}BF_4N_2$	254.08
[omim][BF$_4$]	244193-52-0	1-methyl-3-octylimidazolium tetrafluoroborate	$C_{12}H_{23}BF_4N_2$	282.13
[bmim][BF$_4$]	174501-65-6	1-butyl-3-methylimidazolium tetrafluoroborate	$C_8H_{15}BF_4N_2$	226.02
[bmim][PF$_6$]	174501-64-5	1-butyl-3-methylimidazolium hexafluorophosphate	$C_8H_{15}F_6N_2P$	284.18
[emim][Tf$_2$N]	174899-82-2	1-ethyl-3-methylimidazolium bis(trifluoromethylsulfonyl)imide	$C_8H_{11}F_6N_3O_4S_2$	391.31
[emim][EtSO$_4$]	342573-75-5	1-ethyl-3-methylimidazolium ethylsulfate	$C_8H_{16}N_2O_4S$	236.29
[emim][SCN]	331717-63-6	1-ethyl-3-methylimidazolium thiocyanate	$C_7H_{11}N_3S$	169.25

APPENDIX B

Vapor-liquid equilibrium models in this study

PENG-ROBINSON (PR) EOS

The basic expression of Peng-Robinson EOS is [89],

$$P = \frac{RT}{V-b} - \frac{a(T)}{V(V+b)+b(V-b)} \tag{B.1}$$

where V is the molar volume, R is the gas constant. The parameters a and b are defined as,

$$a(T) = 0.457235\frac{R^2T_c^2}{P_c}\alpha \tag{B.2}$$

$$b = 0.077796\frac{RT_c}{P_c} \tag{B.3}$$

where the subscript c represents the critical conditions of the substance. With ω, the acentric factor and $\alpha(T)$, in classical PR EOS, defined as,

$$\alpha^2 = 1 + \left(0.37646 + 1.54226\omega - 0.26992\omega^2\right)\left(1 - \frac{T}{T_c}^{0.5}\right) \tag{B.4}$$

As for the mixtures in low pressure cases, conventional quadratic mixing rule (VdW mixing rule) with two interaction parameters is used to describe the behavior as,

$$a_m = \sum_{i=1}^{N}\sum_{j=1}^{N}\sqrt{a_i a_j}(1-k_{ij})x_i x_j \tag{B.5}$$

where

$$k_{ij} = k_{ji}, k_{ii} = 0 \tag{B.6}$$

and

$$b_m = \frac{1}{2}\sum_{i=1}^{N}\sum_{j=1}^{N}(b_i+b_j)(1-l_{ij})x_i x_j \tag{B.7}$$

where

$$l_{ij} = l_{ji}, l_{ii} = 0 \tag{B.8}$$

The parameters a_i and b_i for all pure components in the mixing rules can be calculated using the aforementioned way for a and b. Thus, there are only two parameters needed to be correlated, i.e., k_{12} and l_{12} for a binary mixture.

For high pressure applications, the PR-EOS is usually combined with the Wong-Sandler (WS) mixing rules [90], which are given by,

$$b_m = \frac{\sum_{i=1}^{N}\sum_{j=1}^{N} x_i x_j \left(b - \frac{a}{RT}\right)_{ij}}{1 - \frac{A_\infty^E(x_i)}{CRT} - \frac{\sum_{i=1}^{N} x_i a_i}{b_i RT}} \tag{B.9}$$

$$a_m = b\left(\sum_{i=1}^{N} \frac{x_i a_i}{b_i} + \frac{A_\infty^E(x_i)}{C}\right) \tag{B.10}$$

$$\left(b - \frac{a}{RT}\right)_{ij} = \frac{1}{2}\left[\left(b_i - \frac{a_i}{RT}\right) + \left(b_j - \frac{a_j}{RT}\right)\right](1 - k_{ij}) \tag{B.11}$$

where k_{ij} is a binary interaction parameter ($k_{ij} = k_{ji}$) and the constant C is -0.62322 for PR-EOS. The excess Helmholtz energy at infinite pressure $A_\infty^e(x_i)$ is calculated through the assumption that $A_\infty^e(x_i) \approx A_0^e(x_i) \approx G_0^e(x_i)$. The excess Gibbs energy, $G_0^e(x_i)$, at low pressure can be obtained from an activity coefficient model, here the conventional NRTL model. For the binary solution, the expression of $G_0^e(x_i)$ is [38, 94],

$$\frac{G_0^e}{RT} = x_1 x_2 \left(\frac{\tau_{21} G_{21}}{x_1 + x_2 G_{21}} + \frac{\tau_{12} G_{12}}{x_2 + x_1 G_{12}}\right) \tag{B.12}$$

where, the expressions of G_{21} and G_{12} are given in Eq. B.23, and the τ_{12} and τ_{21} could be used directly here without the dependence of T. In this case, the parameters of this PRWS model to be correlated are k_{12}, α, τ_{12} and τ_{21}.

GENERIC REDLICH-KWONG (RK) EOS

The generic RK type of cubic EOS can be written in the following form [40],

$$P = \frac{RT}{V - b} - \frac{a(T)}{V(V + b)} \tag{B.13}$$

where a and b are expressed by,

$$a(T) = 0.42748 \frac{R^2 T_c^2}{P_c} \alpha(T) \tag{B.14}$$

and

$$b = 0.08664 \frac{RT_c}{P_c} \tag{B.15}$$

where the temperature-dependent part of the parameter α for pure component is modeled by the following empirical form,

$$\alpha(T)=\sum_{k=0}^{\leq 3}\beta_k\left(\frac{T_c}{T}-\frac{T}{T_c}\right)^k \tag{B.16}$$

As Yokozeki and Shiflett [40] reported, β_2 of ILs could be determined through the binary VLE data analysis with β_0=1 and β_2=β_3=0. β values for the natural refrigerants H_2O and NH_3 along with the critical conditions are summarized in Table 2.2. For the mixtures, three binary interaction parameters τ, l and k are introduced in the parameters a and b for an N-component system via,

$$a_m=\sum_{i=1}^{N}\sum_{j=1}^{N}\sqrt{a_i a_j}f_{ij}(T)(1-k_{ij})x_i x_j \tag{B.17}$$

where, $f_{ij}(T)=1+\frac{\tau_{ij}}{T}$, $\tau_{ij}=\tau_{ji}$ and $\tau_{ii}=0$. $k_{ij}=\frac{l_{ij}l_{ji}(x_i+x_j)}{l_{ji}x_i+l_{ij}x_j}$ and $k_{ii}=0$.

$$b=\frac{1}{2}\sum_{i=1}^{N}\sum_{j=1}^{N}(b_i+b_j)(1-k_{ij})(1-m_{ij})x_i x_j \tag{B.18}$$

where $m_{ij}=m_{ji}$ and $m_{ii}=0$.

For the RK-EOS, the fugacity, $\hat{\phi}_i$, could be derived as follows,

$$\ln\hat{\phi}_i=\ln\frac{RT}{P(V-b)}+b'_i\left(\frac{1}{V-b}-\frac{a}{RTb(V+b)}\right)+\frac{a}{RTb}\left(\frac{a'{}_i}{a}-\frac{b'{}_i}{b}+1\right)\ln\frac{V}{V+b} \tag{B.19}$$

where, the explicit forms of a' ($a'_i\equiv\left(\frac{\partial na}{\partial n_i}\right)_{n_{j\neq i}}$) and b' ($b'_i\equiv\left(\frac{\partial nb}{\partial n_i}\right)_{n_{j\neq i}}$) are respectively,

$$a'_i=2\sum_{j=1}^{N}\sqrt{a_i a_j}f_{ij}x_j\left[1-k_{ij}-\frac{l_{ij}l_{ji}(l_{ij}-l_{ji})x_i x_j}{(l_{ji}x_i+l_{ij}x_j)^2}\right]-a \tag{B.20}$$

$$b'_i=\sum_{j=1}^{N}(b_i+b_j)(1-m_{ij})x_j\left[1-k_{ij}-\frac{l_{ij}l_{ji}(l_{ij}-l_{ji})x_i x_j}{(l_{ji}x_i+l_{ij}x_j)^2}\right]-b \tag{B.21}$$

Thus, the parameters that need to be regressed are β_1 for the ILs along with τ_{12}, l_{12}, l_{21} and m_{12} for the mixtures.

NON-RANDOM TWO-LIQUID (NRTL) MODEL

The non-random two-liquid model is one of the frequently used activity coefficient models. For a binary mixture with a non-volatile component in this study, the model can be expressed as [38],

$$\ln\gamma_i=x_2^2\left[\tau_{21}\left(\frac{G_{21}}{x_1+x_2G_{21}}\right)^2+\frac{G_{12}\tau_{12}}{(x_2+x_1G_{12})^2}\right] \tag{B.22}$$

Table B.1: Group division of the molecules of the studied working pairs

Molecule	Group division
Water	1 H_2O
[emim][DMP]	1 CH_2, 1 CH_3, 1 [mim][DMP]
Ammonia	1 NH_3
[bmim][BF_4]	3 CH_2, 1 CH_3, 1 [mim][BF_4]

where

$$G_{12} = \exp(-\alpha\tau_{12}), G_{21} = \exp(-\alpha\tau_{21}) \tag{B.23}$$

and τ_{ij} is expressed with temperature dependent relations,

$$\tau_{12}=\tau_{12}^{(0)} + \frac{\tau_{12}^{(1)}}{T}, \tau_{21}=\tau_{21}^{(0)} + \frac{\tau_{21}^{(1)}}{T} \tag{B.24}$$

The parameters to be correlated in this model are α, $\tau_{12}^{(0)}$, $\tau_{21}^{(0)}$ and $\tau_{12}^{(1)}$, $\tau_{21}^{(1)}$.

UNIFAC MODEL

Before applying the UNIFAC model to the VLE calculation, the molecule of every component of the binary system needs to be split into functional groups. Parameters used in this model are mainly based on the properties of each functional group. As proposed by Dong *et al.* [83], Lei *et al.* [93], Kim *et al.* [200], H_2O, NH_3 and ILs in this study are divided into groups which are listed in Table B.1.

Using the UNIFAC model, the activity coefficient, γ_i, can be obtained from a combination of two terms via [83],

$$\ln\gamma_i = \ln\gamma_i^C + \ln\gamma_i^R \tag{B.25}$$

where γ_i^C and γ_i^R denote the combinatorial and residual term of species i, respectively. The combinatorial terms represent the difference of size and shape of the molecules, which could be expressed as,

$$\ln\gamma_i^C = 1 - \phi_i + \ln\phi_i - 5q_i\left(1 - \frac{\phi_i}{\theta_i} + \ln\frac{\phi_i}{\theta_i}\right) \tag{B.26}$$

The parameters are defined as,

$$\phi_i = \frac{r_i}{\sum\limits_j r_j x_j}, \theta_i = \frac{q_i}{\sum\limits_j q_j x_j} \tag{B.27}$$

where r_i and q_i, which denote the volume and surface area of i-th species, are defined as the sum of the group volume and area parameters R_k and Q_k,

$$r_i = \sum_k \nu_k^{(i)} R_k \tag{B.28}$$

and

$$q_i = \sum_k \nu_k^{(i)} Q_k \tag{B.29}$$

of which $\nu_k^{(k)}$ is the number of group k in species i. The values of R_k and Q_k for each functional group in this study are listed in Table 2.4.

The residual term, can be described in the following form,

$$\ln \gamma_i^R = \sum_k \nu_k^{(i)} (\ln \Gamma_k - \ln \Gamma_k^{(i)}) \tag{B.30}$$

where Γ_k is the group residual activity coefficient, and $\Gamma_k(i)$ is the residual activity coefficient of group k in a reference solution containing only molecules of type i. The forms are provided as following,

$$\ln \Gamma_k = Q_k \left[1 - \ln(\sum_m \theta_m \varphi_{mk}) - \sum_m (\frac{\theta_m \varphi_{km}}{\sum_n \theta_n \varphi_{nm}}) \right] \tag{B.31}$$

$$\theta_m = \frac{\sum_i \upsilon_m^{(i)} x_i}{\sum_i \sum_k \upsilon_k^{(i)} x_i} \tag{B.32}$$

$$\varphi_{mn} = \exp\left[-\frac{a_{mn}}{T} \right], (a_{mn} \neq a_{nm}) \tag{B.33}$$

When the group volume and area parameters are available, some of the group interaction parameters, a_{mn}, are the only parameters unknown. Thus, they are the ones to be correlated from the experimental VLE data. The number of the group interaction parameters, a_{mn}, depends on the division of the specific molecules. For this work, all of the known and unknown interaction parameters are listed in Table 2.5.

APPENDIX C

Description of the force field for Monte Carlo simulations

Three ionic liquids are investigated with the Monte Carlo simulation. The molecular structures are shown in Fig. C.1. Here, the applied force field is summarized in Tables C.1, C.2, C.3, and C.4. The potential energy of a system of molecules can be divided into intermolecular (E_{inter}) and intramolecular (E_{intra}) energies. We assume that the intermolecular potential between two atoms consists of van der Waals interactions modeled by a Lennard-Jones (12-6) potential and electrostatic interactions:

$$E_{\text{inter}} = E_{\text{Coulombic}} + E_{\text{LJ}} = \frac{q_i q_j}{4\pi\varepsilon_0 r_{ij}} + 4\varepsilon\left[\left(\frac{\sigma}{r_{ij}}\right)^{12} - \left(\frac{\sigma}{r_{ij}}\right)^{6}\right] \tag{C.1}$$

Polarization is not considered explicitly. The intramolecular potential consist of three parts: bond stretching, angle bending, and torsion (dihedral angle):

$$E_{\text{intra}} = E_{\text{stretch}} + E_{\text{bend}} + E_{\text{torsion}} \tag{C.2}$$

Harmonic potentials are used to describe the bond stretching and the angle bending:

$$E_{\text{stretch}} = k_b (r - r_0)^2 \tag{C.3}$$

$$E_{\text{bend}} = \frac{1}{2} k_\theta (\theta - \theta_0)^2 \tag{C.4}$$

Torsions for the ionic liquids are defined as follows:

$$E_{\text{torsion}} = k_\chi \left[1 + \cos\left(n\chi - \delta_\chi\right)\right] \tag{C.5}$$

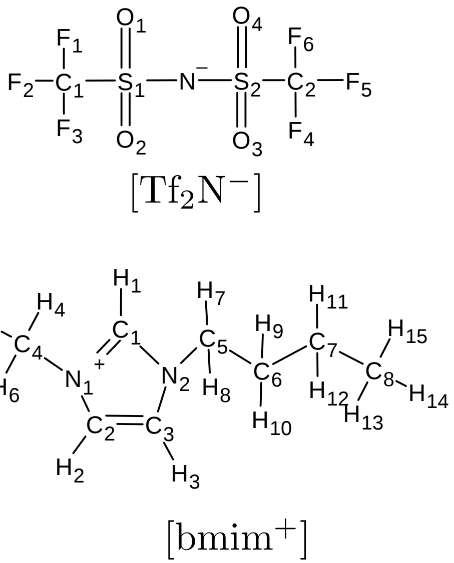

Figure C.1: Structure of the ionic liquids. Atom IDs are reported in this figure. The corresponding atom types, which are used in the definition of force field parameters, are provided in Table C.4. The bond stretching, bond angle bending, dihedral angle, and nonbonded force field parameters are available in Table C.1, C.2, C.3, and C.4, respectively.

Table C.1: Bond stretching potential parameters of the ionic liquids. Sources of force fields: Tenney *et al.* [124] (for cation [emim] and anion [SCN]), Liu *et al.* [146] (for cation [bmim] and anion [Tf_2N]), and Canongia Lopes and Pádua [147] (for anion [BF_4]).

Molecule/ion	Atom types	k_b / [K / Å^2]	r_0 / [Å]
[bmim]	C_3 - N	168427	1.456
	C_3 - H_1	169031	1.093
	C_3 - C_3	152526	1.535
	C_3 - Hc	169736	1.092
[Tf_2N]	N - S_6	197438.4	1.575
	O - S_6	338504.7	1.43
	C_3 - S_6	120411.2	1.82
	C_3 - F	232448	1.315
[SCN]	C_4 - S_6	187097	1.630
	C_4 - N	510516	1.138
[BF_4]	B - F	194540.55	1.394
[emim]	C_3 - N	168427	1.456
	C_3 - H_1	169031	1.093
	C_3 - C_3	152526	1.535
	C_3 - Hc	169736	1.092

Table C.2: Bond angle bending potential parameters of the solvents and the ionic liquids. Sources of force fields: Tenney *et al.* [124] (for cation [emim] and anion [SCN]), Liu *et al.* [146] (for cation [bmim] and anion [Tf_2N]), and Canongia Lopes and Pádua [147] (for anion [BF_4]).

Molecule	Atom types	k_θ / [K/rad^2]	θ_0 / [°]
[bmim]	C_3 - N - Cc	62962	125.09
	C_3 - N - Cd	62962	125.09
	H_1 - C_3 - N	50222	109.45
	C_3 - C_3 - N	66154	112.81
	H_1 - C_3 - H_1	39432	109.55
	C_3 - C_3 - C_3	63616	110.63
	C_3 - C_3 - Hc	46668	110.05
	C_3 - C_3 - H_1	46658	110.07
	Hc - C_3 - Hc	39684	108.35
[Tf_2N]	S_6 - N - S_6	77708.4	127.77
	N - S_6 - O	110781.6	112.6
	C_3 - S_6 - N	92868.6	102.93
	O - S_6 - O	123063.4	118.47
	C_3 - S_6 - O	108961	104.03
	F - C_3 - S_6	80119.8	110.75
	F - C_3 - F	93514.8	108.16
[SCN]	S_6 - C_4 - N	82316	141.0
[BF_4]	F - B - F	80522.3	109.5
[emim]	N - Cc - N	74124	109.33
	C_3 - N - Cc	62962	125.09
	Cc - Cd - N	73380	109.42
	Cc - Cd - H_4	47494	129.11
	H_4 - Cc - N	50544	119.66
	H_5 - Cc - N	50080	122.1
	Cd - Cc - N	73380	109.42
	H_4 - Cd - N	50544	119.66
	H_1 - C_3 - N	50222	109.45
	Cc - N - Cd	64292	128.01
	C_3 - N - Cd	62962	125.09
	Cc - N - Cc	69384	109.9
	C_3 - C_3 - N	66154	112.81
	Cd - Cc - H_4	47494	129.11
	H_1 - C_3 - H_1	39432	109.55
	C_3 - C_3 - Hc	46668	110.05
	C_3 - C_3 - H_1	46658	110.07
	Hc - C_3 - Hc	39684	108.35

Table C.3: Dihedral angle potential parameters of the ionic liquids. Sources of force fields: Tenney *et al.* [124] (for cation [emim]), Liu *et al.* [146] (for cation [bmim] and anion [Tf_2N]).

Atom types	k_χ / [K]	n / -	δ_χ / [°]
[bmim]			
C_3 - C_3 - C_3 - N	- 378.36	1	0
C_3 - C_3 - C_3 - a	117.76	3	0
Hc - C_3 - C_3 - N	78.5	3	0
C_3 - C_3 - C_3 - C_3	90.58	3	0
C_3 - C_3 - C_3 - C_3	125.8	2	180
C_3 - C_3 - C_3 - C_3	100.64	1	180
C_3 - C_3 - C_3 - Hc	80.52	3	0
C_3 - C_3 - C_3 - H_1	78.5	3	0
H_1 - C_3 - C_3 - Hc	78.5	3	0
Hc - C_3 - C_3 - Hc	75.48	3	0
[Tf_2N]			
F - C_3 - S_6 - O	96.45	3	0
S_6 - N - S_6 - O	0	2	0
F - C_3 - S_6 - N	95.58	3	0
S_6 - N - S_6 - C_3	- 489.8	3	0
S_6 - N - S_6 - C_3	- 292.06	2	180
S_6 - N - S_6 - C_3	193.45	1	0
[emim]			
Hc - C_3 - C_3 - N	78.5	3	0
C_3 - C_3 - C_3 - H_1	78.5	3	0
H_1 - C_3 - C_3 - Hc	78.5	3	0

Table C.4: Nonbonded force field parameters of the ionic liquids. The molecule definition of the ionic liquids based on atom IDs is shown in Figure C.1. All bonded force field parameters are reported in Table C.1, C.2, and C.3 are based on the atom types. Atom IDs and the corresponding atom types are provided in columns 1 and 2. Sources of force fields: Tenney *et al.* [124] (for cation [emim] and anion [SCN]), Liu *et al.* [146] (for cation [bmim] and anion [Tf_2N]), and Canongia Lopes and Pádua [147] (for anion [BF_4]).

Atom ID	Atom type	q / [e]	ϵ/k_b / [K]	σ / [Å]
[bmim]				
C_1	Cc	-0.2383	43.277	3.4
C_2	Cd	-0.1261	43.277	3.4
C_3	Cc	-0.0403	43.277	3.4
N_1	N	0.1066	85.547	3.25
H_1	H_5	0.1955	7.548	2.421
H_2	H_4	0.2351	7.548	2.511
H_3	H_4	0.1981	7.548	2.511
N_2	N	0.1788	85.547	3.25
C_4	C_3	-0.2524	55.052	3.4
H_4	H_1	0.1334	7.901	2.471
H_5	H_1	0.1334	7.901	2.471
H_6	H_1	0.1334	7.901	2.471
C_5	C_3	-0.2307	55.052	3.4
C_6	C_3	0.0528	55.052	3.4
H_7	H_1	0.1081	7.901	2.471
H_8	H_1	0.1081	7.901	2.471
C_7	C_3	0.1116	55.052	3.4
H_9	Hc	0.0126	7.901	2.65
H_{10}	Hc	0.0126	7.901	2.65
C_8	C_3	-0.2782	55.052	3.4
H_{11}	Hc	0.0073	7.901	2.65
H_{12}	Hc	0.0073	7.901	2.65
H_{13}	Hc	0.0771	7.901	2.65
H_{14}	Hc	0.0771	7.901	2.65
H_{15}	Hc	0.0771	7.901	2.65

Table C.4 Continued: Nonbonded force field parameters of the ionic liquids. The molecule definition of the ionic liquids based on atom IDs is shown in Figure C.1. All bonded force field parameters are reported in Table C.1, C.2, and C.3 are based on the atom types. Atom IDs and the corresponding atom types are provided in columns 1 and 2. Sources of force fields: Tenney *et al.* [124] (for cation [emim] and anion [SCN]), Liu *et al.* [146] (for cation [bmim] and anion [Tf_2N]), and Canongia Lopes and Pádua [147] (for anion [BF_4]).

Atom ID	Atom type	q / [e]	ϵ / k_b / [K]	σ / [Å]
[Tf_2N]				
N_1	N	-0.6374	85.547	3.25
S_1	S_6	0.9719	125.805	3.564
S_2	S_6	0.9719	125.805	3.564
O_1	O	-0.4847	105.676	2.96
O_2	O	-0.4847	105.676	2.96
O_3	O	-0.4847	105.676	2.96
O_4	O	-0.4847	105.676	2.96
C_5	C_3	0.2483	55.052	3.4
C_2	C_3	0.2483	55.052	3.4
F_1	F	-0.1107	30.696	3.118
F_2	F	-0.1107	30.696	3.118
F_3	F	-0.1107	30.696	3.118
F_4	F	-0.1107	30.696	3.118
F_5	F	-0.1107	30.696	3.118
F_6	F	-0.1107	30.696	3.118
[SCN]				
S	S_6	-0.554	125.805	3.564
C	C_4	0.317	105.676	3.40
N	N	-0.563	85.547	3.25

Table C.4 Continued: Nonbonded force field parameters of the ionic liquids. The molecule definition of the ionic liquids based on atom IDs is shown in Figure C.1. All bonded force field parameters are reported in Table C.1, C.2, and C.3 are based on the atom types. Atom IDs and the corresponding atom types are provided in columns 1 and 2. Sources of force fields: Tenney *et al.* [124] (for cation [emim] and anion [SCN]), Liu *et al.* [146] (for cation [bmim] and anion [Tf_2N]), and Canongia Lopes and Pádua [147] (for anion [BF_4]).

Atom ID	Atom type	q / [e]	ϵ/k_b / [K]	σ / [Å]
[BF_4]				
B	B	0.768	47.808	3.58
F_1	F	-0.392	30.694	3.12
F_2	F	-0.392	30.694	3.12
F_3	F	-0.392	30.694	3.12
F_4	F	-0.392	30.694	3.12
[emim]				
C_1	Cc	-0.101	43.277	3.4
C_2	Cc	-0.151	43.277	3.4
C_3	Cd	-0.131	43.277	3.4
N_1	N	0.206	85.547	3.25
H_1	H_5	0.178	7.548	2.421
H_2	H_4	0.183	7.548	2.511
H_3	H_4	0.19	7.548	2.511
N_2	N	0.072	85.547	3.25
C_4	C_3	-0.296	55.052	3.4
H_4	H_1	0.142	7.901	2.471
H_5	H_1	0.142	7.901	2.471
H_6	H_1	0.142	7.901	2.471
C_5	C_3	-0.035	55.052	3.4
C_6	C_3	-0.12	55.052	3.4
H_7	H_1	0.089	7.901	2.471
H_8	H_1	0.089	7.901	2.471
H_9	Hc	0.067	7.901	2.65
H_{10}	Hc	0.067	7.901	2.65
H_{11}	Hc	0.067	7.901	2.65

APPENDIX D

Diagrams of thermodynamic properties

Pressure-temperature-concentration relationships of the three studied NH_3/ionic liquids mixture at saturated conditions are illustrated in the $\ln P$- $(-1/T)$ diagrams. Each curve represents a mass concentration of NH_3 in the mixture.

Enthalpy-Pressure-temperature-concentration relationships of the three studied NH_3/ionic liquids mixture at saturated conditions are illustrated in the h-w diagrams. Each dashed curve represents a pressure level and solided ones represents temperature level.

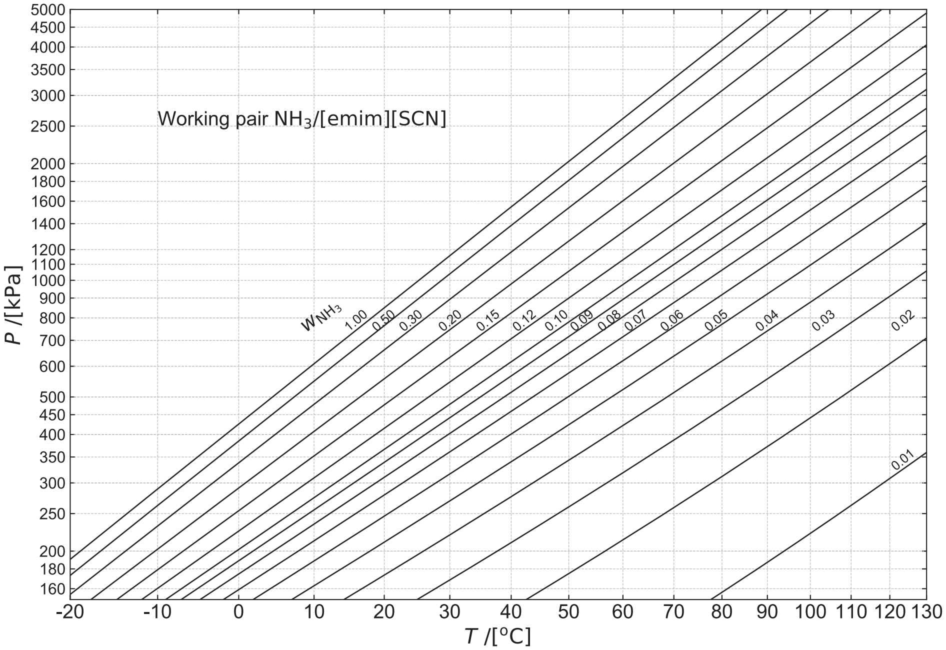
Working pair NH_3/[emim][SCN]
P /[kPa]
5000
4500
4000
3500
3000
2500
2000
1800
1600
1400
1200
1100
1000
900
800
700
600
500
450
400
350
300
250
200
180
160
w_{NH_3}
1.00
0.50
0.30
0.20
0.15
0.12
0.10
0.09
0.08
0.07
0.06
0.05
0.04
0.03
0.02
0.01
-20
-10
0
10
20
30
40
50
60
70
80
90
100
110
120
130
T /[°C]

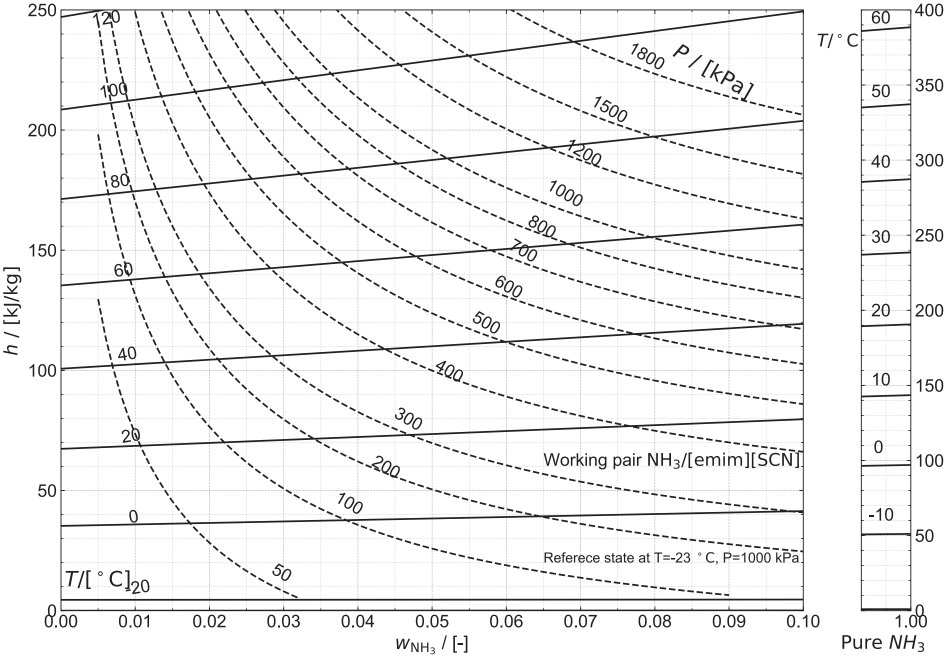
h / [kJ/kg]
250
200
150
100
50
0
120
100
80
60
40
20
0
-20
T/[° C]
P / [kPa]
1800
1500
1200
1000
800
700
600
500
400
300
200
100
50
Working pair NH_3/[emim][SCN]
Referece state at T=-23 ° C, P=1000 kPa
0.00
0.01
0.02
0.03
0.04
0.05
0.06
0.07
0.08
0.09
0.10
w_{NH_3} / [-]
T/ ° C
60
50
40
30
20
10
0
-10
400
350
300
250
200
150
100
50
0
1.00
Pure NH_3

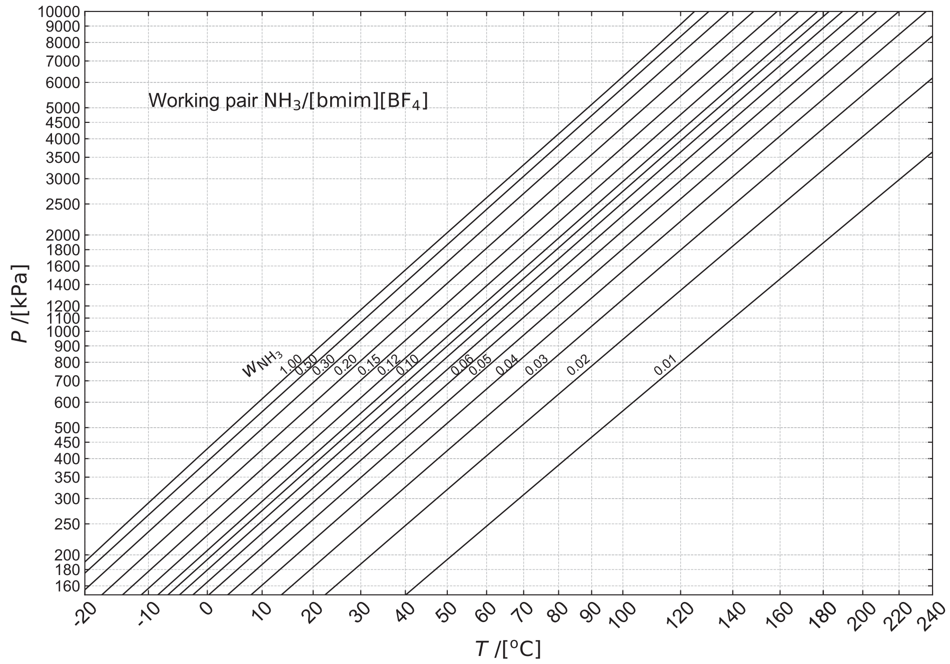
Working pair NH_3/[bmim][BF_4]
P /[kPa]
10000
9000
8000
7000
6000
5000
4500
4000
3500
3000
2500
2000
1800
1600
1400
1200
1100
1000
900
800
700
600
500
450
400
350
300
250
200
180
160
w_{NH_3}
1.00
0.50
0.30
0.20
0.15
0.12
0.10
0.06
0.05
0.04
0.03
0.02
0.01
-20
-10
0
10
20
30
40
50
60
70
80
90
100
120
140
160
180
200
220
240
T /[°C]

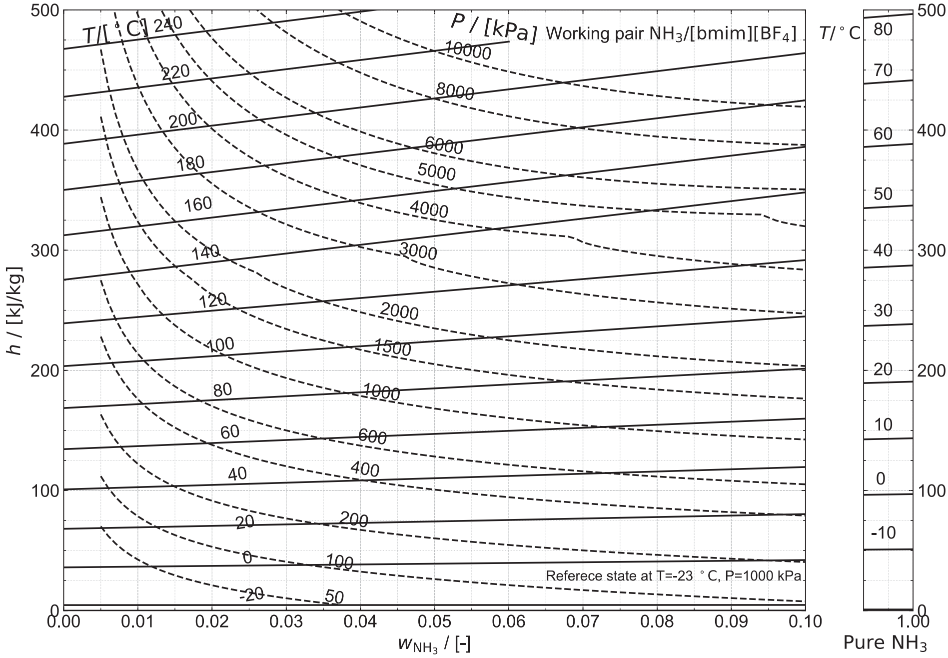
T/[°C]
240
220
200
180
160
140
120
100
80
60
40
20
0
-20
P / [kPa]
10000
8000
6000
5000
4000
3000
2000
1500
1000
600
400
200
100
50
Working pair NH_3/[bmim][BF_4]
Referece state at T=-23 °C, P=1000 kPa
h / [kJ/kg]
500
400
300
200
100
0
0.00
0.01
0.02
0.03
0.04
0.05
0.06
0.07
0.08
0.09
0.10
w_{NH_3} / [-]
T/ °C
80
70
60
50
40
30
20
10
0
-10
1.00
Pure NH_3

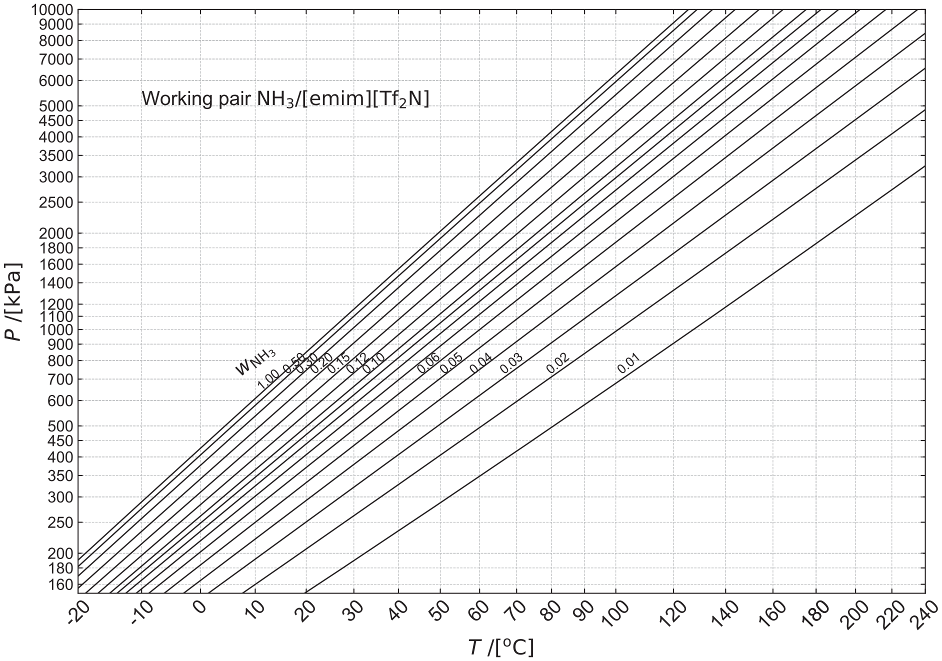
Working pair NH_3/[emim][Tf_2N]
P /[kPa]
10000
9000
8000
7000
6000
5000
4500
4000
3500
3000
2500
2000
1800
1600
1400
1200
1100
1000
900
800
700
600
500
450
400
350
300
250
200
180
160
w_{NH_3}
1.00
0.50
0.30
0.20
0.15
0.12
0.10
0.06
0.05
0.04
0.03
0.02
0.01
-20
-10
0
10
20
30
40
50
60
70
80
90
100
120
140
160
180
200
220
240
T /[°C]

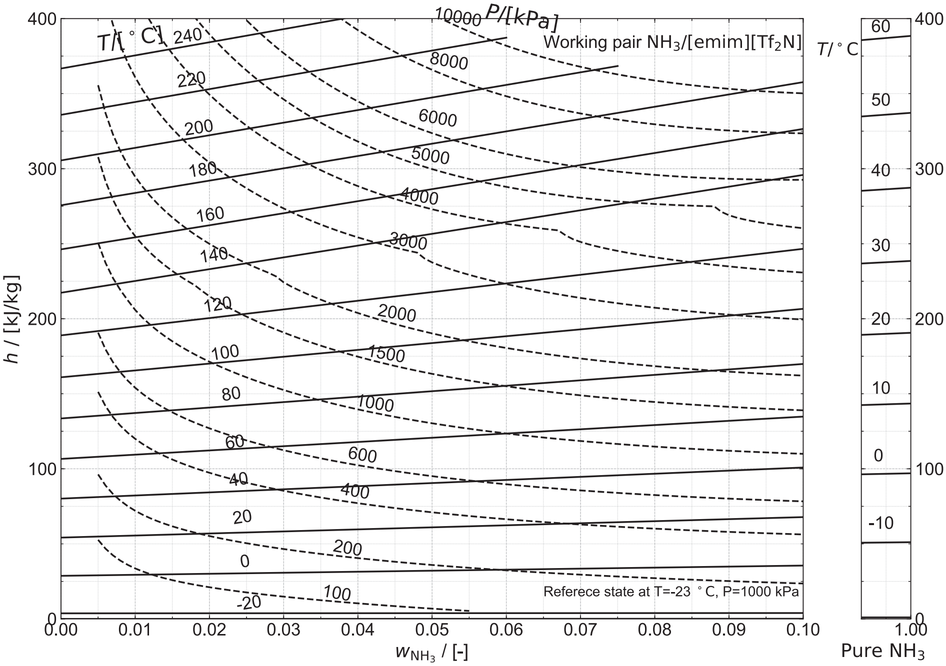
T/[° C]
P/[kPa]
Working pair NH_3/[emim][Tf_2N]
T/ ° C
240
220
200
180
160
140
120
100
80
60
40
20
0
-20
10000
8000
6000
5000
4000
3000
2000
1500
1000
600
400
200
100
60
50
40
30
20
10
0
-10
Referece state at T=-23 ° C, P=1000 kPa
h / [kJ/kg]
400
300
200
100
0
0.00
0.01
0.02
0.03
0.04
0.05
0.06
0.07
0.08
0.09
0.10
1.00
w_{NH_3} / [-]
Pure NH_3

APPENDIX E

Independent experimental data which are used to validate the determined heat and mass transfer characteristics in Section 5.3.1 are listed here.

Case	$\dot{m}_{\mathrm{L}}^{\mathrm{in}}$	$T_{\mathrm{L}}^{\mathrm{in}}$	$w_{\mathrm{L}}^{\mathrm{in}}$	$\dot{m}_{\mathrm{V}}^{\mathrm{in}}$	$P_{\mathrm{L}}^{\mathrm{in}}$	$P_{\mathrm{L}}^{\mathrm{out}}$	$\dot{m}_{\mathrm{cw}}^{\mathrm{in}}$	$T_{\mathrm{cw}}^{\mathrm{in}}$	$\dot{Q}/A$ [kW/m^2]			U [W/(m^2·K)]		
	[kg/h]	[°C]	[-]	[kg/h]	[kPa]	[kPa]	[kg/h]	[°C]	EXP	SIM	RD[-]	EXP	SIM	RD [-]
1	40.23	45.35	0.4491	1.97	516.91	505.68	352.95	42.37	7.97	7.68	-0.037	2613.6	2489.0	-0.048
2	40.56	45.35	0.4491	1.85	516.91	505.68	382.29	42.37	7.46	7.11	-0.047	2665	2425.4	-0.090
3	40.46	45.35	0.4491	1.70	516.91	505.68	416.27	42.37	7.93	7.00	-0.118	2751.3	2688.9	-0.023
4	40.26	45.35	0.4491	1.71	516.91	505.68	219.98	42.37	7.19	7.00	-0.118	2545.1	2688.9	-0.023
5	40.11	45.35	0.4491	1.41	516.91	505.68	182.24	42.37	6.21	5.81	-0.064	2443.1	2446.8	0.001
6	40.21	45.35	0.4491	1.75	516.91	505.68	322.57	42.37	6.32	6.76	0.070	2669.7	2379.5	-0.109
7	39.84	45.35	0.4491	1.26	516.91	505.68	284.04	42.37	6.55	5.54	-0.153	2336.4	2527.2	0.082
8	40.11	45.35	0.4491	1.78	516.91	505.68	250.27	42.37	7.05	6.97	-0.011	2338.6	2327.1	-0.005
9	39.99	45.35	0.4491	1.65	516.91	505.68	132.71	42.37	6.03	6.20	0.028	2799.5	2848.7	0.018
10	40.4	45.35	0.4491	1.64	516.91	505.68	152.19	42.37	6.45	6.35	-0.016	2614.9	2537.2	-0.030
11	40.36	45.35	0.4491	2.39	516.91	505.68	131.55	42.37	10.31	9.91	-0.039	2463.3	2537.0	0.030
12	40.55	45.35	0.4491	2.59	516.91	505.68	214.49	42.37	11.69	11.06	-0.054	2292.2	2283.3	-0.004
13	40.19	45.35	0.4491	2.82	516.91	505.68	299.5	42.37	12.25	11.82	-0.035	2213.8	2282.3	0.031
14	40.02	45.35	0.4491	2.61	516.91	505.68	324.67	42.37	12.83	11.49	-0.105	2273.7	2190.0	-0.037
15	40.18	45.35	0.4491	2.71	516.91	505.68	388.79	42.37	12.88	11.74	-0.089	2254	2190.3	-0.028
16	40.28	45.35	0.4491	2.67	516.91	505.68	450.12	42.37	13.21	11.65	-0.118	2265.3	2136.3	-0.057

APPENDIX F

P&ID diagram of an absorption setup

A experimental setup is designed and constructed to study the absorption of NH_3/[emim][SCN] in a corrugated plate heat exchanger. The P&ID diagram is briefly shown here.

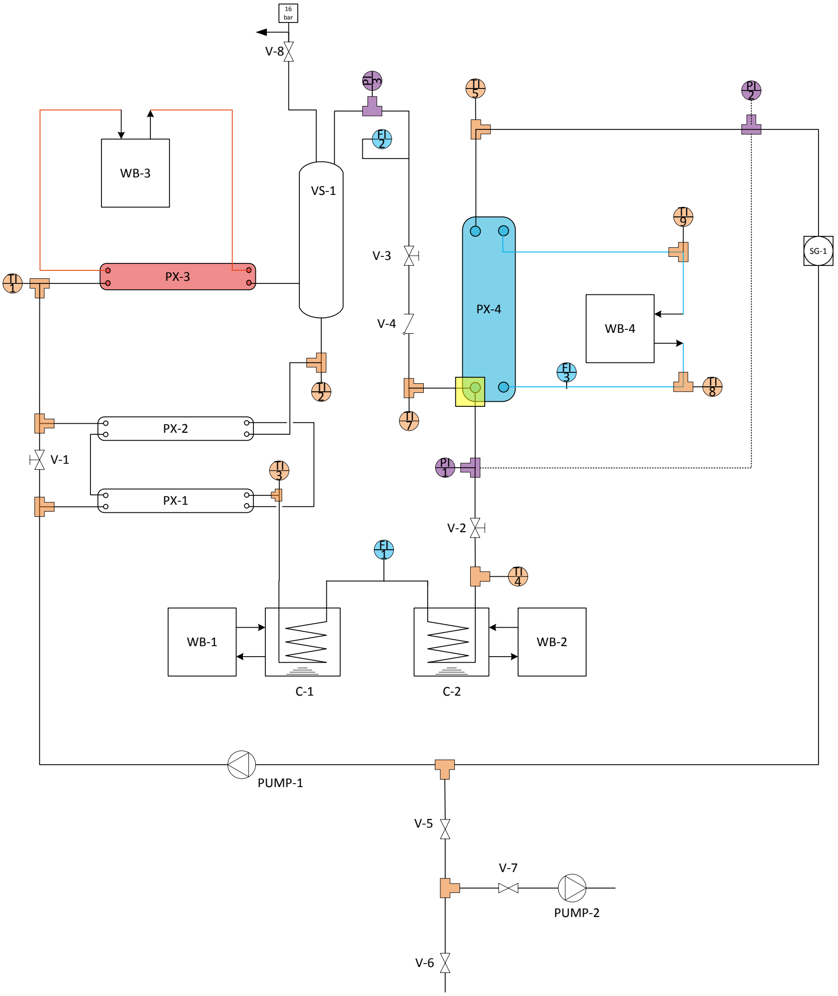

P&ID NH_3-IL absorption setup

Date	23-01-2019
Revision	1
Pages	1/1
Location	
Process & Energy Laboratory Leeghwaterstraat 39 2628 CB Delft	

BIBLIOGRAPHY

BIBLIOGRAPHY

[1] IEA, *Energy, Climate Change & Environment - 2016 Insights*, Tech. Rep. (OECD/IEA, Paris, 2016).

[2] IEA, *Energy Efficiency 2017* (IEA, 2017).

[3] EU Commission, *An EU Strategy on Heating and Cooling*, Tech. Rep. (Brussels, 2016) arXiv:arXiv:1011.1669v3 .

[4] K. Schoots, M. Hekkenberg, and P. Hammingh, *Nationale energieverkenning 2017*, Tech. Rep. (2017).

[5] G. Hieminga, *ING Economics Department*, Tech. Rep. (ING Economics Department, 2013).

[6] N. Pardo, K. Vatopoulos, A. Krook-Riekkola, J. Moya, and A. Perez, *Heat and cooling demand and market perspective*, Tech. Rep. (European Commission, Joint Research Centre, Institute for Energy and Transport, 2012).

[7] C. A. Ramírez, K. Blok, M. Neelis, and M. Patel, *Adding apples and oranges: The monitoring of energy efficiency in the Dutch food industry,* Energy Policy **34**, 1720–1735 (2006).

[8] V. Ruiz, *Analysis of existing refrigeration plants onboard fishing vessels and improvement possibilities,* in *Second International Symposium on Fishing Vessel Energy Efficiency* (Vigo, Spain, 2012).

[9] N. P. Garcia, K. Vatopoulos, A. P. Lopez, and L. Olsen, *Best available technologies for the heat and cooling market in the European Union. JRC Scientif and Policy Reports.*, Tech. Rep. (Joint Research Centre of the European Commission, 2012).

[10] M. Menkveld and L. Beurskens, *Renewable heating and cooling in the Netherlands*, Tech. Rep. June (Energy research Centre of the Netherlands, 2009).

[11] IEA, *Linking Heat and Electricity Systems - Co-generation and District Heating and Cooling Solutions for a Clean Energy Future*, Tech. Rep. (IEA, 2014).

[12] S. Kärkkäinen, *Heat pumps for cooling and heating, Task XVII: Integration of Demand Side Management, Distributed Generation, Renewable Energy Sources and Energy Storages*, Tech. Rep. (International Energy Agency Demand- Side Management Programme, 2011).

[13] A. Oger, *Cogeneration / Trigeneration*, Tech. Rep. January (IIR, 2017).

[14] D. Rutz, *Sustainable heat use of biogas plants*, 2nd ed. (WIP Renewable Energies, 2012).

[15] G. Holdmann, *Geothermal powered absorption chiller,* in *Rural Energy Conference, Valdez, Alaska* (2005).

[16] C. Infante Ferreira and D.-S. Kim, *Techno-economic review of solar cooling technologies based on location-specific data,* International Journal of Refrigeration **39**, 23–37 (2014).

[17] C. Vasilescu and C. Infante Ferreira, *Solar driven double-effect absorption cycles for sub-zero temperatures,* International Journal of Refrigeration **39**, 86–94 (2014).

[18] A. Thekdi and S. U. Nimbalkar, *Industrial Waste Heat Recovery : Potential Applications, Available Technologies and Crosscutting R&D Opportunities*, Tech. Rep. (Oak Ridge National Laboratory, Oak Ridge, 2015).

[19] W. Salmi, J. Vanttola, M. Elg, M. Kuosa, and R. Lahdelma, *Using waste heat of ship as energy source for an absorption refrigeration system,* Applied Thermal Engineering **115**, 501–516 (2017).

[20] P. Margalef and S. Samuelsen, *Integration of a molten carbonate fuel cell with a direct exhaust absorption chiller,* Journal of Power Sources **195**, 5674–5685 (2010).

[21] Z. Yu, J. Han, X. Cao, W. Chen, and B. Zhang, *Analysis of total energy system based on solid oxide fuel cell for combined cooling and power applications,* International Journal of Hydrogen Energy **35**, 2703–2707 (2010).

[22] A. Haywood, J. Sherbeck, P. Phelan, G. Varsamopoulos, and S. K. Gupta, *Thermodynamic feasibility of harvesting data center waste heat to drive an absorption chiller,* Energy Conversion and Management **58**, 26–34 (2012).

[23] K. Ebrahimi, G. F. Jones, and A. S. Fleischer, *A review of data center cooling technology, operating conditions and the corresponding low-grade waste heat recovery opportunities,* Renewable and Sustainable Energy Reviews **31**, 622–638 (2014).

[24] M. Wang and C. A. Infante Ferreira, *Absorption heat pump cycles with* NH_3 *– ionic liquid working pairs,* Applied Energy **204**, 819–830 (2017).

[25] C. Infante Ferreira, *Thermodynamic and physical property data equations for ammonia-lithium nitrate and ammonia-sodium thiocyanate solutions,* Solar Energy **32**, 231–236 (1984).

[26] D.-w. Sun, *Comparison of the performances of* NH_3-H_2O, NH_3-$LiNO_3$ *and* NH_3-*NaSCN absorption refrigeration systems,* Energy Conversion and Management **39**, 357–368 (1998).

[27] L. Garousi Farshi, C. Infante Ferreira, S. Mahmoudi, and M. Rosen, *First and second law analysis of ammonia/salt absorption refrigeration systems,* International Journal of Refrigeration **40**, 111–121 (2014).

[28] M. Zamora, M. Bourouis, A. Coronas, and M. Vallès, *Pre-industrial development and experimental characterization of new air-cooled and water-cooled ammonia/lithium nitrate absorption chillers,* International Journal of Refrigeration **45**, 189–197 (2014).

[29] S. Llamas-Guillén, R. Cuevas, R. Best, and V. Gómez, *Experimental results of a direct air-cooled ammonia–lithium nitrate absorption refrigeration system,* Applied Thermal Engineering **67**, 362–369 (2014).

[30] J. Cerezo, R. Best, and R. Romero, *A study of a bubble absorber using a plate heat exchanger with* NH_3-H_2O, NH_3–$LiNO_3$ *and* NH_3–*NaSCN,* Applied Thermal Engineering **31**, 1869–1876 (2011).

[31] R. H. Reiner, *Evaluation of Ternary Ammonia/Water Fluids for the GAX and Regenerative Absorption Cycles,* Tech. Rep. (Oak Ridge National Lab., TN (United States), 1991).

[32] R. H. Reiner and A. Zaltash, *Densities and viscosities of ternary ammonia/water fluids,* Tech. Rep. (Oak Ridge National Lab., TN (United States), 1993).

[33] S. Steiu, D. Salavera, J. C. Bruno, and A. Coronas, *A basis for the development of new ammonia–water–sodium hydroxide absorption chillers,* International Journal of Refrigeration **32**, 577–587 (2009).

[34] G. Moreno-Quintanar, W. Rivera, and R. Best, *Comparison of the experimental evaluation of a solar intermittent refrigeration system for ice production operating with the mixtures $NH_3/LiNO_3$ and $NH_3/LiNO_3/H_2O$,* Renewable Energy **38**, 62–68 (2012).

[35] F. Táboas, M. Bourouis, and M. Vallès, *Analysis of ammonia/water and ammonia/salt mixture absorption cycles for refrigeration purposes in fishing ships,* Applied Thermal Engineering **66**, 603–611 (2014).

[36] D. Zheng, L. Dong, W. Huang, X. Wu, and N. Nie, *A review of imidazolium ionic liquids research and development towards working pair of absorption cycle,* Renewable and Sustainable Energy Reviews **37**, 47–68 (2014).

[37] J. Palomar, M. Gonzalez-Miquel, J. Bedia, F. Rodriguez, and J. J. Rodriguez, *Task-specific ionic liquids for efficient ammonia absorption,* Separation and Purification Technology **82**, 43–52 (2011).

[38] L. Dong, D. Zheng, N. Nie, and Y. Li, *Performance prediction of absorption refrigeration cycle based on the measurements of vapor pressure and heat capacity of H_2O+[DMIM]DMP system,* Applied Energy **98**, 326–332 (2012).

[39] A. Yokozeki and M. B. Shiflett, *Ammonia Solubilities in Room-Temperature Ionic Liquids,* Industrial & Engineering Chemistry Research **46**, 1605–1610 (2007).

[40] A. Yokozeki and M. B. Shiflett, *Vapor–liquid equilibria of ammonia+ionic liquid mixtures,* Applied Energy **84**, 1258–1273 (2007).

[41] G. Sun, D. Zheng, W. Huang, and L. Dong, *The measurement of ammonia solubility in the ionic liquid 1, 3-dimethylimidazolium dimethylphosphate ([Dmim] DMP),* Journal of Beijing University of Chemical Technology (Natural Science Edition, in Chinese) **39**, 17–21 (2012).

[42] G. Li, Q. Zhou, X. Zhang, L. Wang, S. Zhang, and J. Li, *Solubilities of ammonia in basic imidazolium ionic liquids,* Fluid Phase Equilibria **297**, 34–39 (2010).

[43] W. Chen, S. Liang, Y. Guo, X. Gui, and D. Tang, *Investigation on vapor-liquid equilibria for binary systems of metal ion-containing ionic liquid [bmim]Zn_2Cl_5/NH_3 by experiment and modified UNIFAC model,* Fluid Phase Equilibria **360**, 1–6 (2013).

[44] E. Ruiz, V. R. Ferro, J. De Riva, D. Moreno, and J. Palomar, *Evaluation of ionic liquids as absorbents for ammonia absorption refrigeration cycles using COSMO-based process simulations,* Applied Energy **123**, 281–291 (2014).

[45] A. Cera-Manjarres, *Experimental determination and modelling of thermophysical properties of ammonia/ionic liquid mixtures for absorption refrigeration systems*, Ph.D. thesis, Universitat Rovira i Virgili (2015).

[46] W. Chen, S. Liang, Y. Guo, and D. Tang, *Thermodynamic analysis of an absorption system using [bmim]*Zn_2Cl_5/NH_3 *as the working pair,* Energy Conversion and Management **85**, 13–19 (2014).

[47] Z. Li, X. Zhang, H. Dong, X. Zhang, H. Gao, S. Zhang, J. Li, and C. Wang, *Efficient absorption of ammonia with hydroxyl-functionalized ionic liquids,* RSC Adv. **5**, 81362–81370 (2015).

[48] J. Wang and D. Zheng, *Performance of one and a half-effect absorption cooling cycle of* H_2O*/LiBr system,* Energy Conversion and Management **50**, 3087–3095 (2009).

[49] S. K. Swarnkar, G. Venkatarathnam, D. S. Ayou, J. C. Bruno, and A. Coronas, *a Review on Absorption Heat Pumps and Chillers Using Ionic,* (2012) pp. 35–38.

[50] Y. Kang, Y. Kunugi, and T. Kashiwagi, *Review of advanced absorption cycles: performance improvement and temperature lift enhancement,* International Journal of Refrigeration **23**, 388–401 (2000).

[51] K. Herold, R. Radermacher, and S. Klein, *Absorption Chillers and Heat Pumps, Second Edition* (CRC Press, 2016).

[52] D. Kim and C. Infante Ferreira, *Air-cooled LiBr–water absorption chillers for solar air conditioning in extremely hot weathers,* Energy Conversion and Management **50**, 1018–1025 (2009).

[53] I. Horuz and T. Callander, *Experimental investigation of a vapor absorption refrigeration system,* International Journal of Refrigeration **27**, 10–16 (2004).

[54] N. Darwish, S. Al-Hashimi, and A. Al-Mansoori, *Performance analysis and evaluation of a commercial absorption–refrigeration water–ammonia (ARWA) system,* International Journal of Refrigeration **31**, 1214–1223 (2008).

[55] Y. He and G. Chen, *Experimental study on an absorption refrigeration system at low temperatures,* International Journal of Thermal Sciences **46**, 294–299 (2007).

[56] D.-W. Sun, I. W. Eames, and S. Aphornratana, *Evaluation of a novel combined ejector-absorption refrigeration cycle — I: computer simulation,* International Journal of Refrigeration **19**, 172–180 (1996).

[57] L. Garousi Farshi, A. Mosaffa, C. Infante Ferreira, and M. Rosen, *Thermodynamic analysis and comparison of combined ejector–absorption and single effect absorption refrigeration systems,* Applied Energy **133**, 335–346 (2014).

[58] Q. Dong, C. D. Muzny, A. Kazakov, V. Diky, J. W. Magee, J. A. Widegren, R. D. Chirico, K. N. Marsh, and M. Frenkel, *ILThermo: A Free-Access Web Database for Thermodynamic Properties of Ionic Liquids,* Journal of Chemical & Engineering Data **52**, 1151–1159 (2007).

[59] A. Kazakov, J. Magee, R. D. Chirico, E. Paulechka, V. Diky, C. D. Muzny, K. Kroenlein, and M. Frenkel, *NIST standard reference database 147: NIST ionic liquids database-(ILThermo),* (2013).

[60] P. M. Mathias and J. P. O'Connell, *The Gibbs–Helmholtz Equation and the Thermodynamic Consistency of Chemical Absorption Data,* Industrial & Engineering Chemistry Research **51**, 5090–5097 (2012).

[61] M. B. Shiflett and A. Yokozeki, *Solubility and diffusivity of hydrofluorocarbons in room-temperature ionic liquids,* AIChE Journal **52**, 1205–1219 (2006).

[62] M. Radspieler and C. Schweigler, *Experimental investigation of ionic liquid emim EtSO$_4$ as solvent in a single-effect cycle with adiabatic absorption and desorption,* in *Proceedings of the International Sorption Heat Pump Conference (ISHPC11)* (Padua, Italy, 2011) pp. 125–134.

[63] M.-C. Schneider, R. Schneider, O. Zehnacker, O. Buchin, F. Cudok, A. Kühn, T. Meyer, F. Ziegler, and M. Seiler, *Ionic liquids: new-high performance working fluids for absorption chillers and heat pumps,* in *Proceedings of the International Sorption Heat Pump Conference (ISHPC11)* (Padua, 2011) pp. 95–106.

[64] P. Wasserscheid and M. Seiler, *Leveraging Gigawatt Potentials by Smart Heat-Pump Technologies Using Ionic Liquids,* ChemSusChem **4**, 459–463 (2011).

[65] S. Kim, Y. J. Kim, Y. K. Joshi, A. G. Fedorov, and P. A. Kohl, *Absorption Heat Pump/Refrigeration System Utilizing Ionic Liquid and Hydrofluorocarbon Refrigerants,* Journal of Electronic Packaging **134**, 031009 (2012).

[66] N. Merkel, M. Bücherl, M. Zimmermann, V. Wagner, and K. Schaber, *Operation of an absorption heat transformer using water/ionic liquid as working fluid,* Applied Thermal Engineering **131**, 370–380 (2018).

[67] T. Meyer, R. Kühn, C. Ricart, T. Zegenhagen, and F. Ziegler, *Simulation of an Absorption Refrigerator Working With Ionic Liquids and Natural Refrigerants,* in *Proceedings of the 24th IIR International Congress of Refrigeration* (Yokohama, Japan, 2015) p. 859.

[68] H. M. Ariyadi and A. Coronas, *Absorption Capacity of Ammonia into Ionic Liquids for Absorption Refrigeration Applications,* Journal of Physics: Conference Series **745**, 032105 (2016).

[69] V. V. Wadekar, *Ionic liquids as heat transfer fluids – An assessment using industrial exchanger geometries,* Applied Thermal Engineering **111**, 1581–1587 (2017).

[70] D. B. Boman, D. C. Hoysall, M. A. Staedter, A. Goyal, M. J. Ponkala, and S. Garimella, *A method for comparison of absorption heat pump working pairs,* International Journal of Refrigeration **77**, 149–175 (2017).

[71] D. Chugh, K. Gluesenkamp, O. Abdelaziz, and S. Moghaddam, *Ionic liquid-based hybrid absorption cycle for water heating, dehumidification, and cooling,* Applied Energy **202**, 746–754 (2017).

[72] M. Wang, T. M. Becker, and C. A. Infante Ferreira, *Assessment of vapor–liquid equilibrium models for ionic liquid based working pairs in absorption cycles,* International Journal of Refrigeration **87**, 10–25 (2018).

[73] H. van Ness, *Property changes of mixing,* in *Classical Thermodynamics of Non-Electrolyte Solutions* (Elsevier, 1964) pp. 69–86.

[74] A. Yokozeki and M. B. Shiflett, *Water Solubility in Ionic Liquids and Application to Absorption Cycles,* Industrial & Engineering Chemistry Research **49**, 9496–9503 (2010).

[75] J. Wang, D. Wang, Z. Li, and F. Zhang, *Vapor Pressure Measurement and Correlation or Prediction for Water, 1-Propanol, 2-Propanol, and Their Binary Mixtures with [MMIM][DMP] Ionic Liquid,* Journal of Chemical & Engineering Data **55**, 4872–4877 (2010).

[76] X. Wu, J. Li, L. Fan, D. Zheng, and L. Dong, *Vapor Pressure Measurement of Water+1,3-Dimethylimidazolium Tetrafluoroborate System,* Chinese Journal of Chemical Engineering **19**, 473–477 (2011).

[77] J. Ren, Z. Zhao, and X. Zhang, *Vapor pressures, excess enthalpies, and specific heat capacities of the binary working pairs containing the ionic liquid 1-ethyl-3-methylimidazolium dimethylphosphate,* The Journal of Chemical Thermodynamics **43**, 576–583 (2011).

[78] N. Nie, D. Zheng, L. Dong, and Y. Li, *Thermodynamic Properties of the Water + 1-(2-Hydroxylethyl)-3-methylimidazolium Chloride System,* Journal of Chemical & Engineering Data **57**, 3598–3603 (2012).

[79] X. Zhang and D. Hu, *Performance simulation of the absorption chiller using water and ionic liquid 1-ethyl-3-methylimidazolium dimethylphosphate as the working pair,* Applied Thermal Engineering **31**, 3316–3321 (2011).

[80] X. Zhang and D. Hu, *Performance analysis of the single-stage absorption heat transformer using a new working pair composed of ionic liquid and water,* Applied Thermal Engineering **37**, 129–135 (2012).

[81] Y. J. Kim, S. Kim, Y. K. Joshi, A. G. Fedorov, and P. A. Kohl, *Thermodynamic analysis of an absorption refrigeration system with ionic-liquid/refrigerant mixture as a working fluid,* Energy **44**, 1005–1016 (2012).

[82] S. Kim, N. Patel, and P. A. Kohl, *Performance simulation of ionic liquid and hydrofluorocarbon working fluids for an absorption refrigeration system,* Industrial and Engineering Chemistry Research **52**, 6329–6335 (2013).

[83] L. Dong, D. Zheng, J. Li, N. Nie, and X. Wu, *Suitability prediction and affinity regularity assessment of* H_2O*+imidazolium ionic liquid working pairs of absorption cycle by excess property criteria and UNIFAC model,* Fluid Phase Equilibria **348**, 1–8 (2013).

[84] D. Zheng, L. Dong, and X. Wu, *New Approach for Absorbent Species Selection with Excess Gibbs Function,* Industrial & Engineering Chemistry Research **52**, 9480–9489 (2013).

[85] R. Kato and J. Gmehling, *Measurement and correlation of vapor–liquid equilibria of binary systems containing the ionic liquids* $[EMIM][(CF_3SO_2)_2N]$, $[BMIM][(CF_3SO_2)_2N]$, $[MMIM][(CH_3)_2PO_4]$ *and oxygenated organic compounds respectively water,* Fluid Phase Equilibria **231**, 38–43 (2005).

[86] M. Seiler, C. Jork, A. Kavarnou, W. Arlt, and R. Hirsch, *Separation of azeotropic mixtures using hyperbranched polymers or ionic liquids,* AIChE Journal **50**, 2439–2454 (2004).

[87] P. M. Mathias, *The Gibbs–Helmholtz Equation in Chemical Process Technology,* Industrial & Engineering Chemistry Research **55**, 1076–1087 (2016).

[88] S. I. Sandler, *Chemical, biochemical & engineering thermodynamics* (Wiley India Pvt. Limited, 2006).

[89] D.-Y. Peng and D. B. Robinson, *A New Two-Constant Equation of State,* Industrial & Engineering Chemistry Fundamentals **15**, 59–64 (1976).

[90] D. S. H. Wong and S. I. Sandler, *A theoretically correct mixing rule for cubic equations of state,* AIChE Journal **38**, 671–680 (1992).

[91] A. A. Kiss and C. A. Infante Ferreira, *Heat Pumps in Chemical Process Industry* (CRC Press, 2016) p. 422.

[92] J. O. Valderrama and P. A. Robles, *Critical Properties, Normal Boiling Temperatures, and Acentric Factors of Fifty Ionic Liquids,* Industrial & Engineering Chemistry Research **46**, 1338–1344 (2007).

[93] Z. Lei, J. Zhang, Q. Li, and B. Chen, *UNIFAC Model for Ionic Liquids,* Industrial & Engineering Chemistry Research **48**, 2697–2704 (2009).

[94] M. Ramdin, T. Z. Olasagasti, T. J. H. Vlugt, and T. W. De Loos, *High pressure solubility of* CO_2 *in non-fluorinated phosphonium-based ionic liquids,* The Journal of Supercritical Fluids **82**, 41–49 (2013).

[95] J.-F. Wang, C.-X. Li, Z.-H. Wang, Z.-J. Li, and Y.-B. Jiang, *Vapor pressure measurement for water, methanol, ethanol, and their binary mixtures in the presence of an ionic liquid 1-ethyl-3-methylimidazolium dimethylphosphate,* Fluid Phase Equilibria **255**, 186–192 (2007).

[96] X. Zhang, D. Hu, and Z. Zhao, *Measurement and prediction of excess enthalpies for ternary solutions 1-ethyl-3-methylimidazolium dimethylphosphate + methanol or ethanol + water at 298.15 K and at normal atmospheric pressure,* Journal of Chemical and Engineering Data **59**, 205–211 (2014).

[97] M. S. Kelkar, W. Shi, and E. J. Maginn, *Determining the Accuracy of Classical Force Fields for Ionic Liquids : Atomistic,* Ind. Eng. Chem. Res. **47**, 9115–9126 (2008).

[98] W. Shi and E. J. Maginn, *Molecular simulation of ammonia absorption in the ionic liquid 1-ethyl-3-methylimidazolium bis(trifluoromethylsulfonyl)imide ([emim][Tf_2N]),* AIChE Journal **55**, 2414–2421 (2009), 1402.6991 .

[99] E. W. Lemmon, M. L. Huber, and M. O. McLinden, *NIST reference fluid thermodynamic and transport properties–REFPROP,* (2013).

[100] E.-S. Abumandour, F. Mutelet, and D. Alonso, *Performance of an absorption heat transformer using new working binary systems composed of {ionic liquid and water},* Applied Thermal Engineering **94**, 579–589 (2016).

[101] W. Chen and S. Liang, *Thermodynamic analysis of absorption heat transformers using [mmim]DMP/H_2O and [mmim]DMP/CH_3OH as working fluids,* Applied Thermal Engineering **99**, 846–856 (2016).

[102] M. B. Shiflett and A. Yokozeki, *Absorption Cycle Utilizing Ionic Liquid As Working Fluid,* US patent , US20060197053A1 (2006).

[103] D. S. Ayou, M. R. Currás, D. Salavera, J. García, J. C. Bruno, and A. Coronas, *Performance analysis of absorption heat transformer cycles using ionic liquids based on imidazolium cation as absorbents with 2,2,2-trifluoroethanol as refrigerant,* Energy Conversion and Management **84**, 512–523 (2014).

[104] W. Cai, M. Sen, and S. Paolucci, *Dynamic Modeling of an Absorption Refrigeration System Using Ionic Liquids,* in *Volume 6: Energy Systems: Analysis, Thermodynamics and Sustainability* (ASME, Seattle, 2007) pp. 227–236.

[105] O. Kotenko, *Potential Analysis of Alternative Absorption Heat Pumping Processes with Special Emphasis on Sodium Hydroxide as Additive,* Ph.D. thesis, Graz University of Technology (2012).

[106] B. K. Harrison and W. H. Seaton, *Solution to missing group problem for estimation of ideal gas heat capacities,* Industrial & Engineering Chemistry Research **27**, 1536–1540 (1988).

[107] C. L. Sassen, R. A. C. Van Kwartel, H. J. Van der Kooi, and J. De Swaan Arons, *Vapor-liquid equilibria for the system ammonia + water up to the critical region,* Journal of Chemical & Engineering Data **35**, 140–144 (1990).

[108] Y. U. Paulechka, *Heat Capacity of Room-Temperature Ionic Liquids: A Critical Review,* Journal of Physical and Chemical Reference Data **39**, 033108 (2010).

[109] Z. He, Z. Zhao, X. Zhang, and H. Feng, *Thermodynamic properties of new heat pump working pairs: 1,3-Dimethylimidazolium dimethylphosphate and water, ethanol and methanol,* Fluid Phase Equilibria **298**, 83–91 (2010).

[110] Y. H. Yu, A. N. Soriano, and M. H. Li, *Heat capacities and electrical conductivities of 1-ethyl-3-methylimidazolium-based ionic liquids,* The Journal of Chemical Thermodynamics **41**, 103–108 (2009).

[111] D. Waliszewski, *Heat capacities of the mixtures of ionic liquids with methanol at temperatures from 283.15K to 323.15K,* The Journal of Chemical Thermodynamics **40**, 203–207 (2008).

[112] Y. U. Paulechka, A. V. Blokhin, and G. J. Kabo, *Evaluation of thermodynamic properties for non-crystallizable ionic liquids,* Thermochimica Acta **604**, 122–128 (2015).

[113] G. J. Kabo, A. V. Blokhin, Y. U. Paulechka, A. G. Kabo, M. P. Shymanovich, and J. W. Magee, *Thermodynamic Properties of 1-Butyl-3-methylimidazolium Hexafluorophosphate in the Condensed State,* Journal of Chemical & Engineering Data **49**, 453–461 (2004).

[114] Y. Paulechka, A. Blokhin, G. Kabo, and A. Strechan, *Thermodynamic properties and polymorphism of 1-alkyl-3-methylimidazolium bis(triflamides),* The Journal of Chemical Thermodynamics **39**, 866–877 (2007).

[115] P. Navarro, M. Larriba, E. Rojo, J. García, and F. Rodríguez, *Thermal Properties of Cyano-Based Ionic Liquids,* Journal of Chemical & Engineering Data **58**, 2187–2193 (2013).

[116] J. Salgado, T. Regueira, L. Lugo, J. Vijande, J. Fernández, and J. García, *Density and viscosity of three (2,2,2-trifluoroethanol + 1-butyl-3-methylimidazolium) ionic liquid binary systems,* The Journal of Chemical Thermodynamics **70**, 101–110 (2014).

[117] A. Hofmann, M. Migeot, and T. Hanemann, *Investigation of Binary Mixtures Containing 1-Ethyl-3-methylimidazolium Bis(trifluoromethanesulfonyl)azanide and Ethylene Carbonate,* Journal of Chemical and Engineering Data **61**, 114–123 (2016).

[118] M. G. Freire, A. R. R. Teles, M. A. A. Rocha, B. Schröder, C. M. S. S. Neves, P. J. Carvalho, D. V. Evtuguin, L. M. N. B. F. Santos, and J. A. P. Coutinho, *Thermophysical Characterization of Ionic Liquids Able To Dissolve Biomass,* Journal of Chemical & Engineering Data **56**, 4813–4822 (2011).

[119] J. M. Wimby and T. S. Berntsson, *Viscosity and density of aqueous solutions of lithium bromide, lithium chloride, zinc bromide, calcium chloride and lithium nitrate. 1. Single salt solutions,* Journal of Chemical & Engineering Data **39**, 68–72 (1994).

[120] J. Römer and M. Jong, *Warmte- en koedevraagpatronen in de utiliteitsbouw (in Dutch)*, Tech. Rep. (ECN, 1999).

[121] Y.-Y. Yan, H.-C. Lio, and T.-F. Lin, *Condensation heat transfer and pressure drop of refrigerant R-134a in a plate heat exchanger,* International Journal of Heat and Mass Transfer **42**, 993–1006 (1999).

[122] M. S. Khan, T. S. Khan, M.-C. Chyu, and Z. H. Ayub, *Experimental investigation of evaporation heat transfer and pressure drop of ammonia in a 30° chevron plate heat exchanger,* International Journal of Refrigeration **35**, 1757–1765 (2012).

[123] B. Thonon and A. Bontemps, *Condensation of Pure and Mixture of Hydrocarbons in a Compact Heat Exchanger: Experiments and Modelling,* Heat Transfer Engineering **23**, 3–17 (2002).

[124] C. M. Tenney, M. Massel, J. M. Mayes, M. Sen, J. F. Brennecke, and E. J. Maginn, *A Computational and Experimental Study of the Heat Transfer Properties of Nine Different Ionic Liquids,* Journal of Chemical & Engineering Data **59**, 391–399 (2014).

[125] DACE, *DACE (Dutch Association of Cost Engineers) priceprice booklet November 2015*, 31st ed. (The Hague, 2015).

[126] Eurostat, *Energy price statistics,* (2016).

[127] L. Chen, M. Sharifzadeh, N. Mac Dowell, T. Welton, N. Shah, and J. P. Hallett, *Inexpensive ionic liquids: $[HSO_4]^-$-based solvent production at bulk scale,* Green Chem. **16**, 3098–3106 (2014).

[128] Honeywell UOP, *Honeywell UOP Introduces Ionic Liquids Alkylation Technology,* (2016).

[129] M. J. Earle, J. M. Esperança, M. A. Gilea, J. N. Canongia Lopes, L. P. Rebelo, J. W. Magee, K. R. Seddon, and J. A. Widegren, *The distillation and volatility of ionic liquids,* Nature **439**, 831–834 (2006).

[130] M. Wang, T. M. Becker, B. A. Schouten, T. J. H. Vlugt, and C. A. Infante Ferreira, *Ammonia/ionic liquid based double-effect vapor absorption refrigeration cycles driven by waste heat for cooling in fishing vessels,* Energy Conversion and Management **174**, 824–843 (2018).

[131] T. W. P. Smith, J. P. Jalkanen, B. A. Anderson, J. J. Corbett, J. Faber, S. Hanayama, E. O'Keeffe, S. Parker, L. Johansson, L. Aldous, C. Raucci, M. Traut, S. Ettinger, D. Nelissen, D. S. Lee, S. Ng, A. Agrawal, J. J. Winebrake, M. Hoen, S. Chesworth, and A. Pandey, *Third IMO GHG Study 2014*, Tech. Rep. (International Maritime Organization (IMO), London, 2014).

[132] G. Shu, Y. Liang, H. Wei, H. Tian, J. Zhao, and L. Liu, *A review of waste heat recovery on two-stroke IC engine aboard ships,* Renewable and Sustainable Energy Reviews **19**, 385–401 (2013).

[133] MAN Diesel & Turbon LTD, *Thermo Efficiency System for Reduction of Fuel Consumption and* CO_2 *Emission*, Tech. Rep. (Copenhagen, 2014).

[134] J. Fernández-Seara, A. Vales, and M. Vázquez, *Heat recovery system to power an onboard* NH_3-H_2O *absorption refrigeration plant in trawler chiller fishing vessels,* Applied Thermal Engineering **18**, 1189–1205 (1998).

[135] T. Cao, H. Lee, Y. Hwang, R. Radermacher, and H. H. Chun, *Performance investigation of engine waste heat powered absorption cycle cooling system for shipboard applications,* Applied Thermal Engineering **90**, 820–830 (2015).

[136] M. Wang and C. A. Infante Ferreira, *Performance analysis of double-effect absorption heat pump cycle using* NH_3*/ILs pairs,* in *Proc. of the 12th IEA Heat Pump Conference* (Rotterdam,NL, 2017).

[137] B. Schouten, *Advanced NH3 based absorption refrigeration cycles: Modelling of the ionic liquid based double-effect cycles*, Master's thesis, Delft University of Technology (2017).

[138] T. M. Becker, M. Wang, A. Kabra, S. H. Jamali, M. Ramdin, D. Dubbeldam, C. A. Infante Ferreira, and T. J. H. Vlugt, *Absorption Refrigeration Cycles with Ammonia–Ionic Liquid Working Pairs Studied by Molecular Simulation,* Industrial & Engineering Chemistry Research **57**, 5442–5452 (2018).

[139] D. Frenkel and B. Smit, *Understanding molecular simulation: from algorithms to applications* (Academic press, 2001).

[140] M. P. Allen and D. J. Tildesley, *Computer simulation of liquids* (Oxford University Press, 2017).

[141] H. Liu and E. Maginn, *A molecular dynamics investigation of the structural and dynamic properties of the ionic liquid 1-n-butyl-3-methylimidazolium bis(trifluoromethanesulfonyl)imide,* The Journal of Chemical Physics **135**, 124507 (2011).

[142] M. Ramdin, S. P. Balaji, J. M. Vicent-Luna, J. J. Gutiérrez-Sevillano, S. Calero, T. W. de Loos, and T. J. H. Vlugt, *Solubility of the Precombustion Gases CO_2 , CH_4, CO, H_2,N_2, and H_2S in the Ionic Liquid [bmim][Tf_2N] from Monte Carlo Simulations,* The Journal of Physical Chemistry C **118**, 23599–23604 (2014).

[143] W. Shi and E. J. Maginn, *Continuous Fractional Component Monte Carlo: An Adaptive Biasing Method for Open System Atomistic Simulations,* Journal of Chemical Theory and Computation **3**, 1451–1463 (2007).

[144] M. Ramdin, T. M. Becker, S. H. Jamali, M. Wang, and T. J. H. Vlugt, *Computing equation of state parameters of gases from Monte Carlo simulations,* Fluid Phase Equilibria **428**, 174–181 (2016).

[145] A. Poursaeidesfahani, R. Hens, A. Rahbari, M. Ramdin, D. Dubbeldam, and T. J. H. Vlugt, *Efficient Application of Continuous Fractional Component Monte Carlo in the Reaction Ensemble,* Journal of Chemical Theory and Computation **13**, 4452–4466 (2017).

[146] H. Liu, E. Maginn, A. E. Visser, N. J. Bridges, and E. B. Fox, *Thermal and Transport Properties of Six Ionic Liquids: An Experimental and Molecular Dynamics Study,* Industrial & Engineering Chemistry Research **51**, 7242–7254 (2012).

[147] J. N. Canongia Lopes and A. A. H. Pádua, *Molecular Force Field for Ionic Liquids III: Imidazolium, Pyridinium, and Phosphonium Cations; Chloride, Bromide, and Dicyanamide Anions,* The Journal of Physical Chemistry B **110**, 19586–19592 (2006).

[148] L. Zhang and J. I. Siepmann, *Development of the trappe force field for ammonia,* Collection of Czechoslovak Chemical Communications **75**, 577–591 (2010).

[149] D. Dubbeldam, A. Torres-Knoop, and K. S. Walton, *On the inner workings of Monte Carlo codes,* Molecular Simulation **39**, 1253–1292 (2013).

[150] D. Dubbeldam, S. Calero, D. E. Ellis, and R. Q. Snurr, *RASPA: Molecular simulation software for adsorption and diffusion in flexible nanoporous materials,* Molecular Simulation **42**, 81–101 (2016).

[151] D. Matkowska and T. Hofman, *High-pressure volumetric properties of ionic liquids: 1-butyl-3-methylimidazolium tetrafluoroborate, [C4mim][BF4], 1-butyl-3-methylimidazolium methylsulfate [C4mim][MeSO4] and 1-ethyl-3-methylimidazolium ethylsulfate, [C2mim][EtSO4],* Journal of Molecular Liquids **165**, 161–167 (2012).

[152] L. E. Ficke, R. R. Novak, and J. F. Brennecke, *Thermodynamic and Thermophysical Properties of Ionic Liquid + Water Systems,* Journal of Chemical & Engineering Data **55**, 4946–4950 (2010).

[153] M. Tariq, A. P. Serro, J. L. Mata, B. Saramago, J. M. Esperança, J. N. Canongia Lopes, and L. P. N. Rebelo, *High-temperature surface tension and density measurements of 1-alkyl-3-methylimidazolium bistriflamide ionic liquids,* Fluid Phase Equilibria **294**, 131–138 (2010).

[154] C. A. Nieto de Castro, M. J. V. Lourenço, A. P. C. Ribeiro, E. Langa, S. I. C. Vieira, P. Goodrich, and C. Hardacre, *Thermal Properties of Ionic Liquids and IoNanofluids of Imidazolium and Pyrrolidinium Liquids,* Journal of Chemical & Engineering Data **55**, 653–661 (2010).

[155] A. F. Ferreira, P. N. Simões, and A. G. Ferreira, *Quaternary phosphonium-based ionic liquids: Thermal stability and heat capacity of the liquid phase,* The Journal of Chemical Thermodynamics **45**, 16–27 (2012).

[156] C. Vasilescu and C. A. Infante Ferreira, *Solar driven multi-effect sub-zero ammonia based sorption cycles,* in *Proceedings of the International Sorption Heat Pump Conference (ISHPC11)* (Padua, Italy, 2011) pp. 885–892.

[157] Wartsila, *Wartsila 38 Project Guide*, Tech. Rep. (Wartsila Ship Power Technology, 2008).

[158] B. E. Poling, J. M. Prausnitz, and J. P. O'Connell, *The properties of gases and liquids* (McGraw-Hill, 2001).

[159] M. Arun, M. Maiya, and S. Murthy, *Performance comparison of double-effect parallel-flow and series flow water–lithium bromide absorption systems,* Applied Thermal Engineering **21**, 1273–1279 (2001).

[160] G. Petrecca, *Industrial Energy Management: Principles and Applications* (Springer Science & Business Media, Boston, MA, 1993) Chap. 9. Cogeneration Plants.

[161] Y. Cao and T. Mu, *Comprehensive Investigation on the Thermal Stability of 66 Ionic Liquids by Thermogravimetric Analysis,* Industrial & Engineering Chemistry Research **53**, 8651–8664 (2014).

[162] P. Liu, M. Wang, and Z.-M. Cheng, *Thermal Stability and Vapor–Liquid Equilibrium for Imidazolium Ionic Liquids as Alternative Reaction Media,* Journal of Chemical & Engineering Data **60**, 836–844 (2015).

[163] W.-q. Feng, Y.-h. Lu, Y. Chen, Y.-w. Lu, and T. Yang, *Thermal stability of imidazolium-based ionic liquids investigated by TG and FTIR techniques,* Journal of Thermal Analysis and Calorimetry **125**, 143–154 (2016).

[164] F. Heym, B. J. M. Etzold, C. Kern, and A. Jess, *Analysis of evaporation and thermal decomposition of ionic liquids by thermogravimetrical analysis at ambient pressure and high vacuum,* Green Chemistry **13**, 1453–1466 (2011).

[165] M. Villanueva, A. Coronas, J. García, and J. Salgado, *Thermal Stability of Ionic Liquids for Their Application as New Absorbents,* Industrial & Engineering Chemistry Research **52**, 15718–15727 (2013).

[166] B. K. Sovacool, *Valuing the greenhouse gas emissions from nuclear power: A critical survey,* Energy Policy **36**, 2950–2963 (2008).

[167] M. Wang, L. He, and C. A. Infante Ferreira, International Journal of Heat and Mass Transfer , 1302–1317.

[168] T. Meyer, M. Winker, S. Bergemann, R. Kühn, C. Ricart, and F. Ziegler, *Experimental Investigation of an Absorption Refrigerator Working With Ionic Liquid and Ethanol,* (2017), 10.18462/iir.tptpr.2017.0035.

[169] J. Bedia, J. Palomar, M. Gonzalez-Miquel, F. Rodriguez, and J. J. Rodriguez, *Screening ionic liquids as suitable ammonia absorbents on the basis of thermodynamic and kinetic analysis,* Separation and Purification Technology **95**, 188–195 (2012).

[170] H. M. Ariyadi, A. Cera-Manjarres, and A. Coronas, *Absorption Behaviour and Diffusivity of Ammonia in Ionic Liquids,* in *5th IIR International Conference on Thermophysical Properties and Transfer Processes of Refrigerants* (2017).

[171] W. Chen, B. Zhang, Z. Liu, M. Zhao, and Z. Miao, *Investigation of the mutual diffusion coefficients of [mmim]DMP/H_2O and [mmim]DMP/CH_3OH*

at atmospheric pressure, International Journal of Heat and Mass Transfer **111**, 559–569 (2017).

[172] Y. T. Kang, A. Akisawa, and T. Kashiwagi, *Analytical investigation of two different absorption modes,* International Journal of Refrigeration **23**, 430–443 (2000).

[173] J. Cerezo, M. Bourouis, M. Vallès, A. Coronas, and R. Best, *Experimental study of an ammonia-water bubble absorber using a plate heat exchanger for absorption refrigeration machines,* Applied Thermal Engineering **29**, 1005–1011 (2009).

[174] J. Cerezo, R. Best, M. Bourouis, and A. Coronas, *Comparison of numerical and experimental performance criteria of an ammonia–water bubble absorber using plate heat exchangers,* International Journal of Heat and Mass Transfer **53**, 3379–3386 (2010).

[175] C. Oronel, C. Amaris, M. Bourouis, and M. Vallès, *Heat and mass transfer in a bubble plate absorber with* $NH_3/LiNO_3$ *and* $NH_3/(LiNO_3 + H_2O)$ *mixtures,* International Journal of Thermal Sciences **63**, 105–114 (2013).

[176] D. Triché, S. Bonnot, M. Perier-Muzet, F. Boudéhenn, H. Demasles, and N. Caney, *Experimental and numerical study of a falling film absorber in an ammonia-water absorption chiller,* International Journal of Heat and Mass Transfer **111**, 374–385 (2017).

[177] X. Tao, M. P. Nuijten, and C. A. Infante Ferreira, *Two-phase vertical downward flow in plate heat exchangers: Flow patterns and condensation mechanisms,* International Journal of Refrigeration **85**, 489–510 (2018).

[178] T. Jin, M. Wang, and K. Tang, *Simulation and performance analysis of a heat transfer tube in SuperORV,* Cryogenics **61**, 127–132 (2014).

[179] S. M. Zivi, *Estimation of Steady-State Steam Void-Fraction by Means of the Principle of Minimum Entropy Production,* Journal of Heat Transfer **86**, 247–251 (1964).

[180] C. F. Amaris Castilla, *Intensification of* NH_3 *bubble absorption process using advanced surfaces and carbon nanotubes for* $NH_3/LINO_3$ *absorption chillers,* Ph.D. thesis, Universitat Rovira i Virgili (2013).

[181] T. L. Bergman, A. S. Lavine, F. P. Incropera, and D. P. Dewitt, *Fundamentals of Heat and Mass Transfer* (John Wiley & Sons, Inc., 2011).

[182] B. Michel, N. Le Pierrès, and B. Stutz, *Performances of grooved plates falling film absorber,* Energy **138**, 103–117 (2017).

[183] G. Grossman, *Simultaneous heat and mass transfer in film absorption under laminar flow,* International Journal of Heat and Mass Transfer **26**, 357–371 (1983).

[184] N. Brauner, *Non-isothermal vapour absorption into falling film,* International Journal of Heat and Mass Transfer **34**, 767–784 (1991).

[185] S. Libotean, D. Salavera, M. Valles, X. Esteve, and A. Coronas, *Vapor-Liquid Equilibrium of Ammonia + Lithium Nitrate + Water and Ammonia + Lithium Nitrate Solutions from (293.15 to 353.15) K,* Journal of Chemical & Engineering Data **52**, 1050–1055 (2007).

[186] S. Libotean, A. Martín, D. Salavera, M. Valles, X. Esteve, and A. Coronas, *Densities, Viscosities, and Heat Capacities of Ammonia + Lithium Nitrate and Ammonia + Lithium Nitrate + Water Solutions between (293.15 and 353.15) K,* Journal of Chemical & Engineering Data **53**, 2383–2388 (2008).

[187] Y. Cuenca, D. Salavera, A. Vernet, A. S. Teja, and M. Vallès, *Thermal conductivity of ammonia + lithium nitrate and ammonia + lithium nitrate + water solutions over a wide range of concentrations and temperatures,* International Journal of Refrigeration **38**, 333–340 (2014).

[188] M. Venegas, M. Izquierdo, P. Rodríguez, and A. Lecuona, *Heat and mass transfer during absorption of ammonia vapour by* $LiNO_3$*–*NH_3 *solution droplets,* International Journal of Heat and Mass Transfer **47**, 2653–2667 (2004).

[189] M. E. V. Valkenburg, R. L. Vaughn, M. Williams, and J. S. Wilkes, *Thermochemistry of ionic liquid heat-transfer fluids,* Thermochimica Acta **425**, 181–188 (2005).

[190] A. P. Fröba, M. H. Rausch, K. Krzeminski, D. Assenbaum, P. Wasserscheid, and A. Leipertz, *Thermal Conductivity of Ionic Liquids: Measurement and Prediction,* International Journal of Thermophysics **31**, 2059–2077 (2010).

[191] J. Gao and N. J. Wagner, *Non-ideal viscosity and excess molar volume of mixtures of 1-butyl-3-methylimidazolium tetrafluoroborate (*$[C_4mim][BF_4]$*) with water,* Journal of Molecular Liquids **223**, 678–686 (2016).

[192] H. F. D. Almeida, A. R. R. Teles, J. A. Lopes-Da-Silva, M. G. Freire, and J. A. P. Coutinho, *Influence of the anion on the surface tension of 1-ethyl-3- methylimidazolium-based ionic liquids,* Journal of Chemical Thermodynamics **54**, 49–54 (2012).

[193] M. H. Ghatee and A. R. Zolghadr, *Surface tension measurements of imidazolium-based ionic liquids at liquid-vapor equilibrium,* Fluid Phase Equilibria **263**, 168–175 (2008).

[194] R. B. Bird, W. E. Stewart, and E. N. Lightfoot, *Transport Phenomena*, Wiley International edition (Wiley, 2007).

[195] D. Morgan, L. Ferguson, and P. Scovazzo, *Diffusivities of gases in room-temperature ionic Liquids: Data and correlations obtained using a lag-time technique,* Industrial and Engineering Chemistry Research **44**, 4815–4823 (2005).

[196] Ž. Olujić and A. F. Seibert, *Predicting the Liquid Phase Mass Transfer Resistance of Structured Packings,* Chemical and Biochemical Engineering Quarterly Journal **28**, 409–424 (2014).

[197] W. a. Miller and M. Keyhani, *The Correlation of Simultaneous Heat and Mass Transfer Experimental Data for Aqueous Lithium Bromide Vertical Falling Film Absorption,* Journal of Solar Energy Engineering **123**, 30 (2001).

[198] C. A. Infante Ferreira, *Vertical tubular absorbers for ammonia-salt absorption refrigeration,* Ph.D. thesis, Delft University of Technology (1985).

[199] R. E. Treybal, *Mass-transfer operations*, 3rd ed. (McGraw-Hill. Inc., 1980).

[200] Y. Kim, W. Choi, J. Jang, K.-P. Yoo, and C. Lee, *Solubility measurement and prediction of carbon dioxide in ionic liquids,* Fluid Phase Equilibria **228-229**, 439–445 (2005).

Curriculum Vitæ

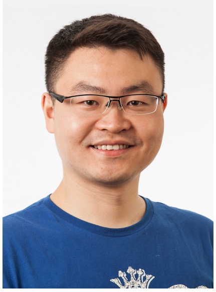

Meng Wang (王 萌) was born on 28th June 1989 in Zhengyangguan of Shouxian, China. He spent his childhood in this small but historical town beside Huai River, before he moved to Lu'an for his senior high school study in 2004. In 2011, he obtained his B.Sc degree in the major of Process Equipment & Control Engineering, from Beijing University of Chemical Technology, after finishing a project of reliability analysis for a double-shell liquefied nitrogen vessel using finite element method. Subsequently, he started an M.Sc. program at Zhejiang University, where he was involved in a research of a novel type of liquefied natural gas vaporizer in the Institute of Refrigeration and Cryogenics. In 2014, he completed his M.Sc study, being recognized as an Outstanding Graduate. With financial support by the China Scholarship Council, he came to Delft University of Technology as a PhD candidate in the Engineering Thermodynamics group headed by Prof.dr.ir Thijs Vlugt in the same year. During this period, he was promoted and daily-supervised by Dr.ir. Carlos A. Infante Ferreira, for the project of ammonia absorption heat pumps with ionic liquids. His research concentrated on the study of the systems from thermodynamic and heat and mass transfer perspectives. Meanwhile he attended various voluntary activities, for instance as a reviewer for journals Applied Energy, International Journal of Refrigeration and Applied Thermal Engineering, and as a volunteer for events organized by the Association of Chinese Students and Scholars in the Netherlands - Delft branch.

Contact: M.Wang-2020@outlook.com

LIST OF PUBLICATIONS

JOURNAL PAPERS

1. **Meng Wang***, Lijuan He, Carlos A. Infante Ferreira. *Ammonia absorption in ionic liquids - based mixtures in plate heat exchanger studied by a semi-empirical heat and mass transfer framework*, International Journal of Heat and Mass Transfer **134**, 1302-1317, (2019).

2. **Meng Wang***, Tim M. Becker, Bob A. Schouten, Carlos A. Infante Ferreira, Thijs J. H. Vlugt. *Ammonia/ionic liquid based double-effect vapor absorption refrigeration cycles driven by waste heat for cooling in fishing vessels*, Energy Conversion and Management **174**, 824-843, (2018).

3. **Meng Wang***, Tim M. Becker, Carlos A. Infante Ferreira. *Assessment of vapor-liquid equilibrium models for ionic liquid based working pairs in absorption cycles*, International Journal of Refrigeration **87**, 10-25, (2018).

4. **Meng Wang***, Carlos A. Infante Ferreira. *Absorption heat pump cycles with NH_3 - ionic liquid working pairs*, Applied Energy **204**, 819-830, (2017).

5. Tim M. Becker, **Meng Wang**, Abhishek Kabra, Seyed H. Jamali, Mahinder Ramdin, David Dubbeldam, Carlos A. Infante Ferreira, Thijs J. H. Vlugt*. *Absorption refrigeration cycles with ammonia - ionic liquid working pairs studied by molecular simulation*, Industrial & Engineering Chemistry Research **57(15)**, 5442-5452, (2018).

6. Mahinder Ramdin, Tim M. Becker, Seyed H. Jamali, **Meng Wang**, Thijs J. H. Vlugt*. *Computing equation of state parameters of gases from Monte Carlo simulations*, Fluid Phase Equilibria **428**, 174-181, (2016).

CONFERENCE PAPERS

1. **Meng Wang***, Tim M. Becker, Carlos A. Infante Ferreira. *Ionic liquid - ammonia double-effect absorption refrigeration cycles for refrigeration in fishing vessels*, In Proceedings of the 13th IIR Gustav Lorentzen Conference (GL2018), **Paper No.1130**, Valencia, Spain, (2018).

2. **Meng Wang***, Tim M. Becker, Carlos A. Infante Ferreira. *Performance analysis of double-effect absorption heat pump cycle using NH_3/ILs pairs*, In Proceedings of the 12th IEA Heat Pump Conference (HPC2017), **O.4.2.1**, Rotterdam, The Netherlands, (2017).

3. Abhishek Kabra, Tim M. Becker, **Meng Wang***, Carlos A. Infante Ferreira, Thijs J. H. Vlugt. *Molecular simulation of NH_3/ionic liquid mixtures for absorption heat pump cycles*, In Proceedings of the 12th IEA Heat Pump Conference (HPC2017), **O.4.6.3**, Rotterdam, The Netherlands, (2017).

4. **Meng Wang***, Carlos A. Infante Ferreira. *Excess enthalpy prediction for ionic liquids based absorption systems*, In Proceedings of the 5th IIR Conference on Thermophysical Properties and Transfer Processes of Refrigerants (TPTPR2017), **Paper No.TP-0092**, Seoul, South Korea, (2017).

5. **Meng Wang***, Carlos A. Infante Ferreira. *Performance prediction of single-effect absorption heat pump cycles using ionic liquids*, In Proceedings of the 12th IIR Gustav Lorentzen Conference on Natural Refrigerants (GL2016), **Paper No.1144**, Edinburgh, UK, (2016).

6. **Meng Wang***, Carlos A. Infante Ferreira. *Screening criteria for ILs used in NH_3 based absorption heat pump systems*, In Proceedings of the 16th International Refrigeration and Air conditioning conference, **Paper No.2285**, West Lafayette, USA, (2016).

7. **Meng Wang***, Carlos A. Infante Ferreira. *Assessment of vapor-liquid equilibrium models for ionic liquids based absorption systems*, In Proceedings of the 24th IIR International Congress of Refrigeration (ICR2015), **Paper No.0578**, Yokohama, Japan, (2015).

ACKNOWLEDGEMENTS

Accomplishing of my PhD study could not be fulfilled without the help from many people. Doing it in a completely different cultural environment makes this journey more attractive and fascinating. At this moment, I would like to express my sincere gratitude to all the people who helped me with my research and my life in different ways during my PhD journey.

My first thankfulness goes to my promoter and daily supervisor - Dr. ir. Carlos A. Infante Ferreira. Thank you for providing me with the chance to study and work at TU Delft. Thanks for your care during my life in NL, especially at the shifting moments at the start and terminal of my PhD study. The work could not be carried through smoothly without your quick responses of manuscripts, patient correction of my language, timely reminding of deadlines, or kind suggestions in the progress meetings. Your comments always hit points of problems I encountered. What I admire is not only your knowledge but also the way how you help young generations. You are full of schedules with students, for lectures or for meetings. You have a strict standard of academic outputs, but your actions in assisting me could be friendly and easy-going. You are open to new ideas from my side, and supporting me constructively. I am grateful for your nomination to the IIR, for your recommendation during my job hunting, and for your introduction of me and my work to peers with pride. Providing me chances of attending conferences all over the world, I was fortunately involved in the international network of refrigeration. The cooperation with you is so enjoyable that I sometimes worried if I can have the same good time with my boss in next career chapters. There were a few moments when I even expected to continue working my PhD study, if I don't need to think about the career and life for next steps. I regret that I cannot go on working with you. Nevertheless, your instructions and impacts definitely benefit me in my life. I will miss you very much, and also your hand-made Dutch apple pies and Portuguese codfish cakes!

I would like to thank my promoter and the Chair of the Group Engineering Thermodynamic - Prof. Dr. ir. Thijs J. H. Vlugt. It is my great honor to have been a member of this group. Thank you for initiating the sub-project on molecular simulation and offering me a chance to collaborate with my colleagues with this expertise. Thanks for the discussion and suggestions during the group meetings.

Prof. Dr. A. Coronas witnessed most of my oral presentations in conferences. Your constant regards and care in the past four years helped me a lot. Thanks

for your time in reading the dissertation and for your presence in my defense. Thanks to Prof. Dr.-Ing. F. Ziegler for being the committee member. I met you at my first international conference experience in Yokohama, Japan. It is my great honor that I have your presences at my first and also the final shows of the project. Dr.ir. M. van der Pal led a nice lab tour of ECN for colleagues from Gree after the 2017 Heat Pump Conference. I happened to be invited to join that visiting. Thank you again for spending time reading my dissertation. It is my honor that Prof. dr. L.C.M. Itard and Prof.dr.ir. B.J. Boersma accepted the invitation to be committee members. Thanks for your time in evaluating the dissertation and your presences in my defense.

It is my luck to have partners to experience the same challenges when pursuing PhD. Especially with Tim, I will always remember the moments we shared during collaborations, students supervision, weekly swimming, nieuwjaarsduik, job hunting and of course when we were awarded the poster prize as a group. Thanks to Abhishek and Bob for your nice work with me! I also learnt a lot when working with you guys!

To Hongxia, Vilborg and Xuan for the deep discussions of our projects and help during constructing setups, and the pleasant memories with you in exploring Hakone, Panmunjom, and Valencia after conferences. Thanks to Mahinder, Seyed. I was happy to work with you and had our names written together in publications. Thanks to Li-Chiang, Brian, Othon, Bernardo, Zhaochuan, Dennis, Martijn, Mariëtte, Karsten, Dion, Julia, Ali, Reza, Sebastian, Noura, Mate, and Hirad in our group for discussions during group meetings. Special thanks to Remco for translating the summary of this dissertation.

I will always remember the colorful life I shared with my junior and senior colleagues in the PE building. Thanks to Guido, Javier, Sergio and Hakan, for your companies and encouragements during our office time. Thank Weiwei, Marloes, Fatemeh, Mohammed, Elyas, Daniel, Yashar, Ali, Jie, Carla, Vikran, Alessandro, Nikolaos, Farnaz, Rong, Lalit, Rumen, Fatma, Maryam, Vincent, Gustavo, Mayra, Sathish, Uttiya, Stephan, Simone, Peng, Liangyuan, Christos, Rishabh, Xiangmei, Ming, Liyuan, Hesheng, Liang, Xu, Likun, Bin, Bala, Sabrina, Zebing, Shufan, Fan and Prof. Dr. Wiebren de Jong, Prof. Dr. Andrzej Stankiewicz, Prof. Dr. Dirk Roekaerts, Dr. Wim Haije, Mr. Theo Woudstra, Dr. René Delfos, Dr. Rene Pecnik and my other colleagues and friends, Thanks for your inspirations, culture and experience sharing, encouragements and assistance.

Thanks for the kind help in the daily work provided by the secretary team: Leslie, Marjolijn, Ilona, Saskia, Helma, Eveline and Rob. I would like to express my gratitude to our DEMO team, especially Jaap, Michel, Martijn and Daniel for the indispensable support when constructing my setup in the lab.

Thanks to Mr. Cees Timmers for initiating the PhD program with the help

of TU Delft and CSC. Thanks to the Chinese Embassy in NL and in particular Counselor Meng and Mr. Wang of the Education Section for the help during my stay in NL. Your kind care made me feel at home as a Chinese overseas student. Special thanks to Xuanzi and Shaobo for your trusts of being my warrantors of my study abroad.

Many thanks to the International Institute of Refrigerant and Institute of Refrigeration (UK) for recognizing this work and granting me a best student paper award in the GL2016 conference.

I would like to express my respect and gratitude to Prof. Dr. ir Henk van der Ree, Prof. Dr. Ruzhu Wang, Prof. Dr. Xianting Li, Prof. Dr. Srinivas Garimella, Prof. Dr. Yong Tea Kang, Dr. Wei Xu, Mr. Jan Gerritsen, Dr. Chaobin Dang, Mr. Rong Zhuang, Mr. Xiangfei Liang and others from refrigeration and heat pump academia and industry for their kind advice and encouragements in conferences.

Also, thanks to Dr. Thomas Mayer from TU Berlin and Dr. Hifni Ariyadi from Universitat Rovira i Virgili for sharing your work on ionic liquids based refrigeration. Thanks to Dr. Sung Joo Hong from Tokyo University for your treats of chimaek and soju in Seoul. The nice gatherings, with you starting from Purdue and then joined by your colleagues, Mr. Jiachen He, and other funny guys such as Mr. Mark Redo from Waseda University and Mr. Yizhou Liu from Broad in Rotterdam and Valencia, were my most expected sub-events besides the conferences. My gratitude also goes to Dr. Monika Ignatowicz, Mr. Pavel Makhnatch, Mr. Mazyar Karampour, Mr. Chang Su and Mr. Tianhao Xu from KTH, Dr. Bin Hu, Dr. Shuai Du and Dr. Yaodong Tu from SJTU, Dr. Zhequan Jin from NTNU, Mr. Tianle Hu from Tsinghua and Hongbo Li from Gree for our meetings and outings together. It is my pleasure to know you, such outstanding young scholars in the refrigeration community! I wish bright futures for all of you!

At the initial stage of my PhD study, Prof. Dr. Guangming Chen, Prof. Dr. Xiaohong Han and Dr. Xuehui Wang from Zhejiang University, and Prof. Dr. Danxing Zheng, Dr. Weijia Huang and Dr. Li Dong from Beijing University of Chemical Technology have guided and inspired me with fundamentals of vapor-liquid equilibria, absorption refrigeration and ionic liquids. This project could have not been kicked off smoothly without your kind help! Besides, I have spent long-term discussions with Prof. Dr. Lijuan He and Dr. Zheng Wang for possibilities of the project. I have also received a lot of advices both about my work and career from Dr. Kai Wang, Dr. Tian Lei, Dr. Neng Gao, Dr. Yuqi Shi, Dr. Zuozhou Chen and Mr. Jiale Huang. In addition, I would also like to convey my thanks to Mr. Changshun Du, Dr. Chenghong Duan, Prof. Dr. Caifu Qian from BUCT, and Prof. Dr. Tao Jin and Dr. Ke Tang from ZJU for a variety of support you provided in my previous studies and development. I would like to thank you for the preparations you gave me in my former universities.

Besides, Miss Yanwei Huang has helped me contact the ionic liquid manufacturer. Mr. Qing He and Dr. Jinlong Li have helped me for the delivery of ionic liquid samples. Dr. Huibao Luan and Dr. Jing Ye have helped me size plate heat exchangers for the absorption testing. I would like to express my gratitude to you for the assistance when building my experimental setup.

To my old buddies, Shuilou, Dongzai, Kimy, Mage, Yuhan, Yinshan, Juanjie Sr., Juanjie Jr., Chaochao, Ruirui, Kang and Jianjian, for your constant encouragements and assistance in the last four years and before. It is always warming and comforting to meet or talk with you as if it happened in our old time. Special and additional thanks go to Xiaoba for your kind help in designing some figures and the cover of this dissertation!

My thanks go to Lige, Haoge, Leizi, Kangge, Lilaoshi, Jerry, Tengge, Fanbo. You showed me how it is living in the Netherlands and how to carry out your PhD studies, which were very important for me during my first days in Delft. Thanks to Tiange, Frank and Jiaojiaojie, not only for our nice time playing various board games and enjoying hand-made noodles but also for your constant help and support! Together with you guys, I met other funny friends in Delft, Peiyao, Daobo, UV, Xinmin and Fenglaoshi, Changzhidao and Wanlaoshi. Thanks for your company! Wish you all grow into better yourselves! Thanks to Hai, Shuai, Yazhou, Jie, Xiao, Jinyu, Meixia, Jian…, for our Phd journey in TU Delft together. Thanks to Shuaizhi, Shuaikai, Shuaiqiang, Hao, Riming, Lunmei, Xuerui, Xinlei, Lizuo and Dylan, Alice, Zhe, CY, Annie, and my USSR instructors for the happy moments in badminton courts. Thank Jiakun and Xiaoyan, Xinyuan and Feifei, Dingding, and Yan for the happy memories during our voluntary work in the ACSSNL-Delft. Thanks to my lovely ZJU alumni communities in the NL and EU.

My most sincere appreciation is for my family. My love will be always with you. Thanks to my parents and my grandma, for your unconditional support since I was born. To my grandpa in the Heaven, I am sure you are still keeping an eye on me, and are proud of my PhD achievements. My deepest gratitude goes to my best friend, Cynthia (Jiafei). Thanks for all the encouragement, support and love you offered to me, in particular here the first editing of this acknowledgment. The cover is inspired by the masterpiece - Composition with Red Blue and Yellow by Dutch painter Piet Mondrian - to memorize our encounter in Den Haag, the Netherlands.

At last, I shall thank and congratulate myself on the accomplishment and persistence along the journey! I will keep growing within myself for myself by myself.

Meng WANG
Delft, The Netherland